# Creating Novel Quantum States of Ultracold Bosons in Optical Lattices

by

Colin Kennedy

Submitted to the Department of Physics
in partial fulfillment of the requirements for the degree of

Doctor of Philosophy

at the

MASSACHUSETTS INSTITUTE OF TECHNOLOGY

June 2017



Author .....
Department of Physics
May 26, 2017

Certified by .....
Wolfgang Ketterle
John D. MacArthur Professor of Physics
Thesis Supervisor

Accepted by .....
Nergis Mavalvala
Associate Department Head

# Creating Novel Quantum States of Ultracold Bosons in Optical Lattices

by

Colin Kennedy

Submitted to the Department of Physics
on May 26, 2017, in partial fulfillment of the
requirements for the degree of
Doctor of Philosophy

## Abstract

Ultracold atoms in optical lattices are among the most developed platforms of interest for building quantum devices suitable for quantum simulation and quantum computation. Ultracold trapped atoms are advantageous because they are fundamentally indistinguishable qubits that can be prepared with high fidelity in well-defined states and read-out with similarly high fidelities. However, an outstanding challenge for ultracold atoms in optical lattices is to engineer interesting interactions and control the effects of heating that couple the system to states that lie outside the Hilbert space we wish to engineer.

In this thesis, I describe a series of experiments and theoretical proposals that address several critical issues facing ultracold atoms in optical lattices. First, I describe experiments where the tunneling behavior of atoms in the lattice is modified to make our fundamentally neutral particles behave as though they are charged particles in a magnetic field. We show how engineering this interaction creates intrinsic degeneracy in the single particle spectrum of the many-body system and how to introduce strong interactions in the system with the goal of producing exotic many-body states such as a bosonic fractional quantum Hall states. Then, I discuss how this technique can be easily generalized to include spin and higher spatial dimensions in order to access a rich variety of new physics phenomena.

Next, I report on the realization of a spin-1 Heisenberg Hamiltonian which emerges as the low energy effective theory describing spin ordering in the doubly-occupied Mott insulator of two spin components. This integer spin Heisenberg model is qualitatively different from the half-integer spin model because it contains a gapped, spin-insulating ground state for small inter-spin interaction energies which we call the spin Mott. Using a spin-dependent lattice to control the inter-spin interactions, we demonstrate high-fidelity, reversible loading of the spin-Mott phase and develop a probe of local spin correlations in order to demonstrate a spin entropy below 0.2 $k_B$ per spin. Progress on adiabatically driving the quantum phase transition from the spin Mott to the $xy$-ferromagnetic is discussed along with the progress towards the creation of a quantum gas microscope for single atom detection and manipulation.

Thesis Supervisor: Wolfgang Ketterle
Title: John D. MacArthur Professor of Physics

# Acknowledgments

The past six years at MIT has been a time of immense personal and professional growth for me. Living in Cambridge and Somerville with the opportunity to work and live in such an amazing place with a diverse set of backgrounds and experiences has truly been a transformative experience for me. Along the way there have been many people, more than can be named here in this thesis, who have influenced me and encouraged me to be a better person and a better physicist.

First and foremost, I acknowledge my thesis advisor Wolfgang Ketterle to whom I owe the deepest debt of gratitude. It is hard to put into words the breadth of what I have learned from him and his fantastic mentorship. His unending optimism, creativity, and energy for physics is truly amazing. I am extremely privileged to have the opportunity to learn from him and to explore physics in the Rb lab. I have also had the privilege of working with and learning from many phenomenal teachers and mentors along the journey to this point, without whom none of this would be possible. Among a list of many excellent teachers, I especially thank Chris Hahn, Jill Pecan-Slattery, Luis Orozco, John Rodgers, and Howard Milchberg for being inspirational figures in my education and research experiences.

When I first started in the Rb lab at MIT, the two senior members at the time were Hiro Miyake and Georgios Siviloglou whom I thank for teaching me in such an open and inviting manner all the ins and outs of operating an ultracold atoms machine. I was an overly-eager first year student, and I cannot thank you enough for your patience with my outlandish ideas and for giving me the room to explore and fail, even if I happen to kill the spin-dependent lattice laser diode. The data and ideas presented in this thesis would not be possible without their help in addition to the insight and enthusiasm brought by the two junior students on the machine, Cody Burton and Woo Chang Chung. Cody and Woo Chang have been excellent lab mates and I thank them for their steady hand in dealing with the various disasters the machine has thrown our way. Between rebuilding the water manifold after the great water disaster, vinegar flushes of blocked coils, dead chillers and pumps, literally

floating magnetic field coils, and stubbornly hot atoms in the lattice, I cannot thank you both enough for your persistence and level-headed approach to solving all the problems the machine has thrown in our way over the years. Wenlan Chen joined the lab recently as a postdoc and has quickly proved to be a valuable lab member. Her quantitative approach to understanding lattice heating and her leadership has helped us make great strides both technically and scientifically during her tenure in the lab. Finally, I thank the undergraduate and masters students who have worked in the lab, Yichao Yu, Benedikt Groever, Yuri Lenskiy, and Samarth Vadia, for their hard work in making many crucial improvements to our experiment.

When I first arrived at MIT, I started working in the BEC3 experiment, where I learned many things from the senior members at the time: Myoung-Sun Heo, Tout Wang, and Timur Rvachov. I thank you all for your patience and I especially thank Timur who, in addition to being an incredibly fast learner, is also an excellent basketball player, and a fun hiking companion. I will forever be indebted to the members of BEC5: Jesse Amato-Grill, Ivana Dimitrova, Niki Jepsen, Michael Messer, and Will Lunden, from whom I have learned much. Our mutual struggles to cool atoms in optical lattices has resulted in a long-running informal collaboration and great friendships. Whether discussed over a Sebastian's lunch or beers at CBC, working through technical problems with laser cooling, optical lattices, feedback and control circuits, etc. with you all has been a wonderful learning experience for me and I cannot thank you enough. I especially thank Jesse and Ivana with whom I have had many insightful discussions about the big picture of career, life, and societal issues. I will miss hanging out in your lab and hearing Niki and Jesse whistling the Star Wars movie soundtracks every time I walk by the lab.

I also thank the members of BEC2, especially Junru Li and Chris Lee, for many valuable discussions. I hope that the collaboration between our labs only increases over time. Dypole is the newest lab in the group, and seeing the planning process and the initial stages of construction has been very exciting. I thank Michael Cantara for taking up the challenge of improving my AOM driver design as well as for bringing his talent for hitting home runs to the softball team.

The CUA has many excellent scientists that I have had the privilege of getting to know over the course of my time here at MIT, including Alan Jamison, our lab senior scientist, whose vision and knowledge of physics, as well as life outside the lab, I respect highly. From the Zwierlein group I learned many valuable lessons about atoms and molecules from Sebastian Will, Julian Struck, and Tarik Yefsah and I thank them for their humorous and friendly approach to discussing these things. I thank Lawrence Cheuk, Matt Nichols, and Katherine Lawrence for kindly answering all my questions about microscopes during the initial phases of our design process. The members of the Zwierlein group have certainly enriched my experience here at MIT and I thank Parth Patel, Zhenjie Yan, Zoe Yan, and Vinay Ramasesh, in addition to Lawrence, Matt, and Katherine for being the friendly and outgoing people that makes the CUA a more human place.

Life outside of lab was enriched immensely with the help of my great friends Boris Braverman, Dan Kolodrubetz, and Reed Essick. I remember fondly our many gastronomical adventures into anything from cheese and scotch to hot dogs and duck prosciutto, as well as various bike trips like going to Walden pond only to get turned away, being stuck in a kayak in a massive thunderstorm on the 4th of July, or simply barbecuing outside of Sidney Pacific. Regardless of what adventure is happening I will enjoy your company. Although she spent most of her time at CERN, Doğa Gülhan was an great addition to our friend group. Her cheerful disposition makes everyone's day a little happier.

For the past five years, I have been fortunate enough to live in an amazing house with some great friends: Anton Goloborodko, Sam Schaub, Becky Schaub, Hong Sio, Hamed Pakatchi, and Sam Markson. Anton, Sam, Becky, Hong, and I share a love for hiking the White Mountains in New Hampshire and I thank them for being such excellent hiking companions. I always enjoy the wide-ranging conversations we have on a hike and I will miss our bad jokes and the inevitable rush to make it down the mountain before the sun sets. Hamed and Sam, in addition to being always ready to go for lunch at the local Indian buffet, have an impressive depth of knowledge from which I have learned a great deal. I am especially thankful for

Hamed for helpful discussions trying to sort out the opaque terminology surrounding the fraction quantum Hall effect and the classifications of different types topological states of matter. The diverse set of backgrounds and perspectives that everyone in the house brings makes me appreciate our discussions of society and politics for which I am thankful.

Rotem and Ronni Gura-Sadovsky have been my friends since the very first months of my time here at MIT. Both have incredibly warm and inviting personalities that makes one feel at ease, or in their own words, "aggressively casual". I am also grateful to Stefanie Le for her friendship and inspiration. Her passion for books and the humanity revealed through their stories has made me more aware of the world around me and has rekindled the interest in literature that my obsession with physics had all but extinguished. There are many people I became friends with in college that I am thankful have remained a part of my life after we all moved away from Maryland, including: Chris DeCaro, Michelle DeCaro, Mary Tellers, Becca Certner, Melanie Turlington, Donnie Turlington, Dylan Rebois, Ethan Schaler, Sydney Chavis, and Vadim Kashtelyan. Whether we are meeting up over the Thanksgiving holiday, traveling to another epic beach weekend, going for a camping trip, or simply eating chive fries and discovering strange beers on tap at Sunset, thank you all for your continued friendship.

An important aspect of my life outside of the lab has been my involvement in many sports leagues and teams. Over the years I have been a part of the physics soccer, basketball, and softball teams as well as the Tang Hall soccer, basketball, and volleyball teams. I especially thank Sydney Do, MJ Abdolhosseini, and Heather Beem for getting me out of the lab and involved with the Tang sports teams. I also thank the Waverly Oaks basketball team, and especially Timur Rvachov and Justin Foster for many entertaining rides to and from the games. I will miss long morning runs along the Charles river and the picturesque views of the Boston skyline that it affords.

Finally, I thank my Mom and Dad, and the rest of my family, Michael, Ryan, Jackie, and Sam, without whom none of this would be possible.

# Contents

# List of Figures

# Chapter 1

# Introduction

Ultracold atoms in optical lattices represent one of the most promising platforms for studying complex many-body quantum systems. One important reason for the intense interest in such atomic systems is the clean, well-characterized, precisely controllable nature of each sample. This enables the experimenter to create and detect physics from intuitive demonstrations of quantum single-particle physics with high signal-to-noise to complex many-body physics with precise controllability. Along these lines the field of ultracold atoms has produced many iconic results ranging from the realization of atomic Bose-Einstein condensates (BECs) [6, 38, 20] and degenerate Fermi gases (DFGs) [63, 132, 177, 176] to detailed studies of superfluidity in these systems at all interaction scales from the weakly interacting limit to the unitary limit [84, 85].

One of the most important examples of a strongly interacting state of matter realized with ultracold atoms is the realization of both bosonic and fermionic Mott insulators by loading an ultracold gas into an optical lattice [62, 78, 139]. For bosons, the optical lattice realizes a quantum phase transition between a superfluid state and a Mott insulating state. The realization of this quantum phase transition has led to groundbreaking studies of the dimensional dependence, including in one-dimension the Tonks-Girardeau gas [126], hidden string-order parameters [45], magnon bound states [50], spin and entanglement transport [49], and direct measurements of entanglement entropy [75]; in two-dimensions the evolution of the Higgs mode [46] and single-atom imaging of the many-particle system [9, 143, 127, 32, 124, 66, 44];

and in three-dimensions the dependence on exotic lattice geometries [77, 150] among many other studies. The more recent realization of fermionic Mott insulators has also quickly led to observation of short range antiferromagnetic correlations in one-, two-, and three-dimensional systems [61, 68, 18, 30, 41] as well as observations of long range antiferromagnetic states [115, 22]. Throughout all the above results, the impeccable cleanliness and control of ultracold atoms in optical lattices has been a key asset for creating and detecting these important states. For these reasons, ultracold atoms in optical lattices remain one of the most promising platforms for realizing and studying exotic quantum many-body states of matter.

In recent years, two important directions have emerged in the ultracold atom community. The first is the creation of synthetic gauge potentials and spin-orbit coupling leading to the realization of topological states of matter [103, 59], and the second is the realization of extremely low temperature states of matter enabling the detection of long-range magnetic correlations [115, 22]. Gauge potentials and, most importantly, gauge symmetry, have been central concepts in modern physics starting with the formulation of quantum electrodynamics, leading to an understanding of non-Abelian gauge fields and electroweak symmetry breaking [36], and culminating with the formulation of the standard model of particle physics [128]. Emergent gauge potentials also play an important role in condensed matter physics, playing a crucial role in our understanding of diverse systems from quantum critical points in two-dimensional magnetic systems [142] to the binding of electrons and vortices in Chern-Simons theories of the fractional quantum Hall states [106].

In cold atoms, these fields do not arise naturally in the many-body context because the constituent particles are neutral, and thus do not couple directly to any gauge potential. An important development in the field has thus been the creation of synthetic gauge fields for neutral ultracold atoms [103, 59]. This accomplishment has also both raised the possibility of creating topologically ordered states of matter by creating states analogous to the two-dimensional electron gas in a magnetic field [76] as well as generated considerable interest in engineering new, effective Hamiltonians using periodic driving of many-body systems – sometimes referred to as Floquet en-

gineering [57, 56]. The creation of such large effective magnetic fields in an optical lattice using such periodic driving techniques is one of the main focuses of the work discussed in this thesis.

A second important direction of theoretical and experimental research in ultracold atoms is towards realization of extremely low entropy states of matter in an optical lattice. For example, in order to study many interesting phases of matter, such as ferromagnetic and antiferromagnetic states, the entropy must be sufficiently low to develop long-range ordering. For magnetic systems, the corresponding temperature scale to realize such low entropies is determined by the exchange interaction energy scale. As a result, to realize a magnetically ordered states of $^{87}$Rb atoms in optical lattices the corresponding temperature one needs to realize is on the scale of many tens of picokelvin, a temperature that has proven difficult so far for the field of ultracold atoms to reach. Realizing extremely low spin entropies, and how to turn this low entropy state into a magnetically ordered, low temperature state, is the second main focus of this thesis.

This structure of the thesis is as follows. I will outline some of the big-picture problems that we hope to address using the study of cold atoms and highlight why these are hard problems to solve. Then I will discuss several useful toy models for understanding the physics to conclude chapter 1. In chapter 2 I will discuss in detail the both the theoretical and experimental aspects of the implementation of an optical lattice in the lab and then the realization of strong artificial magnetic fields in both chapters 3 and 4. The focus will next shift to realization of ultralow temperatures in chapter 5 before concluding with some outlooks in chapter 6.

## 1.1 Many-body Physics - Why is this Hard?

In principle, the physics of a collection of many non-relativistic, interacting particles in a box is fully encapsulated in the many-particle Hamiltonian:

$$H = \sum_{i=1}^{N} \frac{\mathbf{p}_i^2}{2m_i} + \sum_{j \neq i} V(\mathbf{r}_i, \mathbf{r}_j) \tag{1.1}$$

where $\mathbf{p}_i$ is the momentum of the $i$-th particle and $V(\mathbf{r}_i, \mathbf{r}_j)$ is a generic interaction between any two particles $i$ and $j$ in the system. This equation is solvable for systems of one or two particles, but, given a form of the interaction, the solution is not generally accessible for a thermodynamically large number of particles, $N$.

Remarkably, much progress has been made in the understanding of materials by solving for the spectrum of a single particle and using the resulting basis of states to understand at a perturbative level through scattering calculations how interactions both qualitatively and quantitatively change the resulting character of the single particle states compared to the observed many-particle states. Such approaches have given rise to an understanding of many phases of matter such as metals and band insulators and also forms the theoretical basis for the physics underlying the modern semiconductor industry. In this picture, the interacting electron system closely resembles a non-interacting electron system and is understood using Fermi-liquid theory [13].

However, to account for additional and unexpected phases that strong interactions bring we want to move beyond Fermi-liquid theory. One might be tempted to accomplish this task by keeping track of all the states on the Hilbert space and attempt to diagonalize the resulting Hamiltonian. To give a concrete example, take an arbitrary spin-1/2 system and try to write down the basis for increasing numbers of spins. The bases for calculating the Hamiltonian scale as:

$$\text{2 Particles:} \quad \{|\uparrow\uparrow\rangle, |\uparrow\downarrow\rangle, |\downarrow\uparrow\rangle, |\downarrow\downarrow\rangle\} \tag{1.2}$$

$$\text{3 Particles:} \quad \{|\uparrow\uparrow\uparrow\rangle, |\downarrow\uparrow\uparrow\rangle, |\uparrow\downarrow\uparrow\rangle, |\uparrow\uparrow\downarrow\rangle, |\downarrow\uparrow\downarrow\rangle, |\downarrow\downarrow\uparrow\rangle, |\uparrow\downarrow\downarrow\rangle, |\downarrow\downarrow\downarrow\rangle\} \tag{1.3}$$

$$\begin{aligned}\text{4 Particles:} \quad \{&|\uparrow\uparrow\uparrow\uparrow\rangle, |\downarrow\uparrow\uparrow\uparrow\rangle, |\uparrow\downarrow\uparrow\uparrow\rangle, |\uparrow\uparrow\downarrow\uparrow\rangle, |\uparrow\uparrow\uparrow\downarrow\rangle, |\uparrow\uparrow\downarrow\downarrow\rangle \dots \\ &\dots |\uparrow\downarrow\uparrow\downarrow\rangle, |\uparrow\downarrow\downarrow\uparrow\rangle, |\downarrow\downarrow\uparrow\uparrow\rangle, |\uparrow\downarrow\downarrow\downarrow\rangle, |\downarrow\uparrow\downarrow\downarrow\rangle, |\downarrow\downarrow\uparrow\downarrow\rangle, \dots \\ &\dots |\downarrow\downarrow\downarrow\uparrow\rangle, |\downarrow\downarrow\downarrow\downarrow\rangle\}\end{aligned} \tag{1.4}$$

$$\text{5 Particles:} \quad \dots \tag{1.5}$$

From this simple exercise of writing down the basis of a spin-1/2 chain we can see that simply expressing the basis is an exponentially hard problem, scaling as $2^n$. For

comparison, in order to keep track of the full quantum state for just 300 spins we need to store $2^{300} \approx 10^{90}$ exponentially small complex numbers, a number $\sim 10^{10}$ times larger than the number of atoms in the visible universe! The problem is made even worse for the spin-1 chain that will be considered in chapter 5 where the basis size scales as $3^n$. As a result, we wish to find some other way of capturing the essential physics of a many-particle system that does not rely on explicitly writing down the full many-body basis. Otherwise, understanding the physics of a quantum many-body state remains a fundamentally intractable problem due to the scaling of the basis size with particle number.

### 1.1.1 Mean-Field Theory

The simplest and most widely used approach to handling the theoretical complexity of the quantum many-body problem falls under the general scope of mean-field theories. In the case of an interacting spin system, this mean field assumption arises from treating the interaction terms with the assumption that individual quantum particles interact with a classical field composed of the mean-value of the surrounding spins. In this way, much of the complexity of correlations induced by interactions are ignored and, for some theories, is successful in distilling the exponential complexity to a few parameters which describe the physics of the resulting quantum state. Although this works in many cases such as weakly interacting superfluids and three-dimensional ferromagnets, there are many interesting states for which particle correlations play a fundamental role in determining the resulting properties of the quantum state; for example the unitary Fermi gas equation of state [89] or more dramatically the appearance of the fractional quantum Hall states over Wigner crystallization in the ground state of the two-dimensional electron gas [94, 146, 152].

Regardless, the mean-field approximation has proven to be highly effective for many quantum states, so we begin by discussing the underlying reason it is so successful: because fluctuations in such systems are small compared to the average value. This allows for approximating interaction term via what is called a decoupling approximation. For a concrete example, we take a perturbation term such as the tunneling

term perturbing the atomic limit Mott insulator, a result we will see in chapter 2:

$$V' \propto \hat{a}_i^\dagger \hat{a}_j. \tag{1.6}$$

We can exactly re-write this term as fluctuations around some average value we will define to be the order parameter, $\psi = \langle \hat{a}_i \rangle$:

$$\begin{aligned}
\hat{a}_i^\dagger \hat{a}_j &= (\hat{a}_i^\dagger - \langle \hat{a}_i^\dagger \rangle + \langle \hat{a}_i^\dagger \rangle)(\hat{a}_j - \langle \hat{a}_j \rangle + \langle \hat{a}_j \rangle) && (1.7)\\
&= (\hat{a}_i^\dagger - \langle \hat{a}_i^\dagger \rangle)\langle \hat{a}_j \rangle + (\hat{a}_j - \langle \hat{a}_j \rangle)\langle \hat{a}_i^\dagger \rangle + \langle \hat{a}_i^\dagger \rangle \langle \hat{a}_j \rangle + (\hat{a}_i^\dagger - \langle \hat{a}_i^\dagger \rangle)(\hat{a}_j - \langle \hat{a}_j \rangle) && (1.8)\\
&= \delta \hat{a}_i^\dagger \langle \hat{a}_j \rangle + \delta \hat{a}_j \langle \hat{a}_i^\dagger \rangle + \langle \hat{a}_i^\dagger \rangle \langle \hat{a}_j \rangle + \delta \hat{a}_i^\dagger \delta \hat{a}_j && (1.9)
\end{aligned}$$

where we have defined new fluctuation operators $\delta \hat{a}_j = (\hat{a}_j - \langle \hat{a}_j \rangle)$. The underlying assumption that makes mean field theory work is that the fluctuations from the average value are not large. Crucially, this assumption allows us to neglect the last term in equation 1.9 which corresponds to the product of two small numbers. This approximation is generally called the decoupling approximation, and leads to a tractable perturbation term:

$$\begin{aligned}
\hat{a}_i^\dagger \hat{a}_j &\approx \delta \hat{a}_i^\dagger \langle \hat{a}_j \rangle + \delta \hat{a}_j \langle \hat{a}_i^\dagger \rangle + \langle \hat{a}_i^\dagger \rangle \langle \hat{a}_j \rangle && (1.10)\\
&= \hat{a}_i^\dagger \langle \hat{a}_j \rangle + \hat{a}_j \langle \hat{a}_i^\dagger \rangle - \langle \hat{a}_i^\dagger \rangle \langle \hat{a}_j \rangle && (1.11)\\
&= \hat{a}_i^\dagger \psi + \hat{a}_j \psi^* - \psi^2 && (1.12)
\end{aligned}$$

From the form of equation 1.12 we can interpret this decoupling approximation as treating individual states as though they interact with a background field composed of the average value of all other states in the sample, i.e. the mean-field. This order parameter, $\psi$ now becomes a variational parameter used to minimize an energy functional in order to find the ground state configuration of the system. An important example of such a calculation is seen in chapter 2 in order to determine the superfluid to Mott insulator phase diagram.

If we look at the form of the term dropped in making the mean-field approx-

imation: $\delta\hat{a}_i^\dagger \delta\hat{a}_j$ we see that this term can become large, and thus the underlying assumption of this approximation breaks down, when correlations between fluctuations become on the order of the average value of the order parameter. Typically, this approximation can be broken by introducing sufficiently strong inter-particle interactions at which point the position of one particle can become strongly correlated with the positions of all the other particles in the system. In the discussion of fractional quantum Hall states in the next section, this will appear prominently in the two-particle wavefunction as well as the Laughlin wavefunction as the amplitude of the wavefunction of one particle will depend sensitively on its position relative to the other particles in the problem.

### 1.1.2 Why is Magnetism Quantum?

The second part of this thesis will address the questions of preparing low entropy states of matter with a special emphasis on the spin-1 Heisenberg model. In general, the problem of such magnetic states of matter can also highlight the importance of capturing electron correlation in a many-body wavefunction. To understand this, we first examine a classical argument for why magnetism must be quantum-mechanical in origin.

The argument follows that considered in the Bohr-van Leeuwen theorem [17, 47] which considers an isolated, non-rotating ensemble of classical particles. In essence, the proof shows that such classical particles cannot have a magnetic moment in thermal equilibrium. Consider the classical Hamiltonian for a charged particle:

$$H = \sum_i \left( \frac{(\vec{p}_i + q_i \vec{A}_i)}{2m_i} \right)^2 + q_i \phi \tag{1.13}$$

The magnetic moment, $\mu$, can be calculated via the partition function, $Z = \int d^3p \int d^3r e^{-\beta H}$,

where $\beta = \frac{1}{k_B T}$, as the statistical average of the constituent magnetic moments:

$$\langle \mu \rangle = \frac{\partial}{\partial B}\left(\frac{\partial \ln Z}{\partial \beta}\right) = \left[\int d^3r \int d^3p \, \frac{e}{2c}(\mathbf{r} \times \mathbf{v}) e^{-\beta H}\right] \Big/ Z \tag{1.14}$$

$$= \left[\int d^3r \int d^3p \, \frac{e}{2c}\Big(\mathbf{r} \times \Big(\frac{\mathbf{p}}{m} - \frac{e}{mc}\mathbf{A}\Big)\Big) e^{-\beta H}\right] \Big/ Z \tag{1.15}$$

$$\propto \int_{-\infty}^{\infty} dp \, p \, e^{-p^2} = 0 \tag{1.16}$$

Examining the expression in equation 1.15, we see that the integral over all momenta will force the magnetic moment to be identically zero. This is because the scalar and vector potential only depend on the coordinates, $\mathbf{r}$, so the integrand is an odd function of $\mathbf{p}$. As a result, integration over all momenta from positive to negative infinity will always give a classical, magnetic moment that is zero. The interpretation of this result and its many generalizations to broader circumstances is that the origins of magnetism are strictly quantum mechanical in nature [47].

Now that we know we will need a quantum mechanical description of our system to understand magnetism, we consider several energy scales upon which magnetic properties are observed in order to look for clues as to their origins. As a simple example we consider the hydrogen molecule, $H_2$. If we consider that the electron has a quantum-mechanical spin which contains a magnetic moment that may circumvent the Bohr–van Leeuwen theorem, we can calculate the expected interaction energy of aligned versus anti-aligned spins via the dipole-dipole interaction and a mean inter-particle distance of the size of the hydrogen bond length, $\sim 1a_0$. Assuming dipoles aligned head-to-tail, the energy shift of one electron in the field produced by the other electron is on the order of 1 meV. However, we see magnetic materials in our day-to-day lives whose magnetism survives thermal energies of >300 K, an energy scale above ∼40 meV, more than an order of magnitude higher than one would expect from dipole-dipole interactions alone.

The answer to this apparent discrepancy arises instead from the antisymmetrization requirement for a multi-particle fermionic wavefunction. To understand this, we consider the hydrogen molecule as a two-site analog of a many-particle spin sys-

tem. For hydrogen, the two-particle wavefunction must be antisymmetric with respect to particle exchange, so if we write the wavefunction as a separable function, $\psi \propto \psi_{\text{space}}\chi_{\text{spin}}$, of the spatial and spin degrees of freedom, the requirement for total antisymmetry of the wavefunction means that the anti-symmetric or symmetric spin-state of the electronic wavefunction effects the respective symmetry or anti-symmetry of the spatial wavefunction. This is the key to understanding how the triplet or singlet nature of the spin state gets promoted to ∼eV energy scales. To see this, expectation values of the molecular Hamiltonian within the Born-Oppenheimer approximation [91] can be constructed using the symmetric and anti-symmetric spatial wavefunctions, yielding an effective spin model for the total energy as a function of the internuclear separation, $R$:

$$E_{\pm} = \epsilon(R) + J(R)\Big(\hat{S}_1 \cdot \hat{S}_2 + \frac{1}{4}\Big). \tag{1.17}$$

The parameter $J$ sets the energy scale for the spin-dependent energy, which, from the matrix elements of the Hamiltonian, is mostly determined by the exchange part of the electron-electron interaction, a large $\sim$ eV energy scales in the problem!

From this simple model we gain a clear picture as to why having a complete picture of many-body quantum correlations is important in understanding magnetism: spin-spin interactions, which we might normally ignore due to their seemingly low energy scale, can have a profound effect on the macroscopic quantum state. Looking at the hydrogen molecule as a simple, two-site model of an interacting electron system, we see that the spin state can interplay with the charge degrees of freedom in order to make magnetic effects visible on the eV scale as a result of electron-electron interactions. As a result, we are interested in simulating the effects of electron-electron repulsion in a truly many-particle system to see what new states of matter might emerge in such a situation. One classic example of this effect that we will discuss next, is in the strongly interacting regime of the quantum Hall effect wherein the qualitatively new features of the fractional quantum Hall effect are realized.

## 1.2 Topological Phases of Matter

The fractional quantum Hall states are some of the best known examples of topologically ordered phases of matter. Topologically ordered states comprise a class of quantum phases which are not characterized by any symmetry-breaking as in Landau-Ginzberg theory, but instead are characterized by ground state degeneracy [163], long-range entanglement, edge states, and fractional statistics [162]. Such states are gapped in the bulk where the band structure can be characterized by a topological invariant. States with different topologies cannot smoothly be deformed into one another without the closing of a bulk energy gap, so at the boundary of the material there are necessarily protected edge modes. To understand this effect, we work with the toy model of two-dimensional electrons in a magnetic field, the classic problem of Landau levels.

In the next subsection, we will develop the theoretical framework under which we will proceed to discuss in the following subsections the integer and fractional quantum Hall effects. For an intuitive discussion of these states as motivation for ultracold atom experiments, skip to sections 1.2.2 and 1.2.3.

### 1.2.1 Landau levels

We begin with the single-particle Hamiltonian for a particle of mass, $m$, and charge, $e$ coupled to an externally applied vector potential, $\mathbf{A}$:

$$H = \frac{(\mathbf{p} - \frac{e}{c}\mathbf{A})^2}{2m}. \tag{1.18}$$

In the following, we will use the symmetric gauge for the applied field such that, $\mathbf{A} = B(-y\hat{e}_x + x\hat{e}_y)/2$, and $\mathbf{B} = \nabla \times \mathbf{A}$ corresponds to a uniform magnetic field oriented in the $z$-direction. We define the cyclotron frequency such that, $m\omega_c = \frac{eB}{c}$ and the Hamiltonian simplifies to the following form when we express it in terms of

new momentum operators, $\hat{\Pi}_x = \hat{p}_x + \frac{1}{2}m\omega_c\hat{y}$ and $\hat{\Pi}_y = \hat{p}_y - \frac{1}{2}m\omega_c\hat{x}$:

$$H = \frac{1}{2m}\left(\left(\hat{p}_x + \frac{1}{2}m\omega_c\hat{y}\right)^2 + \left(\hat{p}_y - \frac{1}{2}m\omega_c\hat{x}\right)^2\right) = \frac{1}{2m}\left(\hat{\Pi}_x^2 + \hat{\Pi}_y^2\right). \tag{1.19}$$

An important and recurring scale that will become crucial to understanding the physics is the length scale associated with the magnetic flux, $l = \sqrt{\frac{\hbar}{m\omega_c}} = \sqrt{\frac{\hbar c}{eB}}$. Using this definition of the magnetic flux length we find a simple factorization of equation 1.2.1 into a product of the sum and difference of their two constituent operators:

$$\hat{a} = \frac{l}{\sqrt{2}\hbar}\left(\hat{\Pi}_x + i\hat{\Pi}_y\right) \tag{1.20}$$

$$\hat{a}^\dagger = \frac{l}{\sqrt{2}\hbar}\left(\hat{\Pi}_x - i\hat{\Pi}_y\right). \tag{1.21}$$

We can now re-write the Hamiltonian in terms of the raising and lowering operators such that the problem looks like that of a one dimensional harmonic oscillator:

$$\hat{H} = \hbar\omega_c\left(\hat{a}^\dagger\hat{a} - \frac{1}{2}\right). \tag{1.22}$$

It is remarkable that we have taken a two dimensional problem and reduced it to a one-dimensional one by a coordinate transformation! What's going on? The problem becomes more transparent when we change coordinates to a coordinate system that more closely reflects the symmetry of the underlying vector potential. To do so, we identify a new coordinate, $z = x + iy$, and the derivative of that coordinate, $\partial_z = \partial_x - i\partial_y$, (note that $\partial_z z = 2$, an important factor of 2!) such that the raising and lowering operators can be rewritten as:

$$\hat{a} = \frac{-i}{\sqrt{2}}\left(\frac{z}{2l} + l\partial_{z^*}\right) \overset{l=1}{=} \frac{-i}{\sqrt{2}}\left(\frac{z}{2} + \partial_{z^*}\right) \tag{1.23}$$

$$\hat{a}^\dagger = \frac{i}{\sqrt{2}}\left(\frac{z^*}{2l} - l\partial_z\right) \overset{l=1}{=} \frac{i}{\sqrt{2}}\left(\frac{z^*}{2} - \partial_z\right) \tag{1.24}$$

For compactness of notation, we will set $l = 1$ until we want to reintroduce a length scale for interpretive reasons. We can understand the wavefunction of the states which diagonalize the Hamiltonian by applying the lowering operator to the vacuum wavefunction and solving the resulting differential equation:

$$\langle z, z^*|\hat{a}|\mathrm{GS}\rangle = \Big(\frac{z}{2} + \partial_{z^*}\Big)\psi = 0 \tag{1.25}$$

$$\psi_n(z, z^*) = f(z)e^{-zz^*/2} = N_n z^n e^{-|z|^2/2}. \tag{1.26}$$

Most importantly, we see that in solving the integral for the wavefunction in equation 1.26 there exist an infinite family of solutions, all describing the same energy state of the Hamiltonian, each with a different, analytic function of $z$ as a prefactor. Hinting at a future solution to this problem, we will express this arbitrary, analytic function of $z$ as a normalization constant, $N_n = (\pi n!)^{-1/2}$ times a polynomial factor $z^n$.

Examining the wavefunction in 1.26, we see that this family of states corresponds to a series of localized gaussian wavepackets with average radius governed by the power of the polynomial factor, $n$, as $\langle r^2\rangle = \sqrt{2}(n+1)$. Given the form of the ground state wavefunctions as localized, circular states, an interesting question to ask is: are these states also angular momentum eigenstates? We can construct the angular momentum operator in terms of the circular coordinates, $z$ and $z^*$ and use them to operate on the family of wavefunctions, $\psi_n(z, z^*)$:

$$\begin{aligned} L_z\psi_n(z, z^*) &= (xp_y - yp_x)\psi_n(z, z^*) && (1.27)\\ &= \hbar(z\partial_z - z^*\partial_{z^*})\psi_n(z, z^*) && (1.28)\\ &= n\hbar\psi_n(z, z^*). && (1.29) \end{aligned}$$

Therefore, we see that each polynomial of power $n$ is simultaneously both a lowest energy eigenstate of the Hamiltonian and an eigenstate of angular momentum with $z$-projection $n\hbar$.

We can systematically construct these states via canonical quantization of the variables conjugate to the generalized momenta, $\Pi_x$ and $\Pi_y$ introduced earlier, the

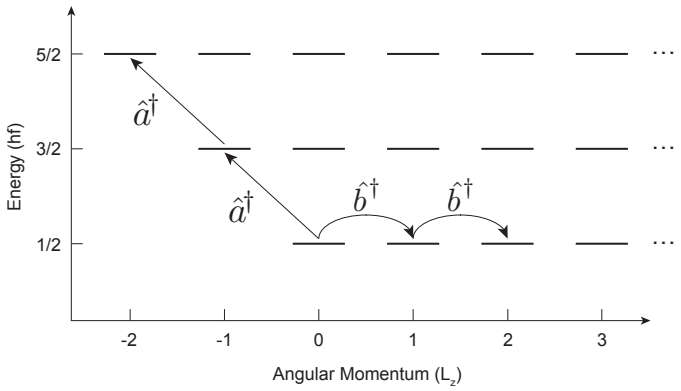


Figure 1-1: The spectrum of Landau levels. Each manifold of states is equally spaced by the cyclotron energy, $\hbar\omega_c$ and is $N$-fold degenerate. Each state in the series of Landau levels can be constructed by sequential application of the two creation operators, $\hat{a}^\dagger$, which promotes a particle to a higher Landau level, and $\hat{b}^\dagger$, which raises the angular momentum state of the particle within a Landau level.

generalized coordinates, $X$ and $Y$. However, we take a different approach here by taking inspiration from equation 1.26 and applying another operator, $\hat{b}$, that annihilates the lowest angular momentum eigenstate:

$$\langle z, z^*|\hat{b}|\mathrm{GS}\rangle = B(z, z^*)e^{-zz^*/2} = 0 \tag{1.30}$$

$$\text{Ansatz: } \Big(\frac{z^*}{2} + \partial_z\Big)e^{-zz^*/2} = 0 \tag{1.31}$$

$$\hat{b} = \frac{1}{\sqrt{2}}\Big(\frac{z^*}{2} + \partial_z\Big) \tag{1.32}$$

$$\hat{b}^\dagger = \frac{1}{\sqrt{2}}\Big(\frac{z}{2} - \partial_{z^*}\Big). \tag{1.33}$$

We can check that the operator $\hat{b}$ is exactly what one would get from canonical quantization, and it properly follows the commutation relation $[\hat{b}, \hat{b}^\dagger] = 1$. In addition, we find that sequential application of the raising operator $\hat{b}^\dagger$ to the ground state wavefunction with polynomial order $n$, has the effect of raising the angular momentum of the state while keeping the state within the ground state manifold,

$$\hat{b}^\dagger|n\rangle = |n+1\rangle \tag{1.34}$$

From the action of both operators $\hat{a}$ and $\hat{b}$ on the gaussian wavefunction we can

construct the entire spectrum of states. This spectrum is sketched in figure 1-1.

### 1.2.2 Landau levels and the IQHE

Now that we have solved for the spectrum and the wavefunctions, we return to the question of topology. How can I see the underlying topology of this state and characterize when it changes?

We begin by formulating the underlying translation symmetry of this state. In analog to a free-particle system where the momentum operator is the generator of translations, we use the canonical momentum of this system to define a translation operator:

$$T(\mathbf{d}) = e^{-i\mathbf{d}\cdot\mathbf{\Pi}/\hbar} = e^{-i\mathbf{d}\cdot(\mathbf{p}-\frac{e}{c}\mathbf{A})/\hbar}. \tag{1.35}$$

Note that this translation operator is gauge-dependent, and related to the translation operator in different gauges by a simple gauge transformation. In addition, different translations do not necessarily commute as shown by operation on the wavefunction at some location, $\psi(x, y)$ with the translation operators:

$$T(d_y)T(d_x)\psi(x,y) = e^{-i\frac{d_y x}{2l^2}} e^{i\frac{d_x(y+d_y)}{2l^2}} \psi(x+d_x, y+d_y) \tag{1.36}$$

$$T(d_x)T(d_y)\psi(x,y) = e^{i\frac{d_x y}{2l^2}} e^{-i\frac{d_y(x+d_x)}{2l^2}} \psi(x+d_x, y+d_y) \tag{1.37}$$

such that the commutation relation between the two directions can be established as:

$$T(d_x)T(d_y)\psi(x,y) = e^{i\frac{d_y d_x}{l^2}} T(d_y)T(d_x)\psi(x,y). \tag{1.38}$$

We now see that, in general, these translation operators do not commute for arbitrary translations. However, for $d_x d_y/l^2 = 2\pi n$, where $n$ is an integer, the operators commute and we then have a good set of operators to formulate a discrete translation symmetry! Formally, this relation is known as the Dirac quantization condition.

We can now use our operators with discrete translation symmetry of $d_{x,y} = l$ to formulate Bloch's theorem to construct a momentum-space wavefunction, as we show for an optical lattice in chapter 2. Since we are interested in the topology of the band,

we wish to evaluate the Berry connection [69]:

$$\mathbf{A} = i\langle\phi_k|\nabla_k|\phi_k\rangle = (-k_y l^2 \hat{e}_x + k_x l^2 \hat{e}_y)/2, \tag{1.39}$$

which, perhaps unsurprisingly, looks like the underlying vector potential. We can prove that the Berry connection is in fact gauge dependent, and changes depending on the underlying vector potential because the symmetry of the vector potential is reflected in the modified translation symmetry used to formulate the Bloch wavefunctions. Despite the apparent gauge-dependence of the Berry connection, we can compute two gauge invariant quantities, the Berry flux, $\mathbf{B}$ and Chern number,$C$:

$$\mathbf{B} = \nabla \times \mathbf{A} = l^2 \hat{z} \tag{1.40}$$

$$C = \int_{\mathrm{BZ}} d\mathbf{k}\, \mathbf{B} = B \times (\mathrm{BZ\ Area}) = 1. \tag{1.41}$$

For a general quantum state, these are gauge-invariant quantities which encode the topological quantum number of the state [69]. The Hall conductance which is traditionally measured by measuring the transverse conductance in a transport experiment can be calculated from the Chern number by the relation:

$$\sigma_{xy} = C\frac{e^2}{\hbar} \tag{1.42}$$

A useful way to visualize this effect is seen in figure 1-2 by plotting the energy of the Landau levels as a function of position in the sample [99]. In the bulk, the system behaves ideally; however, at the interface between the 2D electron gas and a trivial state, such as the vacuum or a high bandgap insulator, the gaps of the Landau level spectrum must close in order to transform into a topologically trivial state with zero Chern number. Therefore, at the edges the Landau levels of the bulk system necessarily cross the chemical potential, $\mu$, shown by the dotted line in figure 1-2, at which point the insulting nature of the bulk breaks down and a conduction channel opens. The Hall conductance is given by the number of states which cross the chemical potential on the edge multiplied by the Chern number of each band. In

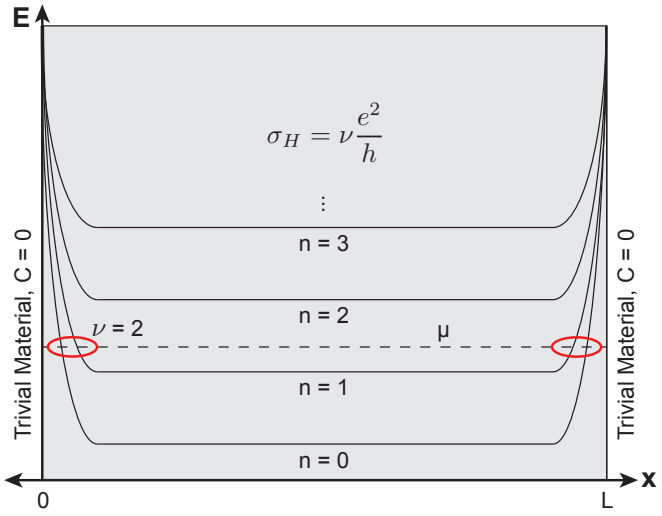


Figure 1-2: Edge states responsible for the integer quantum Hall effect. A schematic of the spectrum of Landau levels changing as a function of the spatial coordinate $x$ at the interface with two topologically trivial materials at $x = 0$ and $L$. In the bulk, all levels below the chemical potential, shown as a dashed line, are occupied with electrons and there are no states close to the chemical potential to carry current, so the bulk is insulting. However, at the edges of the sample, these occupied levels necessarily become unbound and increase in energy, eventually crossing the chemical potential at locations indicated by the red circles. These states crossing the level of the chemical potential open up a discrete number of channels for conductance, resulting in a quantized Hall conductance.

the example given in figure 1-2, at the position of the chemical potential there are two Landau levels which cross at the edge, each carrying a Chern number of one, so the Hall conductance is $2 \times \frac{e^2}{h}$, realizing the $\nu = 2$ quantum Hall effect.

In a condensed matter experiment, transitions between different quantum Hall states can be controlled either by tuning the chemical potential with a gate voltage or by changing the applied magnetic field strength. To move towards the regime of electrons occupying a single Landau level, the density of electrons, given by the chemical potential, is reduced and the Landau level spacing is increased such that the chemical potential lies in between the lowest landau level and the first Landau level. In the process, the effective electron-electron interaction is also tuned relative to the Landau level spacing, $\frac{e^2/l}{\hbar\omega_c} \propto \frac{e^{3/2}}{\sqrt{B}}$. This is important for realizing of the fractional quantum Hall effect because interactions ideally shouldn't be larger than the spacing of Landau levels, and this scaling allows for the preparation of strongly interacting, but not too strongly interacting, electrons in the lowest Landau level.

The regime of electron filling fractions less than one complete Landau level is known as the extreme quantum limit and was challenging to realize with two-dimensional electron gases because in such a dilute regime the effects of disorder come to dominate the physics at very low electron densities. As a result, for very strongly interacting electron systems, the effects of disorder play a prominent role in understanding the resulting transport measurements, and it was advances in doping that helped experiments achieve this regime [152, 146]. This highlights the attractive nature of realizing these states in an ultracold atomic system, whose cleanliness allows such states to be realized and observed free of the competing effects of disorder.

### 1.2.3 FQHE and the Laughlin wavefunction

For developing intuition for the problem of interacting particles in the lowest Landau level, it is instructive to begin with the two-body problem with the coulomb interaction [55]. We begin by writing out the two-particle Hamiltonian, transforming to the center-of-mass and relative coordinates, and showing that the problem, as usual, can be reduced to a one-body problem in the relative coordinate, $\mathbf{r} = \mathbf{r}_1 - \mathbf{r}_2$. The

resulting Hamiltonian is the single-particle, charged particle in a magnetic field problem we solved above, but now also contains an added coulomb interaction term. To get an intuition for how the coulomb interaction changes the Landau level structure in figure 1-1, we evaluate the matrix element:

$$\left\langle \psi_m \left| \frac{e^2}{r} \right| \psi_m \right\rangle = \frac{2\pi e^2}{\pi m!} \int_0^\infty r dr \, r^{2m} e^{-r^2} \tag{1.43}$$

$$= \frac{e^2}{m!} \Gamma\left(m + \frac{1}{2}\right) = \frac{(2m)!\sqrt{\pi} e^2}{2^{2m}(m!)^2} \tag{1.44}$$

which forms the diagonal elements of degenerate perturbation theory. A more intuitive scaling is given by using Stirling's approximation, $n! \approx \sqrt{2\pi n}\left(\frac{n}{e}\right)^n$, to simplify the factorial functions to get the simple scaling relation, valid for large, $m$:

$$\left\langle \psi_m \left| \frac{e^2}{r} \right| \psi_m \right\rangle \approx \frac{e^2}{l\sqrt{m}} \tag{1.45}$$

Recall that the average radius of a state with angular momentum $m$ is $l\sqrt{m}$, so we interpret this relation to indicate that two repulsively interacting particles in the lowest Landau level minimize their interaction energy in the perturbative regime when they are maximally separated, occupying the state where the relative coordinate maximizes its angular momentum state. The result also shows how interactions can lift the degeneracy of the states in the lowest Landau level and provides a natural way of generalizing the two-body wavefunction to a many-body ansatz. Writing the above relative wavefunction in terms of the original coordinates the wavefunction for the relative angular momentum state, $m$, looks like:

$$\psi(z_1, z_2) \propto (z_1 - z_2)^m e^{-(|z_1|^2 + |z_2|^2)/2}. \tag{1.46}$$

The form of the two-particle wavefunction lends itself to a simple interpretation of the nature of the weakly interacting state. First, the electrons try to maximize their interparticle distance by maximizing the relative angular momentum state, the polynomial index, $m$. Second, the probability of the electrons to be at the same location in

space is zero because of the node in the relative wavefunction that multiplies the gaussian, $(z_1 - z_2)$. This factor appears in the wavefunction of many interacting systems and is commonly known as the Jastrow factor. If we model the electron-electron interaction pseudopotential with a short-ranged function then this node in the relative two-particle wavefunction reduces the total interaction energy, and in the limit of a delta-function pseudopotential the interaction energy becomes identically zero. Finally, we see that this wavefunction is properly anti-symmetrized under exchange of coordinates, so it properly obeys fermionic statistics and represents a valid fermionic wavefunction.

Drawing inspiration from the solution to the interacting two-particle problem we now write down an ansatz for the many-particle problem, which turns out to be the celebrated Laughlin wavefunction [93]. The wavefunction should have each electron be localized with the appropriate gaussian factor in addition to having a node in the relative wavefunction corresponding to the location of every other electron in the system. The simplest wavefunction we can think of writing has the following form:

$$\psi_{\text{Laughlin}} = \prod_{i<j}^{N} (z_i - z_j)^m \prod_{k}^{N} e^{-|z_k|^2/2} \tag{1.47}$$

which corresponds to our two-particle wavefunction in the limit that N=2 and corresponds to the Laughlin wavefunction when N is arbitrarily large. We can also see that in the limit of a two-body interaction pseudopotential that is short-ranged like a delta function, the many-body interaction energy also goes to zero! The exponent of the Jastrow factor, $m$, is controlled by the filling fraction of electrons in the lowest Landau level, $1/\nu$. For the 1/3 Laughlin state the ratio of the number of particles to the number of available states in the lowest Landau level is $\nu$ =1:3, so the exponent is $m = 1/\nu = 3$. Intuitively, this is corresponds to larger average spacing between particles with the inter-particle spacing set by $\sqrt{\langle r^2 \rangle} = l\sqrt{m}$, as expected from the minimization of interaction energy by maximizing the angular momentum state of the relative wavefunction. In the limit of a completely filled Landau level, the exponent is $m = 1$ and the state corresponds to the integer quantum Hall state.

It is interesting to construct a quasiparticle and quasihole wavefunction from the Laughlin state by applying the raising or lowering operators $\hat{b}$ and $\hat{b}^\dagger$ to the Laughlin state. The result of this calculation for a quasi-hole is to produce a state with the structure:

$$\psi_{\text{hole}}(z_0) = \prod_i (z_0 - z_i) \prod_{i<j}^{N} (z_i - z_j)^m \prod_k^N e^{-|z_k|^2/2}. \tag{1.48}$$

Using this quasi-hole wavefunction, we can now begin to calculate many quantities of interest such as the charge associated with this excitation or, by creating two quasi-holes, calculating braiding phases associated with permutation of hole indices in the many-particle wavefunction [121].

A final important point to explore is to examine the electron density in the Laughlin wavefunction. Given the strongly repulsive nature of the system, we anticipate that the ground state wavefunction should encode a uniform density. One intuitive way to check this is via the analogy with a two-dimensional plasma potential, $|\psi|^2 = e^{-\beta\Phi}$, such that [93]:

$$\Phi = -2m \ln |\psi| = -2m^2 \sum_{i<j}^{N} \ln |z_i - z_j| + m \sum_k |z_k|^2. \tag{1.49}$$

Here we have set the thermodynamic temperature to be equal to $\beta = \frac{1}{m}$. Recalling the electrodynamics of charged particles in two-dimensions, we examine the right-hand side of equation 1.49. The first term corresponds to the two-dimensional coulomb interaction, $-\nabla^2\Phi = 2\pi m \delta^2(\mathbf{r})$, between particles with charge $m$. The second term corresponds to the interaction with a uniform background charge, $-\nabla^2\Phi = 2\pi\rho_B = -1/l^2$, which accounts for overall charge neutrality [55]. Here the charge neutrality requirement results in the relation between the charge density and the background charge, $\rho_B = -1/2\pi l^2$, arising from applying the Laplacian to equation 1.49:

$$nm + \rho_B = 0. \text{ so: } \quad n = \frac{1}{m}\frac{1}{2\pi l^2}. \tag{1.50}$$

In other words, the charge density in the $\nu = 1/m$ Laughlin state corresponds to a uniform charge density with $1/m$-th of an electron per cyclotron orbit or, equivalently, one electron per a $l \to \sqrt{m}l$ enlarged cyclotron orbit. This system is also incompressible and exhibits sub-Poissonian density fluctuations [55]. In addition to these properties, this system exhibits a novel kind of order, off-diagonal long range order corresponding to the condensation of particles onto fluxes at low temperatures [54].

Examining the form of the Laughlin wavefunction, we see how this state automatically builds in both electron-electron correlations and anti-symmetrization via the Jastrow factor, with an odd exponental factor, multiplying the exponential localization single-particle factor. Intuitively, we see how electron correlations are built in and short-ranged interactions are minimized by forcing a node in the wavefunction of the $i$-th particle at the location of every other particle in the many-body state. Capturing such a state at the mean-field level is understandably hard since the single particle wavefunction contains non-uniform density and we recover uniform density only when considering the truly many-particle wavefunction. Such a system is a promising for realization in an ultracold atomic system. The local control and detection capabilities of such systems might allow the creation of well-localized quasi-particle or quasi-hole excitations for interferometric measurements of exchange phases or local detection of fractional particle statistics [19], and represent an exciting direction for development of many-body interferometric tools in ultracold atoms [86, 75].

So far, we have introduced why the physics of many interacting particles is a challenging task for a classical calculation due to the exponential scaling of the problem size. We discussed situations where mean-field theory works in describing quantum many-body systems and why these approaches are successful for weakly interacting systems with small fluctuations. We then discussed two situations where inherently quantum effects have a profound impact on the ground state of the system. First, the hydrogen molecule, where we saw that the inclusion of quantum-mechanical spin and a fermionic anti-symmetrization requirement results in an effective spin model for the electronic degrees of freedom. Second, we examined the integer and fractional quan-

tum Hall states as examples of topologically ordered states and strongly interacting systems that host fundamentally different types of orders and excitations from normal symmetry-breaking states. In the next chapter, we will discuss a crucial tool we use to realize similar many-particle states of matter: an optical lattice. Throughout, these two toy models will help interpret the resulting physics.

# Chapter 2

# Optical Lattices

The main tool we will use to bring condensed matter phenomena to our cloud or ultracold $^{87}$Rb atoms is an optical lattice. In real crystalline systems the ionic lattice forms a regular array of trapping sites for electrons that can move through the material an interact with each other. The mapping of a cold atoms experiment to a condensed matter model finds the atoms in the lattice playing the role of the electrons and the interfering laser beams that create a regular array of trapping sites playing the role of the ions in a crystal. Similarly to electrons in a crystal, these atoms can both move freely from site-to-site in the lattice as well as interact with each other. In the discussion that follows, I show how this connection can be made rigorous and what unique challenges the implementation of an optical lattice brings to experimental physics.

## 2.1 The Simple Cubic Lattice

For ultracold atoms, we can make a regular array of identical trapping potentials by interfering far-detuned laser beams. This technique creates very clean potentials without the presence of defects and lends itself to a precise description of the resulting physics because all the Fourier components of the lattice are known and the interaction of the atom with the resulting electric field interference pattern is well-characterized. Using various laser configurations and polarizations, a large variety of

lattice geometries have been experimentally realized [62, 9, 77, 151, 79, 150] resulting in a rich literature of new ways to prepare and measure cold atomic systems [16].

To illustrate the machinery of solving for the energy spectrum and eigenstates given the electric field of our laser configuration and the resulting AC Stark shift of an atom, we focus on the simple cubic lattice for clarity. The simple cubic lattice, also called the primitive cubic lattice, consists of a unit cell with sites on the corners of the primitive cell. This lattice is emulated by counter-propagating pairs of laser beams (for simplicity, with equal intensity) along the three orthogonal spatial directions creating the potental:

$$V_{\text{Latt}}(\mathbf{x}) = V_L\big(\cos^2(k_x x) + \cos^2(k_y y) + \cos^2(k_z z)\big), \tag{2.1}$$

where $k_\alpha = 2\pi/\lambda_\alpha$ is the lattice wavevector in the $\alpha$ direction defined by the wavelength of light. Practically speaking, we have assumed that the three wavelengths are close in energy but offset in frequency to avoid any cross-modulation terms between the light fields in different directions, and that the lattice is independent of spin – both assumptions we will break later in this thesis.

With the form of the optical lattice potential known, we can write down the Hamiltonian for a single particle in this potential:

$$H = \frac{\mathbf{p}^2}{2m} + V_{\text{Latt}}(\mathbf{x}). \tag{2.2}$$

Due to the separability of the potential, we can write the wavefunction as a product of functions for each of the spatial directions, $\psi(\mathbf{x}) = \psi_x(x)\psi_y(y)\psi_x(z)$, so the problem reduces to the sum of three one-dimensional differential equations satisfying the energy relation:

$$H\psi_x(x) = \Big(\frac{\hat{p}_x^2}{2m} + V_L\cos^2(k_x x)\Big)\psi_x(x) = E_x\psi_x(x), \quad \text{where: } E = E_x + E_y + E_z \tag{2.3}$$

The solutions of the 1D Hamiltonian presented above are known as the Mathieu functions. However, knowing this does not teach us anything about atoms in optical

lattices so we move for a different approach. We can utilize the discrete translation symmetry of the lattice – translations by the lattice spacing, $a$, do not change the lattice – to invoke Bloch's theorem which allows us to decompose the wavefunction as the product of plane waves and a function that has the same periodicity as the lattice:

$$\psi(x) = e^{iqx}\phi_q(x) \tag{2.4}$$

The states are labeled by a new index, $q$, called the quasimomentum. The quasimomentum acts like momentum, but is only unique within what is called a Brillouin zone – states that cover the space between wavevectors $q \in (-\pi/a, \pi/a]$ – and is only conserved modulo the reciprocal lattice wavevector, $Q = 2\pi/a$. Scattering processes associated with transitions to quasimomentum states outside the Brillouin zone are called *umklapp* processes. The decomposition of the wavefunction into a product of a plane wave and a periodic function allows us to rewrite the Hamiltonian as:

$$H_B = \frac{(\hat{p} + q)^2}{2m} + V_L \cos^2(k_x x). \tag{2.5}$$

We can proceed towards a solution now by expanding the periodic part of the Bloch wavefunction in a plane wave basis:

$$\phi_q(x) = \sum_l c_l^q \, e^{2ilk_x x} \tag{2.6}$$

and writing down a tridiagonal matrix that can be numerically diagonalized.

$$H = E_R \begin{pmatrix} \ddots & \vdots & \vdots & \vdots & \\ \cdots & \left(2(l+1) + \frac{q}{\hbar k}\right)^2 & -\frac{N_R}{4} & 0 & \cdots \\ \cdots & -\frac{N_R}{4} & \left(2l + \frac{q}{\hbar k}\right)^2 & -\frac{N_R}{4} & \cdots \\ \cdots & 0 & -\frac{N_R}{4} & \left(2(l-1) + \frac{q}{\hbar k}\right)^2 & \cdots \\ & \vdots & \vdots & \vdots & \ddots \end{pmatrix} \tag{2.7}$$

Here $E_r$ is the recoil energy, which sets the inherent energy scale of the lattice, and

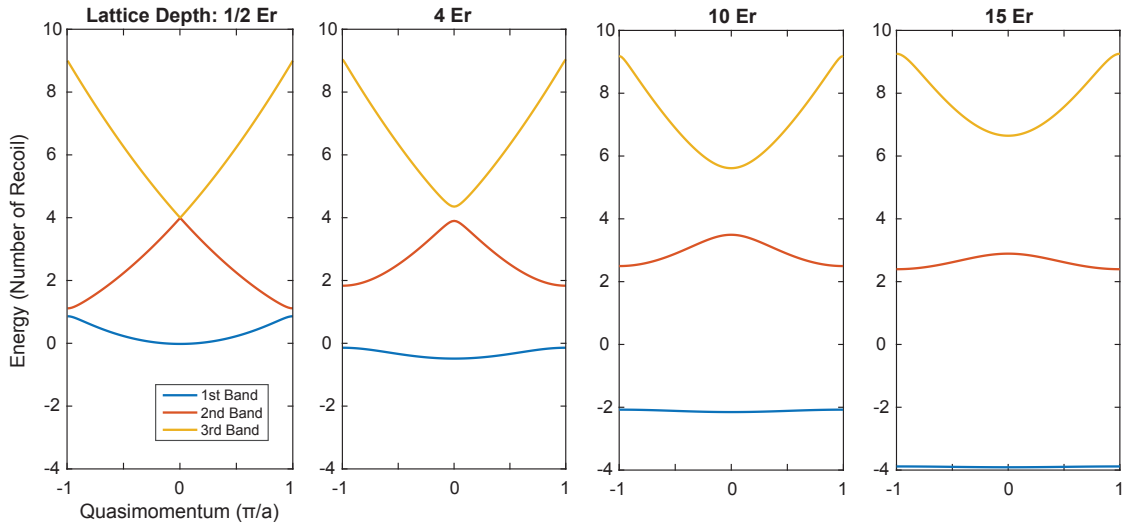


Figure 2-1: The spectrum of the three lowest bands of an optical lattice. From left to right, the band structure for 1/2, 4, 10 and 15 $E_r$ are shown in units of the atomic recoil energy.

is given by:

$$E_R = \frac{h^2}{2ma^2} \tag{2.8}$$

and $a = \lambda/2\sin(\theta/2)$ is the lattice constant set by the laser wavelength and the beam intersection angle, $\theta$. In the Hamiltonian matrix, $N_r$ is the number of recoil energies that compose the total lattice depth, i.e. $V_L = N_r E_r$. This matrix can be diagonalized for each quasimomentum in the first Brillouin zone. Plotting the energy eigenvalues as a function of the quasimomentum yields the familiar picture of energy bands of a lattice seen plotted in figure 2-1.

The numerical solution also gives access to the eigenvectors for each band and for each quasimomentum. Usually, to get convergence towards a value for the energy eigenvalues one need to include 5 or more Fourier coefficients, $c_l^q$. Using the eigenvalues from this diagonalization, we can construct maximally localized Wannier functions, the lattice analogue of the position space eigenstate - the Dirac-delta wavefunction - in free space.

$$w(x - x_i) = N \sum_q e^{-qx_i/\hbar} \phi_q(x) \tag{2.9}$$

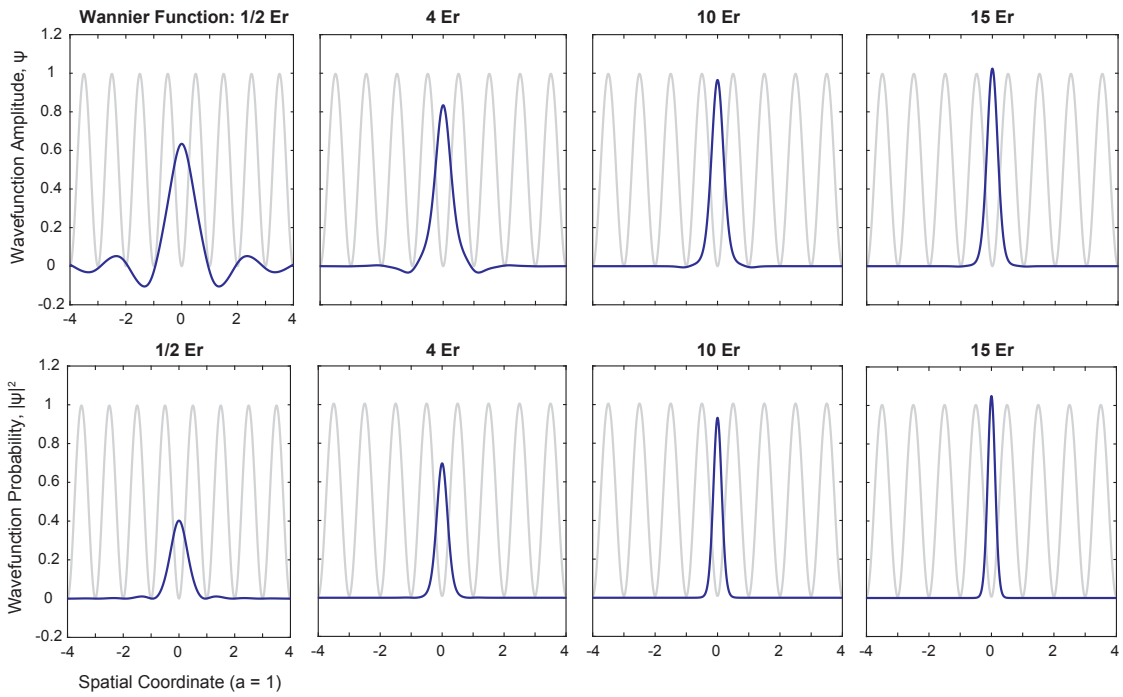


Figure 2-2: Maximally-localized Wannier functions of the lowest band. From left to right, the Wannier function corresponding to lattice depths of $1/2$, 4, 10 and 15 $E_r$ in dimensionless spatial units with the lattice constant setting the length scale, $a = 1$. Note the sharp increase in peak density and reduction in wavefunction width with increasing lattice depth.

For more general lattice geometries, this analogy with the Dirac delta function can be exploited to formulate an alternate approach to construct maximally localized Wannier functions by numerically minimizing the expectation value of the spatial variance operator. While this technique is not covered in detail here, in one dimension, this approach is outlined in the following preprint [96].

The maximally localized wavefunction is important because it allows the calculation of a variety of different lattice parameters such as tunneling matrix elements, interaction energies, excitation probabilities, and more. As we see in the following sections on the formulation of the Bose-Hubbard Hamiltonian from the microscopic model of our atoms in optical lattices, these Wannier functions play an important computational role.

## 2.2 Scalar and Vector AC Stark Shifts

The creation of optical lattices for neutral atoms and molecules using far-detuned laser beams has become a standard tool in ultracold atom experiments [16]. The description above, which models the lattice structure independently of the internal state of the atom, relies on the reduction of the atom-light interaction to that of an effective two-level system with a ground and an excited electronic state, $|g\rangle$ and $|e\rangle$, respectively, and a spin-independent dipole moment, $\mathbf{d}$, connecting the two.

The situation becomes more complex when we consider that the ground and excited states contain additional degrees of freedom, such as the spin of an electron. In the case of alkali atoms with one valence electron, the spin of the unpaired electron couples to the orbital angular momentum to create a ${}^{2s+1}N_J = {}^2S_{1/2}$ ground state and both a ${}^2P_{1/2}$ and ${}^2P_{3/2}$ excited state. If we now consider the interaction of light with this level structure, the assumption of a dipole moment independent of the internal state breaks down and we have to consider situations like that depicted in fig. 2.11, where the coupling to the excited state is very different for different projections of the angular momentum in the ground state, $m_J$, and a given polarization of light. In one limiting case shown schematically in figure 2.11, with $\sigma_+$-polarized light tuned between the D1 and D2 line, there exists a wavelength termed the "tune-out" wavelength, approximately 790 nm, for which the Stark shift of the $m_J = -1/2$ state vanishes but the stark shift of the $m_J = 1/2$ state remains finite. Shown in figure 2.11b, for general wavelengths, the Stark shift of a given state is a combination of a spin-independent contribution, termed the *scalar* Stark shift, and a spin-dependent contribution, the *vector* Stark shift. For an atom without hyperfine structure this can be expressed simply within the rotating wave approximation as the sum of the two terms, and for atoms with hyperfine structure the same argument applies in the regime where the detuning from resonance is much greater than the hyperfine

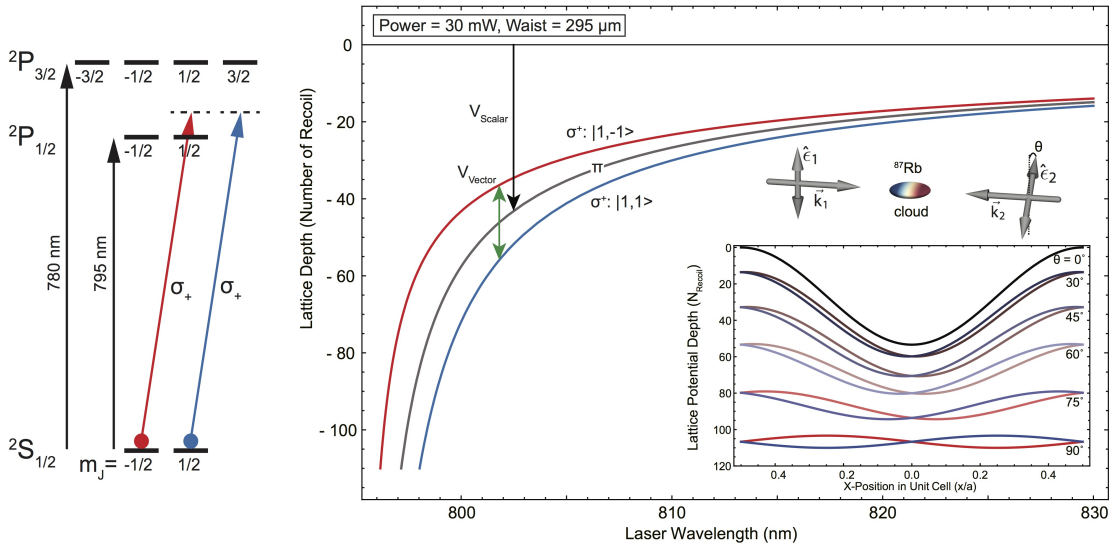


Figure 2-3: Vector stark shifts used to create spin-dependent potentials. (Left) The fine structure energy levels of $^{87}$Rb interacting with $\sigma_+$-polarized light. The two different projections of the spin-orbit coupled angular momentum, $m_J$, in the ground state have different matrix elements with the excited state, producing a spin-dependent stark shift. (Right) The different potentials for hyperfine spins $m_F = \pm 1$ interacting with $\sigma_+$-polarized light are plotted for detunings below the D1 line compared to the spin-independent potential created by $\pi$-polarized light. The difference between the two is the vector stark shift. The resulting lattice potential for different retroreflected polarization angles is shown in the inset.

splitting, $\delta \gg \Delta E_{\mathrm{HFS}}$, leading to a Stark shift given by the general formula [64]:

$$V_{I=0}(\mathbf{r}) = \frac{\pi c^2 \Gamma}{2\omega_0^3}\left(\frac{2 + P g_J m_J}{\delta_2} + \frac{1 - P g_J m_J}{\delta_1}\right) I(\mathbf{r}) \tag{2.10}$$

$$V_{I\neq 0}(\mathbf{r}) = \frac{\pi c^2 \Gamma}{2\omega_0^3}\left(\frac{2 + P g_F m_F}{\delta_2} + \frac{1 - P g_F m_F}{\delta_1}\right) I(\mathbf{r}), \tag{2.11}$$

where $g_{(F),J}$ is the $g$-factor of the populated (hyper-)fine structure ground state, $\delta_i$ is the detuning from either the D1 or D2 lines, $I(\mathbf{r})$ is the spatially inhomogeneous intensity profile of the illumination beam, and $P$ is the laser polarization with respect to the quantization axis of the atoms with $P = \pm 1$ corresponding to right- and left-circularly polarized light, respectively. In this analytic form, we see that circularly polarized light has the same form as an effective magnetic field, generating opposite energy shifts for states of opposite $m_{(J),F}$ and no energy shift for linearly polarized light.

Shown in the inset of figure 2.11b, and as will be discussed later in the thesis, the spin-dependent nature of the vector Stark shift allows the creation of optical lattices whose properties depend on the internal spin state of the atom. Shown as one example, rotating the polarization of the two laser beams that form an optical lattice changes the spatial mode experienced by $|F, m_F\rangle = |1, \pm 1\rangle$ atoms, therefore changing the maximally-localized Wannier functions in a spin-dependent way:

$$w(x - x_i) \rightarrow w_\sigma(x - x_i^\sigma). \tag{2.12}$$

The spin-dependence of the Wannier functions and the interaction and tunneling energies they encode will become a prominent feature of the experiments featured in chapter 6 of this thesis.

One prominent feature of using an optical trap to confine neutral atoms is the presence of heating terms due to light scattering. Creating an AC Stark potential by admixing a bit of the excited state wavefunction inevitably also leads to heating by spontaneous emission due to the finite diople moment created by mixing in the

excited state. For the two-level system, the scattering rate is given by [64],

$$\Gamma_{\mathrm{sc}} = \frac{\pi c^2 \Gamma}{2\hbar\omega_0^3}\left(\frac{\omega}{\omega_0}\right)^3\left(\frac{\Gamma}{\omega-\omega_0}+\frac{\Gamma}{\omega+\omega_0}\right)^2 I(\mathbf{r}). \tag{2.13}$$

Usually, if light scattering is a limiting factor in an experiment, the ratio of AC stark potential to scattering rate can be tuned by changing the detuning of the laser used to trap atoms. In the same way as the detuning dependence of the reactive and absorptive quadratures of a driven harmonic oscillator response, the ratio of the scattering rate to the scalar AC Stark potential depth is given by:

$$\frac{\hbar\Gamma_{\mathrm{sc}}}{V_{\mathrm{scalar}}} = \frac{\Gamma}{\delta}, \quad \text{with: } V_{\mathrm{scalar}} \sim \frac{I(\mathbf{r})}{\delta/\Gamma}. \tag{2.14}$$

Equations 2.14 show that for longer photon scattering times, and therefore lower heating rates, the detuning $\delta/\Gamma$ can be increased at the expense of increasing overall power needed to achieve a constant trap depth. Unfortunately, this argument only holds for the scalar AC stark shift. For the vector shift, we can get a more intuitive picture of the scaling from further detuning by expanding equation 2.11 to first order in the detuning $\delta_0 \gg \Delta E_{\mathrm{FS}}$ relative to the center of the D1 and D2 lines (such that $\delta_1 = \delta_0 - \Delta E_{\mathrm{FS}}/3$ and $\delta_2 = \delta_0 + 2\Delta E_{\mathrm{FS}}/3$) to get an analytic relation between the scalar and vector shifts as a function of the detuning,

$$V_{\delta_0 \gg \Delta E_{\mathrm{FS}}} = \frac{\pi c^2}{2\omega_0^3}\frac{\Gamma}{\delta_0}\left(3 - \frac{\Delta E_{\mathrm{FS}}}{\delta_0} - P g_F m_F \frac{\Delta E_{\mathrm{FS}}}{\delta_0}\right) I(\mathbf{r}) \tag{2.15}$$

From this we can clearly see that the vector Stark shift scales $\propto \frac{\Gamma \Delta E_{\mathrm{FS}}}{\delta^2}$, such that the ratio of the scattering rate to the vector stark shift is independent of detuning!

$$\frac{\hbar\Gamma_{\mathrm{sc}}}{V_{\mathrm{vector}}} = \frac{\Gamma}{\Delta E_{\mathrm{FS}}} \tag{2.16}$$

Practically, this means that given the fine structure splitting of $^{87}$Rb and the natural linewidth of the excited state, the heating rate will be directly proportional to the vector AC Stark shift needed, independent of frequency. Therefore, when utilizing

the vector Stark shift to accomplish a task in an experiment, one should always aim to use the minimum possible vector shift as is needed! This is a critical lesson we will come back to in a later chapter.

## 2.3 The Bose-Hubbard Hamiltonian

With the position space wavefunction in hand, we can construct three very important quantities which will parameterize, how atoms move, how they interact with each other, and the local potentials the confined atoms experience. Movement is typically parameterized with a tunneling rate between two sites $i$ and $j$, $t_{ij}$, interaction is parameterized by a two-body interaction rate, $U_{ij}$, and potential energy (coming from e.g. an external trapping potential or a magnetic field gradient) is given by a local energy, $\epsilon_i$. We can construct these quantities from our microscopic Hamiltonian by taking the appropriate matrix elements:

$$t_{ij} = \int d\mathbf{x}\, w(\mathbf{x}-\mathbf{x}_i)^* \Big(\frac{p^2}{2m} + V_{\text{Latt}}\Big) w(\mathbf{x}-\mathbf{x}_j) \tag{2.17}$$

$$U_{ij} = \int d\mathbf{x}\, V_{\text{int}}(\mathbf{x}_i,\mathbf{x}_j)|w(\mathbf{x}-\mathbf{x}_i)|^2|w(\mathbf{x}-\mathbf{x}_j)|^2 \tag{2.18}$$

$$\epsilon_i = \int d\mathbf{x}\, V_{\text{ext}}(\mathbf{x}_i) w(\mathbf{x}-\mathbf{x}_i)^* w(\mathbf{x}-\mathbf{x}_i). \tag{2.19}$$

For example, in our experiments we might use $^{87}$Rb loaded into the ground band of an isotropic, cubic lattice formed from 1064 nm laser light. This situation simplifies the equations above first because the cubic lattice is a separable potential, so the tunneling matrix element is a one-dimensional integral, and second, the Rb atoms mainly interact via short range, contact interactions, so the interaction matrix element only has an on-site, $i = j$ component. Therefore, the tunneling and interaction matrix elements simplify to:

$$t_{ij} = \int dx\, w(x-x_i)^* \Big(\frac{p^2}{2m} + V_L \cos^2(k_x x)\Big) w(x-x_j) \tag{2.20}$$

$$U_{ii} = \frac{4\pi\hbar^2 a}{m} \int dx\, |w(x-x_i)|^4 \int dy\, |w(y-y_i)|^4 \int dz\, |w(z-z_i)|^4 \tag{2.21}$$

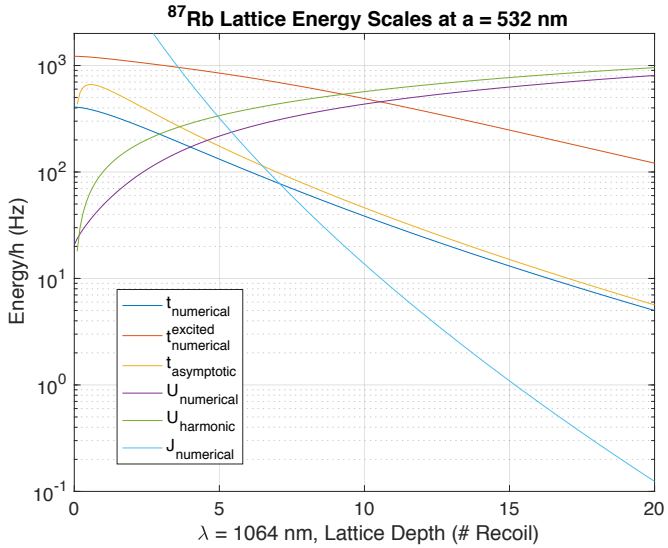


Figure 2-4: Relevant energy scales for atoms in an optical lattice. Comparison of analytic expressions based on an asymptotic approximation and numerical results for the lowest band tunneling and interaction parameters in an isotropic, cubic lattice with lattice constant $a = 532$ nm. From the numerical results we also plot the relevant exchange coupling, $J = \frac{4t^2}{U}$, and the second band tunneling rate.

Numerical results for these elements are shown in figure 2-4 and are compared to the asymptotic expression for the tunneling and the harmonic approximation for the interaction energy:

$$t = \frac{4}{\sqrt{\pi}} E_r N_r^{3/4} e^{-2N_r^{1/2}} \tag{2.22}$$

$$U = \sqrt{\frac{8}{\pi}} (ka_s) E_r N_r^{3/4}. \tag{2.23}$$

More generally, we can use these localized wavefunctions to parameterize any interaction, for example dipolar interactions, by taking the appropriate matrix elements. Using these parameterizations, we can re-write our microscopic Hamiltonian as a Hamiltonian equation expressed with second-quantized position operators:

$$H = -\sum_{ij,\sigma} \left( t_{ij,\sigma} a_{i,\sigma}^\dagger a_{j,\sigma} \ + \ \text{H.c.} \right) + \frac{1}{2} \sum_{i,\sigma,\sigma'} U_{ij,\sigma} a_{i,\sigma}^\dagger a_{j,\sigma'}^\dagger a_{j,\sigma'} a_{i,\sigma} \tag{2.24}$$

which is a realization of the celebrated Hubbard model as the minimal description of ultracold atoms in optical lattices.

In this Hamiltonian, we see two qualitatively different behaviors of the ground state wavefunction for the two terms that compose the Hamiltonian. When the tunneling term dominates over the interaction term, the ground state is a superfluid with a macroscopic occupation of the lowest delocalized Bloch wave. In the strongly interacting limit where the interactions are much larger than tunneling, the system prefers to minimize the local density and number fluctuations are suppressed, leading to the system to occupy the lowest Fock state on each site of the lattice. For bosonic atoms in optical lattices, this model describes the quantum phase transition between a superfluid state and a Mott insulating state.

### 2.3.1 Superfluid to Mott insulator Transition

For electrons, the Mott insulating phase is a gapped (though topologically trivial) phase of matter which, due to electron-electron interactions, does not follow the normal classification of solids with 1/2 filled bands as metals. In such materials, the electron-electron interactions are much larger than the kinetic energy, causing an insulating phase to appear. For ultracold bosons in optical lattices, tuning the interaction parameter with respect to the tunneling parameter allows us to realize the quantum phase transition between the superfluid ground state and a Mott insulating ground state [62].

We can develop a quantitative understanding of this transition in a single bosonic spin component by examining the mean-field solution of the Hubbard Hamiltonian. We begin with the isotropic, $d$-dimensional Hamiltonian for a single bosonic spin component in the lowest band of an optical lattice:

$$H = -t \sum_{\langle ij \rangle} (\hat{a}_i^\dagger \hat{a}_j + \hat{a}_j^\dagger \hat{a}_i) + \frac{U}{2} \sum_i \hat{n}_i(\hat{n}_i - 1) - \mu \sum_i \hat{n}_i \tag{2.25}$$

where the angled bracket sum denotes a sum over only nearest neighbors, $t$ is the hopping amplitude, $U$ is the two body interaction parameter, and $\mu$ is the chemical

potential.

We proceed by assuming that we are close to an insulating state and we can make the following mean field decoupling approximation discussed in chapter 1:

$$\psi = \langle \hat{a}_i \rangle = \langle \hat{a}_i^\dagger \rangle = \sqrt{n_i} \tag{2.26}$$

$$\langle \hat{a}_i^\dagger \hat{a}_j \rangle \approx \langle \hat{a}_i^\dagger \rangle \hat{a}_j + \hat{a}_i^\dagger \langle \hat{a}_j \rangle - \langle \hat{a}_i^\dagger \rangle \langle \hat{a}_j \rangle = (\hat{a}_j + \hat{a}_i^\dagger)\psi - \psi^2 \tag{2.27}$$

We can now substitute this approximation into equation 2.25 to construct a local, effective Hamiltonian.

$$H^{eff} = -zt\psi \sum_i (\hat{a}_i + \hat{a}_i^\dagger) + zt\psi^2 N_s + \frac{U}{2} \sum_i \hat{n}_i(\hat{n}_i - 1) - \mu \sum_i \hat{n}_i \tag{2.28}$$

$$= N_s zt \left( \frac{U}{2} \hat{n}_i(\hat{n}_i - 1) - \mu \hat{n}_i - (\hat{a}_i + \hat{a}_i^\dagger)\psi + \psi^2 \right) \tag{2.29}$$

To simplify notation we define dimensionless parameterizations of $\mu$ and $U$ by normalizing by the tunneling energy, $t$, and the number of nearest neighbors $z$, in the following way:

$$\tilde{U} = \frac{U}{zt}, \qquad \tilde{\mu} = \frac{\mu}{zt}. \tag{2.30}$$

We now have a completely local, effective Hamiltonian for each site of the lattice that we can diagonalize to get energy eigenvalues and eigenstates.

We proceed in two different ways following the procedure of ref. [155]. First, we will find the ground state energy perturbatively and from this extract the mean-field phase boundary. Then, we will find the density profile by direct numerical diagonalization of the effective Hamiltonian. We begin by defining the zeroth order Hamiltonian and perturbation:

$$H_0 = \frac{\tilde{U}}{2} \hat{n}_i(\hat{n}_i - 1) - \tilde{\mu}\hat{n}_i + \psi^2 \tag{2.31}$$

$$V = (\hat{a}_i + \hat{a}_i^\dagger)\psi \tag{2.32}$$

In the number basis, the first part is diagonal and gives a ground state energy for

particles:

$$E_g^{(0)} = \frac{\tilde{U}}{2} g(g-1) - \tilde{\mu} g, \quad \text{for } \tilde{U}(g-1) < \tilde{\mu} < \tilde{U} g. \tag{2.33}$$

We now focus on evaluating the more interesting perturbative part. To first order, the perturbation produces no non-trivial matrix elements, so the first non-zero term appears at second order:

$$E_{GS}^{(2)} = \psi^2 \sum_{n \neq g} \frac{|\langle g|V|n\rangle|^2}{E_g^{(0)} - E_n^{(0)}} \tag{2.34}$$

$$= \frac{g}{\tilde{U}(g-1) - \tilde{\mu}} + \frac{g+1}{\tilde{\mu} - \tilde{U} g} \tag{2.35}$$

The ground state energy is given by the sum of the zeroth and second order energies, $E_g(\psi) = E_0(g, \tilde{U}, \tilde{\mu}) + E_2(g, \tilde{U}, \tilde{\mu})\psi^2 + ...$, and we find the transition point as in Landau-Ginzburg theory by the inflection point of the energy. We find this corresponds to $\psi = 0$ for $E_g^{(2)} > 0$ and $\psi \neq 0$ for $E_g^{(2)} < 0$ so we can set $E_g^{(2)} = 0$ and solve for the phase boundary:

$$\frac{g}{\tilde{U}(g-1) - \tilde{\mu}} + \frac{g+1}{\tilde{\mu} - \tilde{U} g} + 1 = 0 \tag{2.36}$$

$$\tilde{\mu}_{\pm}^{(c)} = \frac{1}{2}[\tilde{U}(2g-1) - 1] \pm \frac{1}{2}\sqrt{\tilde{U}^2 - 2\tilde{U}(2g+1) + 1} \tag{2.37}$$

For aesthetic reasons, I prefer to write this out in terms of a dimensionless tunneling, $\tilde{t} = zt/U$:

$$\frac{\mu_{\pm}^{(c)}}{U} = \frac{1}{2}[(2g-1) - \tilde{t}] \pm \frac{1}{2}\sqrt{1 - 2\tilde{t}(2g+1) + \tilde{t}^2} \tag{2.38}$$

The phase boundary this yields is seen below.

Now to get the full density profile, we can carry forward with higher orders of perturbation theory and find a density term, but we will find this is a poor approximation for reality because between Mott plateaus where the order parameter, $\psi$, approaches unity, the perturbation theory will break down. A more reliable method is to instead use an exact diagonalization approach for the Hamiltonian shown on the second line of equation 2.29. What makes this approach efficient is that we have

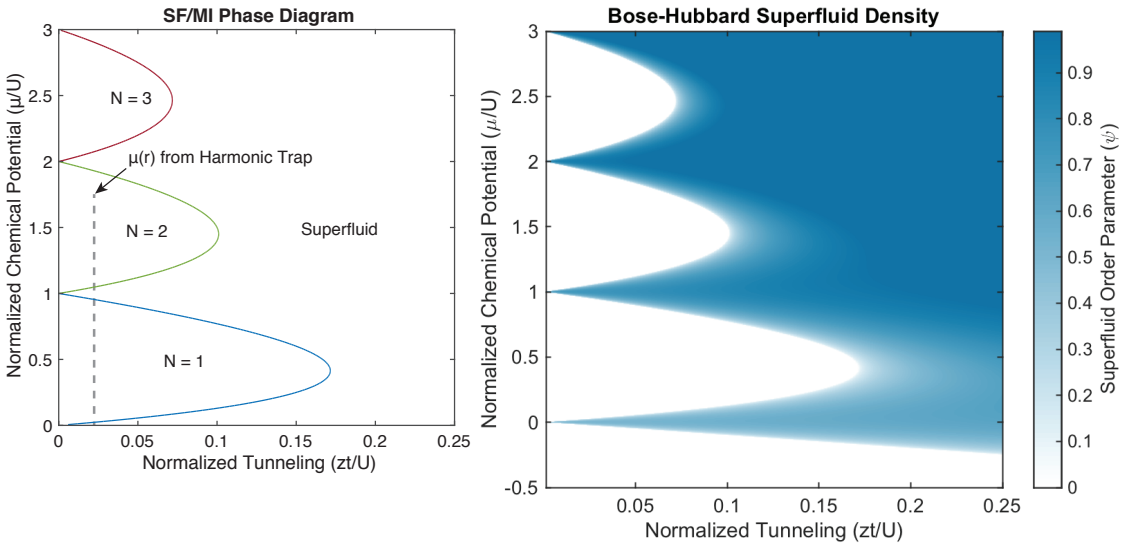


Figure 2-5: The superfluid to Mott insulator mean-field phase diagram. (Left) the phase diagram calculated from a perturbative expansion of the decoupled Hamiltonian for small values of the superfluid order parameter, $\psi$. The dashed vertical line gives an example of the local chemical potentials which exist in one sample due to the Harmonic trap. (Right) The superfluid density extracted from exact diagonalization of the decoupled Hamiltonian, showing agreement with the phase boundary derived from the perturbative expansion in addition to the depletion of the superfluid as the system approaches the Mott transition.

reduced the Hamiltonian to a purely local basis set, and we do not need to keep track of all the states in the many-body Hamiltonian. More precisely, we construct matrix elements of the Hamiltonian in a local number basis and place them into a matrix to diagonalize. The matrix can be safely truncated at a reasonable density higher than the average filling expected in the system. Explicitly:

$$H = \begin{pmatrix} \psi^2 & -\psi & 0 & 0 & 0 & \cdots \\ -\psi & -\tilde{\mu}+\psi^2 & -\sqrt{2}\psi & 0 & 0 & \cdots \\ 0 & -\sqrt{2}\psi & \tilde{U}-2\tilde{\mu}+\psi^2 & -\sqrt{3}\psi & 0 & \cdots \\ 0 & 0 & -\sqrt{3}\psi & 3\tilde{U}-3\tilde{\mu}+\psi^2 & -\sqrt{4}\psi & \cdots \\ 0 & 0 & 0 & -\sqrt{4}\psi & 6\tilde{U}-4\tilde{\mu}+\psi^2 & \cdots \\ \vdots & \vdots & \vdots & \vdots & \vdots & \ddots \end{pmatrix} \tag{2.39}$$

This matrix, properly truncated (example: for n=3 I kept up to n=6 and did not see major impact on adding additional entries), can be directly diagonalized for a given $\tilde{t}$ and $\frac{\mu}{U}$ for each value of $\psi \in [0,1]$. The ground state eigenvalue and eigenvector is then found by minimizing the energy with respect to the order parameter $\psi$. Using these eigenvalues and eigenvectors, we can then directly find the energy of the ground state as well as the density distribution. An example of this is seen in figure 2-6. A quick note on computing tricks: I would only evaluate the matrix for a fine mesh over $\tilde{t}$, $\frac{\mu}{U}$, and $\psi$ once. Afterwards it's much faster to use a lookup table with linear interpolation to match the points you want with what is available in the table.

At the mean field level, we now understand the Mott state as a state for which the superfluid density $\psi$ vanishes and the wavefunction is characterized by the product state of a local density of $n$ particles:

$$|\psi\rangle_{\text{Mott}} = \prod_i^N (\hat{a}_i^\dagger)^n |0\rangle. \tag{2.40}$$

In the plot of the intrap density profile, we see that the transition between different Mott plateaus with uniform density happens in a smooth, continuous fashion. This is reflected in the map of the superfluid density from the exact diagonalization of

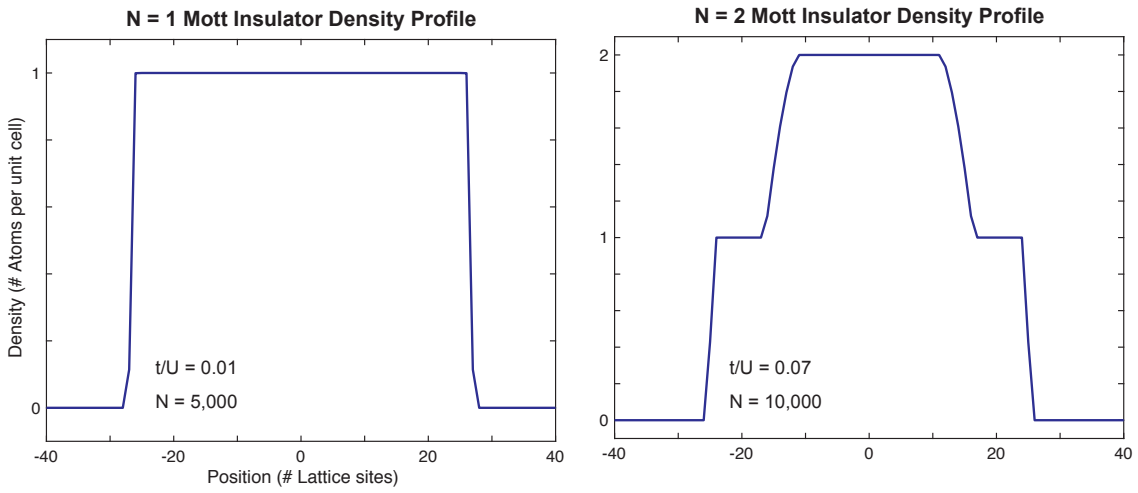


Figure 2-6: Density profiles of the Mott insulator in a harmonic trap. (Left) An example density distribution for the $n = 1$ Mott state at high lattice depth. (Right) An example density distribution for the $n = 2$ Mott state at moderate lattice depths just beyond the transition point.

equation 2.29, between Mott lobes the superfluid develops a finite density, allowing number fluctuations and the average density to smoothly adjust from one Mott region to another. To develop an understanding of the physics happening in this region of the phase diagram, we examine both the effects of finite tunneling at zero temperature as well as the effects of finite temperature in the regime of small tunneling.

One of the defining features of the Mott state is its finite excitation gap at the interaction energy scale, $U$. In the Mott regime, the ground state is divided into a manifold of states all with the same local occupation number defined by $n$. Perturbing this state with the tunneling part of the Hamiltonian couples the local state with $n$ particles per site to one with $n \pm 1$ particles per site:

$$-t \, \langle n_i', n_{i+1}' | \hat{a}_i^\dagger \hat{a}_{i+1} | n_i, n_{i+1} \rangle = -t \, \delta_{n_{i+1}-1, n_{i+1}'} \delta_{n_i+1, n_i'} \tag{2.41}$$

at an energy cost of $U$. Since $t \ll U$ in the Mott regime, this process is energetically forbidden to first order. However, at the edge of the Mott regime the superfluid density becomes finite and the system does contain gapless excitations. It is these excitations that, to first approximation, dominate the thermodynamics of the Mott state.

At zero temperature, the Mott insulating state breaks down in the region of the trapping potential where the chemical potential approaches $\mu \approx nU$, where $n$ is an integer according to the Mott plateau above which the fluctuations are happening. Examining the decoupled, effective Hamiltonian, eq. 2.29, we can understand this state as the result of tuning the energy of two different local densities into degeneracy with each other. At this point, two diagonal elements of the matrix are small, while the rest are higher in energy by the large energy scale, $U$, so we simplify the effective Hamiltonian to an effective two-level system given by the matrix:

$$\begin{pmatrix} n(n+1)U - n(\mu+\epsilon) + \psi^2 & -\sqrt{n+1}\psi \\ -\sqrt{n+1}\psi & (n+1)(n+2)U - (n+1)(\mu+\epsilon) + \psi^2 \end{pmatrix}. \quad (2.42)$$

At the point $\mu = nU$, where $\epsilon = 0$ the system has a particularly intuitive interpretation; the energy eigenvalues are easily solved for and the solutions simplify to $E_\pm = \psi^2 \pm \psi\sqrt{n+1}$, which minimize the energy for superfluid densities $\psi_{\min} = \sqrt{n+1}/2$. The corresponding eigenvectors are symmetric superpositions of the two local densities, $n$ and $n+1$, that give rise to a finite superfluid fraction even in the strongly interacting limit. This superfluid remains gapless and thus dominates the low temperature thermodynamics of the trapped system.

Next, we consider the effect of finite temperature. Assuming no superfluid phase exists, the lowest lying excitations in the gapped Mott state of $n$ particles per site are particle-hole excitations of $n+1$ and $n-1$ particles per site, respectively. If we restrict the Hilbert space to just singly-excited states and ignore the effects of finite tunneling forming Hubbard excitation bands, we can solve the partition function for this situation

$$\begin{aligned} Z &= e^{-\beta\left(\frac{U}{2}(n-1)(n-2)-(n-1)\mu\right)} + e^{-\beta\left(\frac{U}{2}n(n-1)-n\mu\right)} + e^{-\beta\left(\frac{U}{2}(n+1)n-(n+1)\mu\right)} && (2.43) \\ &= e^{-\beta\left(\frac{U}{2}n(n-1)-n\mu\right)}\left[1 + e^{-\beta(nU-\mu)} + e^{-\beta\left(-(n-1)U+\mu\right)}\right] && (2.44) \\ &= Z_{\text{Mott}}^n\left[1 + e^{-\beta(E_p-\mu)} + e^{-\beta(E_h+\mu)}\right], && (2.45) \end{aligned}$$

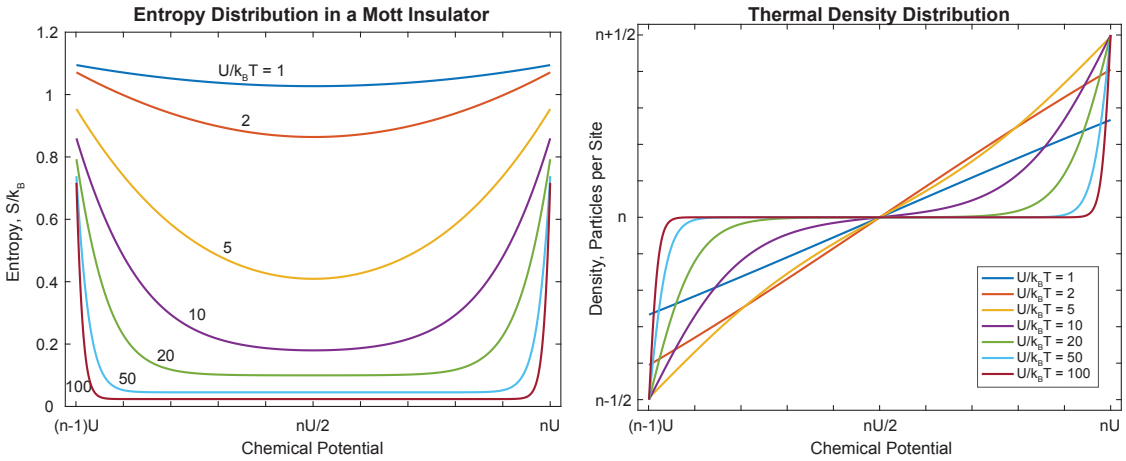


Figure 2-7: Finite temperature entropy and density distribution of the Mott insulator in the atomic limit, $t \approx 0$. (Left) The entropy distribution for various values of $U/k_BT$ at chemical potentials across one Mott plateau. Note the strong suppression of entropy in the middle of the Mott plateau and the localization of entropy at the edges. (Right) The particle and hole excitations which carry entropy change the density distribution at each given chemical potential across a Mott plateau.

where we have introduced the partition function for the Mott state in just the manifold of $n$ states, $Z^n_{\text{Mott}}$, as well as the energy of a particle and hole excitation:

$$E_p = nU, \text{ and: } E_h = -(n-1)U, \tag{2.46}$$

respectively. From this partition function we can compute the free energy and consequently the entropy:

$$\begin{aligned} -\beta F &= \ln Z^n_{\text{Mott}} + \ln\left(1 + e^{-\beta(E_p-\mu)} + e^{-\beta(E_h+\mu)}\right) \\ \frac{S}{k_B} &= \ln\left(1 + e^{-\beta(E_p-\mu)} + e^{-\beta(E_h+\mu)}\right) + \beta\frac{(E_p-\mu)e^{-\beta(E_p-\mu)} + (E_h+\mu)e^{-\beta(E_h+\mu)}}{1 + e^{-\beta(E_p-\mu)} + e^{-\beta(E_h+\mu)}}. \end{aligned} \tag{2.47}$$

The resulting entropy distribution along with the average density distribution is plotted in fig. 2-7. We see that entropy is primarily located in the regions where $\mu \approx nU$ and particle-hole excitations are suppressed in the core of the Mott state. This is consistent with the zero-temperature result derived earlier where we see that chemical potentials approaching integer values of the interaction energy bring two states with different occupation numbers into degeneracy. Therefore, from the combined results,

we anticipate these regions of our Mott insulating state will contain fluctuations both inherent to the superfluid state that occupies the ground state in this parameter regime, but also the low-lying excitations localize the distribution of entropy in the cloud to these regions, producing locally lower-entropy states in the bulk of the Mott insulating plateau.

## 2.4 Floquet Engineering

From the above discussion, we have seen how to account for both the kinetic energy and interaction energy of atoms in an optical lattice or electrons in a crystal and how these natural tendencies lead to the formulation of the celebrated Hubbard model. The qualitatively different nature of these two terms in the Hubbard model lead to a quantum phase transition between a superfluid and a Mott insulating state. Examining how the tunneling and interaction terms arise in the lattice we see that the symmetries of these terms arise directly from the symmetries of the microscopic lattice Hamiltonian from which they were derived. Therefore, it is a useful question to ask whether we can engineer the underlying Hamiltonian in such a way to either break or to introduce new symmetries to an effective Hamiltonian that were not present to begin with?

An important example in solid-state systems is the coupling between electrons and electric and magnetic fields – such as the problem of Landau levels discussed in chapter 1 – that leads to time-reversal symmetry breaking. Understanding these systems has led to a revolution in modern condensed matter physics by the realization of materials that are not ordered according to Landau's classic symmetry-breaking principle, but instead are *topologically* ordered [163]. One paradigm of such states are the Landau levels of electrons in a large, externally applied magnetic field. The applied magnetic field couples to the electrons through the vector potential (in the process breaking time-reversal symmetry) resulting in cyclotron motion of the electrons. The eigenstates of this system are angular momentum eigenstates oriented along the field direction. Recent understanding of this system highlights the fact that this system,

when one Landau level is filled completely, hosts robust edge states that are protected by the topology of the bulk states [69].

In our analog crystalline system, the constituent atoms are neutrally charged, so there is no natural coupling to vector potentials that electrons in a crystal might experience. However, with a desire to realize similar physics or to engineer new, more exotic states that arise from breaking time-reversal symmetry, we are interested in techniques that allow the experimenter to controllably break or establish new symmetries in the underlying Hamiltonian. One powerful tool for accomplishing this task is time-periodic driving of the many-particle system [56, 57]. In order to describe and understand such systems we employ the formalism of Floquet theory [48].

In section 2.1, we utilized the discrete translation symmetry of the spatially periodic optical lattice to employ Bloch's theorem, which allowed us to factorize the wavefunction into the product of a plane wave and a function with the same periodicity as the underlying lattice. In Floquet theory, we utilize the same discrete translation symmetry as in Bloch's theorem (although historically speaking, Floquet's work preceded Bloch's by 45 years! [48, 15]) to reduce the fully time-dependent wavefunction to a plane wave term multiplying a term with the same temporal symmetry as the driving term:

$$\hat{H}(t) = \hat{H}(t+T) \ \text{, thus:} \quad \psi(t) = e^{i\epsilon t/\hbar}\phi_\epsilon(t), \tag{2.48}$$

where $\epsilon$ is known as the *quasienergy*, akin to the quasimomentum of Bloch's theorem, and is periodic in units of the driving frequency, $\epsilon = \epsilon + 2\pi\hbar/T$, and $\phi(t)$ is a periodic function with the same period as the driving frequency. This description allows the solution of the eigenvalue problem between times $0 \leq t < T$ to be sufficient to describe the time-evolution of the wavefunction for all times according to the new Hamiltonian equation:

$$(\hat{H}(t) - i\hbar\hat{\partial}_t)\phi_\epsilon(t) = \epsilon\phi_\epsilon(t). \tag{2.49}$$

What is remarkable about equation 2.49 is that the problem for finding a time-dependent solution to a time-dependent Hamiltonian can be solved by finding a time-*independent* quasienergy eigenvalue! As with Bloch's theorem, when given a solution

to this eigenvalue problem, there exist a whole family of solutions equivalent to the original solution up to a translation in quasienergy, $\epsilon \rightarrow \epsilon + n\hbar\omega$.

This description is both a powerful way of interpreting dynamics in periodically driven systems as a projection of the initial wavefunction onto a superposition of quasienergy eigenfunctions as well as a useful computational tool. However, solutions of equation 2.49 don't necessarily easily lend themselves to an intuitive interpretation of the dynamics of the system during the time evolution. A useful picture, and ultimately an equivalent one, is instead to search for a useful description of the steady-state dynamics in terms of an *effective*, time-independent Hamiltonian, $H_{\text{eff}}$.

Taking inspiration from the above Floquet description and following the general procedure spelled out in refs. [56, 57], we consider the operation of our time-dependent operator, $\hat{H}(t) - i\hbar\hat{\partial}_t$, which produced a time-independent quasienergy eigenvalue, on a generalized transformation of the time-dependent wavefunction:

$$\psi(t) = e^{-i\hat{K}(t)}\phi(t) \tag{2.50}$$

$$(\hat{H}(t) - i\hbar\hat{\partial}_t)\psi(t) = 0 \tag{2.51}$$

$$e^{i\hat{K}(t)}\left(\hat{H}(t)e^{-i\hat{K}(t)} - i\hbar\frac{\partial e^{-i\hat{K}(t)}}{\partial t}\right)\phi(t) = i\hbar\partial_t\phi(t) \tag{2.52}$$

The operator we have defined here, $\hat{K}(t)$ will become known as the "kick" operator, upon which we will bestow time-dependence in a way that both makes the effective Hamiltonian time-independent as well as gives the kick operator a simple experimental interpretation that is explored below. This unitary transformation then acts on the $(\hat{H}(t) - i\hbar\partial_t)$ operator above to define a transformed Hamiltonian:

$$\overline{H} = e^{i\hat{K}(t)}\hat{H}(t)e^{-i\hat{K}(t)} - i\hbar e^{i\hat{K}(t)}\frac{\partial}{\partial t}e^{-i\hat{K}(t)} \tag{2.53}$$

This transformed Hamiltonian, $\overline{H}$, describes the evolution of the wavefunction, $\phi(t)$, within one period of the optical cycle. It follows then that the time-evolution operator over a single modulation cycle integrates $\overline{H}$ over this modulation cycle, and is given by equation 2.54. We can now define the effective Hamiltonian, $H_{\text{eff}}$, as a

*time-independent* Hamiltonian that gives the equivalent time-evolution operator over the same modulation cycle.

$$U(t_f = T, t_i = 0) = \exp\left(\frac{-i}{\hbar}\int_0^T d\tau \overline{H}(\tau)\right) = \exp\big(-iH_{\text{eff}}T/\hbar\big) \tag{2.54}$$

This relation defines the effective Hamiltonian and allows the description of the wavefunction propagation for all times by reintroducing the kick operator:

$$U(t_f, t_i)\psi(t_i) = e^{-i\hat{K}(t_f)}e^{-i\hat{H}_{\text{eff}}(t_f - t_i)/\hbar}e^{i\hat{K}(t_i)}\psi(t_i) \tag{2.55}$$

The power of this effective Hamiltonian description over the Floquet quasienergy description is that the interpretation of the steady state motion as the action of the system in an effective Hamiltonian is made rigorous, and the effective Hamiltonian also highlights the ability of the modulation to change the symmetry properties of the undriven Hamiltonian and provides a way to analyze the new symmetry properties. One famous example is the realization of Floquet topological insulators [105, 131].

To make this transformation more concrete and to highlight its intuitive power, we consider two different exactly solvable models involving a phase-modulated optical lattice. The first will be in the case on non-resonant drive frequencies, and the second will examine the case of resonant driving by adding a linear potential gradient to the optical lattice.

### 2.4.1 Non-Resonant Drive

We begin with the example of a phase-modulated, one-dimensional optical lattice in order to show how this time-dependent drive can renormalize different Hamiltonian parameters. The time-dependent Hamiltonian for the phase-modulated optical lattice is:

$$H_{\text{PM}}(t) = \frac{p^2}{2m} + V_L \cos^2\big(k(x - x(t))\big). \tag{2.56}$$

We approach a solution by transforming into a frame accelerating with the trajectory of the driving term, $x(t)$:

$$\begin{aligned}\hat{H}(x,t) &= \hat{H}_{\mathrm{PM}}(z = x - x(t), t) - F(t)\hat{z} && (2.57)\\ &= \frac{p^2}{2m} + V_L \cos^2(kz) - m\omega^2 x_0 z \sin(\omega t - \theta) && (2.58)\\ &= \hat{H}_0 + \hat{V}(t). && (2.59)\end{aligned}$$

The time-independent part of the Hamiltonian can be immediately solved, yielding the band structure familiar to us from the previous section, and allowing us to construct localized Wannier function operators and recast the Hamiltonian into a second-quantized formulation:

$$\hat{H} = -t \sum_{\langle i,j \rangle} (\hat{a}_i^\dagger \hat{a}_j + \hat{a}_j^\dagger \hat{a}_i) - \xi \sin(\omega t - \theta) \sum_j j \hat{a}_j^\dagger, \hat{a}_j \qquad (2.60)$$

where we have defined the peak force over one site of the lattice as, $\xi = m\omega^2 x_0 a$, where $x_0$ is the amplitude of the shaking motion and $a$ is the lattice constant.

Next, we define the unitary transformation to eliminate the explicit time-dependence of the Hamiltonian, $\hat{R}(t) = e^{i\hat{K}(t)}$, what we will later discover to be the kick operator, and derive an effective Hamiltonian:

$$\begin{aligned}\hat{R} &= \exp\Big[ -i \sum_j \frac{\xi}{\hbar\omega} \cos(\omega t - \theta) j \hat{a}_j^\dagger \hat{a}_j \Big] = \sum_j e^{-i\lambda_j} \hat{a}_j^\dagger \hat{a}_j && (2.61)\\ \overline{H} &= \hat{R}^\dagger \hat{H}(t) \hat{R} - \hat{R}^\dagger i\hbar \hat{\partial}_t \hat{R}. && (2.62)\end{aligned}$$

For simplicity, we define the dimensionless driving parameter, $\zeta = \xi/\hbar\omega$, and the spatially-dependent prefactor of the kick operator, $\lambda_j = j\zeta \cos(\omega t)$. Applying the unitary transformation to derive the effective Hamiltonian, the time-derivative term on the right-hand-side of equation 2.62 cancels out the explicit time-dependence of the driving term in equation 2.60, and we are left with the transformed tunneling

part of the Hamiltonian:

$$\begin{aligned}\overline{H} &= -t\sum_{j'} e^{i\lambda_{j'}}\hat{a}^\dagger_{j'}\hat{a}_{j'}\sum_i(\hat{a}^\dagger_{i+1}\hat{a}_i+\hat{a}^\dagger_i\hat{a}_{i+1})\sum_{j''}e^{-i\lambda_{j''}}\hat{a}^\dagger_{j''}\hat{a}_{j''} &(2.63)\\ &= -t\sum_j\Big(e^{i\zeta\cos(\omega t-\theta)}\hat{a}^\dagger_{j+1}\hat{a}_j+e^{-i\zeta\cos(\omega t-\theta)}\hat{a}^\dagger_j\hat{a}_{j+1}\Big). &(2.64)\end{aligned}$$

We have arrived at equation 2.64 by repeated application of the commutation relation of the bosonic commutation relation, $[\hat{a}_i,\hat{a}_j]=\delta_{ij}$. To arrive at the effective Hamiltonian we are interested in the time evolution operator over the modulation cycle and the corresponding time-independent effective Hamiltonian. We get this from integrating $\overline{H}$ over the optical period, and setting the result equal to $H_{\text{eff}}T$:

$$\begin{aligned}H_{\text{eff}} &= \frac{1}{T}\int_0^T d\tau\overline{H}(\tau) &(2.65)\\ &= \frac{-t}{T}\int_0^T d\tau\sum_j\Big(e^{i\zeta\cos(\omega t-\theta)}\hat{a}^\dagger_{j+1}\hat{a}_j+e^{-i\zeta\cos(\omega t-\theta)}\hat{a}^\dagger_j\hat{a}_{j+1}\Big) &(2.66)\\ &= -J_0(\zeta)t\sum_j(\hat{a}^\dagger_{j+1}\hat{a}_j+\hat{a}^\dagger_j\hat{a}_{j+1}), &(2.67)\end{aligned}$$

which is equivalent to the lattice Hamiltonian we began with but now with renormalized tunneling parameter, $t\to J_0(\zeta)t=J_0(\xi/\hbar\omega)t$. Here we have used the Bessel function identity, $2\pi J_0(z)=\int_0^{2\pi}d\gamma\exp(iz\cos\gamma)$, to evaluate the time integral analytically. It is important to note that this Hamiltonian is the effective description of the time-periodic wavefunction, $\phi(t)$. The time-evolution of this state is given by its phase evolution under the effective Hamiltonian, $\phi(t_f)=U(t_f,t_i)\phi(t_i)=\exp(iH_{\text{eff}}(t_f-t_i)/\hbar)\phi(t_i)$, which can be evaluated as the phase evolution of Bloch eigenstates in the lattice with modified tunneling parameters.

Unfortunately, $\phi(t)$ is not directly observable in the lab frame because to get to this effective picture we had to make the unitary transformation $\psi(t)=e^{-i\hat{K}(t)}\phi(t)$ to get to this effective Hamiltonian picture. Therefore, the time evolution as observed in the lab frame wavefunction propagator is modified by the driving term as we transform

back to the lab frame as:

$$\psi(t_f) = U(t_f, t_i)\psi(t_i) = e^{-i\hat{K}(t_f)} e^{-i\hat{H}_{\text{eff}}(t_f - t_i)/\hbar} e^{i\hat{K}(t_i)} \psi(t_i). \tag{2.68}$$

This propagator now has a very straightforward physical interpretation in terms of the experimental implementation of the phase-modulated lattice.

Starting from the rightmost term, we begin with some initial state described by $\psi(t_i = 0)$; for example, a BEC in the $\mathbf{q} = 0$ Bloch state of the optical lattice. When we turn on the modulation sequence, there are different initial phases of the modulation the driving term can take, encoded in the kick operator as $e^{-ij\zeta\cos\theta}$. For example, we could use a sine drive where the lattice starts at it's average position and begins the modulation sequence with maximal velocity. For this case the initial phase $\theta = 0$ and the kick operator is a uniformly increasing phase $e^{-ij\zeta}$. On the other hand, if we start at the maximum extent of the modulation amplitude and at an initial velocity of zero – a cosine modulation – the resulting kick operator has $\theta = \pi/2$ and the phase is unity. Examining these two limiting cases, it becomes clear the interpretation of the initial kick operator as the change in momentum when going from a stationary frame into a modulated frame. Note also that the modulation amplitude $\zeta \propto x_0$, so starting the modulation with zero modulation strength can also send the initial kick operator to unity.

Now that we have understood the transition of the state from the lab frame to the modulation frame via the initial kick operator, we now see that the state is undergoing unitary evolution under the effective Hamiltonian of interest. After some experimental time where the effective Hamiltonian is experienced by the initial state, we now wish to measure the system. As with the initial kick operator, the final kick operator tells us how the phase of the modulation imprints a phase on the ensemble as we transform from the modulation frame back to the lab frame for a measurement. Putting these three parts together, we have come to a complete understanding of the effective Hamiltonian description and how it provides an intuitive explanation of not just the modification of the terms of the undriven Hamiltonian, but also the effect

on the wavefunction as we transform into and out of this rotating frame for state initialization and detection.

### 2.4.2 Resonant Drive

A second exactly solvable model that helps us understand the effects of time-periodic modulation comes from the case where the driving term is now resonantly coupling states offset in energy by some large gap, which we will call $\Delta$. There have been several implementations of this type of energy offset with important examples being in double well potentials, uniformly tilted lattices, and using the first and second bands of the lattice. To see the similarities and differences with the case of non-resonant driving, we analyze the case of a uniformly tilted lattice which is resonantly driven by phase-modulation.

The calculation proceeds similarly as above but with a uniform acceleration term added along with the transformation of the coordinates to one accelerated with the modulation trajectory:

$$\begin{aligned} H_{\mathrm{WS}}(t) &= \frac{p^2}{2m} + V_L \cos^2\left(k(x - x(t))\right) + \frac{\Delta}{a}x && (2.69) \\ H(t) &= \frac{p^2}{2m} + V_L \cos^2(kz) + \frac{\Delta}{a}z - m\omega^2 x_0 \sin(\omega t - \theta)z && (2.70) \\ &= H_0 + V(t) && (2.71) \end{aligned}$$

The eigenstates of the stationary Hamiltonian are known in the deep lattice ($\Delta \ll E_{\mathrm{gap}}$) and strongly tilted ($4t \ll \Delta$) limits as the Wannier-Stark ladder. The spectrum consist of states localized on each lattice site with local energy, $E_0$ and the energy of the $j$-th site spaced uniformly by $j\Delta$ so the energy in the Wannier-Stark basis before introduction of the modulation is $E_j = E_0 + j\Delta$. Modulation now has two effects when we examine the matrix elements $\langle w_i|z|w_j\rangle$. The diagonal contribution, when $i = j$, gives a time-dependent acceleration term identical to that of the non-resonant modulation. In addition, there are now off-diagonal matrix elements we must consider where $i = j \pm 1, j \pm 2, \ldots$. In the off-resonant modulation we ignored these terms

because they are off-resonance and tunneling is dominated by the nearest-neighbor, direct exchange, $t$. However, in the tilted lattice, tunneling is off-resonance because of the strong tilt and the first term which gives rise to particle exchange is the resonant, off-diagonal matrix element, $i = j \pm 1$. Including both diagonal and off-diagonal terms the second-quantized Hamiltonian becomes:

$$\hat{H}(t) = \sum_j \big(\Delta - \xi \sin(\omega t - \theta)\big) j \hat{a}_j^\dagger \hat{a}_j - K \sin(\omega t - \theta) \sum_j (\hat{a}_{j+1}^\dagger \hat{a}_j + \hat{a}_j^\dagger \hat{a}_{j+1}), \quad (2.72)$$

where we have defined what we will call the laser-assisted tunneling rate, $K = \xi \langle w_j | z | w_{j+1} \rangle / a$. The calculation proceeds similarly to the non-resonant case, we define a kick operator, $\hat{R}(t) = e^{i\hat{K}(t)}$ that eliminates the diagonal time-dependence of the Hamiltonian and then construct a transformed Hamiltonian, $\overline{H} = \hat{R}^\dagger \hat{H}(t) \hat{R} - \hat{R}^\dagger i\hbar \hat{\partial}_t \hat{R}$ such that:

$$\begin{aligned} \hat{R} &= \exp\Big[ -i \sum_j \big(j(\omega t - \theta) + \zeta j \cos(\omega t - \theta)\big) \hat{a}_j^\dagger \hat{a}_j \Big] = \sum_j e^{-i\lambda_j} \hat{a}_j^\dagger \hat{a}_j \quad (2.73) \\ \overline{H} &= \sum_j (\Delta - \hbar\omega) j \hat{a}_j^\dagger \hat{a}_j \ldots \\ &\quad -K \sin(\omega t - \theta) \sum_j \Big( e^{i((\omega t - \theta) + \zeta \cos(\omega t - \theta))} \hat{a}_{j+1}^\dagger \hat{a}_j + \text{H.c.} \Big). \quad (2.74) \end{aligned}$$

On resonance, $\hbar\omega = \Delta$ the diagonal term disappears and we are left with a Hamiltonian describing tunneling of our previously localized states through the optical lattice. If we now set the single-period time-evolution operator equal to the time-evolution operator for an equivalent effective Hamiltonian we get a relation between the two, which can be evaluated either by successive use of the Jacobi-Anger Bessel function identity, $e^{i\alpha\cos(\gamma)} = \sum_m (i)^m J_m(\alpha) e^{im\gamma}$, or by using the Bessel function identity, $\int_0^{2\pi} d\gamma \sin\gamma e^{i(\gamma + \alpha\cos(\gamma))} = 2\pi i J_1(|\alpha|)/|\alpha|$ to come to the effective Hamiltonian:

$$\begin{aligned} H_{\text{eff}} &= \frac{1}{T} \int_0^T d\tau \overline{H}(\tau) \quad (2.75) \\ &= -iK J_1(\zeta) \sum_j \big( \hat{a}_{j+1}^\dagger \hat{a}_j - \hat{a}_j^\dagger \hat{a}_{j+1} \big). \quad (2.76) \end{aligned}$$

In moving to the final line above we have defined a new laser-assisted tunneling strength, $K = \hbar\omega\langle w_j|z|w_{j+1}\rangle/a$.

There are some curious differences immediately visible from the effective Hamiltonian for resonant modulation, equation 2.76 and its associated kick operator 2.73, and the effective Hamiltonian for off-resonant modulation, equation 2.67 and its associated kick operator 2.61. The first is in the structure of the kick operators. Note that for off-resonant modulation the phase imprinted on the system from the initial and final kick operators can be eliminated by ramping the modulation amplitude to zero, $\xi \propto x_0 \to 0$. In contrast, for the case of resonant modulation there are two terms that compose the kick operator; one term corresponds to the modulation, which can be eliminated by ramping the modulation amplitude to zero, whereas the other term corresponds to the energy offset between states that are being resonantly coupled and cannot be ramped to zero by turning down the modulation strength, but must be eliminated by the separate process of turning off the gradient field.

A second important difference between the resonantly driven system and the off-resonant system appears in the perturbative limit of weak drive amplitude. The tunneling term in the resonantly driven system is proportional to the first Bessel function, compared to the zeroth Bessel function for the off-resonant driving case. This means that constructing a perturbative understanding of the process appears at first order in the resonantly driven case. In this case the process can be understood in the weak drive limit as the coherent coupling by lattice vibrations of nearest-neighbor lattice sites that are offset in energy. In contrast, for the off-resonantly driven lattice an understanding of the effect in the perturbative limit involves second-order processes that virtually mix in other quasimomentum states, producing a band structure with modified curvature and thus effective mass. Either way, the discussion presented above both serves to introduce the machinery of the periodically driven lattice as well as provide an exactly solvable limit in both the off-resonant and resonantly driven limits that will become useful for understanding and interpreting other modulation experiments that aim to introduce synthetic magnetic fluxes into the effective Hamiltonian.

## 2.5 Heating in an Optical Lattice

In the ideal limit, optical lattices are limited in temperature and entropy purely by the lowest temperatures achievable from evaporative cooling of a BEC. Light scattering places a fundamental limitation on the heating rate, but for typical intensities in far-detuned lattices, this time-scale exceeds vacuum limits by orders of magnitude. Empirically, the lifetime of a BEC in an optical lattice is much shorter than one might naively expect, and the entropies achieved in deep lattices are significantly higher than those achieved in BEC's in harmonic traps.

In this section, I present several mechanisms by which atoms in optical lattices might absorb energy from the environment and discuss a model for how these excitations thermalize and share entropy with the bulk of the particles remaining in the condensate. Throughout the discussion we will see how important a role the average density plays in not just the heating rate, but also the allowed thermalization processes, highlighting the importance of low density atomic samples in the lattice. Finally, we will discuss the role light scattering plays when near-resonant lattices are employed, in addition to a practical example of how we set bounds on the entropy in the Mott state when there is no finite temperature signal in time-of-flight measurements.

For a more lab-specific and humorous discussion of the lattice we have constructed in the lab in response to the various challenges the machine has presented, see appendix A.

### 2.5.1 Amplitude Noise

When we make our lattice with a laser beam or project it with an temporally incoherent source illuminating a phase mask, the potential depth is determined by the intensity of the optical lattice light. We often sample this light with a photodiode before it illuminates the atoms, compare the light level with some voltage set point, and then servo the intensity of the laser beam to match the voltage set point. This system does a good job of stabilizing the average intensity of the light field, but is

fundamentally limited in its ability to stabilize the intensity to the shot noise of the current generated at the photodiode. Often at low and high frequencies the feedback will instead be technical, but this is beyond the scope of the discussion here. For a more detailed treatment, see Appendix A.

Fundamentally, a small modulation of the amplitude of the light produces a time-dependent potential that modulates the effective spring constant of the trap:

$$H(x,t) = \frac{p^2}{2m} + \frac{1}{2}m\omega_0(1+\epsilon(t))x^2 \tag{2.77}$$

Where $m$ is the mass of the trapped atom, $\omega_0$ is the trap frequency, and $\epsilon$ is the amplitude of the small intensity noise on the laser beam. We proceed with the usual perturbative calculation by separating the problem into a zeroth order, solvable, time-independent Hamiltonian, $H_0$, and a time-dependent perturbation, $H'$:

$$H' = \frac{1}{2}m\omega_0^2\epsilon(t)x^2. \tag{2.78}$$

After solving the zeroth order Hamiltonian for the energy eigenstates, the excitation rate from the ground state, 0 to an excited state, n, can now be calculated within time-dependent perturbation theory:

$$\left(H_0 + H'(t) - i\hbar\partial_t\right)\sum_n a_n(t)|n\rangle e^{i(\omega_f-\omega_n)t} = 0 \tag{2.79}$$

$$\frac{da_f(t)}{dt} = \frac{-i}{\hbar}\sum_n \langle f|H'|n\rangle a_n(t)e^{i(\omega_f-\omega_n)t} \tag{2.80}$$

Integrating this equation over a timescale, $T$, that is long compared to the fluctuations in $\epsilon$, but short compared to the final transition rate, we can calculate the population

transferred in $T$ and derive a transition rate:

$$|a_f(t)|^2 = \left| \frac{-i}{\hbar} \int_0^T dt' \langle f|H'(t')|n\rangle e^{i\omega_{fn}t} \right|^2 \tag{2.81}$$

$$R_{n\to f} = \frac{\delta p_f}{\delta T} = \frac{1}{T} \left| \frac{-i}{\hbar} \int_0^T dt' \langle f|H'(t')|n\rangle e^{i\omega_{fn}t} \right|^2 \tag{2.82}$$

$$R_{n\to f} = \left( \frac{m\omega_0^2}{2\hbar} \right)^2 \int_{-\infty}^{\infty} d\tau \langle \epsilon(t)\epsilon(t+\tau)\rangle |\langle f|x^2|n\rangle|^2 \tag{2.83}$$

Note that due to the symmetry of the matrix element, $\langle f|x^2|n\rangle$, amplitude noise can only change the state index by $n \to n \pm 2$. This is easily seen in the decomposition of the $x^2$ operator into harmonic raising and lowering operators, where the expansion of the operator gives terms proportional to: $(\hat{a}+\hat{a}^\dagger)^2 = \hat{a}\hat{a} + \hat{a}\hat{a}^\dagger + \hat{a}^\dagger\hat{a} + \hat{a}^\dagger\hat{a}^\dagger$. Therefore, starting in the ground state of the harmonic oscillator, only the last term can drive transitions of population to the second excited state.

In addition, we have assumed that the noise is a stochastic, fluctuating background, so that the driving terms appear in the time correlation function:

$$\langle \epsilon(t)\epsilon(t+\tau)\rangle = \frac{1}{T} \int_0^T dt \epsilon(t)\epsilon(t+\tau). \tag{2.84}$$

Now using the definition of the x-coordinate in terms of the harmonic oscillator raising and lowering operator, $x = \sqrt{\frac{\hbar}{2m\omega_0}}(\hat{a}+\hat{a}^\dagger)$, we can express the rate for the transition to the second band as:

$$R_{0\to 2} = \frac{\pi\omega_0^2}{8} S(2\omega_0), \tag{2.85}$$

where $S(\omega_0)$ is the one-sided spectral power density function defined as:

$$S(\omega) = \frac{2}{\pi} \int_0^\infty d\tau \cos(\omega\tau) \langle \epsilon(\tau)\epsilon(t+\tau)\rangle. \tag{2.86}$$

The sum of the spectral power density function over all positive frequencies gives the total RMS intensity noise, $\epsilon_0$. A particularly rich intensity noise spectrum for one direction of our optical lattice is shown in fig. 2-8. As seen here, the character

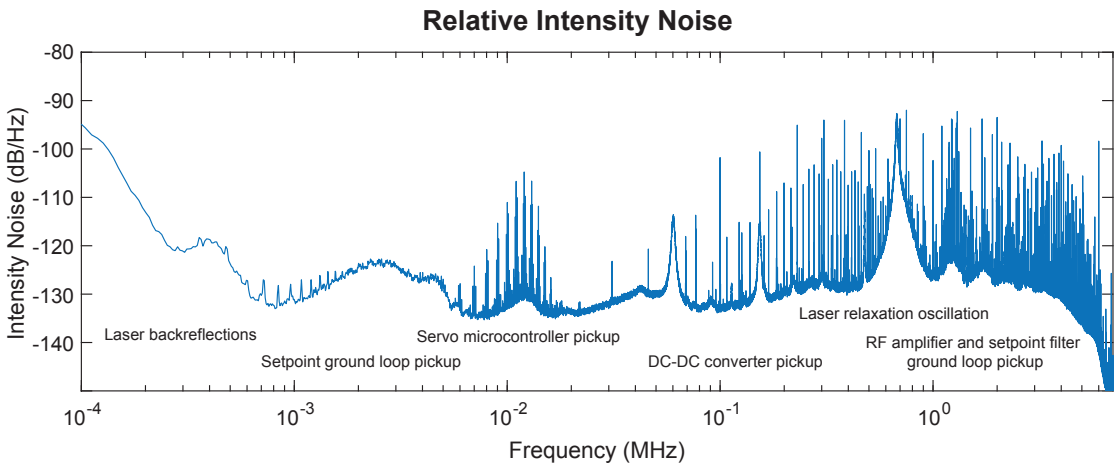


Figure 2-8: Intensity noise spectrum of the optical lattice light. The spectrum is collected by a digital spectrum analyzer monitoring the AC coupled signal from a shot-noise limited, transimpedance amplified monitor photodiode. The source of most of the structure in the spectrum is indicated. For more discussion, see appendix.

of the spectrum generally depends on the frequency region of interest. The largest contributors to noise are at low frequencies from back reflections in the optical lattice beam path as well as at high frequencies due to the relaxation oscillation peak of the master laser, as well as ground loops in the connections between the RF amplifier, control electronics and lab grounds. After eliminating these contributors, the largest noise sources appear at intermediate frequencies typical of an optical lattice band gap at several tens of kHz, where the spectrum is punctuated by a series of large peaks corresponding to poor signal and ground control in the servo electronics, poor placement (and construction) of DC-DC converters, and, again, ground loops in the setpoint generation. For a detailed analysis of these spectra and demonstration of shot-noise limited optical lattices, see the appendix.

In our quantum gas experiments, when we talk about maintaining the fidelity of a quantum state, the quantity of interest is the population in the coherent portion of the atoms. In a BEC this is the condensate fraction and in a Mott insulator this is the atoms which adiabatically connect to the BEC when the system is ramped back to the superfluid phase. To calculate the effect of scattering on the fraction of atoms in this state, we need to know the average energy increase of each scattering event, and

then – assuming the excitation thermalizes and assuming that we know the equation of state – we are interested in the relationship between this average energy increase and, for example, the condensate fraction.

The energy increase per scattering event is easy to calculate from the scattering rate given that each scattering event imparts $2\hbar\omega_0$ of energy and every atom starts out in the ground state with $\hbar\omega_0/2$ of energy, giving an exponential rate equation for the energy increase,

$$\dot{E} = \hbar\omega_0 R_{0\to 2} = \frac{\pi\omega_0^2}{4} S(2\omega_0) E \tag{2.87}$$

$$\gamma = \frac{\pi^2}{2}\nu_0^2 S(2\nu_0) \tag{2.88}$$

The above equation holds for small excited state populations. For larger occupation probabilities in the excited state, both transitions to higher bands, $R_{2\to 4}$, as well as transitions from higher bands back down to lower bands, $R_{2\to 0}$, must be considered in the rate equation. Nevertheless, from this analysis we see that the rate of energy increase shows an exponential scaling with a characteristic timescale, $\gamma$.

Examining the spectrum in figure 2-8, we see that for typical trap frequencies of few to many tens of kHz, the scattering rate ranges from $10^{-2}$ to $10^{-4}$ $s^{-1}$ depending on the location of the trap frequencies with respect to the switching peaks from the integrated microcontroller in the servo electronics. Regardless, if we take the scattering rate to be even $\sim 10^{-3}$ $s^{-1}$ for a trap frequency $> 10$ kHz, this corresponds to an exponential rate coefficient of $\gamma \approx 10^{-3}$ $s^{-1}$ and an initial heating rate for a modest initial temperature of 10 nK of 10 pK/s. Given the low rate of increase due to the experimentally observed intensity noise spectrum, we can safely disregard this process as the dominant heating rate in the current experiment.

### 2.5.2 Phase Noise

In addition to the fluctuations in the effective spring constant of the on-site harmonic confinement that can be driven either by fundamental or technical laser intensity noise, heating can also occur due to fluctuations in the trapping center. For different

geometry lattices these fluctuations can have different fundamental sources, but in our experiment we typically use the retroreflected lattice geometry. In this case, noise in the center position of the trapping potential is driven by a few main sources: the finite linewidth of the trapping laser, fluctuations in the position of the retroreflecting mirror surface, and fluctuations in the pointing direction of any confining laser beams in other directions can all produces trapping potential minima noise.

To model this behavior, we begin as in the case of amplitude noise by making a harmonic approximation to our trapping potential

$$H = \frac{p^2}{2m} + \frac{1}{2}m\omega_0^2(x - \delta(t))^2 \tag{2.89}$$

with a stochastically fluctuating time dependent term, $\delta(t)$ driving the trap center. Expanding the square of the position, we recover a zeroth order Hamiltonian, $H_0$, that is the normal harmonic oscillator, in addition to a uniform off set term quadratic in $\delta$ that we can ignore, and a perturbation Hamiltonian:

$$H' = -\delta(t)m\omega_0^2 x. \tag{2.90}$$

The calculation for this phase noise term proceeds in similar fashion through time-dependent perturbation theory as the amplitude noise analysis with only the dimensionality of $\delta$ (length) differing from $\epsilon$ (dimensionless). Defining the position noise one-sided spectral power density function as:

$$S_x(\omega) = \frac{2}{\pi}\int_0^\infty d\tau \cos(\omega\tau)\langle\delta(t+\tau)\delta(\tau)\rangle, \tag{2.91}$$

with $\langle\delta(t+\tau)\delta(\tau)\rangle = \frac{1}{T}\int_0^T dt\delta(t)\delta(t+\tau)$ we come to a similar expression for the scattering rate from the ground state to an excited state:

$$R_{n\to f} = \left(\frac{m\omega_0^2}{\hbar}\right)^2 \int_{-\infty}^{\infty} d\tau\langle\delta(t)\delta(t+\tau)\rangle|\langle f|x|n\rangle|^2 \tag{2.92}$$

In contrast to the amplitude noise heating rate, note the different dependence of

the matrix element on the position operator. Expressing the position operator as $x = \sqrt{\frac{\hbar}{2m\omega_0}}(\hat{a}+\hat{a}^\dagger)$, we see that this noise source can only drive $n \rightarrow n+1$ transitions. Therefore, starting out in the ground state we only have a matrix element to the first excited state with a rate:

$$R_{0\rightarrow 1} = \frac{\pi}{2\hbar} m\omega_0^3 S_x(\omega_0) = \frac{2\pi^2}{\hbar} m\nu_0^3 S_x(\nu_0), \tag{2.93}$$

Similar to the discussion of amplitude noise, each scattering event carries $\hbar\omega_0$ of energy, so the rate of energy increase can be written as $\dot{E} = \hbar\omega_0 R_{0\rightarrow 1}$.

For a laser beam that creates an optical lattice, there are two types of fluctuations that we might be sensitive to, transverse beam pointing fluctuations in addition to longitudinal phase fluctuations. Without knowing *a priori* which is of greater importance, we can make a qualitative estimation of their relative importance by modeling an atoms confinement by two harmonic oscillators: first, the lattice trapping potential with frequency $\omega_1$, and second, a lower spring constant confinement with frequency $\omega_2$. Fluctuations in the potential minima of both potentials will appear in the harmonic approximation to the higher spring constant potential, $\omega_1$, potential as:

$$m\omega_1^2\left(x - x_1(t) - \frac{\omega_2^2}{\omega_1^2}x_2(t)\right) \tag{2.94}$$

where the amplitude of $x_2$ fluctuations are attenuated by the ratio of trap frequencies squared. Practically speaking, for optical lattice trap frequencies typically in the range of many 10's of kHz, and harmonic trapping frequencies ranging from 10 to 100 Hz, this means the effect of transverse pointing noise fluctuations is $10^4$ to $10^6$ times less important than longitudinal noise for on-site harmonic oscillator excitations. As a result, we hypothesize that the direction with the highest trap frequencies, i.e. the strongest spring constant, will dominate the heating rate.

Figure 2-9 shows the typical vibration spectrum measured using a Michelson-Morley interferometer setup with the lattice retroreflection mirror as one arm of the interferometer. The blue trace is taken with the mirrors that form both arms of the interferometer placed on the same breadboard, and the orange is taken with one mirror

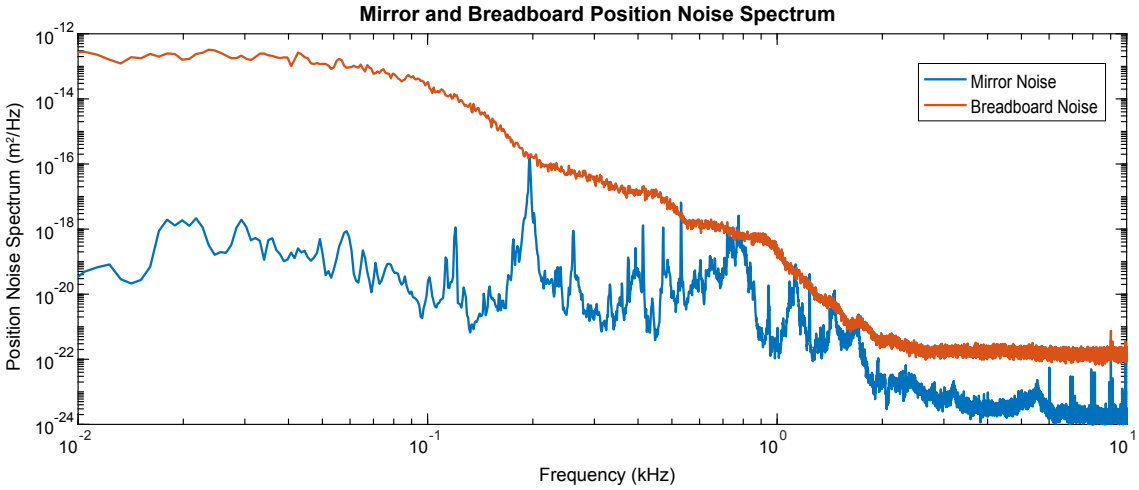


Figure 2-9: Position noise spectrum of the lattice retroreflection mirror. Data is collected by monitoring the output port of a Michelson-Morley interferometer, approximately set to a half-fringe condition, with a shot-noise limited, transimpedance amplified photodiode. The blue curve is taken with all mirrors on the same breadboard compared to the orange trace taken with the retroreflection mirror on a separate, vibration isolated breadboard, forming one path of the Michelson-Morley interferometer.

placed on an independent breadboard which is vibrationally isolated from the table using four Newport VIB100 mechanical isolators. Therefore, the orange trace plots the vibration noise spectrum between the inertial frame of the floating breadboard from the unfloated optical table. As we can see, above 1 kHz the spectrum falls sharply and quickly drops below the shot noise of the photodiode used for measurement. If we evaluate the scattering rate at 1 kHz from equation 2.93 we get 85 Hz. For higher lattice depths, since the spectrum falls faster than $1/\nu^3$, the lifetime gets longer. Close to the point where the spectrum meets the noise floor at 2 kHz, the corresponding noise-limited scattering rate has fallen to 0.2 Hz. From this spectrum we postulate that the lifetime for scattering to higher bands at extremely low lattice depths might be strongly limited by the phase noise inherent in the retroreflection mirrors of our lattice setup.

Examining the heating rates from amplitude and phase noise of the optical lattice light, we see several general features of the two different types of excitation. First of all, we have that parametric excitation can only drive population to the second band of an optical lattice compared to shaking excitation which can only drive to the first band. Secondly, the relevant amplitudes are the spectral densities of each type of excitation evaluated at the relevant frequencies of interest, $2\omega$ and $\omega$, respectively. Third of all is the scaling of their relative importance with increasing trap frequency. For both excitation channels, the scattering rate increases with increasing trap frequency. However, the relative importance of the two depends on frequency via the ratio:

$$\frac{R_{0\to 1}}{R_{0\to 2}} = \frac{4m}{\hbar}\omega_0 \frac{S_x(\omega_0)}{S(2\omega_0)}. \tag{2.95}$$

Empirically, in our lab, the amplitude noise spectrum of the lattice light generally has an (approximately) white spectrum within the gain bandwidth of our lattice servo controllers and a rising spectrum out to the relaxation oscillation peak our our lattice laser, followed by a $1/f$ behavior (with the exception of large, discrete peaks) out to higher frequencies. However, the phase noise we measure from the retroreflection mirror generally falls like a power higher than $1/f^3$ for the observable frequencies.

With this hierarchy, we determine that moving to a lighter atom or going to a shorter spacing lattice constant has a positive effect in the total lifetime when counted in terms of the total coherence time relative to the tunneling rate. The tunneling rate increases linearly in the recoil energy, whereas the phase noise becomes less of a limitation at low frequencies. This scaling is reasonable until the phase noise spectrum begins to fall more gently than $1/\nu^3$.

We can test these ideas by examining the heating observed in the lattice as a function of the lattice depth, which changes the on-site trapping frequencies and greatly changes the heating rates. To measure the heating rate, we load a single component condensate into an isotropic, three-dimensional lattice ($\lambda = 1064$ nm) and vary the lattice depth and hold time. In order to measure lifetimes on both sides of the superfluid to Mott insulator transition the condensate fraction is probed in the bulk BEC by ramping the lattice off again. Figure 2-10 shows a comparison of two different hold times of zero and two seconds, as a function of the lattice depth. At low lattice depths, we observe no strong heating as indicated by the phase noise calculation. For no hold time, the condensate fraction decays only weakly as the lattice depth is increased, indicating either that the ramp does not create much entropy or that the entropy created in the lattice ramp has not had time to thermalize with ground band atoms at deep lattice depths. Interestingly, for two seconds hold time the condensate fraction at low lattice depths remains high, but as the lattice depth increases the condensate fraction drops precipitously from 6 to 14 $E_r$. The condensate fraction is at a minimum at 14 $E_r$, a lattice depth that corresponds to the Mott insulating transition for the $n = 1$ Mott state, before recovering modestly past the transition region up to 20 $E_r$. This non-monotonic behavior around the Mott transition suggests a low-frequency heating mechanism related to the many-particle physics happening at the transition region – perhaps due to the vanishing gap and critical slowing down of dynamics at the quantum phase transition – and not the single particle effects discussed above. In the following sections we will discuss some collisional physics in an effort to understand how single particle excitations can interact with the many-body state in the ground band.

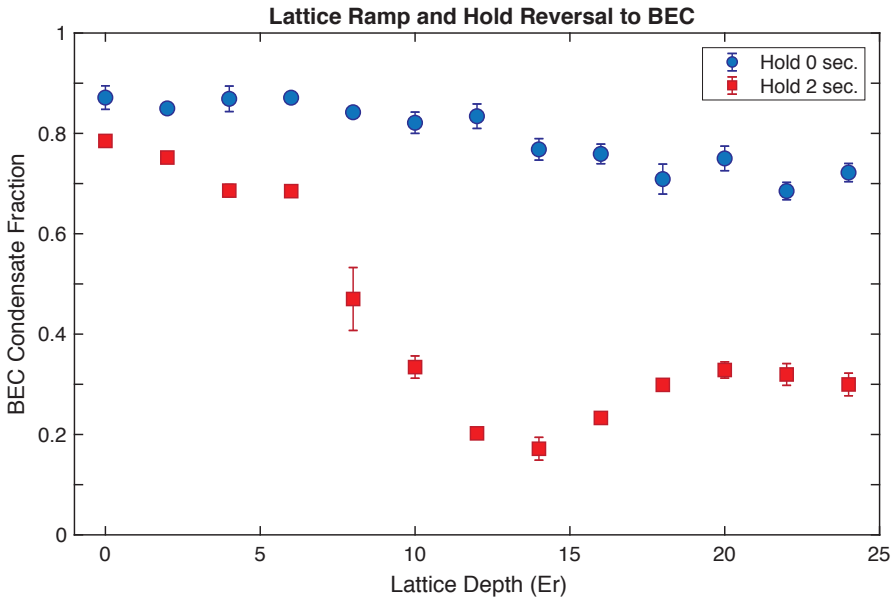


Figure 2-10: Condensate fraction after holding in the lattice. A single component BEC in the $|1,-1\rangle$ state is loaded into a three-dimensional, isotropic optical lattice and then adiabatically ramped down to zero lattice depth after no hold at the final lattice depth (blue circles) compared to after a 2 second hold (red squares). Of note is the non-monotonic behavior of the data for a two second hold time. The pronounced minimum in the condensate fraction corresponds to the location of the phase transition from superfluid to Mott insulator.

### 2.5.3 Light Scattering

In the latter part of this thesis, near-detuned light will be used to exploit the vector stark shift in an optical lattice. As a result, light scattering will become the dominant contributor and important limiting factor on our lattice temperature and heating rate. We have discussed in section 2.2 the scattering rate for near detuned light and how the scaling with detuning is not favorable for the ratio of the scattering rate to the vector stark shift. In this section, we discuss the final state effects of light scattering and how the process of light scattering transfers energy to the atoms in an optical lattice.

In our discussion, we will consider the limit of a BEC in an optical lattice where the lattice is deep enough to produce well-defined bands in the spectrum. Light scattering serves to localize the initially delocalized particle as well as transfer a photon recoil worth of energy and momentum to the atoms in the process. Starting with an atom in the lowest band, the light scattering process which localizes the particle can promote an atom to a higher band of the lattice. The excitation probability for this process from the ground state $n = 0$ to an excited state $m$ in the harmonic oscillator approximation is:

$$A_{0,m} = \langle m|e^{i\eta(\hat{a}^\dagger+\hat{a})}|0\rangle \approx \langle m|1 + i\eta(\hat{a}^\dagger + \hat{a}) + \ldots|0\rangle, \tag{2.96}$$

where we have introduced the Lamb-Dicke parameter, $\eta$, that tells us the overlap between the initial ground state and the first excited state wavefunction. The Lamb-Dicke parameter is defined by the product of the excitation laser wave vector and the harmonic oscillator length or alternately, and equivalently as the ratio of corresponding energies:

$$\eta = k_L a_0 = k_L\sqrt{\frac{\hbar}{2m\omega_0}} \tag{2.97}$$

$$\eta^2 = \frac{\omega_r}{\omega_0}. \tag{2.98}$$

In the right side of equation 2.96 we have assumed a deep lattice limit where $\eta < 1$,

and used this small parameter to expand the exponential to first order. Keeping only the first two terms in the series, from this expression we can see that the probability of exciting a ground state atom to the first excited state is given by $P_1 = \eta^2$ whereas the probability of scattering to the ground band is $E_0 = 1-\eta^2$. Therefore, the average energy can be written as:

$$\langle E \rangle = P_0 E_0 + P_1 E_1 + \dots \tag{2.99}$$

For a typical lattice the Lamb-Dicke parameter is between a factor of 1/3 to 1/8, so in principle multiple bands might need to be accounted for for an accurate treatment. The localized final state in each band means that the atom occupies a superposition of many quasimomentum eigenstates, uniformly filling the band, therefore, we can express the energy of a particle that ends up in the $n$-th band as the sum of the bandgap plus the band width, $E_n = E_n^{\text{gap}} + W_n$. It is now clear that the scattering of a particle by spontaneous emission process has the potential to raise the energy of a many-body system not just by producing holes where a particle once occupied, but also when we consider that a single particle in an excited band has both the energy of the band gap as well as the energy of the band width that it can redistribute to other particles in the many-body system via collisional processes.

In the following section, we will explore how an excitation, once it is created in the upper bands of a lattice can thermalize through different collisional processes in order to decrease the condensate fraction by more than just the particle removed from the initial state by the scattering processes discussed here.

### 2.5.4 Density, Collisions, and Thermalization in a Lattice

In a typical experimental sequence, a nearly pure BEC in a trap is illuminated with the optical lattice light. The light intensity is adiabatically ramped from zero to a desired lattice depth in an finite amount of time. Ideally, the entropy of the initial condensate is preserved in this operation. As described above, practically speaking there are a multitude of processes that can lead to heating during this process including inelastic

light scattering, amplitude, and phase noise. In this section we describe one additional heating process, non-adiabaticity, in conjunction with a description of how these excitations lead to heating through collisions and thermalization with ground state atoms. In this discussion, we will see the important role that density plays in the resulting dynamics and the lowest achievable temperatures in a deep lattice.

In figure 2-11, the relative energy of the first, second, and third bands are plotted as a function of the lattice depth, expressed in units of the number of recoil energies deep the total potential is. The strength of the three directions of the cubic lattice are assumed to be equal such that the first excited band consists of one direction of singular excitation and the other two are of the lowest occupation number, i.e. all cyclical permutations of the band occupation numbers $\{n_x, n_y, n_z\} = \{1, 0, 0\}$. At low lattice depths, $N_r < 2.4$, note that the lowest eigenstates of the first excited band lies below the highest excited state of the ground band. This phenomena arises for states near the Brillouin zone boundary, where the highest states of the ground band at quasi-momentum $ka = (\pi, \pi, \pi)$ have energy relative to the absolute ground state of $\sim 12t$ whereas the lowest states of a $q_x$ excited band at quasimomentum $ka = (\pi, 0, 0)$ have energy $4t$.

This energy hierarchy implies that at low lattices, thermal excitations at the scale of 1 $E_r$ can occupy states that are adiabatically connected to the first excited band in a deep lattice. Fortunately, the condensate wavefunction primarily occupies states near $k = 0$, which is gapped for all lattice depths. This effect is more important for ultracold fermions, who, even at zero temperature, can have finite occupation probabilities at large quasi-momenta. Restricting the discussion to bosonic particles, these state can be thermally occupied at low lattice depths and, upon increase of the lattice depth to its final value, this thermal population is then adiabatically transferred to the excited band. This effect is what I (admittedly, incorrectly) call here the non-adiabatic effect that leads to finite population of thermal particles in the excited band of a deep optical lattice.

This naturally leads to the following questions: what mechanisms are responsible for populating these excited states and how do these excited band particles thermalize

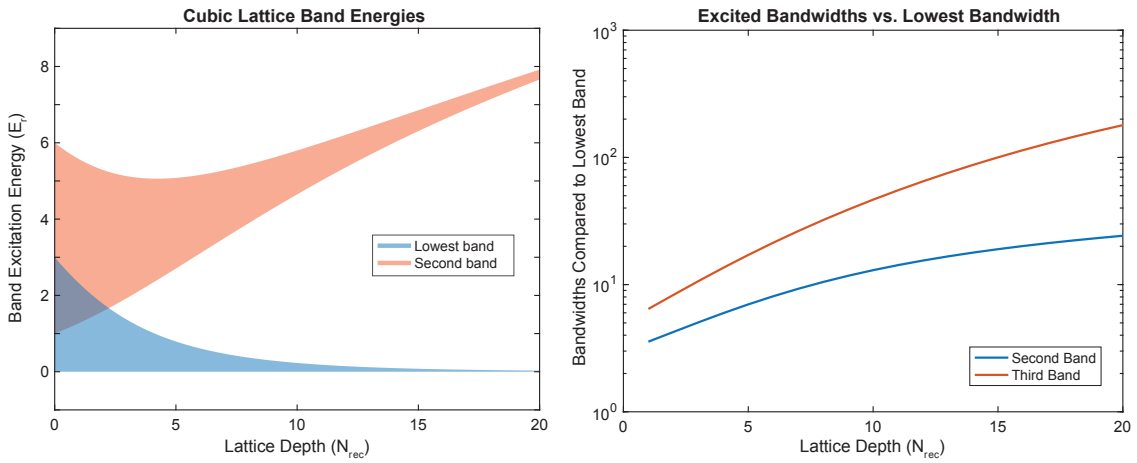


Figure 2-11: Bands of the isotropic cubic lattice as a function of the lattice depth. (Left) Shaded regions correspond to the states contained within the lowest (blue) and first excited (orange) bands. Of special interest is the overlap of the two bands at low lattice depths where the lowest states of the upper band are lower in energy than the highest states of the lower band. (Right) The ratio of the excited band width to the lowest band width showing the average energy one excited band particle can impart to the ground band particles via band-conserving collisions.

with the condensate atoms in the ground band? To address this question we begin by describing the different collisional processes that can happen in the lattice. The mathematics proceeds a bit differently than elastic collisions in free-space since now momentum isn't strictly conserved, but instead the quasi-momentum is conserved modulo the reciprocal lattice vector, $Q$. This enables scattering processes known as *umklapp* processes – scattering to final states outside of the first-Brillouin zone. In the following, we do not explicitly take into account such processes, but nevertheless such final states contribute to the overall scattering amplitude.

In general, there are two different collisional processes happening between ground band and excited band particles: band-conserving collisions, and band-changing collisions.

We begin by discussing band-conserving collisions. This class of collisions changes the quasi-momentum of the ground and excited band particles while preserving their band index. These collisional processes allow the energy of the excited bands to be transferred to the atoms in the ground band. In a classical picture of the scattering process of an excited band particle and a condensate atom initially in the $\mathbf{q} = 0$

ground state, the two-body collision conserves quasi-momentum, modulo $Q$:

$$\mathbf{q}_{1,i} = \mathbf{q}_{1,f} + \mathbf{q}_{2,f} \tag{2.100}$$

and energy:

$$E_{1,i}(\mathbf{q}) = E_{1,f}(\mathbf{q}) + E_{2,f}(\mathbf{q}). \tag{2.101}$$

In the lattice, writing the momentum as the product of the mass and velocity is not advantageous since the effective mass of the initial and final states are different because the band curvature is different at every point:

$$m^* = \hbar^2 \left( \frac{\partial^2 E}{\partial q_i^2} \right)^{-1}. \tag{2.102}$$

Instead, to visualize the scattering process, diagrams like figure 2-12 are useful to draw, showing an exemplary collision that can remove an atom from the condensate. Note that at the bottom of the upper band the effective mass diverges and there are no more lower energy states to relax to, so without a band-changing collision, population in the excited state will accumulate at the bottom of the second band, after releasing their energy through collisions with atoms in the lower band.

With this model in mind, we can quantify how much energy the relaxation of an excited band particle adds to the ground band atoms. To begin, we assume that the excited band particle is prepared in some energy and momentum state, $E_{2,i}(\mathbf{q})$, and relaxes down to an energy close to the excited band minimum, $E_2^{\min}(\mathbf{q})$. On average, the energy lost by an atom in a uniformly distributed, random starting position in the band will be $\Delta E = \langle E_{2,i}(\mathbf{q}) - E_2^{\min}(\mathbf{q}) \rangle_{\mathbf{q}} = W_n/2$, where the angled brackets denote the average over a uniform distribution and $W_n$ is the bandwidth of the $n$-th band.

The energy lost by the excited band atom is absorbed by the ground band atoms. For simplicity, we assume the ground band atoms are an ideal Bose gas in a uniform potential. With these assumptions, the heat capacity can be calculated from the

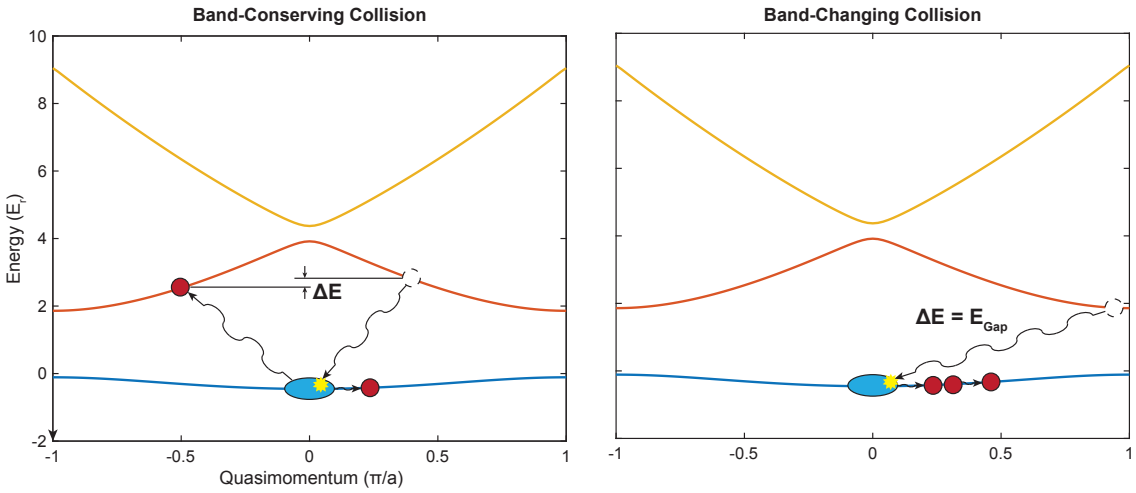


Figure 2-12: Schematic of possible collision channels between ground and excited atoms. Excited band particles can thermalize with lowest band atoms via quasimomentum-, energy-, and band-conserving collisions (left) shown for a second band particle, and can also be constructed for a third band particle. A second thermalization mechanism occurs via band-changing collisions (right) causing an excited band particle to fall to the lowest band and produce multiple excitations to satisfy quasimomentum- and energy-conservation.

Bose-Einstein distribution to be:

$$\frac{C_V}{Vk_B} = \frac{1}{Vk_B}\frac{\partial E}{\partial T}\bigg|_V = \frac{3}{2\lambda^3}\left[\frac{5}{2}f_{5/2}(z) - \frac{3f_{3/2}(z)^2}{2f_{1/2}(z)}\right] \tag{2.103}$$

For a typical experiment we begin with a condensate well below the condensation temperature, $T_c$, so the second term in the bracket is negligible and we expand the first term to get the heat capacity at low temperatures:

$$\frac{C_V}{Nk_B} = \frac{1}{n}\frac{C_V}{Vk_B} = \frac{15}{4n\lambda^3}\zeta(5/2) \propto T^{3/2}. \tag{2.104}$$

With this knowledge in hand we can now calculate the expected temperature increase for a small excited state population totaling $N_{\text{ex}}$ particles out of $N_{\text{BEC}}$ condensate atoms, whose ratio give the excited state fraction, $f = N_{\text{ex}}/N_{\text{BEC}}$, as a function of starting temperature and lattice depth via:

$$\Delta T = N_{\text{ex}}\Delta Q/C_V = \frac{N_{\text{ex}}W_n}{2}\Big/\frac{15N_{\text{BEC}}k_B\zeta(5/2)}{4n\lambda^3} = \frac{2fW_n n\lambda^3}{15k_B\zeta(5/2)} \tag{2.105}$$

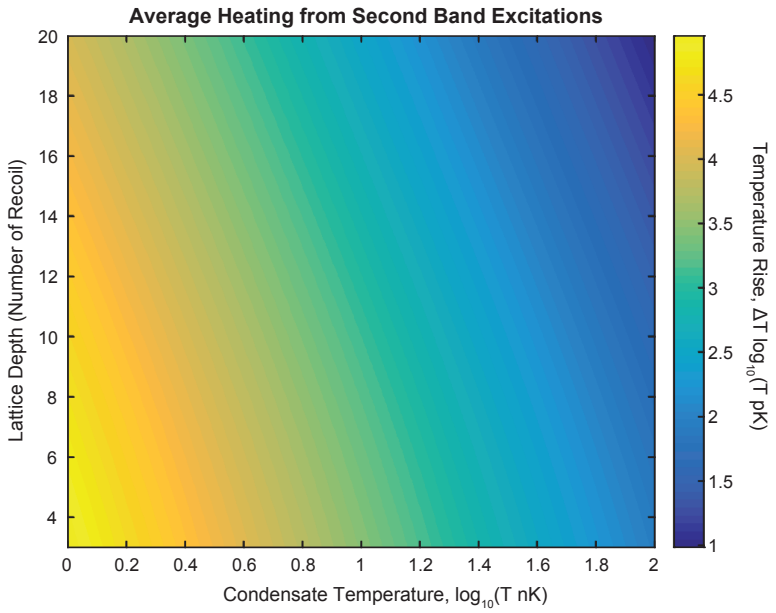


Figure 2-13: The average temperature increase for band-conserving collisions with 0.1% excited band probability. Assuming a uniform initial occupation probability within the second band and complete relaxation to the lowest state in the second band, the average temperature increase of the condensate in the ground band as a function of the starting temperature and the lattice depth. Results are calculated for a non-interacting gas in a uniform potential, thermalizing with a 0.1% excited band probability, and show how the cloud becomes increasingly sensitive to a low excitation probability as the starting gas becomes colder.

Figure 2-13 shows these quantities in a contour plot for an arbitrarily chosen excited state fraction to be 0.1% – chosen to be small since very large populations would be easily detectable using standard time-of-flight and band-mapping imaging techniques. We see that the effect of the excited band atoms gets worse as the starting condensate temperature is lower. In fact, as the system approaches zero temperature the heat capacity goes to zero – as required by the third law of thermodynamics – so the effect of any finite amount of energy added to the system is magnified, making the temperature increase on each scattered excited band atom worse. In addition, we see that the temperature increase scales linearly with phase space density, $n\lambda^3$. Therefore, at fixed temperature, as we increase the average occupation of the lattice from unity to higher fractions, the temperature increase with each relaxation process should scale with the occupation number. For example, at a typical temperature of 10 nK and

unity lattice occupation in a 14 $E_r$ lattice – close to the transition point from the superfluid to a Mott insulating state – the average temperature increase for a single excited state atom is 721 pK. However, if the filling is increased to 5, an occupation number we can easily (and often have for experiments that require a high signal-to-noise ratio) prepared in the lab, the average temperature increase per excited state atom is 3.6 nK! As a result, an experiment with a cloud of a few ten thousand atoms, can be sensitive to less than a percent-level occupations of states in the excited band. This sensitivity to the total atom number and density is a result we see here first, and it will be a recurring theme in our continuing discussion and experimental results.

A more refined calculation may take into account the heat capacity of an interacting BEC in the limit of phonon excitations. This linear spectrum gives a $T^3$ scaling of the heat capacity, or if numerical precision is required, the full integral with the Bogoliubov quasiparticle spectrum can be numerically evaluated. Note that in a realistic experiment the excited fraction may not necessarily be in thermal equilibrium with the ground band atoms at all stages of the ramp, and that dynamical effects may play a role. One such effect that we have so far ignored is the additional heating process of band-changing collisions.

As discussed above, when a particle is in the lowest state of an excited band, there are no more states within that band the excited atom can relax to. In fact, for each state in the excited bands, each collision with ground band atoms carries a finite probability of relaxation to a lower band. This process is depicted schematically in Fig. 2-12. Once again, just like with band-conserving collisions, this collision must obey energy and quasi-momentum conservation (modulo $\mathbf{Q}$!) rules. An interesting situation arises when the excited band gap becomes much larger than the lower band width; how can a band-changing collision conserve energy?

Looking at Fig. 2-14, we see, for example, at a moderate lattice depth of 14 $E_r$ – close to the superfluid to Mott insulator transition for a lattice of singly-occupied $^{87}$Rb atoms – the ratio of the band gap to the lowest band width is 62. In the simple scattering model we then expect that in order to conserve energy in the relaxation process the final state must be one that has at least 62 excitations of a state with

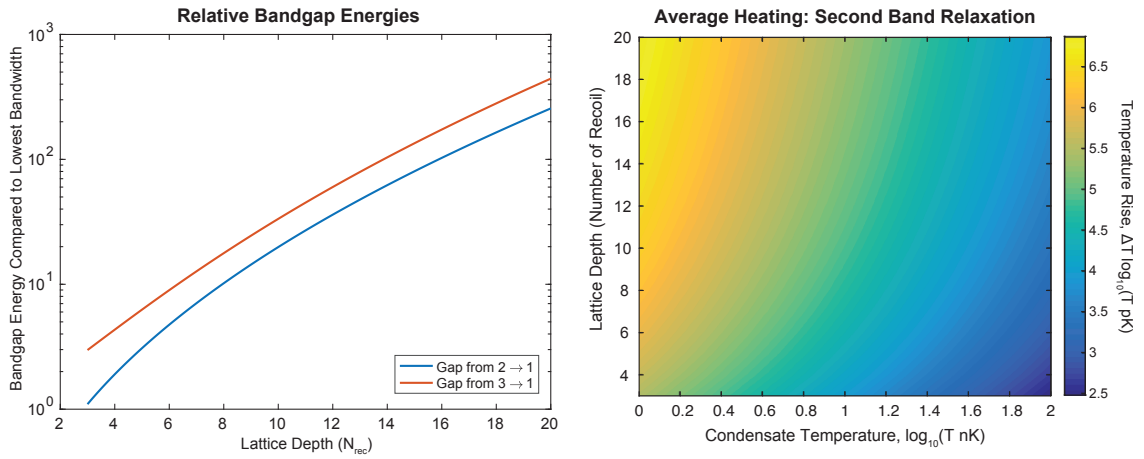


Figure 2-14: The average temperature increase for one excited band relaxation process. Plotted as a function of the starting temperature and the lattice depth, the results – similarly to the band-conserving case – are calculated for a non-interacting gas in a uniform potential and once again show how the cloud becomes increasingly sensitive to a low excitation probability as the starting gas becomes colder. For sufficiently low densities, multi-particle collision events are suppressed leading to a freeze-out of these relaxation processes at high lattice depth.

the maximum lowest band energy – a highly unlikely collision! For this reason, when considering band-changing collisions, we treat these processes as being frozen out at high lattice depths. However, at low lattice depths, the ratio of the band gap to the lowest band width is much more favorable. At 4 $E_r$ this ratio is a factor of 2, so for typical densities of bosons in an optical lattice, usually less than three or four particles per site, this process is not frozen out. Therefore, we can see that, as with the band-conserving collisions, the density of atoms in the lattice plays a crucial role in the collisional physics. If we consider the requirement for energy conservation during the relaxation process, then these band-changing processes can only occur for occupation numbers of:

$$E_{\text{gap}} \leq n_{\max} W_1, \tag{2.106}$$

where $E_{\text{gap}}$ is the band gap at a given lattice depth between the ground band and an excited band, $n_{\max}$ is the maximum on-site density of the lattice (we restrict ourselves here to on-site collisions only), and $W_1$ is the bandwidth of the lowest band in the optical lattice. In Fig. 2-14(b) we plot the ratio of the $1 \rightarrow n$*th* band gap to the lowest

band width as a function of lattice depth. For a given lattice depth, the two plots can be used to determine the energy deposited in the ground band by a band-changing collision, as well as whether the maximum lattice occupation allows such processes to occur.

For example, we consider the case of a shallow lattice with average filling of one particle per site. Consider the initial state with one atom sitting in the lowest energy state of the first excited band and another condensate atom in the $\mathbf{q} = 0$ state of the ground band. Assuming that this collision is energetically allowed, the relaxation of the excited state atom to the ground band will create a final state of two ground band particles in different quasimomentum states that both satisfy quasimomentum and energy conservation. These particles can collide and thermalize with the rest of the atoms in the ground band, thus raising the energy of the ground band atoms by $\Delta Q = E_{\text{gap}}$. Utilizing the heat capacity of the condensate presented above, we can calculate the temperature increase as a result of this process, shown in figure 2-14.

The average temperature increase per single excited band relaxation is calculated, for demonstration purposes for a peak density of three particles per lattice site, or approximately $2 \times 10^{13}$ cm$^{-1}$.

In the above discussion I have assumed that there is a continuous band of final states for scattering from the initial states. However, for cold atoms in optical lattices this is not necessarily true. In the superfluid phase, the ground band has a gapless excitation spectrum; however, crossing the phase transition to the Mott insulating phase, the system becomes gapped at low energy. In this regime, we will have to account for the gapped nature of the final states in evaluating both the energetics of scattering as well as the heat capacity of the many-body state. For example, in deep lattices $\sim 17E_r$ for $^{87}$Rb in a 532 nm lattice, the Mott gap can exceed the first excited state bandwidth, meaning that collisions between the ground state atoms and all states in the first excited band are suppressed. This is an interesting collisional regime, but further treatment of this situation lies outside the scope of the current discussion.

One final source of heating in an optical lattice is apparent in the plot of the band

energies as a function of lattice depth in fig. 2-11. At lattice depths between 0 and 2.4 $E_r$ the lowest eigenstates of the second band lie lower in energy than the highest eigenstates of the lowest band. This means that in the lowest parts of the lattice ramp, the states that will adiabatically become high-energy states in the first excited band are not energetically gapped from those states that will become the lowest band states, and in fact they are even energetically preferable to be populated either thermally or via technical noise! More fundamentally, the condensate is trapped in a harmonic confining potential which breaks translational symmetry in the system. Therefore, the translational symmetry we used to invoke Bloch's theorem and model our lattice energies in terms or quasimomentum eigenstates is broken and the trap causes mixing between momentum eigenstates. Therefore, if we load a trapped condensate into a lattice, the initial state can have some admixture of quasimomentum states that project into excited states of the lattice. If the initial ramp is not slow enough to adiabatically follow the ground state at every quasimomentum to the lowest trapped band then some population of the the initial state will be excited to an upper band where it can undergo the damaging relaxation processes detailed above.

# Chapter 3

# The Harper-Hofstadter Hamiltonian

The ability to create vector potentials for neutral atoms akin to the interaction of an electron with an electromagnetic field is a crucial step towards creating quantum simulators of interacting gauge theories, creating new gauge theories not observable in the context of high energy physics, as well as experimentally investigating gauge structures that don't exist in nature. More immediately, the ability to have neutral atoms act as though they are charged particles in a static background field allows creation of states that are more analogous to the two-dimensional electron gas in a magnetic field. In certain regimes, the action of this *synthetic* magnetic field can create topologically nontrivial bandstructure and realizations of strongly interacting topological states of matter. A famous example of such a nontrivial state and a goal for quantum simulation is the hierarchy of fractional quantum Hall states observed in the two-dimensional electron gas [146, 152].

Despite such lofty goals, the ultracold atoms we have in the lab are neutral and any potential $\frac{e}{c}\mathbf{A}$ will automatically be zero! At first glance, it may appear that we are out of luck. However, if we further consider what a vector potential means for the electron wavefunction a work-around becomes immediately obvious. Specifically, consider how the vector potential and matter wavefunction are inexorably linked by local gauge symmetry. If we create a unitary transformation that produces a local

rotation of the phase of the matter wavefunction:

$$\psi \rightarrow \hat{U}\psi = e^{i\theta(\mathbf{x})}\psi, \tag{3.1}$$

then the Hamiltonian transforms as $\hat{U}H\hat{U}^{\dagger}$, with the canonical momentum transforming as:

$$\mathbf{\Pi} \rightarrow e^{i\theta(\mathbf{x})}\Big(\mathbf{p} - \frac{e}{c}\mathbf{A}\Big)e^{-i\theta(\mathbf{x})} = \Big(\mathbf{p} - \hbar\nabla\theta(\mathbf{x}) - \frac{e}{c}\mathbf{A})\Big). \tag{3.2}$$

If we associate the phase gradient with the vector potential, we can write an effective vector potential,

$$\mathbf{A}_{\text{eff}} = \mathbf{A} + \frac{\hbar c}{e}\nabla\theta(\mathbf{x}). \tag{3.3}$$

This effective vector potential has a provocative form since as $e \rightarrow 0$, the effective vector potential term in the Hamiltonian approaches a finite value: $\frac{e}{c}\mathbf{A}_{\text{eff}} \rightarrow \hbar\nabla\theta(\mathbf{x})$!

Physically, this vector potential emerges from the ability to create some spatially-textured phase pattern in the wavefunction. To accomplish this task, experiments generally take several different approaches. One approach is to physically rotate the system to imprint a phase associated with a centrifugal force [112, 1]. A second approach pioneered experimentally by the NIST group involves coherently coupling the levels of a two-level system with a laser beam that transfers momentum in a spatially-varying way [103]. A third, method involves time-modulating an optical lattice system in a circular way that produces time-reversal symmetry breaking and generates new tunneling matrix elements that contain spatially-varying phases [147, 79]. A final method, outlined here in this thesis, involves coherently coupling sites of a tilted optical lattice with an incommensurate running-wave lattice that imprints spatially-varying tunneling matrix elements [76, 88, 3].

For the experiments we will discuss, this imprinted vector potential behaves akin to a static magnetic field from an electromagnet like that imposed on a two-dimensional electron gas to enter the quantum Hall regime. However, in principle the laser configuration used to imprint such phases can be made to be dynamically generated by the atomic positions – for example by superradiant scattering into the mode of a

high-finesse cavity – in such a way to realize a dynamical gauge field which couples back to the atomic motion via the recoil momentum. This direction lies outside the scope of the research described here, but there have been many proposals towards this effect [76, 125, 174, 11].

## 3.1 Landau Levels meet the Lattice

In chapter 1, we discussed the physics of an electron in a magnetic field and how this system realizes a simple, solvable model of a topological, many-body system. In condensed matter systems, often we can ignore the underlying lattice structure of the material we are working with because the magnetic flux length far exceeds the lattice constant, $l \gg a$. In this case, the resulting physics is well-described by that of the continuum Landau levels.

The problem of a charged particle in a uniform magnetic field becomes more interesting when we try to formulate it in the presence of a lattice. In the tight binding limit of an isolated Bloch band the Hamiltonian can be written by making the Peierls substitution such that the tight-binding Hamiltonian becomes [72, 67, 8]:

$$H = -t \sum_{\langle m,n \rangle} \left( e^{-i\theta_{m,n}} \hat{a}^\dagger_{m+1,n} \hat{a}_{m,n} + \hat{a}^\dagger_{m,n+1} \hat{a}_{m,n} + \text{H.c.} \right) \tag{3.4}$$

where the action of the gauge field is to imprint a spatially-varying phase on each link of the lattice with a phase accumulation given by:

$$\theta_{m,n} = \frac{e}{\hbar c} \int_{x_m}^{x_{m+1}} d\mathbf{r} \cdot \mathbf{A}. \tag{3.5}$$

Here, for simplicity, we choose to work in the Landau gauge so that $\mathbf{A} = -By\hat{e}_x$.

A more intuitive understanding of the underlying physics can be gathered by considering the competing length scales of the lattice constant, $a$, and the magnetic flux length $l = \sqrt{\frac{eB}{\hbar c}}$. For the purpose of defining a unit cell and diagonalizing the Hamiltonian using Bloch's theorem, we begin by attempting to find translation

symmetry vectors of the Hamiltonian. In the Landau gauge, the canonical momentum operator in the $x$-direction commutes with the Hamiltonian, and can be used like the normal translation operator, now modified to reflect the presence of the lattice. In the $y$-direction, the momentum operator does not commute with the Hamiltonian, and instead must be modified by adding a term proportional to the vector potential [172]:

$$T_x = \sum_m \hat{a}^\dagger_{m+1,n} \hat{a}_{m,n} \tag{3.6}$$

$$T_y = \sum_n \hat{a}^\dagger_{m,n+1} e^{-ia^2 m/l^2} \hat{a}_{m,n}. \tag{3.7}$$

To find a valid translation symmetry in the problem, we are interested in how the wavefunction changes as a particle is translated along different paths to the same final point – a path equivalent to moving an atom or electron in a circle back to the same starting position. In this case, we know that the system contains two competing length scales, the lattice constant, $a$, and the magnetic flux length, $l$, so we look for a translation symmetry that is $q$-fold expanded along the direction of the broken translation symmetry. As in the continuum case, we look at moving to the same final point along two different paths by alternating application of the two translation operators [130]:

$$\big(T_y\big)^q T_x \psi = \bigg( \sum_{n'} \hat{a}^\dagger_{m,n'+1} e^{-ia^2 m/l^2} \hat{a}_{m,n'} \bigg)^q \sum_{m'} \hat{a}^\dagger_{m'+1,n} \hat{a}_{m',n} \psi \tag{3.8}$$

$$T_x \big(T_y\big)^q \psi = \sum_{m'} \hat{a}^\dagger_{m'+1,n} \hat{a}_{m',n} \bigg( \sum_{n'} \hat{a}^\dagger_{m,n'+1} e^{-ia^2 m/l^2} \hat{a}_{m,n'} \bigg)^q \psi. \tag{3.9}$$

With a little manipulation we find that the wavefunction of a particle translated by one lattice constant, $a$, along the $x$-direction and then one lattice constant along the $y$-direction differs from that of a particle translated first along $y$ and then the $x$-direction by a phase factor:

$$T_y T_x = e^{-i(a/l)^2} T_x T_y \tag{3.10}$$

so repeated use of this relation $q$-times yields a the phase accumulated along the two separate paths:

$$q\frac{a^2}{l^2} = q\frac{eBa^2}{\hbar c} = 2\pi q\frac{\Phi}{\Phi_0} \tag{3.11}$$

Finally, we see that for special values of the magnetic field and corresponding magnetic flux lengths, the phase factor equals an integer number of $2\pi$ and the system recovers translation symmetry.

$$2\pi q\frac{\Phi}{\Phi_0} = 2\pi\alpha, \quad \text{so: } \alpha = \frac{p}{q} \tag{3.12}$$

where $p$ is an integer, $p \in \mathbb{Z}$. When the flux per unit cell takes on rational values, $p, q \in \mathbb{Z}$, we find that we can always find a translation operator for which the magnetic unit cell and the underlying lattice unit cell are commensurate that is equal to a translation by $d_y = qa$. Note that the gauge we chose is a $y$-dependent potential in the $x$-direction, but the unit cell has dimensions of $a$ in the $x$-direction and $qa$ in the $y$-direction! Particularly, we see that the translation symmetry operators of the Hamiltonian depend on the gauge we are using, meaning the definition of the unit cell may also change depending on the gauge. However, the Dirac quantization condition given in equation 3.12 that fixes the flux per unit cell, is independent of gauge as one might expect, since the strength of the magnetic field is fixed independent of gauge choice.

Additionally, the translation symmetry operators allows us to quantify the degeneracy of the spectrum in the magnetic unit Brillouin zone. To do this, we assume the field takes the value of a commensurate flux, $\alpha = \frac{p}{q}$, so we can form a well-defined Brillouin zone and Bloch wavefunctions. Then if we consider the eigenvalue problem for the translation operators:

$$T_xT_y|q_x, q_y\rangle = e^{2\pi i\alpha}T_yT_x|q_x, q_y\rangle = e^{i(2\pi\alpha + k_ya)}T_y|q_x, q_y\rangle, \tag{3.13}$$

we see that the translation in the $y$-direction leads to a shift in the eigenvalue of the $x$-translation operator. Since both translation operators commute with the Hamilto-

nian, this must mean that:

$$T_y|q_x, q_y\rangle \propto |q_x + \frac{2\pi\alpha}{a}, q_y\rangle, \quad \text{where: } E(k_x, k_y) = E(k_x + 2\pi\alpha/a, k_y). \tag{3.14}$$

We therefore conclude that for a flux of $\alpha = \frac{p}{q}$ the spectrum is $q$-fold degenerate for all quasimomenta in the first Brillouin zone. Reassuringly, when we take the continuum limit where $\alpha \to \frac{1}{q}$, where $q \to a/l$ we recover precisely the translation symmetry of continuum Landau levels and the N-fold degeneracy as well.

Given the Hamiltonian and a commuting set of translation operators for some rational flux $\alpha = \frac{p}{q}$, we can solve the tight-binding Hamiltonian in the basis of states in the unit cell by taking the Fourier transform of the creation operator [130]:

$$\hat{a}_{\mathbf{x}_i} = \sum_{\mathbf{k}} e^{i\mathbf{k}\cdot\mathbf{x}_i} \hat{a}_{\mathbf{k}} \tag{3.15}$$

and substituting into the Hamiltonian. Note that the good momentum-space wave vectors now run over the magnetic Brillouin zone, $\{q_x, q_y\} \in \{\left(-\frac{\pi}{a}, \frac{\pi}{a}\right], \left(-\frac{\pi}{qa}, \frac{\pi}{qa}\right]\}$ and the momentum-space wavefunction contains $q$ components arising from the different phase factors of the $q$ sites within the magnetic unit cell.

As a concrete example, we consider the case of $\alpha = 1/3$, where the vector potential takes the form, $\theta_{m,n} = 2\pi n\alpha = 2\pi n/3$. The lattice now has an enlarged translation symmetry in the $y$-direction, $3\hat{a}_y$, and a Brillouin zone that is reduced in size from the $2\pi/a \times 2\pi/a$ of the underlying lattice to a size $2\pi/a \times 2\pi/3a$, where we have chosen the vector potential to be oriented in the $x$-direction. Fourier transforming the creation and annihilation operators gives a $3\times3$ Hamiltonian in the basis of states $\{n = 2; 1; 0\}$:

$$H = -t \begin{pmatrix} 2\cos(k_x a + 4\pi/3) & e^{ik_y a} & e^{-ik_y a} \\ e^{-ik_y a} & 2\cos(k_x a + 2\pi/3) & e^{ik_y a} \\ e^{ik_y a} & e^{-ik_y a} & 2\cos(k_x a) \end{pmatrix} \tag{3.16}$$

Given this Hamiltonian matrix, the spectrum is easily solved and the first Brillouin

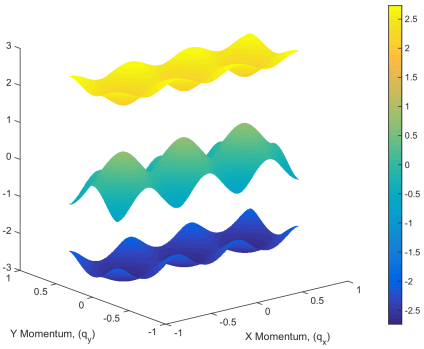


(a) Bands of the 1/3-flux Hamiltonian.

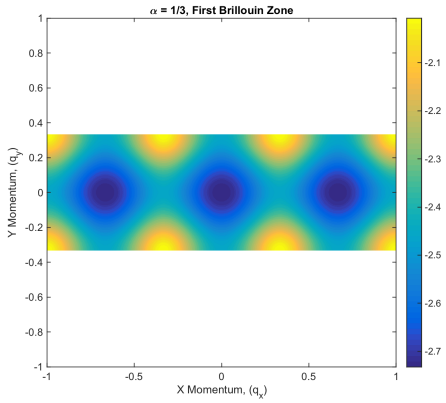


(b) Lowest band of the 1/3-flux Hamiltonian.

Figure 3-1: Bandstructure of the $\alpha = 1/3$ Hamiltonian. Using the Landau gauge oriented in the $x$-direction, $\mathbf{A} = -By\hat{e}_x$, the single particle spectrum displays three bands emerging from the lowest band of the cubic lattice (a). Note the modified shape of the Brillouin zone indicating an enlarged real space translation symmetry of $3 \times a$ in the $y$-direction in addition to the triple degeneracy of every point in the spectrum upon translation in quasimimentum, $k_x + 2\pi/3a$. The spectrum of the lowest band (b) shows the lowest band energies and the triple degeneracy of the ground state.

zone is shown in figure 3-1b. We immediately notice the reduced magnetic Brillouin zone compared to the lattice unit cell in addition to the fact that the spectrum now contains three bands, shown in figure 3-1a, thus preserving the number of states contained within the Brillouin zone when compared to the Brillouin zone of the underlying lattice. Finally, looking at the spectrum of a single band, for example the lowest band shown in figure 3-1b, each state is triply-degenerate with states separated by translations within the zone of $k_x + 2\pi/3a$. Remarkably, this includes the ground state of the lattice which is itself triply-degenerate. As predicted by the eigenvalues of the translation operator, we will find this ground state degeneracy a generic feature for all fluxes. In the continuum limit this smoothly connects to the $N$-fold degeneracy of a Landau level. We will discuss the implications of this ground state degeneracy in a later section when we add interactions to the system.

## 3.2 Hofstadter's Butterfly, Gaps, and Topology

For a given flux, we can analyze the unique translation symmetry of the Hamiltonian in order to obtain a unit cell and diagonalize the Hamiltonian to obtain its band structure. However, without information about the unit cell we can solve for the the energy spectrum as a function of the applied flux to the system. To obtain this spectrum as a function of the flux, we begin with the Hamiltonian in it's real space basis shown in equation 3.4. Following the original solution from Hofstadter [72, 67, 8], when we consider the wavefunction as a sum of local wavefunctions with weights, $\psi(m,n)$, on site $(x = ma, y = na)$,

$$|\psi\rangle = \sum_{m,n} \psi(m,n)|m,n\rangle, \tag{3.17}$$

the Hamiltonian in the Landau gauge oriented in the $x$-direction generates a recursion relation between the wavefunction weights on adjacent sites:

$$e^{2\pi i\alpha n}\psi(m+1,n)+e^{-2\pi i\alpha n}\psi(m-1,n)+\psi(m,n+1)+\psi(m,n-1) = -\frac{E}{t}\psi(m,n). \tag{3.18}$$

In free space, the wavefunction in the Landau gauge is factorizable into an plane wave component that commutes with the Hamiltonian and a harmonic oscillator component in the other direction. Taking inspiration from this wavefunction, we write an ansatz that separates the wavefunction weights into two parts:

$$\psi(m,n) = e^{ik_x x}g(y) = e^{ik_x am}g(n) \tag{3.19}$$

such that the recursion relation between sites becomes:

$$2\cos(2\pi\alpha n + k_x a)g(n) + g(n+1) + g(n-1) = -\frac{E}{t}g(n). \tag{3.20}$$

The recursion relation in equation 3.20 is known as Harper's equation. To get the spectrum of the Hamiltonian, rational values of the flux and transverse quasimomen-

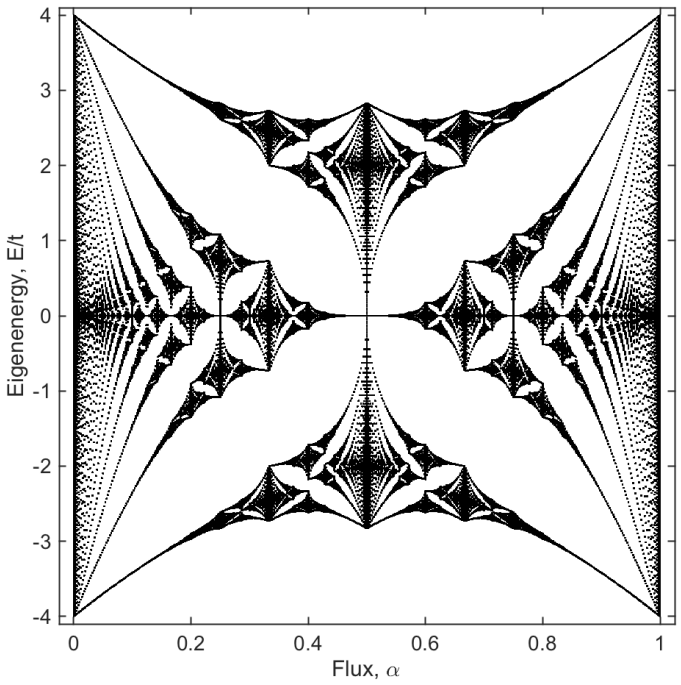


Figure 3-2: The spectrum of Hofstadter's butterfly. The horizontal axis encodes the magnetic field strength in terms of the magnetic flux quantum and lattice unit cell area, $\alpha = \frac{\Phi}{\Phi_0} = \frac{Ba^2}{hc/e}$, and the vertical axis corresponds to eigenenergies of the Harper equation. Spectra are plotted for all rational fluxes $\alpha = \frac{p}{100}$ with $p \in [0,\ 100]$.

tum, $k_x a \in (-\pi, \pi]$ can be specified and the resulting $N \times N$ tri-diagonal matrix for lattice of $N$ sites and periodic boundary conditions can easily be diagonalized. The result is the famous fractal picture of Hofstadter's butterfly, shown in figure 3-2. Equation 3.20 also arises in the context of quasi-periodic potentials applied to one-dimensional systems. In this context, the diagonal cosine term is a local, quasi-periodic potential applied to a one-dimensional system of tunnel junctions and gives rise to an identical spectrum for fixed $k_x a$.

Examining the spectrum of Hofstadter's butterfly, there are many interesting features to note. First of all, as we saw in the last section in the limit of small fluxes, when $\alpha \to \frac{1}{q}$ and $q \to \frac{a}{l}$, we should recover the behavior of Landau levels. Looking at the spacing of the lowest eigenvalues for small fluxes away from zero in the lower righthand corner of figure 3-2, we see that the levels are equally spaced and that the spacing increases linearly with the strength of the flux, consistent with the behavior

of Landau levels. The next thing to notice about this spectrum is the limits of fluxes $\alpha \in [0, 1]$. The single-particle wavefunction is periodic in the amount of flux applied to the system because a phase accumulated upon tunneling around one plaquette of the lattice of $2\pi$ is completely indistinguishable from any integer multiple, $2\pi n$, where: $n \in \mathbb{Z}$. Therefore, the band structure at both zero flux and $\alpha = 1$ flux are identical and correspond to the band structure of a cubic lattice with bandwidth $4t$. Additionally, the behavior of the energy levels for small deviations from $\alpha = 1$ are identical to the behavior of Landau levels for small fluxes near $\alpha = 0$.

Another symmetry we notice in the spectrum is a particle-hole symmetry around zero energy. This becomes very important when we consider even denominator fluxes. All fluxes with even denominators have Dirac points at zero energy. This can be clearly seen as the absence of a band gap at zero energy for the even denominator fluxes in figure, 3-2. The massless nature of the spectrum at zero energy means that, as the flux moves away from commensurability, the system exhibits a half-integer quantum Hall effect similar to that observed in graphene [123, 173]. The zero energy mode emerging from the Dirac point is clearly visible as a straight line of states at zero energy that connect to every even denominator state at the Dirac point. Figure 3-3 shows a zoomed-in section of Hofstadter's butterfly close the the $\alpha = 1/2$ limit where this effect is clearly apparent. Clearly visible as well for small deviations away from the commensurate flux of $\alpha = 1/2$ is the scaling of the Landau level energies for massless particles at zero energy with $E_n \propto \sqrt{nB'}$, where $n$ is the Landau level index and $B'$ denotes the deviation of the magnetic field from a commensurate value. This is in contrast to the linear energy relation for Landau levels emerging from a massive band where $E_n \propto nB'$. This linear scaling is visible for the gap opening from the bottom of the band at $\alpha = 1/2$ in figure 3-3. As discussed in Chapter 1 for Landau levels in the continuum limit, the gap that opens from a massive band would normally carry a Chern number and corresponding Hall conductance of $n = 1$. However, the gap that opens at the bottom of the $\alpha = 1/2$ band in figure 3-3 has a Chern number of $n = 2$! We can develop an intuitive understanding of this by considering that the 1/2-flux model has two sites per magnetic unit cell and the spectrum has a corresponding two-

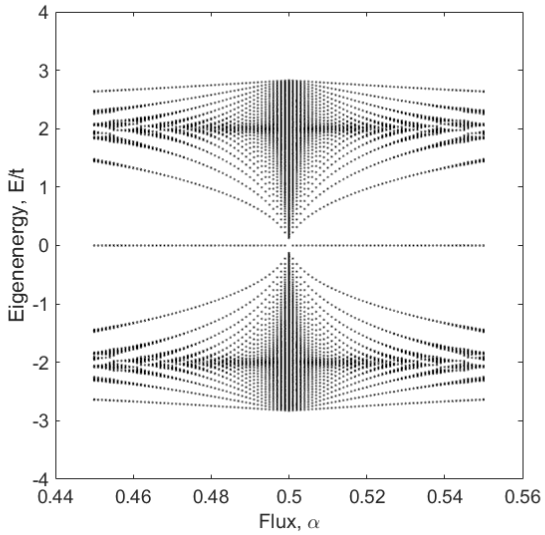


Figure 3-3: Spectrum for small deviations from $\alpha = 1/2$. Small deviations of the field from commensurability act like a magnetic field applied to particles occupying the spectrum determined by a commensurate flux. For $\alpha = 1/2$, note the half-integer Landau levels of massless Dirac particles for small field departures from $1/2$ commensurability, including the zero-energy mode – first observed in the quantum Hall effect in graphene – that does not open up a gap as a function of magnetic field and instead stays pinned to zero energy [123, 173]. Also note the effective Landau levels for massive particles opening at the bottom and top of the $1/2$-flux band.

fold degeneracy. If we consider small flux deviations from a commensurate value with a quasi-continuum model, then each degenerate state in the Brillouin zone contributes one state to the resulting Hall conductance, resulting in a Chern number of $n = 2$. The same logic applies to the half-integer Hall effect at the zero-energy states. The lowest gap has a Chern number of one, but increasing the Fermi energy to cross the first Landau level increases the Chern number to $n = 3$.

A more systematic study of the topological features of the spectrum comes when we calculate the topological index associated with each filled band. This task can be accomplished in general by looking at solutions of the Diophantine equation [58, 136]. Alternately, upon solving the band structure for a specific flux, the eigenvectors of the Hamiltonian can be used to calculate Berry's curvature at each point in the first magnetic Brillouin zone. Then for a band that is completely filled, either thermally or by setting the Fermi energy inside a band gap, the populated states can be summed over, giving rise to the Chern number of the populated bands. The Chern numbers of each gap in the spectrum have been calculated [58], and above we highlight just a few particularly relevant ones for understanding the general structure.

## 3.3 Realization of Strong, Uniform Fluxes in an Optical Lattice

Before this work began, generation of artificial magnetic fields had been demonstrated in a series of pioneering experiments demonstrating different physical mechanisms by which effective magnetic fields could be generated. The first platform used to demonstrate effective magnetic fields is that of a rotating superfluid. This was used to generate large vortex arrays in both bosonic and fermionic superfluids. Unfortunately, for many experiments, these fluxes were limited to the regime of low flux number to particle number. Generating higher flux to particle ratios and loading the system into an optical lattice has proven to be a more challenging task.

Pioneering work by the NIST group showed that effective fluxes can also emerge

by Raman coupling different hyperfine states with the momentum transfer of a laser recoil to an atom. Applying a magnetic field gradient to the sample engineers a spatial dependence of the dressed state mixing angle, giving rise to an effective vector potential. Unfortunately, this method is also limited to low flux to particle number ratio and suffers from intrinsic heating processes of spontaneous emission due to the need for spin-changing Raman transitions.

Effective magnetic fields in an optical lattice generated with far-detuned light was first demonstrated in pioneering work by the Hamburg group that used off-resonant driving of the optical lattice to implement Floquet engineering of staggered fluxes into an optical lattice. This scheme succeeded in producing synthetic fluxes with far-detuned light, but only produces staggered magnetic fluxes that lack easily implementable generalization to produce topological band structures analogous to electrons in a magnetic field. In addition, the scheme only produces fluxes in the strong-driving limit and an adiabatic pathway to prepare the many-body ground state is not obvious in addition to the inability to prepare the system in a three-dimensional lattice in which strong interactions can be implemented.

Staggered magnetic fields were also demonstrated by the Munich group in a lattice of asymmetric double wells. In contrast to the off-resonant Floquet engineering implemented by the Hamburg group, this system features a resonant drive that coherently couples states localized on the upper and lower states of an asymmetric double well in addition to a momentum transfer that provides a tunneling matrix element and imprints an additional phase. Although the synthetic fields generated in this work were only staggered fields not yielding a topologically nontrivial system, this work provides crucial insights on how to generalize this scheme to create uniform fluxes in an optical lattice and provides a clear path forward to generating topological states of matter.

Two important points we learn from this work include how to generate laser-assisted tunneling – a technique pioneered by the Arimondo group [144] – with a spatially-varying phase which is imprinted directly onto the ground state wavefunction as well as how to generalize the staggered flux configuration to uniform fluxes with

arbitrary strength.

Previous theoretical work suggested the ability of a strongly accelerated system to realize uniform flux systems; however, these proposals are implemented in the Landau gauge which features a laser configuration with an inhomogeneous driving field which produces a very small tunneling matrix element. The Landau gauge produces a vector potential oriented in the $x$-direction which features a phase shift dependent on the $y$-position. Intuitively, the simplest implementation of this potential term is to have an acceleration or potential offset between sites in $x$ and then a two-photon resonant driving laser which produces a transition between energetically-offset nearest neighbors and simultaneously imparts a momentum transfer in the transverse, $y$ direction. Unfortunately, by definition, the Wannier states localized on the two different lattice sites we wish to drive transitions between are orthogonal:

$$K_{\text{Landau}} \propto \int dxdy\, w(x - x_i, y - y_i) V_{\text{drive}}(y) w(x - x_{i+1}, y - y_i) = 0 \tag{3.21}$$

where we have denoted the laser-assisted tunneling rate between adjacent wells of the lattice by the energy, $K_{\text{Landau}}$.

A key insight of the Munich work is that if the laser drive term contains both an $x$- and $y$-component of the momentum transfer the drive field can both provide a tunneling matrix element in addition to imprinting a phase for generating an effective magnetic flux. This can be seen in a straightforward way in the perturbative limit in the frame rotating with the energy difference between adjacent sites:

$$\begin{aligned}
K_{\text{pert}} &\propto \int dxdy\, w(x - x_i, y - y_i) e^{i(k_x x + k_y y)} w(x - x_{i+1}, y - y_i) && (3.22)\\
&= \int dxdy\, w(x, y) e^{i(k_x(x - x_i) + k_y(y - y_i))} w(x - a_x, y) && (3.23)\\
&= e^{-i(k_y y_i + k_x x_i)} \int dx\, w(x) e^{ik_x x} w(x - a) \int dy\, w(y) e^{ik_y y} w(y) && (3.24)\\
&\approx e^{-i(k_y y_i + k_x x_i)} |K_{\text{pert}}| \propto e^{-ik_y y_i} |K_{\text{pert}}| && (3.25)
\end{aligned}$$

where the momentum transfer in the $x$-direction, $k_x$, provides a non-zero tunneling matrix element, and the momentum transfer in the $y$-direction, $k_y$, provides a

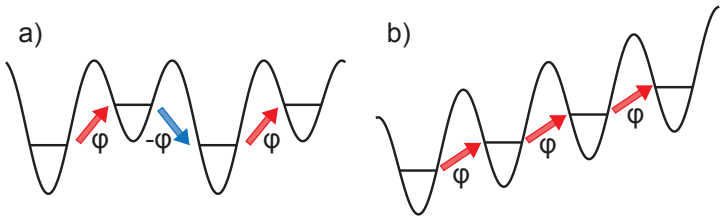


Figure 3-4: Schematic of the flux rectification scheme. In a double well potential, the same momentum-transfer from the Raman drive imparts staggered phases due to the sign of the site-to-site energy offset changing on each link (left). By comparison, in a uniformly tilted lattice as a particle tunnels in one direction, each link has the same energy offset, allowing a single Raman drive to imprint a uniform phase. In this manner, an arbitrarily strong, staggered flux can be rectified to produce a uniform flux.

spatially-varying phase which imprints flux.

A second key insight of the Munich work is in explaining why this experimental geometry leads to a staggered instead of uniform magnetic flux. Using the perturbative picture used to understand the tunneling matrix elements, we consider the phases imprinted on adjacent links of the lattice composed of offset double wells. To derive the picture above we considered a potential $\propto \cos(\mathbf{k}\cdot\mathbf{r} - \Delta t)$ and transformed into the frame rotating with the energy offset between adjacent sites. However, in a double well potential, as a particle tunnels in one direction each adjacent link is offset in energy with alternating sign as portrayed in figure 3-4. Considering the phase of the tunneling matrix element we derived in the perturbative limit, the alternating energy offset between adjacent links means that the rotating frame used on each link is different, and thus the sign of the momentum transfer alternates between links of the lattice:

$$\Delta E = \pm\Delta, \rightarrow K_{\text{pert}} \propto e^{\pm i\theta_j}. \tag{3.26}$$

Understanding this feature of the double well potential immediately points to a way to generalize the results of the Munich experiments to generate uniform fluxes.

In short, the key to generating a uniform flux is to engineer a potential such that either the sign of the energy offset between sites does not change, and thus one driving laser imprints uniform phases in the lattice or the sign of the momentum transfer is

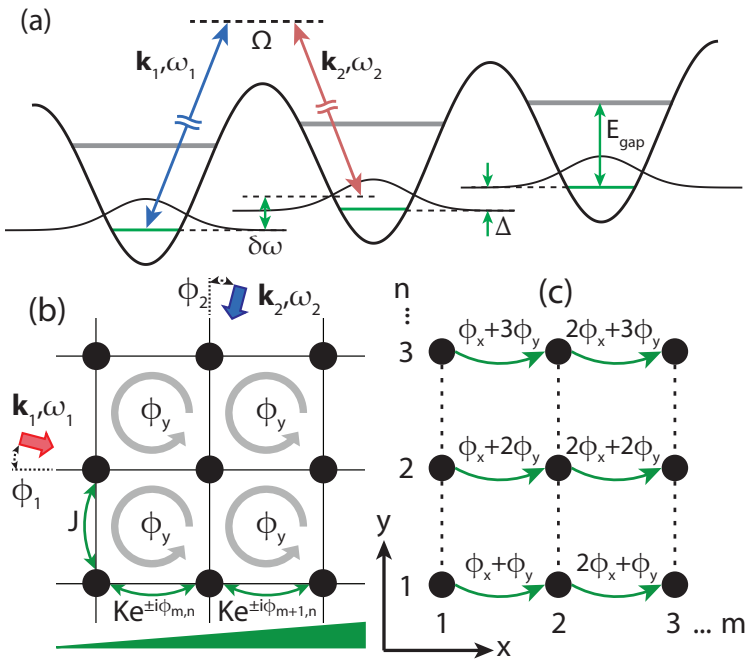


Figure 3-5: Flux rectification in a two-dimensional lattice. (a) Raman-assisted tunneling between localized states in the lowest band of a uniformly tilted lattice with an energy offset $\Delta$ between neighboring sites and two-photon Rabi frequency $\Omega$. (b) Tunneling along the $x$-direction, given by $K$, imprints a spatially varying complex phase $\phi_{m,n}$ into the system due to the momentum transfer in the $y$-direction. (c) The resulting position-dependent phases imprinted in the lattice. Translation around one plaquette of the lattice yields a flux per unit cell of $-\phi_y$.

changed appropriately between different links of the lattice. In the work described here we choose the first method described in figure 3-5(b), where, instead of a double well potential, a uniform gradient is applied to the cloud such that each site is offset by the same energy with the same sign as one moves along a lattice direction. A schematic experimental setup is shown in figure 3-5(a) and (b). As depicted in part (a) of the figure, the uniform gradient offsets nearest neighbor sites in the lattice by an energy, $\Delta$. In the strongly tilted regime, that is when $\Delta$ is much larger than the bandwidth, $4t$, the atoms are strongly localized by the gradient and the spectrum and wavefunctions are described by the Wannier-Stark ladder. For a complete derivation of the spectrum and representation of the wavefunction in the Wannier-Stark ladder, see Appendix A. We wish to work with initially localized wavefunctions and imprint tunneling only through our two-photon drive, so we are limited in the strength of

the tilt we can apply such that the atoms in one site do not couple to the second band of adjacent sites. To satisfy this criteria, we require $\Delta \ll E_{\text{gap}}$, such that our experimental window is bounded by the energy hierarchy: $4t \ll \Delta \ll E_{\text{gap}}$.

After we apply a uniform gradient to the lattice, the atoms are localized to each site. We can restore tunneling by weakly driving the system with a two-photon Raman drive with a tunable detuning. When the detuning between the two legs of the two-photon Raman drive is equal to $\Delta$, particles initially localized on a site can use the energy from the Raman drive in order to delocalize via adjacent lattice sites. From equation 3.25 we understand that each time an atom undergoes a two-photon transition and moves to another lattice site the Raman drive also imprints a phase given by the momentum transfer of the two-photon process.

One nontrivial consequence of needing momentum-transfer in the $x$-direction for tunneling is that the vector potential we realize is not purely that of a Landau gauge. Instead, we realize a vector potential oriented in $x$ that depends on both the $x$- and $y$-coordinate, $\mathbf{A} = \frac{\hbar}{a}(k_x x + k_y y)\hat{e}_x$, where $k_x$ is the momentum transfer of the Raman lasers in the (tilted) $x$-direction of the lattice, and $k_y$ is the momentum transfer in the $y$-direction. For understanding the spectrum, this vector potential can be converted into the Landau gauge by a simple gauge transformation that adds a scalar potential, $\lambda = -\hbar k_x x^2/2a$. Since the energy eigenvalues are gauge invariant, the spectrum is invariant under any gauge transformation. However, the form of the vector potential has important consequences for understanding the wavefunction – a quantity that is NOT gauge invariant. Specifically, the form of the vector potential is visible in a time-of-flight measurement, it impacts the translation symmetry of the magnetic unit cell, and affects how the interacting ground state is decomposed into non-interacting ground state wavefunctions. This will be discussed in detail later in section 3.7.

A common question arises looking at the spatially-varying phase in front of the laser-assisted tunneling term: how do I understand this type of phase leading to a synthetic magnetic flux imprinted on each plaquette of a square lattice? For this it is instructive to consider the vector potential on each link of the lattice as depicted in figure 3-5 and consider a circular path that encloses one plaquette of the lattice, for

example the path starting at site $(m, n) = (1, 1)$ and following the path:

$$(1, 1) \rightarrow (2, 1) \rightarrow (2, 2) \rightarrow (1, 2) \rightarrow (1, 1). \tag{3.27}$$

Adding up the phases, the total phase shift accumulated after enclosing one plaquette of the lattice is, $2\pi\alpha = \phi_{1,1} + 0 - \phi_{2,1} - 0 = k_y a$. This circular path argument can be repeated for any plaquette in the lattice and results in the same phase, $2\pi\alpha$, corresponding to a uniform magnetic field applied to the sample.

This technique for generating uniform magnetic fields has many beneficial features that enable the study of many-body physics with such a platform. First, this technique uses only far-detuned lasers so the intrinsic heating rate set by the spontaneous emission lifetime can be longer than the vacuum lifetime of the sample by detuning from the atomic resonance. Second, this technique is not unique to any one atomic species, but can be employed for any atom that can be cooled to sufficient temperatures. This is especially attractive for fermionic alkali gases since neither $^6$Li nor $^{40}$K have large fine-structure splittings large enough for spin-flipping Raman laser schemes to have long lifetimes. A third benefit of this scheme is the ability to continuously tune the effective magnetic flux by changing the Raman laser wavelength or the angle of the laser beams with respect to the lattice axes. As we can see from the spectrum of Hofstadter's butterfly, shown in figure 3-2, changing fluxes allows one to realize dramatically different band structures, ranging from the gapped and gapless commensurate lattices to the effective Landau level picture of incommensurate fluxes. Finally, as we will discuss in detail in Chapter 4, this scheme immediately points to interesting generalizations that can be made by adding new elements such as new dimensions and spin degrees of freedom.

### 3.3.1 Derivation of the Effective Hamiltonian

To make this picture more concrete, we use the Floquet formalism outlined in Chapter 2 to derive an exact expression for the form of our Hamiltonian as well as the kick operators associated with the transformation from the lab frame to the rotating

frame, and back. The derivation begins with the microscopic Hamiltonian for a two-dimensional lattice uniformly accelerated in the $x$-direction and subject to a traveling wave potential created by a pair of far-detuned Raman laser, as outlined in figure 3-5:

$$H = \frac{\mathbf{p}^2}{2m} + V_{\text{latt}}(\mathbf{r}) - \frac{\Delta}{a}\mathbf{x} + \Omega \sin\Big(\delta\mathbf{k}\cdot\mathbf{r} - \frac{k_x a}{2} - \omega\tau\Big). \tag{3.28}$$

The phase term, $-k_x a/2$, is included for later computational convenience, and does not change the physics of the problem as any arbitrary phase can be added to the potential without changing the time-averaged Hamiltonian. In addition, $\tau$ is used as the variable of time to avoid confusion with the tunneling energy, commonly denoted by the letter, $t$. Ignoring interactions, the Wannier-Stark Hamiltonian is projected onto the lowest band of a cubic lattice using a basis of localized Wannier-Stark functions in the $x$-direction and Wannier functions in the $y$-direction:

$$H = \sum_{m,n}\Big( - m\Delta|m,n\rangle\langle m,n| - t_y|m,n+1\rangle\langle m,n| + \text{H.c.}\ldots. \tag{3.29}$$

$$\ldots + \sum_{m',n'} \Omega|m',n'\rangle\langle m',n'| \sin\Big(\delta\mathbf{k}\cdot\mathbf{r} - \frac{k_x a}{2} - \omega\tau\Big)|m,n\rangle\langle m,n|\Big) \tag{3.30}$$

There are two matrix elements of interest here: the diagonal term as well as overlap of adjacent sites in the $x$ and $y$ directions. In general these have the form:

$$\langle m,n| \sin\Big(\delta\mathbf{k}\cdot\mathbf{r} - \frac{k_x a}{2} - \omega\tau\Big)|m+l,n+p\rangle \tag{3.31}$$

The phase shift of the Raman drive, $k_x a/2$, is associated with a spatial shift for the tunneling matrix elements and a temporal shift for the onsite matrix elements making their self-consistent evaluation based on symmetry arguments easier. Using $\mathbf{R}_{m,n} = ma\hat{x} + na\hat{y}$ for the position of the lattice sites, the relevant matrix elements can be re-written as:

$$\langle 0,0| \sin\big(\delta\mathbf{k}\cdot(\mathbf{r} + \mathbf{R}_{m,n}) - k_x a/2 - \omega\tau\big)|l,p\rangle \tag{3.32}$$

To condense notation, we define: $\theta_{m,n} = \omega\tau - \delta\mathbf{k}\cdot\mathbf{R}_{m,n} = \omega t - \phi_{m,n}$, with $\phi_{m,n} = mk_x a + nk_y a$. Expanding the $\sin(a+b-c)$ form of the Raman operator into four terms one obtains the relevant matrix elements:

$$\begin{aligned}
\langle 0|\sin(k_y y)|p=0\rangle &= 0 && (3.33)\\
\langle 0|\cos(k_y y)|p=0\rangle &= \Phi_{y0}(k_y) && (3.34)\\
\langle 0|\sin(k_x x)|l=0\rangle &= 0 && (3.35)\\
\langle 0|\cos(k_x x)|l=0\rangle &= \Phi_{x0}(k_x) && (3.36)\\
\langle 0|\sin(k_x(x-a/2))|l=1\rangle &= \Phi_{x1}(k_x) && (3.37)\\
\langle 0|\cos(k_x(x-a/2))|l=1\rangle &= \Phi'_{x1}(k_x) && (3.38)
\end{aligned}$$

The expressions above are evaluated using maximally localized Wannier functions in the $y$-direction and Wannier-Stark wavefunctions in the $x$-direction. Due to the symmetric nature of the localized Wannier function, all matrix elements of an anti-symmetric function are zero. The Wannier-Stark wavefunctions do not have definite parity so the overlap elements must be individually evaluated. In the tight-binding limit, the tunneling term is dominated by $\Phi_{x1} \approx -2J_x \sin(k_x a/2)/\Delta$. However, at lower lattice depths $\Phi'_{x1}$ can become significant so we keep both terms. Collecting terms for the coupling between adjacent sites in the tilted, $x$-direction, the prefactor becomes:

$$\Omega\Phi_{y0}\big(\Phi_{x1}\cos\theta_{m,n} - \Phi'_{x1}\sin\theta_{m,n}\big) \tag{3.39}$$

and in addition, the Raman-coupling induces an on-site modulation given by:

$$-\Omega\Phi_{x0}\Phi_{y0}\sin(\theta_{m,n} + k_x a/2). \tag{3.40}$$

Given the above form for the on- and off-diagonal terms, we arrive at a time-dependent,

single band Hamiltonian,

$$\begin{aligned} H &= \sum_{m,n}\Big[\big(-m\Delta-\Omega\Phi_{x0}\Phi_{y0}\sin(\theta_{m,n}+k_xa/2)\big)|m,n\rangle\langle m,n|\ldots \\ &\quad \ldots+\Omega\Phi_{y0}\big(\Phi_{x1}\cos\theta_{m,n}-\Phi'_{x1}\sin\theta_{m,n}\big)|m+1,n\rangle\langle m,n|\ldots \\ &\quad \ldots-t_y|m,n+1\rangle\langle m,n|+h.c.\big)\Big], \end{aligned} \tag{3.41}$$

and, as in the case of the resonantly phase modulated lattice, we can define a corresponding kick operator such as to eliminate the time dependence of the diagonal terms,

$$\begin{aligned} \hat{R} &= \exp\Big[i\sum_{m,n}\left(m\omega\tau-\frac{\Omega\Phi_{x0}\Phi_{y0}}{\hbar\omega}\cos\left(\theta_{m,n}+\frac{k_xa}{2}\right)\right)|m,n\rangle\langle m,n|\Big] \\ &= \sum_{m,n}e^{i\Lambda_{m,n}}|m,n\rangle\langle m,n| \end{aligned} \tag{3.42}$$

where $\Lambda_{m,n}=m\omega\tau-\frac{\Omega\Phi_{x0}\Phi_{y0}}{\hbar\omega}\cos(\theta_{m,n}+k_xa/2)$. To simplify the notation moving forward, we will define a modified Rabi frequency, $\Omega'=\Omega\Phi_{y0}$, and a normalized driving strength, $\zeta_{x(y)}=2\frac{\Omega'\Phi_{x0}}{\hbar\omega}\sin(k_{x(y)}a/2)$.

We can now transform to the frame rotating with $\hat{R}$, where we arrive at a transformed Hamiltonian $\overline{H}=\hat{R}^\dagger H\hat{R}-i\hbar\hat{R}^\dagger\partial_\tau\hat{R}$. For the case of resonant drive where $\hbar\omega=\Delta$, the diagonal terms are zero, leaving only off-diagonal elements for tunneling in the $x$-and $y$-directions. Considering tunneling in the $x$-direction first, the exponential factor multiplying the tunneling term is:

$$e^{-i(\Lambda_{m+1,n}-\Lambda_{m,n})} = \exp\Big[-i\Big(\omega\tau-\frac{\Omega'\Phi_{x0}}{\hbar\omega}(\cos\theta_{m+1,n}-\cos\theta_{m,n})\Big)\Big] \tag{3.43}$$

$$= \exp\Big[-i\Big(\omega\tau-\zeta_x\sin(\omega\tau-\phi_{m,n})\Big)\Big] \tag{3.44}$$

For tunneling in the $y$ direction, the transformation into the rotating frame multiplies

the tunneling rate by the exponential factor:

$$e^{-i(\Lambda_{m,n+1}-\Lambda_{m,n})} = \exp\Big[i\frac{\Omega'\Phi_{x0}}{\hbar\omega}(\cos\theta_{m,n+1}-\cos\theta_{m,n})\Big] \quad (3.45)$$

$$= \exp\Big[i\zeta_y \sin\Big(\omega\tau+\frac{(k_x-k_y)a}{2}-\phi_{m,n}\Big)\Big]. \quad (3.46)$$

Collecting all the terms, we find that when the system is resonantly driven we have a transformed Hamiltonian with the form:

$$\overline{H} = \Big(\sum_{m,n} K_{m,n}(\tau)|m+1,n\rangle\langle m,n| + t(\tau)|m,n+1\rangle\langle m,n| + \text{H.c.}\Big) \quad (3.47)$$

$$K_{m,n}(\tau) = \Omega'\big(\Phi_{x1}\cos(\omega\tau-\phi_{m,n}) - \Phi'_{x1}\sin(\omega\tau-\phi_{m,n})\big)e^{-i(\omega\tau-\zeta_x\sin(\omega\tau-\phi_{m,n}))}$$

$$t(\tau) = -t_y e^{i\zeta_x\sin(\omega\tau+\frac{(k_x-k_y)a}{2}-\phi_{m,n})}$$

We are interested in the time-evolution of the system over one cycle such that we can define an effective, time-independent Hamiltonian that gives an equivalent time-evolution, $U(\tau_f = T, \tau_i = 0) = \exp(\frac{-i}{\hbar}\int_0^T d\tau\overline{H}(\tau)) = \exp(-iH_{\text{eff}}T/\hbar)$, such that:

$$H_{\text{eff}} = \frac{1}{T}\int_0^T d\tau\overline{H}(\tau) \quad (3.48)$$

The resulting integrals of the time-dependent tunneling amplitudes over the modulation period can be explicitly evaluated with the help of the following Bessel function integrals:

$$\frac{1}{2\pi}\int_0^{2\pi} d\alpha\, e^{i\gamma\sin\alpha} = J_0(\gamma) \quad (3.49)$$

$$\frac{1}{2\pi}\int_0^{2\pi} d\alpha\, \cos(\alpha)e^{-i(\alpha-\gamma\sin\alpha)} = \frac{J_1(|\gamma|)}{|\gamma|} \quad (3.50)$$

$$\frac{1}{2\pi}\int_0^{2\pi} d\alpha\, \sin(\alpha)e^{-i(\alpha-\gamma\sin\alpha)} = -i\Big(\frac{J_1(\gamma)}{\gamma}-J_2(\gamma)\Big) = -i\frac{dJ_1(\gamma)}{d\gamma} \quad (3.51)$$

$$\frac{1}{2}(J_0(\gamma)+J_2(\gamma)) = \frac{J_1(\gamma)}{\gamma} \quad (3.52)$$

$$\frac{1}{2}(J_0(\gamma)-J_2(\gamma)) = \frac{dJ_1(\gamma)}{d\gamma} \quad (3.53)$$

explicitly:

$$
\begin{aligned}
K_{m,n} &= \frac{\Omega'}{T}\int_0^T d\tau\big(\Phi_{x1}\cos\theta_{m,n} - \Phi'_{x1}\sin\theta_{m,n}\big)e^{-i(\omega\tau-\zeta_x\sin(\omega\tau-\phi_{m,n}))} && (3.54)\\
&= \frac{\Omega'}{2\pi}\int_0^{2\pi} d\alpha\big(\Phi_{x1}\cos\alpha - \Phi'_{x1}\sin\alpha\big)e^{-i(\alpha+\phi_{mn}-\zeta_x\sin\alpha)} && (3.55)\\
&= \Omega' e^{-i\phi_{m,n}}\left(\Phi_{x1}\frac{J_1(\zeta_x)}{\zeta_x} + i\Phi'_{x1}\frac{dJ_1(\zeta_x)}{d\zeta_x}\right) && (3.56)\\
&= Ke^{-i\phi_{m,n}} && (3.57)\\
t &= \frac{-t_y}{T}\int_0^T d\tau e^{i\zeta_y\sin(\omega\tau-\phi_{m,n})} && (3.58)\\
&= \frac{-t_y}{2\pi}\int_0^{2\pi} d\alpha e^{i\zeta_y\sin\alpha} && (3.59)\\
&= -t_y J_0(\zeta_y) && (3.60)
\end{aligned}
$$

the resulting effective Hamiltonian is exactly that of charged particles on a lattice in a magnetic field and when expressed in second quantized notation becomes:

$$
H_{\text{eff}} = \sum_{\langle m,n\rangle}\left(Ke^{-i\phi_{m,n}}\hat{a}^\dagger_{m+1,n}\hat{a}_{m,n} + t\hat{a}^\dagger_{m,n+1}\hat{a}_{m,n} + \text{H.c.}\right) \tag{3.61}
$$

which is known as the Harper-Hofstadter Hamiltonian. The spatially-varying phase, $\phi_{m,n}$, arises from the momentum transfer of the two-photon Raman drive projected onto the lattice axes, $\phi_{m,n} = \delta\mathbf{k}\cdot\mathbf{R}_{m,n} = mk_xa + nk_ya$. In a continuum description, this corresponds to a vector potential of the form: $\mathbf{A} = \frac{\hbar}{a}(k_xx + k_yy)\hat{e}_x$.

For sanity checks, we can approximate the matrix elements within the tight-binding model, such that $\Phi_{x1} \approx -2t_x\sin(k_xa/2)/\Delta \gg \Phi'_{x1}$ and $\Phi_{y0} = \Phi_{x0} \approx 1$, where $t_x$ is the tunneling matrix element in the $x$-direction without any tilt applied. As a result, in this tight-bonding limit the expression for the tunneling amplitude in the $x$ direction becomes:

$$
K \approx -t_xJ_1\left(\frac{2\Omega}{\Delta}\sin\left(\frac{k_xa}{2}\right)\right) = -t_xJ_1\left(\frac{2\Omega}{\Delta}\right) \tag{3.62}
$$

where the last equality is for the specific case where $k_xa = k_ya = \pi$, as will be shown for our experiment. Furthermore, in the limit of low Raman lattice depths, $\zeta_x \ll 1$,

where $J_0(\zeta_x) \approx 1 \gg J_2(\zeta_x)$, Eq. 3.58 reduces to the perturbative expression for laser-assisted tunneling given in the beginning of this section:

$$K_{\text{eff}} \approx \frac{\Omega}{2} e^{-i\phi_{m,n}} \left( \Phi_{x1} + i\Phi'_{x1} \right) \approx \frac{\Omega}{2} e^{-i\phi_{m,n}} \langle 0,0 | e^{-i\delta \mathbf{k}\cdot\mathbf{r}} | 1,0 \rangle \tag{3.63}$$

### 3.3.2 Realization of the $\alpha = 1/2$ Harper-Hofstadter Hamiltonian

Now that we understand how to create uniform fluxes from an intuitive and mathematical perspective, I now outline the physical implementation of the Hamiltonian corresponding to one particular flux of the Harper-Hofstadter model. As discussed above, the flux we realize is set by the momentum transfer in the direction transverse to the tilt; in this case, the tilt will be defined to be in the $x$-direction and therefore the flux is set by $k_y a_y$. In addition, we must also maintain a momentum transfer in the $x$-direction in order to have a tunneling matrix element. For a first implementation, we wish to realize a commensurate flux, placing an additional constraint on the system.

Practically, the fluxes we can possibly implement are further limited by the optical access provided by the vacuum chamber windows in addition to the availability of different laser sources. We choose one axis of our lattice, the $x$-direction, to be aligned to gravity because we want to use the acceleration due to gravity as a uniform gradient. Therefore, we have the $y$ and $z$-lattice axes in the horizontal plane. Given that in the $x-y$ plane there are only vacuum viewports at 90 degree angles, each leg of the Raman lasers are thus constrained to propagate close to (within $\pm 10$ degrees) the lattice axis. Given the three main colors available in the lab – near-resonant at 780 nm, far-detuned at 1064 nm and doubled IR light at 532 nm – the simplest flux to realize is that at $2\pi\alpha = k_y a = (2\pi/1064) \times (1064/2) = \pi$, or $\alpha = 1/2$. The Raman lasers thus propagate coaxially with the lattice lasers and has the added benefit of a straightforward beam alignment. This flux has the added benefit that the momentum transfer of $k_x a = \pi$ in the $x$-direction also means that the tunneling

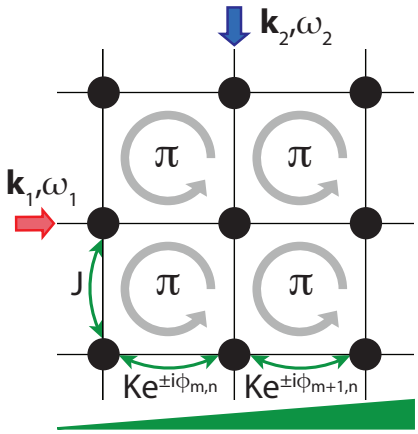


Figure 3-6: Schematic of the experimental setup. To realize the $\alpha = 1/2$ state, each of the Raman drive lasers are aligned to propagate co-linearly with the $x$- and $y$-lattices. Choosing the same laser wavelength, $\lambda = 1064$ nm, for the optical lattice and the Raman drive realizes the momentum transfer and subsequent gauge: $\phi_{m,n} = \delta\mathbf{k} \cdot \mathbf{a} = \left(\frac{2\pi}{\lambda}\hat{e}_x + \frac{2\pi}{\lambda}\hat{e}_y\right) \cdot \left(\frac{\lambda}{2}\hat{e}_x + \frac{\lambda}{2}\hat{e}_y\right) = \pi(m+n)$.

matrix element provided by the Raman lasers is maximized, and thus we need a minimal amount of modulation to achieve certain tunneling rates compared to other choices of $x$-momentum transfer.

The physical setup is depicted in figure 3-6. This gradient and laser arrangement produces the spatially-varying phase pattern, $\phi_{m,n} = \pi(m+n)$ corresponding to the experimental gauge, $\mathbf{A} = \pi\hbar(x+y)/a^2\hat{e}_x$. Practically, the mapping of the Raman-driven tilted lattice to the Harper-Hofstadter model requires the energy hierarchy $4J \ll \Delta \ll E_{\text{gap}}$. The second inequality emphasizes that the Harper-Hofstadter model requires population in a single band of the lattice, so we want to minimize the probability for atoms to be excited to the excited bands of the lattice. In the experiment, this requirement is even more stringent, because atoms can be excited via higher-order multiphoton processes in addition to direct excitation via tunneling or by laser excitation from the Raman drive. In a strongly tilted lattice, population that is excited to higher-lying bands is quickly lost from the lattice via Landau-Zener processes to progressively higher bands. The bandwidth of the higher bands is considerably larger than the ground band, and the bands gaps are smaller as well, so population in the higher bands is not localized to one site and can easily transition

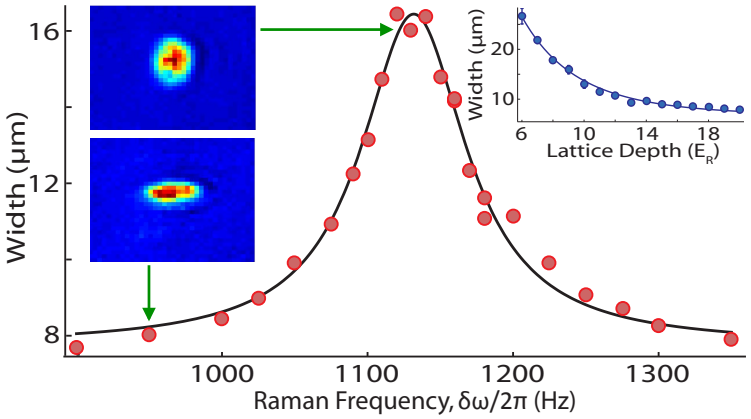


Figure 3-7: *In situ* cloud width as a function of Raman detuning $\delta\omega$ after 500 ms hold. The solid line is a Lorentzian fit to the experimental data (dots) and is consistent with the expected offset between sites due to gravitational acceleration. Images with field of view 135×116 $\mu$m show typical column densities on or off resonance. Inset: Dependence of the laser-assisted tunneling on optical lattice depth.

between bands until the excited band particles become untrapped from the lattice and lost from the system. In parameter regime of our experiments, all population excited to the second band of the lattice is quickly lost on the sub-millisecond timescale.

In the derivation of the effective Hamiltonian, we assumed that the system is resonantly driven such that the diagonal term vanishes after transformation to the rotating frame. However, we can choose to detune the driving frequency from resonance such that we introduce a diagonal term in the effective Hamiltonian that depends on the detuning of the drive term from resonance:

$$H_{\text{eff}} = \sum_{m,n}(\hbar\omega - \Delta)m\hat{a}^{\dagger}_{m,n}\hat{a}_{m,n} + \sum_{\langle m,n\rangle}(Ke^{-i\phi_{m,n}}\hat{a}^{\dagger}_{m+1,n}\hat{a}_{m,n} + t\hat{a}^{\dagger}_{m,n+1}\hat{a}_{m,n} + \text{H.c.}). \quad (3.64)$$

In the effective Hamiltonian we can thus continuously tune the effective gradient from zero to high value by changing the Raman detuning from resonance. This serves as a simple first observable to determine whether the process of laser-assisted tunneling is proceeding as anticipated. One simple way of measuring the effect of tunneling is to release the atoms from the external trapping potential and measure the expansion of the cloud width as a function of time. Looking at the amplitude of Bloch oscillations away from Raman resonance in the effective Hamiltonian for atoms in the lowest band,

we expect the atoms remain localized to a length scale on the order of $\frac{K}{(\hbar\omega-\Delta)}a \ll a$ – even though the atoms are strongly accelerated by a large potential gradient [65]. As the Raman drive becomes resonant with the offset between adjacent sites the gradient term drops out of the effective Hamiltonian and the atoms become free to delocalize in the lattice. From this picture, we expect a resonance feature in the Raman drive spectrum at $\Delta$ with a width on the order of the lowest band width $\sim 4K$. Examining the resonance seen in figure 3-7, we see that the full-width at half-maximum of the resonance is ∼100 Hz. Compared to the theoretically expected bandwidth of $4\times30$ Hz and a measured bandwidth of $4\times12$ Hz calculated from the observed tunneling rate in figure 3-11, the width of the resonance is consistent with this picture of delocalization when the effective tilt is less than the bandwidth.

To verify this picture experimentally, we begin with a BEC in a crossed dipole trap as described in the experimental cycle section of the appendix. The intensity of the Raman lasers is ramped to the final amplitude in 30 ms at a large detuning of 200 kHz – far detuned from any lattice resonance such as to avoid producing excitation in the condensate – at which point the condensate is loaded into a two-dimensional optical lattice in 100 ms to a depth of 9 $E_r$. To apply a large gradient to the vertical, $x$-direction of the lattice, the confining dipole traps are ramped down, creating an energetic offset between adjacent lattice sites of $\sim m_{\mathrm{Rb}} \times g \times 532$ nm$/h = 1136$ Hz. At the same time, the Raman detuning is changed to a tunable final value around the resonance condition. The resulting expansion of the cloud along the $x$-direction (vertical) is shown in the insets in figure 3-7 for Raman drive both on- and off-resonance. Tracking the expansion of the cloud as a function of detuning we see a clear resonance at 1133 Hz, consistent with laser-assisted tunneling of atoms through the lattice enabled by resonant Raman driving.

In addition to the resonance corresponding to laser-assisted nearest neighbor tunneling, Raman drive of the tilted lattice can also induce longer-range tunneling as well as higher-order laser-assisted tunneling processes. Figure 3-8(a) shows an example spectrum with nearest neighbor tunneling driven by both a single two-photon Raman process at 1133 Hz in addition to driving the same link with a four-photon

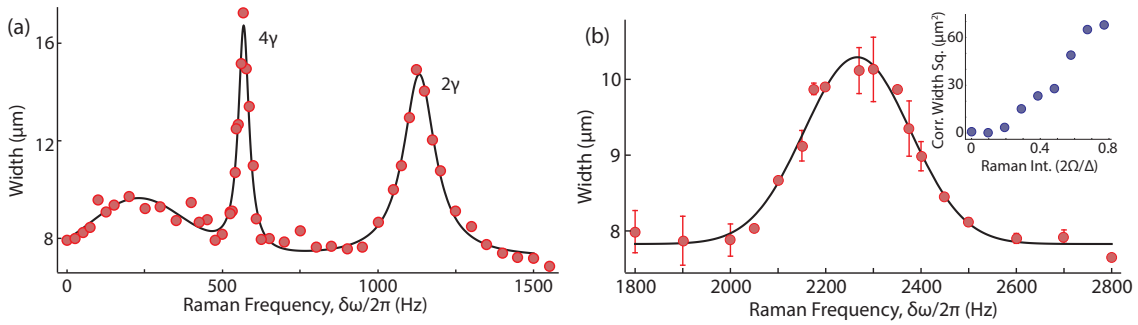


Figure 3-8: Spectrum of tunneling resonances. (a) A strong, four-photon, nearest-neighbor tunneling resonance appears at $\Delta/2h$ along with the $K$ resonance at $\Delta/h$. These data were taken at a lattice depth of 9 $E_r$, for a two-photon Raman Rabi frequency of 1092 Hz and 500 ms expansion time. A weak, broad peak at low frequencies may arise from higher order nearest-neighbor tunneling processes or may be due to thermally-driven hopping arising from heating the atoms in the lowest band on-site. (b) Observation of next-nearest-neighbor laser-assisted tunneling at $2\Delta/h$ and the expansion of the cloud as a function of Raman drive strength, $\Omega$. Inset: No saturation is reached. Expansion time of 1500 ms

process visible as an additional resonance at 567 Hz. In addition to providing multiple ways the nearest neighbor tunneling link can be driven, longer range tunneling can be induced by driving higher harmonics of the site offset, $\Delta$. Figure 3-8(b) shows the expansion of the atomic ensemble induced by resonant driving of the cloud at the next-nearest-neighbor resonance at $2\Delta$. The ability to drive tunneling processes of varying range and strength highlights the power of the laser-assisted tunneling scheme to engineer new Hamiltonians in an optical lattice.

In summary, observing the expansion of the cloud under resonant Raman driving confirms our ability to drive laser-assisted tunneling processes as part of a Floquet engineering scheme to imprint synthetic magnetic fluxes in an optical lattice. In addition, seeing tunneling on such long time scales – 500 to 1500 ms of holding time for the figures above – provides confidence that the atomic population remains in the lowest band long enough to prepare the atoms in the ground state of our effective Hamiltonian, potentially opening a door to an exciting future of studying atoms in strong synthetic magnetic fields.

## 3.4 How do Floquet Systems Heat Up?

In the experiments in the previous section the potential gradient we used to energetically offset neighboring lattice sites and localize the atoms in the lowest band of the optical lattice was provided by gravity due to the removal of the external confining potential that normally holds the atoms against gravity and confines the ensemble spatially. In addition, these experiments have also been accomplished using magnetic field gradients to accomplish the same energetic offset between neighboring sites. Using a magnetic field gradient has the added benefit that the acceleration can be applied to the atoms at the same time as they remain trapped in an external confining potential, maintaining the flatness of the global chemical potential and thus the ground-state Thomas-Fermi density profile. If we remain in the ground state of the density profile, can we prepare the ground state of the superfluid in our effective Hamiltonian? Using the procedure outlined above, the answer is no. In this section, we explore the interesting question of how our atomic ensemble is excited and absorbs heat and how we can control these processes to realize low entropy states of matter.

### 3.4.1 Transitions to Higher Bands

Without considering the microscopic details of the problem, a naive picture of heating would say that applying an force with a certain RMS displacement for a certain amount of time implies a certain power transferred to the atomic system. The balance of input power and cooling power then tells us what equilibrium temperature the system will reach. Unfortunately, ultracold atoms in optical lattices have no cooling mechanism – they are fortunately superbly isolated from thermalization with the surrounding environment – so given some input power the atoms should heat to infinite temperature on some thermodynamic time scale unless prevented to do so by some non-ergodic behavior.

The situation becomes more complicated when we consider the microscopic mechanisms by which the system can absorb this energy. At the single particle level, raising the average energy corresponds to making transitions to higher bands of the lattice.

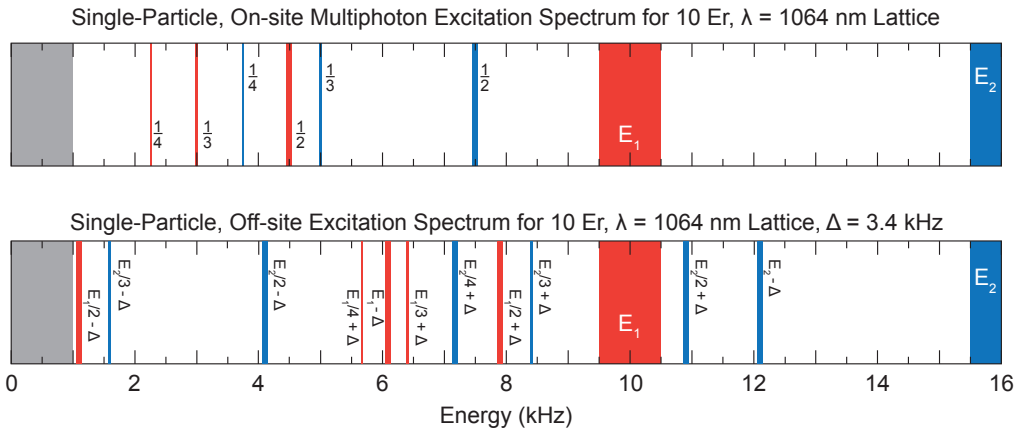


Figure 3-9: Expected spectrum of on- and off-site multiphoton absorption processes. Shown for a lattice depth of 10 $E_r$ lattice with lowest, first, and second bands shaded in grey, red, and blue, respectively. (Top) The expected spectrum of on-site multiphoton resonances including processes up to fourth order in the modulation frequency. (Bottom) The spectrum of off-site resonances for an applied gradient of $\Delta = 3.4$ kHz per site.

Figure 3-9(a) shows the spectrum of band-changing multiphoton excitations that can occur on-site in a lattice with integer divisors of the first and second band gap representing progressively higher-order excitations. For clarity, we show just the first few integer multiphoton resonances one might expect to excite. At lower frequencies the spacing of adjacent lines of very high-order excitations become dense, however, in the weakly driven limit, the strength of these lines decreases in turn so on experimental timescales, we neglect these high-order band excitation processes. Figure 3-9(b) shows the off-site transitions a single particle can make in a lattice tilted by $\Delta/h =$ 3.4 kHz per site.

In the tilted lattice, the Raman transition to an excited state has a resonance at the on-site band energy, for example the transition to the first excited band at an energy of $E_1$, in addition to sidebands corresponding to an excitation to the higher band in the nearest sites, $E_1 \pm \Delta$, next-nearest sites, $E_1 \pm 2\Delta$, and so on. We expect the transition rate for exciting an atom to the next band in an adjacent site to be similar to that for excitation on-site, but with the amplitude of this coupling to be reduced by a factor proportional to $\langle w_0(x - x_i)|x|w_1(x - x_{i\pm1})\rangle / \langle w_0(x - x_i)|x|w_1(x - x_i)\rangle$, where $w_n(x)$ denotes the $n$-th band Wannier functions. Looking at figure 3-9 we see

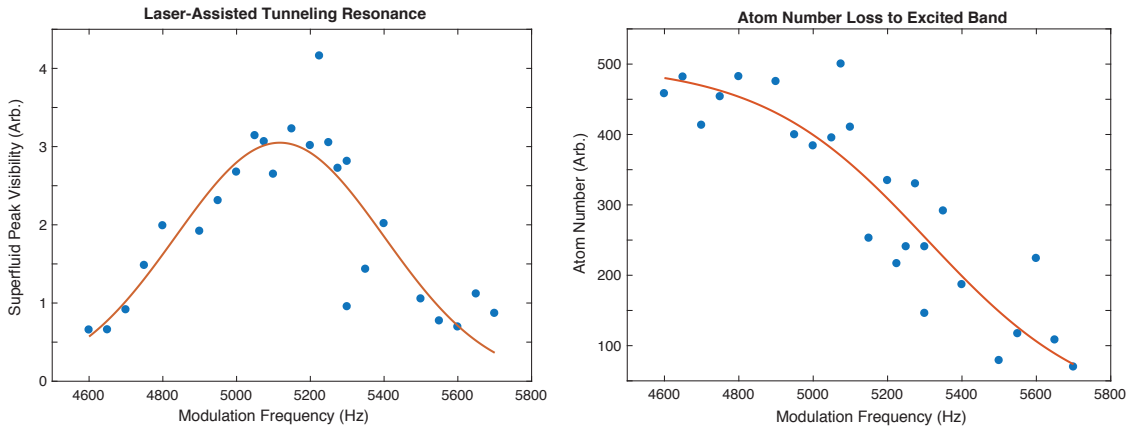


Figure 3-10: Laser-assisted tunneling with amplitude modulation at high values of the tilt. (Left) Visibility of the superfluid diffraction pattern as a function of the driving frequency at increased values of the tilt, clearly showing a tunneling resonance centered around 5120 Hz. (Right) At higher modulation frequencies we run into strong atom loss at a resonance corresponding to the first band gap in an energetically lower well, $E_1 - \Delta$. In this figure the tilt is at 5120 Hz and the lattice depth is 12 $E_r$ such that the coupling to the excited band occurs starting around 5600 Hz, as we see experimentally.

several different potential windows for the energy scale $\Delta$ which avoids any proximity to higher band resonances. We wish to stay at a high enough frequency to satisfy the localization condition $4t \ll \Delta$, so we limit ourselves to $\Delta > 1$ kHz. One potential window is at low frequencies, but we know that there is a high density of high-order resonances at the same time we are minimally satisfying the localization condition. Looking to higher frequencies, we see that the largest gaps in the spectrum come in the regions between $E_n$ and $E_n/2$ as well as $E_n/2$ and $E_n/3$. Considering the tilt in addition to the band energies, we see that there exists an upper bound on $\Delta$ that is lower in frequency than the band gap coming from a strong matrix element for nearest-neighbor tunneling to a lower well at a frequency of $E_1 - \Delta$. We can see this upper bound experimentally in figure 3-10. Increasing the tilt we establish tunneling by resonantly amplitude modulating the lattice intensity. We see a corresponding tunneling resonance at 5120 Hz. However, if we try to modulate at higher frequencies we see a sudden loss of the atom number. If we apply the argument given above, this resonance should correspond to atoms tunneling to a higher band in a lower well of the tilted lattice and subsequently being accelerated out of the lattice. In

this experiment, the lattice depth was 12 $E_r$, so with a tilt of 5120 Hz this picture predicts an atom-loss resonance at 5600 Hz, precisely what we see experimentally in figure 3-10.

Looking back at figure 3-9, the frequency chosen for $\Delta$ reveals the punch line of our story here, a convenient frequency of 3.4 kHz satisfies all of the constraints of the band heating argument: it is far away from multiphoton resonances by being located in between the second and third harmonic of the transition to the first excited band, it is far away from resonances to excited bands in adjacent wells, and as an added bonus it is exactly three times the acceleration due to gravity for our atoms. The exact procedure for realizing this tilt will be discussed later, but it is relevant to mention here that choosing a frequency of 3.4 kHz also helps the fidelity with which we can prepare the atoms in the tilted state.

If we consider the *gedanken* experiment where we choose a modulation frequency that is exactly incommensurate with all band gap frequencies in the lattice, how can the system absorb the applied modulation power and heat up? In the absence of multiphoton absorption processes that limit the lifetime, we consider that the Raman lasers that produce the running wave potential which drive laser-assisted tunneling transitions in the lattice have some noise associated with them. In principle, this could either be intensity or phase noise, but for now we consider the case of phase noise. In the picture of the effective Hamiltonian, phase noise of the Raman lasers corresponds to a modulation of the parameters $K$ and $\delta = \hbar\omega - \Delta$. We can formulate this precisely by modifying the time evolution of the Raman drive and the corresponding kick operator to have a time-dependent phase such that $\omega\tau \rightarrow \omega\tau + \alpha(\tau)$. If we assume that the amplitude of $\alpha(\tau)$ is small and the phase-noise is lower frequency than that of the modulation such that it does not integrate to zero upon time-averaging, we can repeat the Floquet description derived in the previous sections to first order in $\alpha$ to show we recover the Harper-Hofstadter Hamiltonian with the parameters:

$$\sum_{m,n} m\delta(\tau)\, \hat{a}^\dagger_{m,n}\hat{a}_{m,n} + \sum_{\langle m,n\rangle} (K(\tau)e^{-i\phi_{m,n}}\hat{a}^\dagger_{m+1,n}\hat{a}_{m,n} + t(\tau)\hat{a}^\dagger_{m,n+1}\hat{a}_{m,n} + \text{H.c.}). \quad (3.65)$$

The time dependence of $t$ integrates to zero to first order, and we are left with the relation between our effective Hamiltonian parameters and $\alpha$ in the perturbative regime of small driving amplitude $\zeta \approx \frac{2\Omega}{\Delta} \ll 1$ (ignoring higher order Bessel functions):

$$\delta(\tau) = -\hbar \frac{d\alpha(\tau)}{d\tau} \tag{3.66}$$

$$K(\tau) = K\left(1 + i\alpha(\tau) - \alpha(\tau)\frac{\Phi'_{x1}}{\Phi_{x1}}\right). \tag{3.67}$$

As a result, we can see how, even in the absence of resonant multiphoton excitation to higher bands, phase noise of the Raman drive couples to noise in the diagonal and off-diagonal terms of the Hamiltonian. More generally, this highlights how in the effective Hamiltonian noise of the driving frequency and phase can appear as effective low frequency noise in the same way that low frequency noise on any other beam that forms the lattice or trapping potentials can heat the atomic sample by driving transitions between bands.

Of central importance for this work, is the noise mechanism driving transitions between the bands that emerge from the lowest band of the lattice due to the presence of the synthetic flux. Due to the structure of Hofstadter's butterfly, the lowest band of the lattice is split into multiple mini-bands of opposite parity that can be coupled by either the diagonal noise term, $\delta(\tau)$, or of even parity that can be coupled by the off-diagonal noise term $\alpha(\tau)$ similarly to the discussion of amplitude and phase noise from Chapter 2. In the experiments described in the previous section, the Raman phase was not stabilized to a phase reference so we assume that heating due to phase noise may play an important role in understanding heating in the system.

We can get a sense for the decoherence coming from heating within the minibands that emerge from the lowest band in the system by looking more closely at how the tunneling we create in the system with laser-assisted tunneling depends on the experimental parameters we can control. From the derivation of the laser-assisted tunneling rates, in the weakly-driven, tight-binding regime, $\frac{2\Omega}{\Delta} < 1$, the laser-assisted

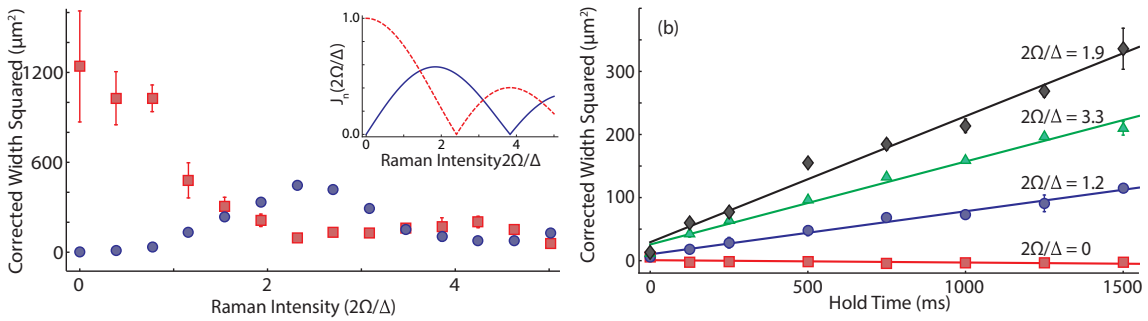


Figure 3-11: Time and intensity-dependence of the cloud expansion. Varying the Raman laser intensity (a) changes the laser-assisted tunneling rate, $K$, along the tilt direction (blue circles) and the tunneling rate along the transverse direction, $J$ (red squares). Data taken at lattice depths of 9 $E_r$ and hold time of 1500 ms. Inset: Theoretical prediction for the tunneling rates $K$ and $J$. (b) Time evolution of the squared width for different Raman laser intensities. From the slope of the lines, we obtain the laser- assisted tunneling rates and their statistical errors: 0.2±0.08 (red squares), 4±0.5 (blue circles), 12±1 (black diamonds), and 8±0.5 Hz (blue triangles).

tunneling rate and transverse lattice tunneling should scale as:

$$K = t_x J_1(\zeta), \text{ and: } t = t_y J_0(\zeta). \tag{3.68}$$

However, as we see in figure 3-11 the scaling of the tunneling with the normalized Raman drive strength in both the $x$- and $y$-directions does not follow what one might expect from the simple picture of our effective Hamiltonian. Qualitatively, looking at the limit of small drive amplitudes, we see that the laser-assisted-tunneling strength does not increase linearly with drive amplitude, but instead begins quadratically and at higher powers behaves like a higher power of the first Bessel function. We can understand this behavior in the limit where the decoherence rate is larger than the tunneling rate as modifying the effective tunneling rate from that given in equation 3.68 to a second order process with a rate $K^2/\Gamma = t_x^2 J_1(\zeta)^2/\Gamma(\zeta)$. We can quantify this by looking at the expansion rate of the cloud also shown as a time series in figure 3-11. If the laser assisted tunneling rate is calculated to be approximately 28 Hz at a driving amplitude of $\zeta = 1.9$, but we measure a tunneling rate of 12 Hz, then the expression above would place the decoherence rate at 65 Hz. Repeating this argument we see that the relative decoherence rate decreases with increasing amplitude indicating some

process that is reduced as we increase the laser-assisted tunneling rate. One culprit for such a process would come from large low-frequency modulation of the applied gradient for which mobile atoms are more able to adiabatically follow than slower-tunneling atoms. A particularly humorous anecdote that might indicate this was a limiting process in the initial experimental effort was the discovery that the main magnetic field coil in the experiment was not physically secured to any mount or to the chamber. Therefore, when we applied a large current to produce a strong gradient in the system the coil physically lifted up, against gravity, lifting off the chamber and literally floated in air for the duration that the gradient was applied before falling back onto the chamber at the conclusion of the experiment. This was remedied by epoxying the coil to a set of brass threaded rods which were in turn clamped securely onto a breadboard added above the chamber. This upgrade also allowed more secure mounting of the high resolution objective and vertical retroreflector and together with current feedback – detailed in the appendix – eliminated a large amount of low-frequency noise as well as shot-to-shot field fluctuations.

A second source of large-amplitude low frequency noise is from the phase of the Raman drive relative to the frame of reference of the lattice. To measure the phase noise of the Raman drive, the two beams were recombined on a 50:50 beam cube and detected with balanced photodiodes as seen in the schematic optical setup shown in Figure 3-12. Ideally, the two beams that compose the Raman drive would be phase stabilized to a cube that sits in the same inertial reference frame as the lattices to which the atoms are confined. Unfortunately, since we have chosen the vertical direction to apply our energy gradient for the tilted lattice, the two laser beams that compose the Raman drive are located on different optical breadboards separated by $\sim$1 meter of optical path length. Consequently, stabilizing the Raman phase at the position of the atoms is a tough task. The optical setup depicted in figure 3-12 shows several elements crucial for this task. The most important optical elements include the two retroreflection mirrors that define the position of the atoms trapped in the optical lattice (acceleration noise of these surfaces is discussed in detail in the phase noise section of Chapter 2) and their motion relative to the 50:50 beamsplitter that

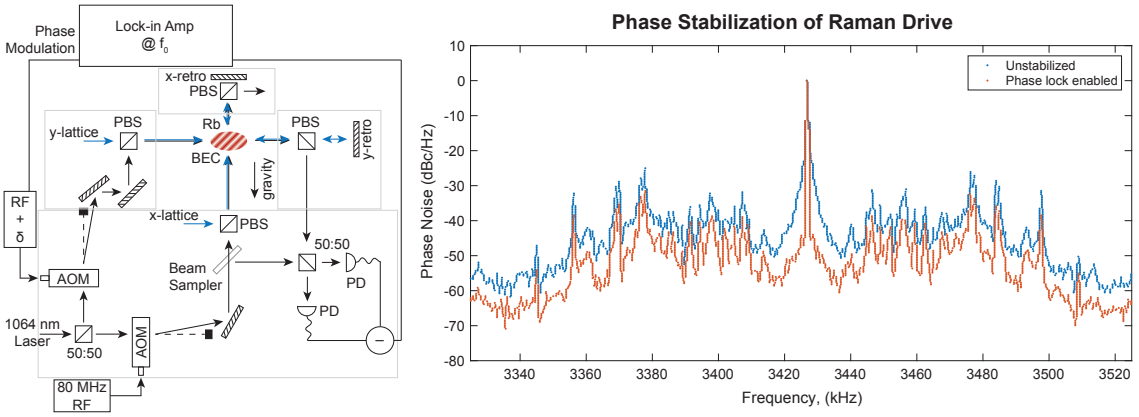


Figure 3-12: Raman phase noise measurement and feedback setup. (Left) Schematic of the optical setup for measurement and feedback-cancellation of Raman phase noise. Gray outlines indicate which optical elements are located on the same optical breadboards. In total there are four different breadboards which carry different components of the optical path. The interference of the two Raman lasers is detected on balanced photodiodes (PD) and can be seen at right before (blue) and after (red) feedback. Feedback is seen to lower the noise floor in the region of interest by ∼10 dB. Abbreviated labels include: polarizing beam splitter (PBS), acousto-optic modulator (AOM), and non-polarizing, balanced beam splitter (50:50).

defines the phase of the Raman drive in addition to the optical surfaces between the detection surface and atoms that adds noise to the Raman drive at the position of the atoms relative to the noise detected at the beam splitter used for stabilization.

A sample beatnote between the Raman lasers, and its associated noise spectrum, is shown in Figure 3-12. The photodioide signal is sent to a lock-in amplifier where it is referenced to a master oscillator set equal to the detuning between the Raman lasers. The lock-in amplifier serves as the master clock for the two RF signal generators established by a shared 10 MHz reference signal. The Raman lasers are aligned to the atoms by overlapping the beams with those that create the $x$- and $y$-lattices. Since both are derived from the same laser source, to avoid any unwanted interferences between the two, the $x$- and $y$-lattice beams are frequency shifted by $+28$ and $-32$ MHz, respectively, and the Raman lasers are offset by $+80$ MHz and $80 + \omega$ MHz, where $\omega$ is an adjustable frequency that is our Raman drive frequency. To retroreflect the lattices without reflecting the Raman lasers, the Raman drive is separated from the lattices by a PBS cube (with front surface reflections purposefully misaligned from

the incoming beam) and the polarization extinction is optimized with both quarter and half waveplates (not shown in figure 3-12) by looking with a camera at the residual transmitted Raman light. With this method, no detectable backreflection of the Raman lasers is seen. The Rabi frequency resulting from the interference of the Raman lasers is independently calibrated from the lattice by time-resolved measurement of Rabi oscillations of the condensate between the $p = 0$ and $p = \sqrt{2}\hbar k$ momentum states at a driving frequency of $2E_r$.

For phase-locking the Raman beatnote to the lock-in amplifier reference, the phase of one RF signal generator is modulated by an output signal from the lock-in amplifier. The amplifier can produce varying amounts of gain, a gain of 10 dB is illustrated in the phase-locked spectrum shown in figure 3-12. In steady state operation, the amplifier can produce higher gain, however, we are limited in the gain we can apply by the transient nature of the experiment – we ramp the intensity of the Raman lasers from zero to finite value in a period of a few milliseconds. With the available hardware, the simplest way to achieve this task was to engage the lock with a serial command to the lock-in amplifier once the Raman lasers had achieved finite intensity, achieving the effect of shorting the integrator of the servo loop without having direct access to the integrator. Future implementations of such an experimental setup should account for the transient nature of the lock initialization in the design of the feedback loop with a design that allows tunable gain as the signal strength is changed from zero to maximum value.

With the ability to provide feedback to the RF signal and stabilize the phase of the Raman drive at the position of the 50:50 beam cube in the detection setup, we now must account for the phase noise reintroduced to the Raman drive as the beams propagate from the position of the atoms to the reference surface. In figure 3-12 these optical elements are the beam sampler and polarizing beam cube in addition to steering mirrors not shown in the schematic used for correctly mode-matching the Raman beams on the detection cube. The dominant contribution to the phase noise reintroduced by these elements comes from the relative motion of the optical breadboards these elements are mounted on. In fact, in the first iteration of this setup,

the relative motion of the breadboards was so severe that we were unable to even acquire a phase lock because the RMS amplitude of the phase noise was greater than the $2\pi$ radian capture range of the phase lock! One major improvement that allowed the acquisition of a phase lock was to replace all the existing optical breadboards of 1/2" thickness in the system with 1.25" thick, solid aluminum breadboards. The improved stiffness of a thicker breadboard reduces the amplitude of drum-like modes in the vertical direction. Each breadboard is supported by four aluminum 80/20 posts with inner cavity filled with vibration-damping lead shot. These posts are attached to the breadboard and optical table by multiple right-angle brackets oriented in different directions to reduce the amplitude of bending modes and subsequent vibration in the $x$-$y$ plane. Despite this upgrade, we still see significant breadboard motion in the $x$-$y$ plane coming from the flexure of this mounting – see the plot of phase noise in Chapter 2 – so we hypothesize that the residual motion of the breadboards is dominated by these degrees of freedom and future designs should incorporate more rigid mounting to reduce the amplitude of support deflection. Despite these qualifications, the improved vibration noise properties of the thicker breadboards reduced the amplitude of Raman phase noise fluctuations to the point where the residual amplitude was within the capture range of the phase lock.

To summarize the above findings, we have discussed how, even with a modulation frequency carefully chosen to avoid prominent multiphoton resonances to the first- and second-excited bands, noise in the modulation phase can still drive transitions between the lowest bands in the system. This low frequency noise is heavily dictated by the structural stability of the optical setup since the ability to apply feedback to the Raman phase and stabilize it to the same inertial frame as the lattice retros is hampered by the relative position stability of multiple breadboards separated on the order of one meter. Regardless, with multiple upgrades to the optical and magnetic field setup we have made much progress in understanding how phase noise couples to the system and in attempting to stabilize the Raman phase relative to the lattices. After implementing all the improvements discussed above, in addition to those we will cover in the next section, the coherence lifetime of the sample increased from

a few milliseconds to almost 100 ms, as we will see in the following section. As a result, once the heating from single-particle effects is controlled and characterized, we begin to look at multi-particle effects; specifically, we are interested in how collisions in such Floquet systems might provide additional channels for heating. For the purpose of evaluating multiple heating sources and optimizing the state preparation and detection, we will rely heavily on a resonantly amplitude-modulated tilted lattice; a system very similar to the resonantly Raman-driven lattice presented in this section and the resonantly phase modulated lattice presented in Chapter 2.

### 3.4.2 Amplitude Modulation as an Optimization Tool

As eluded to in figure 3-10, laser-assisted tunneling can also be driven by resonant amplitude modulation of the lattice intensity in order to create an effective Hamiltonian similar to that derived in Chapter 2 for the resonantly phase modulated lattice. The exact form of the resulting effective Hamiltonian we leave it as an exercise for the reader to derive, but the final result yields:

$$H = \frac{p^2}{2m} + V_L(1 + \alpha \sin(\omega\tau - \theta)) \cos^2(kx) + \frac{\Delta}{a}x \tag{3.69}$$

$$\hat{R} = \sum_j e^{-ij\omega\tau} \hat{a}_j^\dagger \hat{a}_j \tag{3.70}$$

$$H_{\text{eff}} = \sum_j (\Delta - \hbar\omega) j \hat{a}_j^\dagger \hat{a}_j + iK_{\text{AM}} \sum_j \left( \hat{a}_{j+1}^\dagger \hat{a}_j - \hat{a}_j^\dagger \hat{a}_{j+1} \right) \tag{3.71}$$

In the preceding we have defined the matrix element $K_{\text{AM}} = \langle j+1 | \cos(2k(x - x_j)) | j \rangle / 4$. In improving the technical aspects of our experiment, this model has proven to be an invaluable tool. A key difference between amplitude modulation and Raman modulation is that there is no phase noise introduced by the modulation because the lattice simultaneously provides both the trapping potential as well as the modulation terms. In addition, the diffraction pattern of a superfluid in the effective Hamiltonian generated by amplitude modulation is identical to that of the simple cubic lattice, so it provides a useful benchmark for understanding how the kick operators affect the time-of-flight diffraction pattern in the lab frame compared to that in the rotating,

or Floquet frame.

A typical modulation sequence is depicted in figure 3-13(a). The condensate in the $|F, m_F\rangle = |1, -1\rangle$ state is adiabatically loaded into the ground band of an optical lattice and after the lattices have reached full strength the strong potential gradient or tilt is applied after which the modulation begins. As mentioned previously, working at higher gradients of 3.4 kHz compared to the original experiments is desirable for satisfying the inequality $4t \ll \Delta \ll E_{\text{gap}}$ while avoiding multiphoton processes resonant with band excitations as shown in figures 3-9 and 3-10. We can access such gradients very conveniently by levitating the atomic sample against gravity with a magnetic field gradient (before turning on the lattice) and once the lattice is ramped to its final value by rapidly changing the spin to the $|2, -2\rangle$ state by sweeping the frequency of an RF transverse magnetic field. The magnetic moment of the $|2, -2\rangle$ state is opposite that of the initial $|1, -1\rangle$ state and it is twice the magnitude due to the doubled value of $m_F$. Therefore, the resulting gradient experienced by the $|2, -2\rangle$ atoms is three times that due to gravity: $2g$ comes from the field gradient and $1g$ comes from the fact the initial state was levitated and did not experience an acceleration due to gravity.

Initializing the gradient in this manner has several advantages compared to a more traditional approach of turning on or off a current-carrying field coil. First, since the current value does not change in the process, there are no stray fields or eddy currents to compensate for so the gradient magnitude and direction will not change as a function of time as eddy currents relax after a sudden change. In addition, the gradient can be very precisely aligned to the direction of gravity by looking at very long time-of-flight in the levitation field. Aligning the lattice to gravity then provides automatic alignment of the gradient direction to the lattice direction. In our setup, without any shimming of the gradient direction, it is within several degrees of the lattice direction after levitation.

After we apply the tilt by flipping the spin state, the condensate is undergoing Bloch oscillations which decay quickly over several Bloch oscillation cycles. This is reflected in the low initial visibility of the matter wave diffraction pattern seen

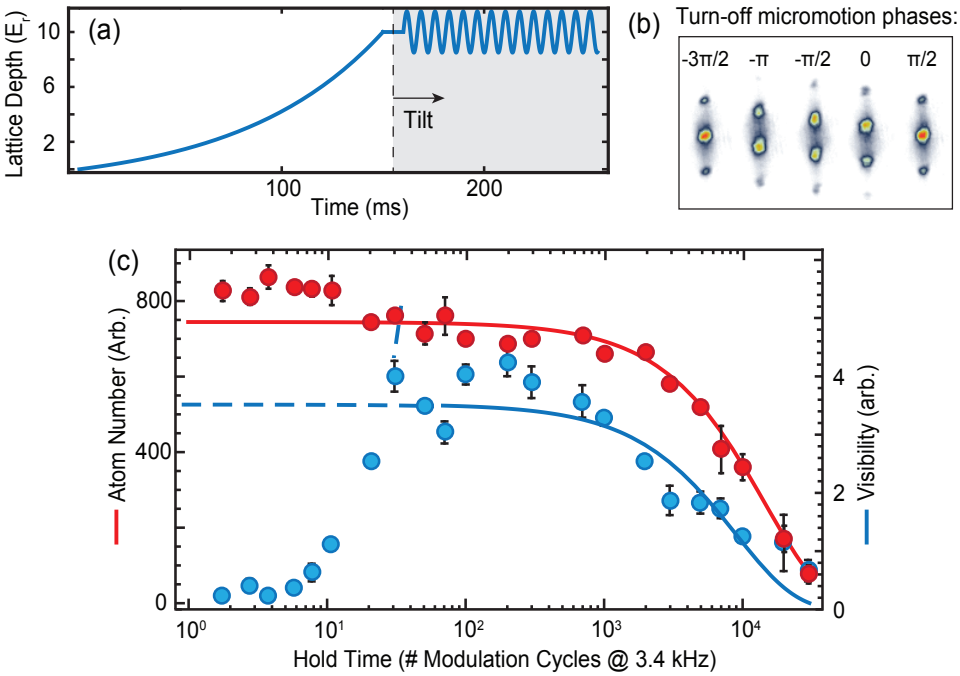


Figure 3-13: Realization of the superfluid ground state of an effective Hamiltonian created with resonant amplitude-modulation. (a) Experimental sequence for loading the BEC into a one-dimensional, 10 $E_r$ lattice, initializing a $\Delta = 3.42$ kHz gradient, and restoring tunneling with resonant amplitude-modulation. (b) Images of the resulting superfluid ground state at different phases of the micromotion, indicated by the label accompanying each frame. (c) Plot of the atom number (red) and visibility of the superfluid diffraction pattern (blue) as a function of hold time counted in the number of modulation cycles. Note that after the tilt is applied there is no visible superfluid but after sufficient hold time, the state relaxes to the superfluid ground state.

in figure 3-13(b) and (c). However, as we hold in the lattice, the visibility of the diffraction pattern increases to a maximum value reflected in the sharp superfluid peaks we see in the images in figure 3-13(b). These peaks persist for hold times on the order of one second, consistent with the lifetime of atom number loss in the tilted lattice. Both loss curves are seen in figure 3-13(c).

Perhaps more interestingly, from the pictures of the condensate in the lattice we see that the peaks change position in a periodic fashion as a function of the phase of the modulation cycle in which we turn off the lattice and perform a time-of-flight measurement. We can easily understand this effect from the derivation of the effective Hamiltonian where we transformed into a frame rotating with the time-dependent

kick operator, $\hat{R} = e^{i\hat{K}(t)}$, in order to derive the equivalent time-evolution over one modulation cycle that defines the effective Hamiltonian. Mathematically, this is given by the decomposition of the time-evolution operator:

$$U(\tau_f, 0)\psi(0) = e^{-i\hat{K}(t_f)} e^{-i\hat{H}_{\text{eff}} t_f/\hbar} e^{i\hat{K}(0)} \psi(0). \tag{3.72}$$

In our experiment, the effective Hamiltonian is the one derived in equation 3.71 and the kick operator is given by equation 3.71. The modulation is a sine-wave such that the initial phase, $\theta$ is zero and the initial time is zero as well. As a result, we can understand the time-dependence of the condensate wavefunction as a steady state evolution under the effective Hamiltonian for some time, $t_f$ and a kick or a projection of the wavefunction from the basis of states of the Floquet description to a basis of states in the laboratory frame of reference. The form of this kick depends on the phase of the drive at the final time, $t_f$. By varying the time that we turn off the lattices within one modulation cycle we can vary this phase and see different diffraction patterns in time-of-flight as demonstrated in figure 3-13.

Similarly, in a two-dimensional lattice laser-assisted tunneling can be driven with amplitude modulation to create a Hamiltonian similar to that given by equation 3.71. In a cubic lattice, the tilted direction and the untiled directions are separable, so the effective Hamiltonian for a two-dimensional cubic lattice with laser-assisted tunneling in one-dimension and a normal lattice in a second direction is simply the sum of the two terms. Figure 3-14(a) shows the result of amplitude-modulating one direction of a two-dimensional lattice where one direction is tilted according to the protocol outlined above for the one-dimensional lattice. Like the one-dimensional case, after some hold time in the effective Hamiltonian we see the appearance of matter wave diffraction patterns from the lattice. Although the formation time of the diffraction pattern is similar in timescale to experiments in a one-dimensional lattice, unlike the one-dimensional case, the coherence lifetime is shorter and very sensitive to the alignment of the gradient to the lattice axes.

Figure 3-14(b) shows the sensitivity of the visibility of the superfluid diffraction

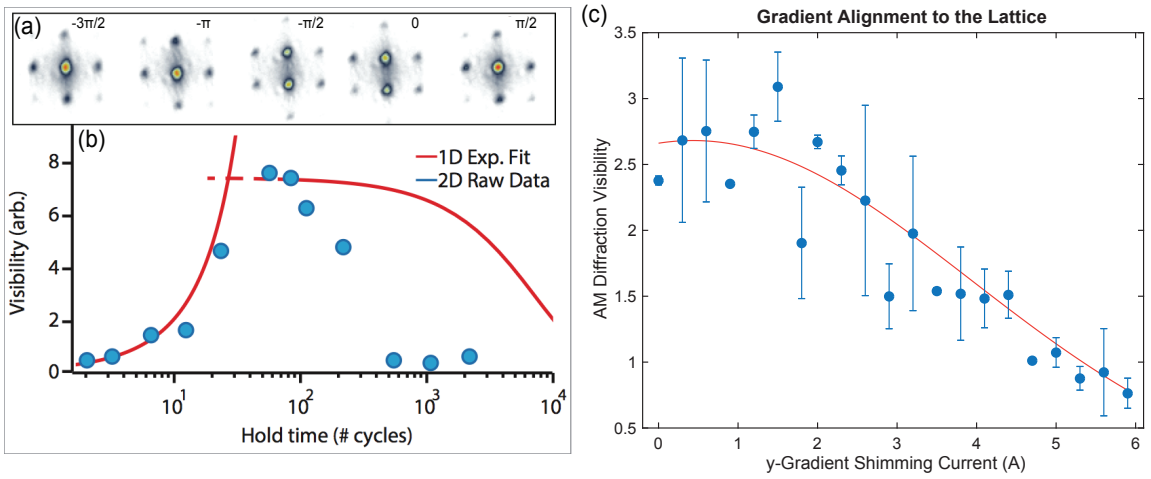


Figure 3-14: The superfluid ground state of the effective Hamiltonian created by amplitude-modulation in a two-dimensional lattice. (a) Superfluid diffraction from a two-dimensional lattice under an effective Hamiltonian created with resonant amplitude modulation. The phase of the micromotion upon switch-off of the effective Hamiltonian is indicated for each frame. (b) Time evolution of the diffraction visibility in units of the modulation period (blue dots) compared to the lifetime of the one-dimensional lattice (red line). The lifetime of the two-dimensional lattice is almost an order of magnitude shorter. (c) Optimizing the alignment of the gradient to the lattice direction by optimizing the diffraction visibility from the amplitude-modulated two-dimensional lattice. The atomic cloud is perfectly levitated at 4 amps of current in the $y$-coil, whereas the diffraction pattern is most sharp around 0.5 amps, indicating the mismatch between the $x$-lattice and the direction of gravity. The hold time is for 200 modulation cycles or about 60 ms for a modulation frequency of 3.4 kHz.

pattern as the value of a bias field in the $y$-direction is changed, effectively steering the direction of the gradient which nominally pointed in the $x$-direction. In this figure, the atom cloud was perfectly levitated against gravity at 4 amps of current in the coil along the $y$-direction. However, we can clearly see that the optimal alignment of the gradient to the lattice direction happens closer to $\sim$0.5 amps, indicating a misalignment of the lattice to the direction of gravity. Indeed, when examined carefully, we see a misalignment of several degrees between the two. The importance of the alignment of the applied force to the lattice axis becomes apparent when one considers the competition between relevant energy scales in the problem. For a $\Delta = 3.4$ kHz per lattice site gradient in the $x$-direction, a $\sim 10^\circ$ misalignment of angle means that there is a $\sim$40 Hz energy offset per site in the $y$-direction, an energy scale comparable to the tunneling and close to the regime where $\Delta_y \sim 4t_y$ and tunneling is inhibited in the lowest band in the $y$-direction. To successfully compensate for the misalignment of the gradient to the lattice direction and eliminate this effect, we use the visibility of the superfluid diffraction pattern in the amplitude modulated lattice to compensate for stray gradients as shown in figure 3-14(b).

With the gradient properly aligned to the lattice direction we observe high-contrast, moderately long-lived superfluid diffraction patterns from the amplitude-modulated, two-dimensional lattice. However, as shown in figure 3-14(a), the lifetime is still reduced by an order of magnitude compared to the one-dimensional lattice. To understand this we consider the details of state preparation in addition to many-particle effects that may potentially limit the experiment once heating due to single-particle effects has been eliminated.

After we turn on the gradient, the undriven system undergoes Bloch oscillations. These Bloch oscillations decay quickly to a final state consisting of an incoherent population of two-dimensional BECs. Although it will not be discussed in detail here, the physical mechanisms behind the decay of these Bloch oscillations is quite interesting. In short, if we take the model of these localized condensates as a phased array – a valid model deep in the localized limit $4t \ll \Delta$ – then the phase procession on each site is given by the potential gradient in combination with the local chemical

potential on each plane of the tilted lattice. Since we rapidly project from a coherent state with number fluctuations in site $i$ of $\sqrt{N_i}$, these number fluctuations are frozen in the lattice when we tilt, resulting in a fundamentally disordered interaction energy on each plane of the lattice and therefore a difference precession frequency for each lattice plane. With this mechanism in mind, there is a fundamental limitation to the Bloch oscillation coherence lifetime of a single-component, weakly interacting BEC. Interestingly, this limit can be circumvented by adding a second superfluid component to the system, a mechanism we experimentally demonstrated and we call superfluid shielding. For more information see the appendix and see ref. [24].

Regardless of the physical mechanism, after applying the tilt, different planes of the lattice have no definite phase relationship before the modulation is applied. Viewed in the rotating frame of the modulation, this implies that the initial state is a uniformly occupied band in the effective Hamiltonian and as such has an average energy of 1/2 the bandwidth, or $2t_x$. Once we apply the modulation and restore resonant tunneling, this uniformly filled band can then thermalize with the degrees of freedom in the transverse directions and relax to a condensed ground state with a reduced condensate fraction according to the amount of energy released from the filled band. From this argument we see that relaxation to the ground state is assisted by the presence of a free third dimension with many atoms. In our two-dimensional lattices, this third direction, the $z$-direction, is a loosely confined tube-shaped trap containing many hundreds of atoms. As a result, there are many atoms and a continuous set of degrees of freedom to deposit energy in and thermalize with to reach a high final condensate fraction as the energy per particle is very low. Unfortunately, when we wish to move to a three-dimensional lattice this energy becomes detrimental to formation of a condensate because the atom number on each site becomes small and the band in the $z$-direction becomes much flatter and less able to absorb energy. As a result, demonstrating a condensed state in a three-dimensional lattice becomes a much tougher challenge, and is addressed in the final section of this chapter about adding strong interactions.

A second mechanism by which the condensate lifetime is limited is the increased

role of density and collisions which can absorb energy from the modulation. This mechanism, first pointed out to us by Erich Mueller and described in detail in ref. [35], involves an off-site collision between two particles which then scatter to a pair of final states in the transverse degrees of freedom which conserve momentum and energy. In the tilted and modulated lattice, there are two main processes contributing to this instability of the condensate. Wannier-Stark states – which are mostly localized in a given well $n$ – have small components in lower wells $n-1$, with amplitude $\propto 2t_x/\Delta$. This small component, which has energy $\Delta$ higher than the Wannier-Stark state localized in the well $n-1$, can collide with atoms in the lower lattice site, thus creating two excitations with energy $\Delta/2$ in the transverse direction (the creation of two excitations is necessary for conservation of transverse momentum). The second mechanism involves the counter-rotating term of the laser-assisted tunneling process. Depicted schematically in figure 3-15, the co-rotating term enables resonant tunneling to a higher lattice site by a resonant two-photon process while in the counter-rotating process the atom virtually tunnels to the lower lattice site, off-resonant by an energy of $2\Delta$, where it can collide with the population in this site. The collision fragments can then scatter into the transverse degrees of freedom, with each atom gaining an energy of $\Delta$ in the process. This two-body elastic collision represents a way in which the interacting system can resonantly convert the energy of the modulation or tilt into thermal energy along the transverse directions. The characteristic relaxation times of the two processes are given by $\tau_1$ and $\tau_2$:

$$\frac{1}{\tau_1} \propto \frac{4t^2}{\Delta^2} \sum_k 2\pi\delta(E_k^{(0)} - \Delta/2) \tag{3.73}$$

$$\frac{1}{\tau_2} \propto \frac{K^2}{\Delta^2} \sum_k 2\pi\delta(E_k^{(0)} - \Delta). \tag{3.74}$$

We can associate $\tau_1$ with the process that occurs even in the absence of modulation – the rate is proportional to the tunnel coupling squared between neighboring sites, whereas the rate of the $\tau_2$ process is proportional to the square of the phonon induced tunneling rate. Both decay processes are rather general and should apply to both

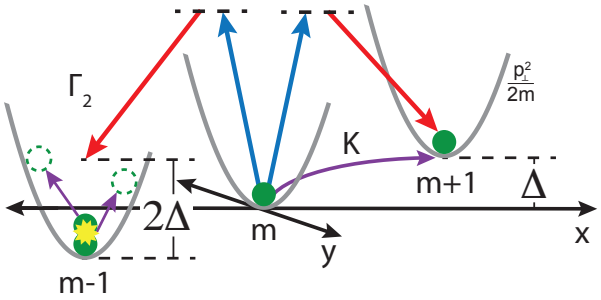


Figure 3-15: Transverse heating mechanisms for both Wannier-Stark states and modulation sidebands. A schematic drawing of a two-particle collision originating from a modulation sideband of the Wannier-Stark state on one lattice site colliding with another Wannier-Stark state on a lower lattice site. The collision causes the atoms to absorb $2\Delta$ of energy from the modulation by scattering atoms from the condensate into thermal states in the transverse degrees of freedom. Similarly, in the absence of modulation the Wannier-Stark states can also produce a sideband of the wavefunction in the lower well which also produces a collision which releases $\Delta$ of energy.

tilted lattices and lattices modulated by superlattices.

If we put in numbers for the expected lifetime limitations these collisional relaxation processes place on our amplitude modulated lattices we get a predicted lifetime of $1/\tau_2 = 0.003 - 0.005\,\mathrm{s}^{-1}$ and $1/\tau_1 = 0.13 - 0.20\,\mathrm{s}^{-1}$, for the one-dimensional lattice and $1/\tau_2 = 0.006 - 0.014\mathrm{s}^{-1}$ and $1/\tau_1 = 0.29 - 0.67\mathrm{s}^{-1}$ for the two-dimensional lattice. Both decay rates are much smaller than the decay rates measured in the experiment, so we conclude that we are not yet limited by these processes. However, this model does make one important prediction for how to suppress this decay channel. In a three-dimensional lattice of sufficient depth, the transverse modes that the collisional fragments scatter into as final states are gapped out, effectively suppressing this decay rate and extending the lifetime of the sample.

All told, we have reviewed a wide variety of mechanisms by which an atomic sample in a periodically-modulated lattice can absorb energy and heat to high temperatures. These mechanisms include direct absorption of the modulation energy by multiphoton excitation to higher bands, noise-driven modulation of the parameters of the effective Hamiltonian driving transitions within the Hofstadter sub-bands, energy absorbed by the condensate by non-adiabatic state preparation, and finally by collisions between

different Wannier-Stark states or their modulation sidebands. Given the success of using amplitude modulation to create a superfluid in the effective Hamiltonian we now move to replace the modulation by amplitude modulation of the lattice with that of the Raman modulation. As we will see in the next section, we observe a difference in the lifetime between amplitude modulation and Raman driving of the tilted lattice that might indicate low frequency phase noise of the Raman lasers, magnetic gradient noise, or inelastic collisions limit the overall lifetime of the state.

## 3.5 Bose-Einstein Condensation in $\alpha = 1/2$

Now that we have understood the various heating mechanisms affecting our implementation of the Harper-Hofstadter model in a tilted and driven lattice and have subsequently demonstrated the ability to prepare the superfluid ground state of an effective Hamiltonian with amplitude modulation to restore resonant tunneling in the system, we wish to replace resonant amplitude modulation with a Raman drive that can imprint a large synthetic magnetic field.

We begin by examining the symmetries and corresponding unit cell and spectrum of the $\alpha = 1/2$ Hamiltonian. Using the same laser geometry described in figure 3-5 in the third section of this chapter, the corresponding phase imprinted on each link of the lattice is $\phi_{m,n} = \pi(m+n)$. Examining the symmetry of the Hamiltonian we find that, in this gauge, the translation symmetry vectors of the lattice are $\mathbf{R} = a(\hat{e}_x \pm \hat{e}_y)$ such that the unit cell is greater in area by a factor of two and therefore the unit cell encloses an integer number of flux quanta. The unit cell and corresponding Brillouin zone are illustrated in figure 3-16.

In general, what we call the *magnetic unit cell* is the smallest unit cell which encloses an integer number of flux quanta. For a general rational flux $\alpha = p/q$ per plaquette, the unit cell is $q$-times larger than the $a \times a$ lattice unit cell and the magnetic unit cell encloses $p$ flux quanta. This is an important distinction from the definition of the *gauge unit cell* which arises from the translation symmetry of the Hamiltonian which mirrors the translation symmetry of the vector potential. For

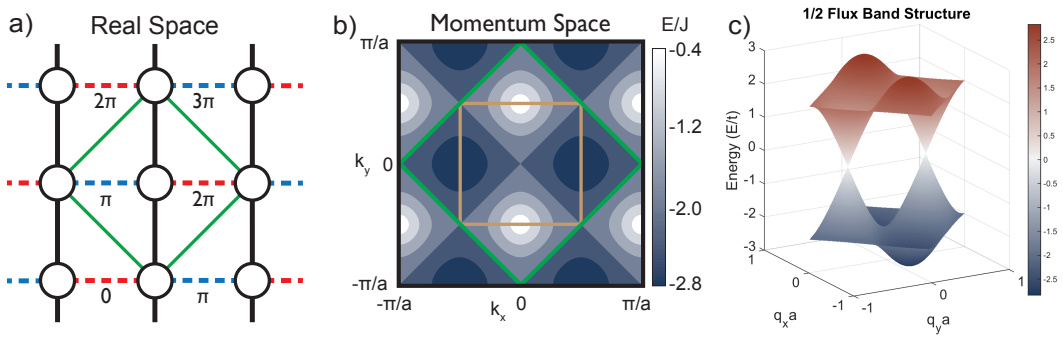


Figure 3-16: Unit cell and spectrum of the $\alpha = 1/2$ Hamiltonian. The unit cell for the experimentally implemented gauge $\phi_{m,n} = \pi(m+n)$, is shown by a green diamond in (a) with translation symmetry vectors, $a(\hat{e}_x \pm \hat{e}_y)$. The unit cell encloses two lattice sites and has an area of $2a^2$. (b) The spectrum in the lowest band in reciprocal space with the magnetic Brillouin zone shown by a green diamond. Due to the two-fold degeneracy of the spectrum a doubly-reduced Brillouin zone can be defined, and is shown by the brown square. (c) The spectrum contains two bands which touch at two Dirac points inside the magnetic Brillouin zone in addition to a two-fold degenerate ground state.

maximally symmetric gauges such as our experimental gauge and the Landau gauge the gauge unit cell and the magnetic unit cell are the same and there is no need to differentiate between the two.

In our experimental gauge, the Hamiltonian written in the basis of states in the unit cell is:

$$H_{1/2} = \begin{pmatrix} 0 & -2t\cos(k_y a) + 2iK\sin(k_x a) \\ -2t\cos(k_y a) - 2iK\sin(k_x a) & 0 \end{pmatrix} \tag{3.75}$$

which results in the energy dispersion relation:

$$E_\pm = \pm 2\sqrt{t^2\cos^2(k_y a) + K^2\sin^2(k_x a)}. \tag{3.76}$$

The resulting spectrum in the lowest band is seen in figure 3-16(a). Note the two-fold degeneracy in the ground state. For an arbitrary rational flux the unit cell contains $q$ indistinguishable and thus the spectrum is $q$-fold degenerate in the ground state. In the continuum limit of Landau levels, this degeneracy becomes the $N$-fold degeneracy of each Landau level. This $q$-fold degeneracy was discussed earlier in this chapter in

the context of the commutation properties of the translation operators.

In figure 3-16 we can see that the spectrum of the 1/2-flux Hamiltonian contains two bands, as expected, that meet at two inequivalent Dirac points located at the positions $q_y = \pm\pi/2a$. The 1/2 flux is unique within Hofstadter's butterfly because it is the only Hamiltonian that is time-reversal symmetric by the fact that a $\pi$ phase and a $-\pi$ phase both produce a real-valued, staggered tunneling amplitude of $\pm 1$ on alternating links in the lattice. This model is also known as the fully frustrated Bose-Hubbard model and is equivalent to a staggered flux with 1/2 flux per plaquette [102, 119, 129]. Examining the spectrum of this Hamiltonian, we immediately see that atoms prepared in the ground state of this effective Hamiltonian will show a four-fold increase in the number of Bragg peaks in time-of-flight and will also display a new, enlarged translation symmetry, giving a clear experimental signature to observe.

The experiment begins similarly to the amplitude modulation sequence with a magnetically levitated BEC in the $|F, m_F\rangle = |1, -1\rangle$ state and is then adiabatically loaded into a two-dimensional optical lattice with the $x$-direction oriented in the vertical direction and the $y$-direction oriented horizontally. Both the lattices and the Raman lasers are derived from the same 1064.2 nm laser source such that the lattice constant is 532 nm and the artificial flux we imprint on the cloud is 1/2 flux per plaquette. The lattices are ramped to a full power of 11 $E_r$ in both the $x$- and $y$-directions, in the presence of a very weak Raman lattice ($< 0.1\ E_r$) with relative frequency detunings equal to the Bloch oscillation frequency, 3.420 kHz. As detailed in the previous section, the Raman lasers are beat together on a 50:50 beam cube located as close to the atoms as the optical system allows and the resulting beat note is detected on balanced photodioides. This beat note is detected using a lock-in amplifier and the resulting error signal is used to feed back to the phase of the RF used to derive one of the Raman beams. The weak Raman lattice is used to engage a phase lock derived from the master 3.420 kHz oscillator of the lock-in amplifier. Once a phase lock is achieved, we turn on a large tilt by sweeping the frequency of an RF field in 0.29 ms to transfer all the atoms to the $|2, -2\rangle$ hyperfine state, which reverses and doubles the magnetic moment. The resulting energy offset per lattice

site is $\Delta = 3.420$ kHz. On completion of the RF sweep, the initial system represents an array of 1D tubes resonantly coupled in the $y$-axis and un-coupled in the tilted $x$-axis.

After completion of the RF sweep that initializes the tilt, the intensity of the Raman drive is linearly increased in 0.58 ms to its final value of $\zeta = 2\Omega/\Delta = 1.6$ corresponding to a Raman lattice depth of $\Omega = 1.6\Delta/2 = 2736$ Hz. After a variable hold time, all laser beams are switched off to allow 20 ms time of flight, followed by absorption imaging. Figure 3-17 shows the resulting time-of-flight images.

From the images in figure 3-17 (g)-(i) we immediately see the sharp peaks characteristic of the diffraction pattern of a superfluid BEC from a periodic potential. These peaks are long-lived and indicate the successful preparation of a low entropy state in the effective Hamiltonian corresponding to a uniform synthetic magnetic flux of $1/2$ flux per plaquette. As predicted from the single-particle calculation, the diffraction pattern shows a four-fold increase in the number of diffraction peaks indicating a lower lattice translation symmetry despite the indistinguishability of individual sites in the unit cell. Fundamentally, this lower translation symmetry reflects the enlarged unit cell due to the presence of magnetic flux. These images allow us to directly demonstrate that, despite the translation symmetry of the lattice and homogeneity of the synthetic magnetic field, the vector potential is more fundamental and necessarily breaks translation symmetry.

The reduced translation symmetry of the vector potential is visible when the condensate occupies one of the two degenerate minima in the first magnetic Brillouin zone, seen in figures 3-17 (b),(g). These images directly reveal the gauge-dependent translation symmetry of the Hamiltonian of $\mathbf{R} = a(\hat{e}_x \pm \hat{e}_y)$, a counterintuitive result given the common argument that gauge-dependent observables are not physical. Physically, we can understand this result from considering that the time-of-flight process allows us to observe the momentum distribution of the wavefunction: $|\langle \mathbf{k}|\psi\rangle|^2$. The wavefunction itself is a gauge-dependent quantity, so the ability to directly observe its momentum distribution allows us to make such a gauge-dependent measurement. An in-depth discussion of the specific appearance of these peaks and their

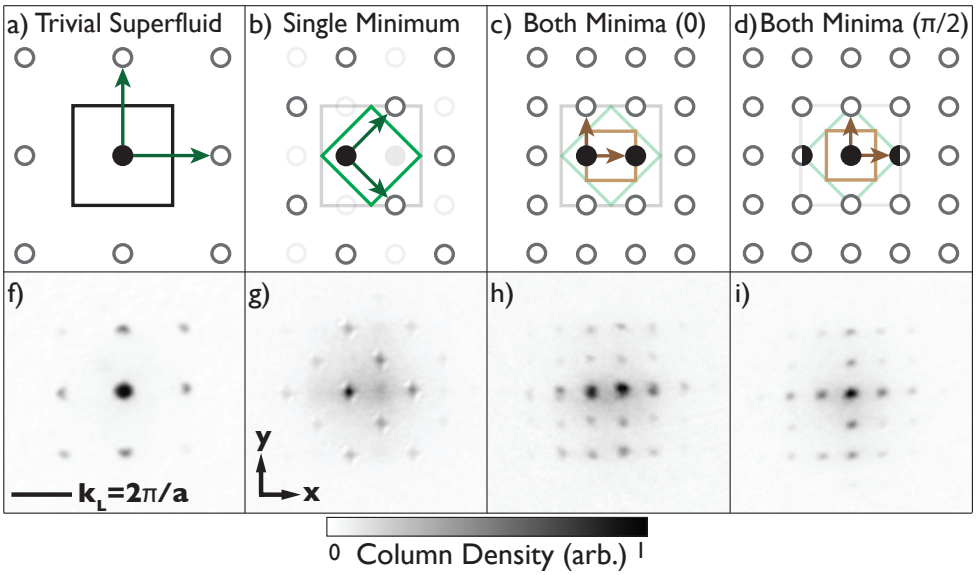


Figure 3-17: Observation of Bose-Einstein Condensation in the $\alpha = 1/2$ Harper-Hofstadter Hamiltonian. The superfluid diffraction pattern in time-of-flight pictures (f-i) from the lattice reveals the momentum distribution of the wavefunction. (a-d), Schematics of the momentum peaks of a superfluid. The dominant momentum peak (filled circle) is equal to the quasimomentum of the ground state. Owing to the spatial periodicity of the wavefunction, additional momentum peaks (open circles) appear, separated by reciprocal lattice vectors (green arrows) or vectors connecting degenerate states in the band structure (brown arrows). (f-i), Time-of-flight images. The superfluid ground state of the normal cubic lattice is shown in (f) compared with different repetitions of the same sequence for the superfluid ground state of the HH lattice (g-i). In (g), only one minimum of the band structure is filled, directly demonstrating the symmetry in our chosen gauge. The number of momentum components in (h-i) is doubled again owing to population of both degenerate ground states. The micromotion of the Floquet Hamiltonian is illustrated in (c,d,h,i) as a periodically shifted pattern in the $x$-direction, analogous to a Bloch oscillation. All diffraction images have a field of view of 631 $\mu$m $\times$ 631 $\mu$m and were taken at a lattice depth of 11 $E_r$ and 2.7 kHz Raman coupling, with at least 30 ms hold in the HH lattice.

gauge-dependence is presented for the next section.

The most common appearance of the diffraction peaks visible in a time-of-flight measurement is shown in figures 3-17 (h) and 3-17 (i) where a condensate appears in both of the minima in the first magnetic Brillouin zone of the lattice. The positions of the peaks can be understood by the combination of the translation symmetry of each minima in combination with the basis vector that connects the two degenerate minima, $\mathbf{b} = a\hat{e}_x$. A useful computational tool in addition to a higher level of simplification is possible when both minima are occupied by defining a doubly-reduced Brillouin zone [130]. Noting that the magnetic Brillouin zone is $q$-fold degenerate for a flux $\alpha = p/q$, keeping track of each state within the magnetic Brillouin zone is not necessary because of the redundancy of description. As a result of this symmetry, an additional reduction of the Brillouin zone is possible, shown in figure 3-17 (c)-(d). For a weakly interacting system, repulsive mean field interactions disfavor density modulation of the many-body wavefunction, so in our gauge occupation of both minima is disfavored at the mean-field level. The interacting system will be treated in detail in a later section; however, our interpretation of the appearance of condensate in both minima is that the system has formed domains of different superfluid order produced by the non-adiabatic preparation of the state.

A final observation from the superfluid diffraction peaks seen in time-of-flight measurements is shown in figures 3-17 (h)-(i) demonstrating the effect of the kick operator acting on the system at different phases of the modulation. From the form of the kick operator for the Harper-Hofstadter model,

$$\hat{R} = \exp\left[i\sum_{m,n}\left(m\omega\tau - \zeta\cos\left(\omega\tau - \phi_{m,n} + \frac{k_x a}{2}\right)\right)|m,n\rangle\langle m,n|\right], \tag{3.77}$$

we see that the initial kick operator is the identity operator because we ramp the modulation amplitude, $\zeta$, from zero (very low) amplitude and we define the time the tilt is initialized by the tilt to be zero. After evolution for an integer number of modulation cycles we turn off the lattices and Raman drive and project the atoms into free space for time-of-flight imaging. The kick operator at the final time describes the

additional phase evolution of the system from the last integer of the modulation cycle to the final time within the period of the modulation. This phase causes an apparent precession of the diffraction peaks relative to the free space momentum eigenstates as seen in the difference of the peak positions in figures 3-17 (g) and 3-17 (i). In the limit of zero Raman lattice depth, this kick operator corresponds exactly to the phase precession of a Bloch oscillation in a uniformly accelerated lattice.

As previously mentioned, almost all images show a roughly equal population of both degenerate ground states. The occupation of only one state, which reveals the underlying symmetry of the vector potential, is observed in less than 1% of the shots. Fitting all of the peaks seen in figure 3-17, and assigning a sublattice designation in order to count the relative population condensed in each minima is difficult because of the large number of peaks and the corresponding large number of degrees of freedom for fitting a function to each peak in addition to the low signal-to-noise of many of the smaller peaks. To alleviate this issue and allow for a better quantitative determination of the relative sublattice populations, we developed a band mapping technique that first adiabatically connects the Harper-Hofstadter ground states to cubic lattice quasimomentum by adiabatically lowering the modulation strength, and then maps to free momentum states with a rapid adiabatic lowering of the lattice depth. A plot of the timing of the different lattice ramps is shown in figure 3-18. Band-mapping the population from the sub-bands of Hofstadter's butterfly to unique free-space quasimomenta presents a unique set of challenges compared to a more traditional band mapping procedure in an optical lattice. First, the two Hofstadter sub-bands are connected at Dirac points and the band gap is therefore zero. Thus, any adiabatic mapping technique will break down for those quasimomentum eigenstates where the gap closes. However, since the atoms are condensed, they are sufficiently localized to quasimomentum states that are far away from the Dirac points and remain locally gapped. Therefore, the first step in our band mapping procedure is to map Harper-Hofstadter quasimomentum onto cubic lattice quasimomentum by adiabatically lowering the modulation amplitude. A second complication arises due to the presence of a strong potential gradient that drives Bloch oscillations in the lab

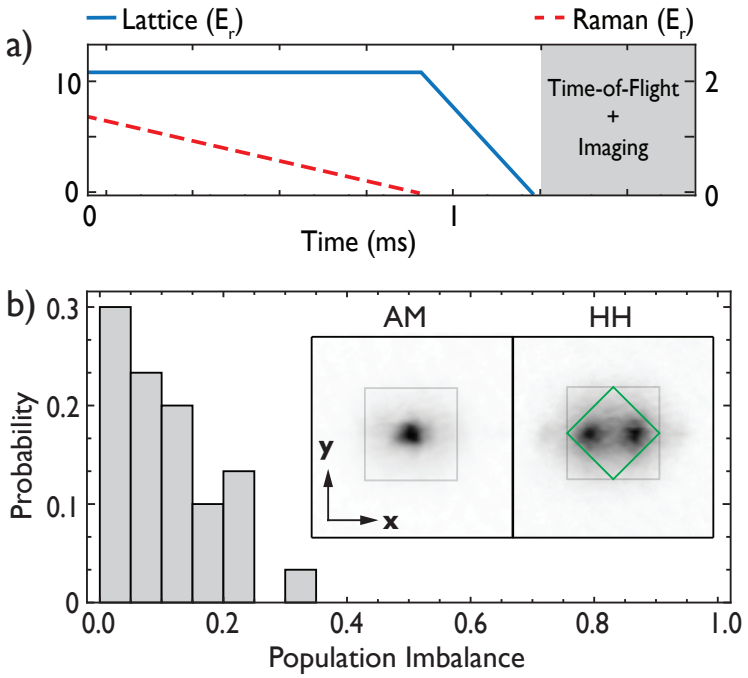


Figure 3-18: Equal populations of two minima determined by band mapping. (a) Sequence for adiabatically ramping population from the rotating frame of the effective Hamiltonian to the lab frame lattice and finally from the lattice to free-space momentum. (b) Histogram of population imbalances between the two minima demonstrating that the minima are most often occupied equally. Inset: Time-of-flight images of the band mapping procedure comparing the amplitude-modulated lattice to the Rama-driven one.

frame. For low lattice depths, the gradient can cause Landau-Zener transitions to higher bands of the cubic lattice. The second step of our band mapping procedure addresses this issue by ramping down the cubic lattice at a rate comparable to the Bloch oscillation frequency. For the Harper-Hofstadter superfluid, the Raman beams are first linearly ramped down in 0.88 ms and then the cubic lattice is linearly ramped down in 0.43 ms as shown schematically in figure 3-18 (a).

The resulting momentum distributions for both a trivial superfluid created by amplitude modulation and the Harper-Hofstadter superfluid are shown in the inset of figure 3-18 (b). Fitting the distribution for the Harper-Hofstadter ground state to a function with with peaks on top of a broad thermal background, the populations in each of the degenerate ground states can be counted. The difference between the two populations is shown in the histogram in figure 3-18 (b) showing that the minima are most frequently populated with equal proportion, demonstrating the degeneracy of the minima and the robustness of the loading procedure to technical fluctuations. For a more detailed discussion of the interacting ground state and it's decomposition into single-particle eigenstates, see the following section on interaction effects. Conveniently, the gauge we implement experimentally allows a straightforward interpretation of the observed equal populations to be a result of domain formation due to non-adiabatic state preparation.

A final, crucial, question for evaluating the usefulness of this technique of creating an effective Hamiltonian for studying many-body physics is the coherence lifetime of the condensate. Figure 3-19 shows the decay of both the superfluid in the amplitude-modulated effective Hamiltonian in addition to the Harper-Hofstadter effective Hamiltonian. The lifetime of the superfluid in the Harper-Hofstadter lattice is similar to that in the amplitude-modulated lattice. Fitting the decay of the fringe visibility to an exponentially decaying function gives lifetimes of 142 $\pm$ 15 ms and 71 $\pm$ 8 ms, for the amplitude modulation superfluid and the Raman driven superfluid, respectively. Both superfluids are susceptible to many of the same heating mechanisms discussed earlier in the chapter on how Floquet systems heat up – multiphoton band excitations, lattice noise, non-adiabatic state preparation, magnetic gradient

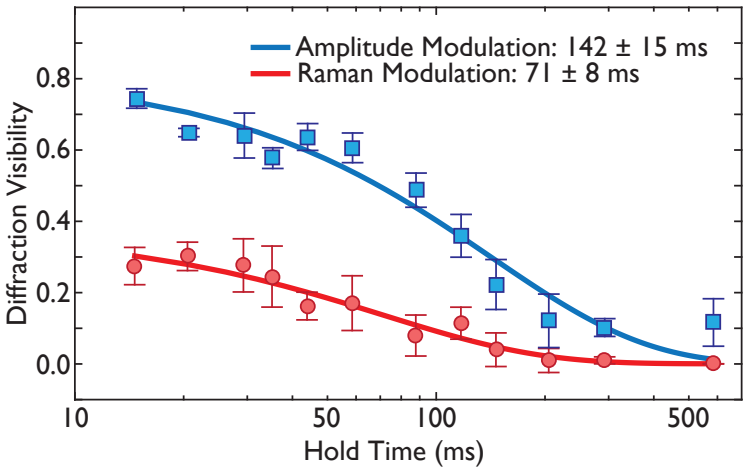


Figure 3-19: Coherence lifetime of the effective Hamiltonian created with amplitude modulation and Raman drive. Note that the lower visibility of the Harper-Hofstadter superfluid is due to the peak doubling, which at the same condensate fraction leads to lower visibility. Exponential fits to the decay of the visibility of the diffraction patterns give lifetimes of 142 ± 15 ms and 71 ± 8 ms, respectively.

noise, and collisional noise – with the addition of Raman phase noise for the Harper-Hofstadter superfluid that is not applicable for the amplitude modulation superfluid. In addition, for both types of modulation, we observe lifetimes for the number of trapped atoms that are much longer than the coherence lifetime in either case, with no discernible loss of atom number up to 500 ms, indicating no excitation of atoms to higher bands or inelastic particle collisions.

We therefore conclude that the decay in figure 3-19 is dominated by transitions within the lowest band caused by technical noise in the magnetic field gradient or by elastic collisions that transfer energy from the micromotion into heat. In addition, we can attribute the difference between these two lifetimes as arising from the additional heating and sub-band transitions driven by noise in the Raman drive phase in addition to possibly a different starting entropy due to the different structure of the superfluid ground states and thus different relaxation channels to the ground state of the effective Hamiltonian.

To summarize, in this chapter we presented experimental data on the first observation of a superfluid BEC in an optical lattice with a strong, uniform synthetic magnetic field. This result is the culmination of a long-process of understanding the

system and its heating channels and subsequently controlling them. Along the way we discussed the value of the superfluid groundstate of the amplitude modulated lattice as an effective tool for optimization of the system, and as a helpful comparison for evaluating the lifetime and lattice manipulations of a superfluid in an effective Hamiltonian in a rotating frame. In the next sections we discuss many of the implications of these results and how they are extended to interacting systems and generalized to realize other paradigmatic models of condensed matter physics.

## 3.6 Gauge-Dependence of Observables

Previously, we saw that under action of a local gauge transformation the canonical momentum and vector potential transform as:

$$\psi \to \hat{U}\psi = e^{i\theta(\mathbf{x})}\psi \qquad \text{so: } \mathbf{\Pi} \to \hat{U}\mathbf{\Pi}\hat{U}^\dagger = \left(\mathbf{p} - \frac{e}{c}\mathbf{A})\right) \tag{3.78}$$

$$\text{and: } \mathbf{A} \to \hat{U}\mathbf{A}\hat{U}^\dagger = \mathbf{A} + \frac{\hbar c}{e}\nabla\theta(\mathbf{x}), \tag{3.79}$$

under the insistence that the physics of interacting charges and fields should be invariant under any particular description of the field. This line of reasoning offers a powerful argument for the statement that observables are not dependent on the gauge description. For example, we can calculate the spectrum for the $\alpha = 1/2$ Harper-Hofstadter Hamiltonian in the Landau gauge and our experimental gauge – or any other gauge for that matter – and the spectrum is identical as seen in figure 3-20. A simple gauge transformation, $\hat{U} = \sum_{m,n} e^{im\pi}|m,n\rangle\langle m,n|$, relates the two pictures.

Despite the equivalence of the two descriptions at the level of the Hamiltonian, the translation symmetry which defines the unit cell is not identical for different choices of gauge, as shown in the different shape of the Brillouin zone in 3-20 for the two different gauges. As demonstrated from the pictures in the previous section where the condensate only forms in one of the two degenerate minima, the translation symmetry of the underlying Hamiltonian is observable from the symmetry of the

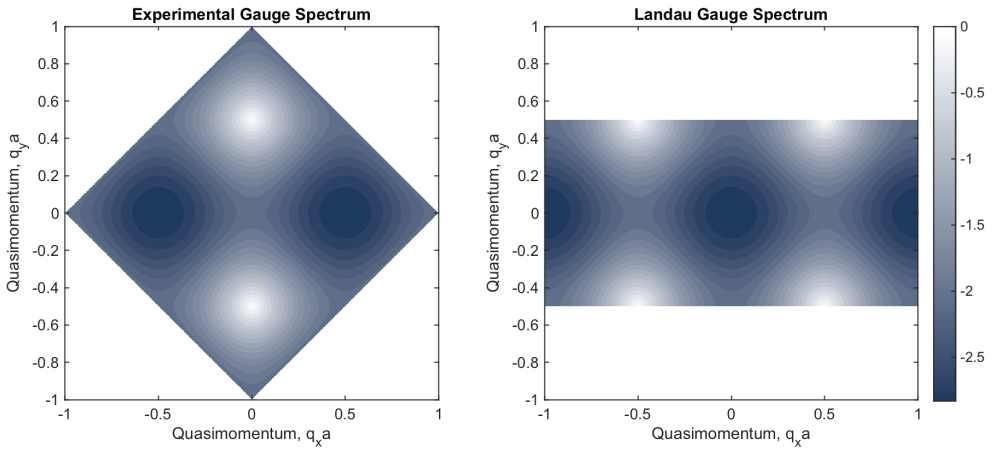


Figure 3-20: The spectrum of the $\alpha = 1/2$ Hamiltonian in two different gauges. The experimental gauge is shown at left and at right we perform the gauge transformation to the Landau gauge and plot the spectrum in this gauge. The spectrum is only plotted for those states within the gauge Brillouin zone.

resulting diffraction peaks from the occupation of just a single minimum. This seemingly contradictory behavior raises the question: does a self-consistent explanation of this behavior exist? How can we understand when gauge-dependent measurements can be made and when is the system truly gauge-invariant?

Essentially, gauge-dependent observations can be made in time-of-flight images of ultracold atoms when the momentum distribution of the wavefunction is observed. The sudden switch-off of all laser beams preserves the wavefunction, and canonical momentum, which is gauge-dependent, becomes mechanical momentum, which is readily observed [95]. More precisely, at the point the lattices are turned off, the wavefunction is projected into a superposition of plane wave eigenstates of free space, $\sum_{\mathbf{k}} |\mathbf{k}\rangle\langle\mathbf{k}|\psi\rangle$, which propagate under a Hamiltonian for which $\mathbf{A} = 0$ for some time-of-flight long enough such that we can neglect the initial spatial distribution, and observe the momentum distribution of the initial wavefunction. In practice, 20 ms is not long enough time-of-flight to quantitatively ignore the initial spatial extent of the trapping potential when considering the shape of each Bragg peak, but for an understanding of the symmetry and population in each peak, 20 ms is sufficient.

A more general argument can be formulated for electromagnetic fields which obey Maxwell's equations and can then be applied to systems of electrons in a real magnetic

fields (note that the synthetic fields created for ultracold atoms in optical lattices do not obey Maxwell's equations!). In terms of the gauge-invariant quantities of momentum and the electric field generated by the switch-off of a magnetic field, the momentum transfer imparted upon an electron upon switching off the magnetic field is:

$$\Delta \mathbf{p} = \frac{e}{c} \int_{\tau_i}^{\tau_f} d\tau \, \mathbf{E}(\tau) \tag{3.80}$$

In general, this changing magnetic field creates an electric field which is related to the vector potential by, $\mathbf{E} = -\partial_t \mathbf{A} - \nabla \phi$. In the Coulomb gauge, where $\nabla \cdot \mathbf{A} = 0$, the scalar potential is proportional to the integrated charge density, so if the system is overall charge neutral, $\rho = 0$, then the scalar potential is also zero, $\phi = 0$. In this configuration, the electric field generated by the switch-off of a magnetic field is determined solely by the vector potential: $\mathbf{E} = -\partial_t \mathbf{A}$. As a result, equation 3.80 becomes:

$$\Delta \mathbf{p} = -\frac{e}{c} \int_{\tau_i}^{\tau_f} d\tau \, \partial_\tau \mathbf{A}(\tau) \overset{\mathbf{A}(\tau_f)=0}{=} \frac{e}{c} \mathbf{A}(\tau_i), \tag{3.81}$$

showing an exact relation between the vector potential and the momentum transfer! Since the electric field and mechanical momentum are gauge-invariant operators, we interpret this result to indicate that the momentum distribution of the electron seen in time-of-flight measurements are always that of the Coulomb gauge.

We can further see this relation when we perform a gauge transformation away from this special Coulomb gauge, $\mathbf{A} \to \mathbf{A} + \nabla \chi$, and $\phi \to \phi - \partial_t \chi$, such that the electric field generated by the turn-off of a magnetic field becomes:

$$\mathbf{E} \to -\partial_t (\mathbf{A} + \nabla \chi) - \nabla(-\partial_t \chi) = -\partial_t \mathbf{A}. \tag{3.82}$$

We see that in this new gauge the momentum transfer is identical to that of the Coulomb gauge described above. This argument highlights the unique position the Coulomb gauge plays in such time-of-flight measurements.

One final aspect to note is that within the Coulomb gauge there are multiple distinct gauges which satisfy the divergence-less definition of the gauge in free space,

two examples being the Landau gauge and the symmetric gauge describing a uniform magnetic field. A common misconception is that electron dynamics are independent of the specific choice of gauge; however, we point out that the divergence-less condition should hold for all space, including the boundaries of the system. Using the Landau gauge for a field generated by a solenoid means that at the surface of the solenoid the gauge will indeed have a non-zero divergence condition, and only the symmetric gauge will produce zero surface divergence. The same argument holds for using a symmetric gauge for a field generated by a current sheet compared to the Landau gauge.

In ultracold atoms, this concept of a "natural" synthetic gauge for time-of-flight measurement also appears in GPE simulations of the spatial shear of a BEC released in time-of-flight from a weak synthetic magnetic field [95]. This interpretation highlights the possibility of observation of this effect in electrically charged systems by possibly comparing electron momentum distributions in time-of-flight for different "natural" Coulomb gauges such as the Landau gauge compared to a symmetric gauge.

## 3.7 The Weakly Interacting Ground State of $\alpha = 1/2$

Due to the indistinguishability of the sites within the unit cell, the single-particle ground state of the $\alpha = 1/2$ Harper-Hofstadter Hamiltonian shown in figure 3-16 is two-fold degenerate. At first glance, the simultaneous occupation of the condensate in different single-particle states should imply some density modulation in real space of the resulting wavefunction due to interference terms between the two single-particle Bloch waves. However, given a repulsively interacting background scattering length of $\sim 100a_0$ in $^{87}$Rb, the BEC that emerges in the effective Hamiltonian should disfavor density modulation that arises due to interference between Bloch waves. An interesting question then is what is the nature of the ground state in the presence of these weak repulsive interactions?

An interesting result of the gauge-dependence of the ground state wavefunction is that the nature of the interacting ground state in terms of the single particle states

depends on the specific gauge implemented. Previously in the literature, the interacting ground state in the Landau gauge is discussed [119, 130], and it is found that a superposition of the single-particle ground state minimizes interactions and creates a uniform density ground state. We can understand this intuitively by examining the single particle ground states in the Landau gauge, up to a normalization factor: $\psi_{k_1} \propto \{(\sqrt{2}-1), 1\}$ and $\psi_{k_2} \propto \{1, (\sqrt{2}-1)\}$, in the basis of states centered on $\{A, B\}$ sites. From these wavefunctions, we see from $|\psi_{k_i}|^2$ in this gauge that the two sites do not carry equal population and thus if the condensate forms in either individually it will result in a density modulation in real space. As a result, the mean-field wavefunction for the interacting state involves a superposition that removes this imbalance with the form: $\psi_{\pm} = \frac{1}{\sqrt{2}}(\psi_{k_1} \pm i\psi_{k_2})$. Note that either the positive or negative combination results in an equivalent mean-field wavefunction, indicating that the ground state degeneracy is preserved in the presence of interactions. More fundamentally, this is the result of time-reversal symmetry that is restored in the $\alpha = 1/2$ Hamiltonian by the equivalence of a $\pi$ and a $-\pi$ flux in each plaquette.

In contrast, in our experimental gauge the Hamiltonian is purely off-diagonal so the ground state wavefunction for the individual single-particle states are given by: $\psi_{k_{1,2}} = \{(1 \pm i)/2, 1/\sqrt{2}\}$. Examining the weight of the wavefunction on each sublattice via: $|\psi_{k_i}|^2$, we see that the single particle eigenstates already host a pair of time-reversal symmetric states that have no sublattice population imbalance and therefore no density modulation in the ground state. Therefore, we interpret this as a gauge-dependent composition of the interacting ground state wavefunction. As a result, the balanced sublattice populations we observe in figure 3-18 should be the result of domain formation after a non-adiabatic quench from the condensed ground state of the Bose-Hubbard model to the condensed state in the Harper-Hofstadter model rather than an observation of the single-particle ground state superposition that constitutes the interacting ground-state.

## 3.8 Strong Interactions Meet Strong Fluxes

So far, the experiments we have covered have all been performed in a two-dimensional lattice consisting of elongated tubes of condensate containing with many hundreds of atoms. We have also seen how even weak interactions can qualitatively change the nature of the interacting ground state and how our initial state preparation impacts the first experimental results. To address several of these issues, we wish to prepare the interacting ground state in a three-dimensional lattice.

As previously mentioned, the existence of a tube of many atoms is crucial for the appearance of a BEC in the realization of the Harper-Hofstadter Hamiltonian. The relaxation of the initial condensate to one that occupies degenerate ground states creates entropy in the system and the large number of degrees of freedom in the $z$-direction in the system provides a reservoir for this entropy to thermalize with on timescales fast compared to the experimental lifetime. Unfortunately, the timescale for thermalization increases with increasing lattice depth in the $z$-direction, so direct – what we will call non-adiabatic – preparation of the effective Hamiltonian from the Bose-Hubbard ground state via an experimental sequence seen in the top of figure 3-21 becomes unpractical.

Examining the Bose-Hubbard model and the Harper-Hofstadter model with interactions we naively see that the two share a ground state for strong interactions and integer filling, the Mott insulating state. Therefore, we identify an alternative route to adiabatically load the ground state of the three dimensional lattice with strong fluxes – seen in the bottom of figure 3-21 – by first entering the three-dimensional Mott insulator, then switching spatially-uniform tunneling to that which imprints the synthetic magnetic flux, before ramping out of the Mott insulator into the superfluid ground state of the three-dimensional lattice. This method of changing the nature of the superfluid state from the Bose-Hubbard ground state to another ground state that that does not smoothly connect to the starting configuration of the condensate has been successfully used to prepare other interesting states, such as a superfluid at negative temperature for motional degrees of freedom [21], and is a powerful tool for

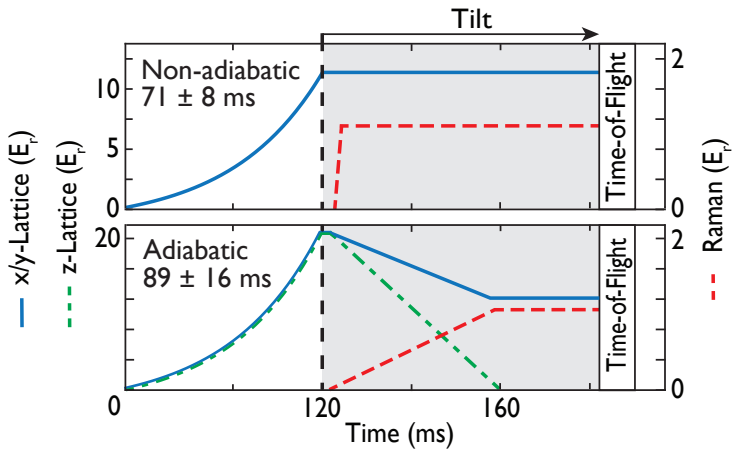


Figure 3-21: Lifetime of the $\alpha = 1/2$ ground state prepared in a three dimensional lattice. A comparison of experimental sequences for a non-adiabatic state preparation as well as an adiabatic state preparation sequence. The adiabatic scheme utilizes the many-body gap of the Mott insulating state to protect the system from excitation and successfully prepare the superfluid ground state of the Harper-Hofstadter Hamiltonian in a three-dimensional lattice. The resulting lifetimes of the adiabatic versus the non-adiabatic sequences are indicated in the top right of each panel.

adiabatic state preparation of highly frustrated superfluids.

Applying the experimental sequence in figure 3-21 to our system where we add a lattice along the $z$-direction, also with a lattice constant of $\lambda/2 = 532$ nm, we successfully prepare a superfluid in the ground state of the three dimensional lattice. The lifetime of this superfluid, measured from the end of the ramp of the $z$-lattice power to zero and the Raman lattice to full strength is indicated in the corner of figure 3-21 and is comparable, and even slightly longer than, the non-adiabatic sequence. What's powerful about this success is that the final depth of the $z$-lattice can be varied and at each lattice depth the condensed ground state of the Harper-Hofstadter Hamiltonian is clearly visible. An even more encouraging result comes from figure 3-22, which shows the lifetime of the superfluid diffraction pattern as a function of the $z$-lattice depth. Remarkably, not only is this experimental sequence able to prepare the superfluid ground state of the effective Hamiltonian, but the superfluid diffraction is visible and moderately-long lived for varying $z$-lattice depths. The $z$-lattice here, as indicated by the upper axis in figure 3-22, controls the interaction energy scale in the system, the Hubbard $U$ parameter, and thus the proximity of the system to the

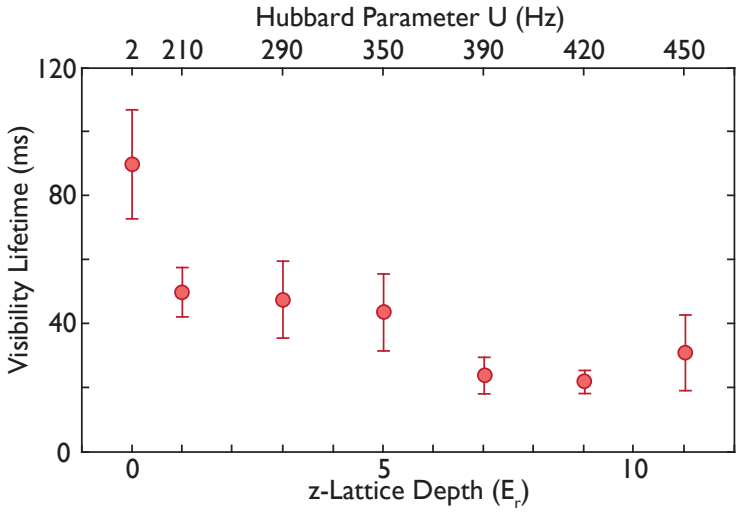


Figure 3-22: Coherence lifetimes of the $\alpha = 1/2$ ground state in various three-dimensional lattice depths. Plotted are the measured coherence lifetimes of the superfluid diffraction pattern visibility in the three-dimensional lattice as a function of the $z$-lattice depth. Changing the $z$-lattice depth also changes the Hubbard interaction parameter, $U$, shown on the top axis.

Mott insulating transition in our effective Hamiltonian.

The critical value for the $n = 1$ Mott transition in the Harper-Hofstadter Hamiltonian happens at lower ratios of $U/t$ compared to the superfluid-to-Mott insulating transition in the Bose-Hubbard model [154]. For our lattice parameters, the Mott transition in the Harper-Hofstadter Hamiltonian happens close to 12 $E_r$, meaning the lifetimes recorded at the highest lattice depths in figure 3-22 approach the transition for those parts of the cloud with average density $\sim 1$. The peak density of the samples used in 3-22 is close to $n = 5$, so the Mott transition for the isotropic lattice at these occupancies happens between 15-16 $E_r$. The lattice we realize has lattice depths of 11 $E_r$ in the $x$- and $y$-directions, and a variable depth in the $z$-direction. In this configuration, we observe weak diffraction peaks in three-dimensional lattices for $z$-lattice depths up to 20 $E_r$, shown in figure 3-23. The images in figure 3-23 represent a selection of shots immediately after the $\sim$35 ms ramp out of the Mott insulator state into the 1/2-flux superfluid. The doubling structure is clearly visible at lattice depths close to the Mott insulating transition for filling factors n $>$ 2. Unfortunately, no systematic studies were done for $z$-lattices greater than 11 $E_r$

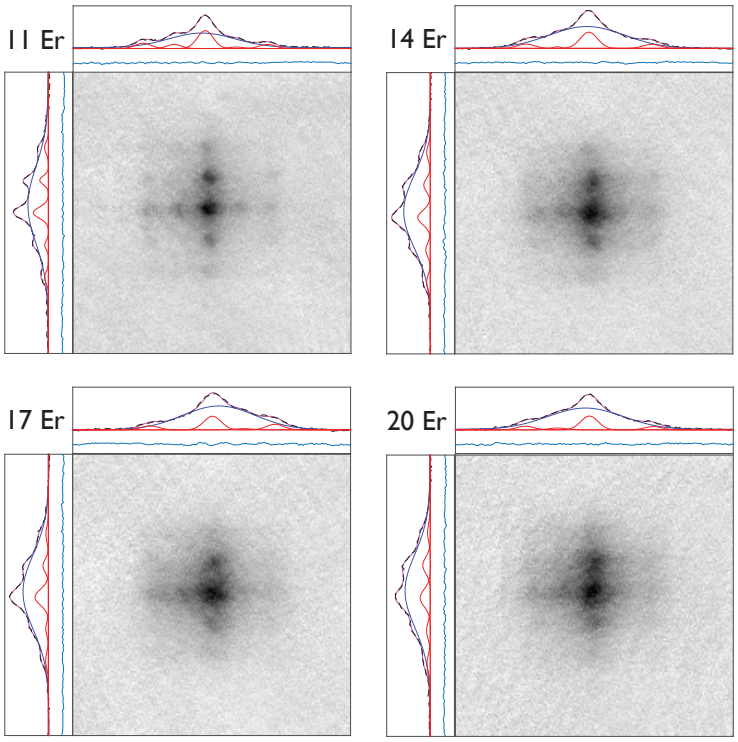


Figure 3-23: Time-of-flight images of the interacting $\alpha = 1/2$ state close to the Mott insulating transition. For these images, the $x$- and $y$-lattices are at a lattice depth of 11 $E_r$ and the $z$-lattice depth is varied as indicated in the upper left corner of each image. For the peak density of $\sim n = 5$ for the samples shown above, the Mott transition for the isotropic lattice happens between 15-16 $E_r$.

since much larger shot-to-shot fluctuations were encountered, probably due to larger sensitivity to technical noise sources.

Despite the technical challenges associated with probing the Mott insulating transition in the Harper-Hofstadter Hamiltonian we realize, it is useful to consider the qualitative new features predicted to exist in such a system with both strong synthetic magnetic fluxes and strong interactions. The first effect is mentioned above: the location of the phase transition is predicted to shift towards a lower critical interaction strength with the critical $(U/t)_c$ as a function of the applied flux mapping out the shape of the lowest eigenvalues in Hofstadter's butterfly [154]. A second qualitatively new feature that appears in numerical studies of small systems that may extend to larger systems in the strongly interacting state is the existence of a chiral Mott insulating state [40]. This is a state that appears as an intermediate between

the Mott state and the superfluid that can be seen as a vortex supersolid with a small number of crystallized insulating regions coexisting with the staggered fluxes of the fully-frustrated superfluid. While this has been calculated for small systems with $\alpha = 1/2$, further investigation may reveal whether this is also happens for general fluxes and larger system sizes.

In systems of coexisting strong fluxes and strong interactions the filling fraction $\nu$ – the ratio between the particle number and the flux number – plays an important role in determining the resulting nature of the ground state. Most famously, this hierarchy of states with rational values of the filling fraction label the series of integer and fractional quantum Hall states found in electronic systems [94, 146, 152]. Although no experimental measurement of fractional states in ultracold atomic systems exists to date, many proposals for implementing such a state have been put forward. One challenging aspect of the realization of fractional systems with ultracold atoms in optical lattices is avoiding the formation of a Mott insulating state. For example, when realizing a system with on average one particle per site (regardless of the flux realized) at sufficiently strong interactions a Mott insulating state will generally form – seen trivially in the atomic limit ($U \gg t$) of the microscopic Hamiltonian. As a result it is advantageous to either realize densities with particle numbers below unity filling to suppress the Mott transition or to suppress the Mott state with a chemical potential set between the Mott lobes in the regime: $\mu \approx nU$. One example of the interesting states that are realizable in cold atomic systems with synthetic magnetic fluxes are the $\nu = 1/2$ bosonic Laughlin state and the $\nu = 1$ Moore-Read states found by exact diagonalization in an optical flux lattice [37]. Critically, the particle density controls which state is the interacting ground states, highlighting the necessary control over the density required to reach such states.

In summary, the work described in this chapter details how we proposed and implemented a system of strong, uniform magnetic fields in an optical lattice. This method improves upon many of the limitations of the previous schemes by demonstrating how to generate any arbitrary, uniform flux with the tools of atomic physics: a magnetic field gradient and far-detuned lasers. In addition, we have investigated,

understood, and solved many heating issues for these types of Floquet systems and along the way realized the superfluid ground state on an effective Hamiltonian created with amplitude modulation in order to evaluate the importance of many of the heating effects. Finally, we demonstrated the superfluid ground state of the 1/2-flux Harper-Hofstadter Hamiltonian and shown the necessarily lower symmetry of the vector potential than the lattice, which gives rise to a rich diffraction structure in time-of-flight measurements. Interestingly, we discovered that we are able to make gauge-dependent measurements by looking at the symmetry properties of the vector potential acting on the time-of-flight images, and proposed this is also a feature in real electron systems. Finally, we demonstrated the superfluid ground state in a three-dimensional lattice and showed that the superfluid persists for even strong interactions raising the prospect of investigating exotic many-particle states close to the Mott transition. Moving forward, we look at several new directions for experiments that this research accomplishment opens.

## 3.9 Outlook

To conclude this chapter, we discuss some outstanding experimental problems and present a vision for solving these issues. Imprinting synthetic magnetic fields can be achieved within the framework of Floquet engineering an effective many-body Hamiltonian as first derived in chapter 2 earlier in chapter 3. Despite its power and successes to date, there are several outstanding issues to be addressed with the practical implementations of effective Hamiltonians. Two of the most prominent among these issues include: how to adiabatically prepare the ground state of the Hamiltonian of interest, and: how to detect interesting topological orders. In the superfluid groundstate of the $\alpha = 1/2$ model, the enlarged translation symmetry and the subsequent superfluid diffraction pattern served as an effective probe of the new order in the system; however, in strongly interacting or insulating phases – as in the superfluid to Mott insulator phase transition – time-of-flight measurements may not always directly reveal the ordering of the system. In addition, for the Harper-

Hofstadter system we were not able to reproducibly prepare a pure ground state consisting of a single superfluid domain. Even in the preparation sequence which utilizes the Mott insulator to switch between superfluid groundstates, the quantum phase transition from the Mott state to the superfluid state still features a ground state degeneracy on the superfluid side of the phase transition which produces domains of different superfluid order when the transition is crossed at a finite rate [135, 175].

This difficulty loading the ground state highlights a general problem associated with creating topologically ordered states of matter and loading the ground state with high fidelity. A topologically ordered state generally contains some level of ground state degeneracy – defined by the degeneracy of the ground state upon mapping the system onto a torus [163, 121] – as such, this presents a difficulty in deterministically preparing pure states in the ground state of the many-body system. Given the ability to load a topologically ordered ground state, an additional difficulty is to detect this topological order in a cold-atom system. Since information on the topological state is encoded non-locally in the many-body state, an important question is what kind of local observables can we detect, or correlation functions we can measure, that will reveal this nonlocal ordering?

Both questions are prominent issues to be addressed moving forward in realizing such topological states in optical lattices. For the states discussed in this chapter, engineered by laser-assisted tunneling in a tilted lattice, one tool that becomes useful for addressing these two questions is the ability to control site-offsets within the magnetic unit cell in the laser-assisted tunneling process. This importance is highlighted in the all-optical flux rectification scheme implemented in Munich [4], where a superlattice with the same unit cell as the magnetic unit cell was used to drive the topological phase transition in the lowest band of the effective Hamiltonian with $\alpha = 1/4$ flux per plaquette. To this end, we propose a new all-optical technique for flux rectification via a triple-superlattice potential. Shown in figure 3-24, the tripled superlattice is the minimal geometry superlattice needed for rectification of an arbitrary flux because it breaks the inversion symmetry of the symmetric double-well superlattice (Note that for the special flux of $\alpha = 1/4$ the rectification scheme used

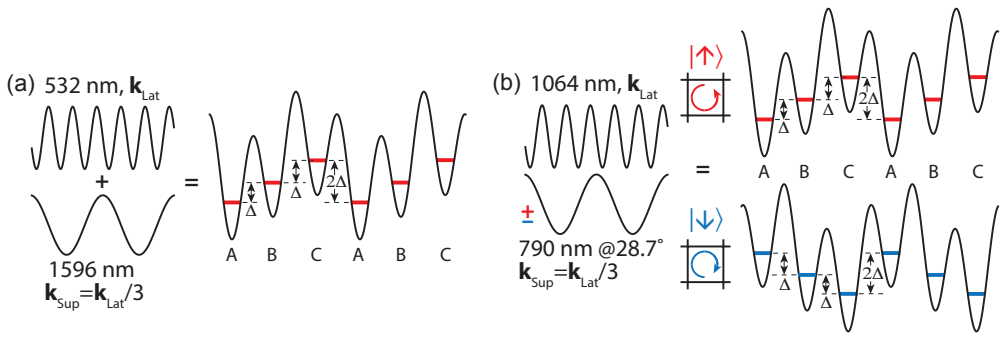


Figure 3-24: Proposal for flux rectification with a tripled-superlattice. (a) Proposal for flux rectification with a tripled superlattice and a Raman modulation which spectroscopically resolves upward tunneling links at $\Delta$ from downward tunneling links at $2\Delta$ and drives each process but with opposite momentum transfer. (b) This scheme can also realize the quantum spin Hall effect by using a vector stark shift for the long-wavelength lattice and the same Raman modulation as (a).

in [4] is possible by spatially-resolving different links of the lattice and driving each with different momentum transfers). Intuitively, we can understand the triple-well superlattice as a ratchet mechanism – driving the links separated in energy by $\Delta$ with a Raman modulation allows a particle to move with a constant phase imprinted in one direction until it runs into the downward link which has a tunneling resonance at $2\Delta$. The links at this higher resonant frequency are spectroscopically resolved from the upward links of the lattice, so tunneling on these links can be driven with the opposite momentum transfer such at to imprint a uniform flux on all links of the lattice. Figure 3-24 shows both a spin-independent 3-24(a) as well as a spin-dependent 3-24(b) implementation of the superlattice geometry.

The proposal to use a tripled-superlattice to imprint uniform fluxes is advantageous when considering the problems presented earlier on adiabatic preparation of a single many-body groundstate and detection of topological states. First of all, in contrast to the linear potential gradient, the superlattice has a stable ground state that does not require working with a metastable excited state of the tilted lattice. One drawback of the Wannier-Stark ladder is that it is a metastable state which is prepared non-adiabatically by rapid projection of the initial condensate into the tilted lattice. As a result, the initial state of the effective Hamiltonian has a phase arising from the initial kick operator and, in a frame rotating at $\Delta$, the Raman modulation

does not break the symmetry between the degenerate ground states of the effective Hamiltonian. In contrast, the triple-period superlattice has a stable ground state, the lowest Bloch eigenstate of the long-period lattice, which can be adiabatically ramped into the eigenstates of the superlattice with Raman modulation. As a result, by varying the Raman detuning from the superlattice offset energies, we can selectively control a term which breaks the indistinguishability of the different sites in the unit cell, allowing more robust preparation of a specific ground state before re-establishing the symmetry.

The triple-superlattice potential also helps probing of the topological state by providing a sharp edge in a two-leg ladder geometry. Often, the topological nature of the many-body state can be characterized by the states which propagate along the surface of the state and its interface with a topologically distinct state. Unfortunately, optical lattice systems are often trapped in harmonic potentials which lack the sharp edges of a material system. One method to circumvent such shortcomings has been to realize systems in geometries of finite width where the edge is set by a detuning from resonance with adjacent states, effectively providing a sharp edge for states to propagate along [7, 148, 113, 149, 87]. In the same spirit, the tripled-superlattice with a two-tone drive allows controllable introduction of sharp edges to the system such that we can selectively choose to do experiments either in two-leg ladder geometries, in uniform flux geometries, or dynamically switching between the two.

As we have seen, the realization of the Harper-Hofstadter Hamiltonian in an optical lattice is an exciting development for realizing exotic states of matter with ultracold atoms in optical lattices. The realization of low entropy states of matter in such an effective Hamiltonian paves the way for studies of strongly interacting physics, spin-ful physics, and three-dimensional topological materials at the same time that it highlights the difficulties that remain to be solved and potential paths towards their solution.

# Chapter 4

# Extensions of the Scheme for Uniform Fluxes

In this chapter we show how the experimental realization of the uniform flux Harper-Hofstadter Hamiltonian provides a clear path forward towards realizing several other paradigmatic models of condensed matter physics in an optical lattice. Namely, we discuss how the inclusion of both a spin or pseudo-spin degree of freedom as well as laser-assisted tunneling in higher dimensions can lead to nontrivial extensions of the model realized in the previous chapter to other areas of physics.

Specifically, we begin by discussing three different theoretical flux configurations which highlight the unique physics this laser-assisted tunneling configuration allows us to realize. We start by examining the case where different pseudo-spins feel oppositely oriented fluxes and we show how this model is an ideal realization of a textbook case of spin-orbit coupling. Next, we examine the case where one spin state feels a synthetic magnetic flux that the other does not and show how inter-spin interactions can qualitatively change the resulting physics. Finally, we examine the case of two spin states which feel the same synthetic magnetic flux and show how this configuration may lead to a non-trivial bosonic quantum Hall state.

In addition to controlling the spin and flux configurations of the system, we also examine how the scheme for uniform fluxes can be extended to realize topologically nontrivial states in a three-dimensional lattice by realization of the Weyl Hamiltonian.

Finally, we give an outlook on a new way to realize such states utilizing a triple-period optical superlattice.

## 4.1 The Spin-Hall Effect and Spin-Orbit Coupling

Beginning with the case of oppositely oriented fluxes, we gain intuition for these systems by looking at the underlying mechanisms behind spin-orbit coupling and the spin-Hall effect in solid state systems. We are especially interested in understanding these effects at the level of the electromagnetic fields so that we can use the intuition from the previous section to translate this understanding into the language of the vector potentials and finally into the framework of Raman drive and laser-assisted tunneling in an optical lattice.

We being by considering an electron moving through a solid with some crystalline electric field $\mathbf{E}$ arising, for example, from some strain in the crystal. In the frame of the electron, this electric field appears as a magnetic field, $\mathbf{B}$, through the relativistic transformation of electric and magnetic fields, which interacts with the electron spin, $\sigma$, to produce an effective spin-dependent Zeeman splitting $\propto (\mathbf{p}\times\mathbf{E})\cdot\sigma$. If we simply let the crystalline electric field to point in the $z$-direction, the resulting magnetic field in the frame of the electron gives rise to the Rashba spin-orbit coupling, $(\sigma\times\mathbf{p})_z = \sigma_x p_y - \sigma_y p_x$, by cyclic permutation of the triple scalar product. Rashba spin orbit coupling is one form that the coupling between spin and momentum can possibly take. Notably, with this Hamiltonian the spin-orbit coupling has an intuitive interpretation as a translation in one direction, for example the $y$-direction, accompanied by a spin-rotation along the $x$-axis. This interpretation has motivated some efforts towards a multi-step Floquet realization of such a Rashba coupling term [25]. A different interaction, known as Dresselhaus coupling, is also important in the description of one-dimensional and non-centrosymmetric crystals. In general the spin-orbit coupling in a material is a combination of Rashba and Dresselhaus couplings.

From the viewpoint of ultracold atoms, the form of the interaction of the electron with the effective magnetic field provides a useful starting point for generating spin-

orbit coupling of bosonic and fermionic atoms. Examining the form of the coupling in the Rashba term we see that this term has a simple interpretation in an ultracold atomic setting as a physical process which transfers some momentum to an atom and subsequently rotates the atomic spin. This interpretation leads to a natural understanding of the pioneering results from the NIST group realizing a spin-orbit coupled BEC and the miscible to immiscible transition at low Raman coupling strengths [104]. In fermionic systems, the same spin-orbit coupling mechanism implemented in BEC's was used to map out the spin-orbit coupled bands [160, 33]. Comparing the form of the spin orbit coupling first achieved in these experiments we see that the spin-orbit coupling is a combination of Rashba and Dresselhaus that results in a purely one-dimensional coupling. This is unsurprising given that in the experimental implementation there is only momentum transfer associated with a spin flip in one direction. More recently, since the publication of the work described in this section, this one-dimensional spin-orbit coupling has been extended to two-dimensional spin-orbit coupling in both BEC's and degenerate Fermi gases [166, 73]. In addition, this type of spin-orbit coupling has been used with Raman driving of a double-well potential, which serves as an external pseudo-spin degree of freedom, to observe supersolidity in the spin-orbit coupled BEC [101, 100].

In the above argument, we arbitrarily assigned the $z$-axis for the crystalline field direction. What happens if instead the electric field is oriented in the plane of our two-dimensional system? Again, the coupling of the motion of the electron to the electric field produces a magnetic field in the frame moving with the electron with the resulting field taking the form: $(E_y p_x - E_x p_y)\sigma_z$. For the case of a radially increasing field like that in a strained material or a uniformly charged cylinder this field takes the form $(xp_y - yp_x)\sigma_z$, or equivalently to $\sigma \cdot \mathbf{L}$, where $\mathbf{L}$ is the angular momentum of the electron [14].

This spin-coupling term is identical to the $\mathbf{A}\cdot\mathbf{p}$ term for the Hamiltonian describing an electron in a magnetic field. Using the symmetric gauge for the vector potential $\mathbf{A} = \sigma_z B(-y\hat{e}_x + x\hat{e}_y)/2$, one obtains a term in the Hamiltonian proportional to $\sigma_z B(xp_y - yp_x)$. Therefore, this form of spin-orbit coupling is equivalent to a spin-

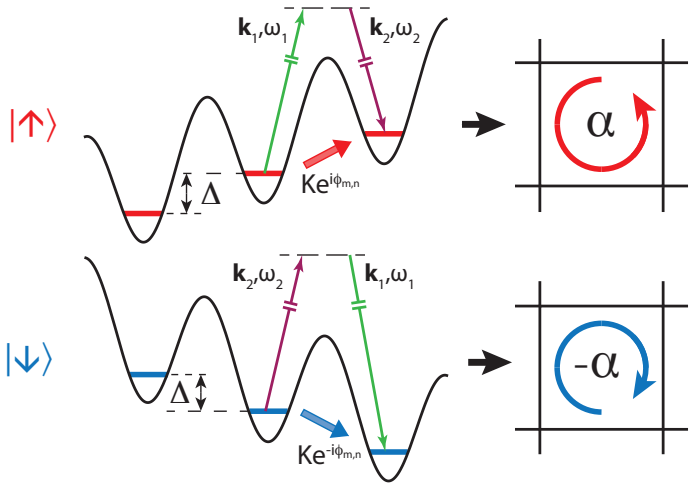


Figure 4-1: Creation of a spin-dependent, uniform synthetic magnetic field. Using two internal hyperfine states of an atom with equal but opposite magnetic moments the application of a uniform magnetic field gradient and Raman drive results in oppositely oriented synthetic magnetic fields and is an idealized realization of the quantum spin Hall Hamiltonian.

dependent magnetic field which exerts opposite Lorentz forces on spin-up and spin-down atoms. The $\mathbf{A}^2$ term constitutes a parabolic spin-independent potential which is irrelevant for the spin physics discussed here. In the condensed matter context, it has been shown that this spin-dependent magnetic field leads to the spin Hall effect which creates a transverse spin current and no charge or mass currents [80, 14].

In the context of generating spin-orbit coupling for ultracold atoms, the spin-dependent magnetic field, $\sigma_z B(xp_y - yp_x)$, has a clear interpretation as a spin-dependent synthetic magnetic field. In the framework of the Harper-Hofstadter Hamiltonian, creating a spin-dependent magnetic field is as simple as either creating a spin-dependent tilt or a spin-dependent momentum transfer from the Raman drive. Shown in figure 4-1, a system that uses a single, spin-independent Raman drive can generate a spin-dependent magnetic field if the tilt is made to be spin dependent. This can be achieved using two atomic hyperfine ground states with the same absolute value of the magnetic moment but opposite sign in combination with either a magnetic field gradient or a vector AC stark shift at an atomic tune-out wavelength. This setup was proposed in both [83, 2] and seen experimentally as oppositely-handed cyclotron motion of a wavepacket on isolated plaquettes in [2]. This experimental setup

imprints a spin-dependent spatially-varying phase on the atoms in the lattice:

$$\phi_{m,n;\sigma} = (mk_x a + nk_y a)\hat{\sigma}_z. \tag{4.1}$$

which is equivalent to the following spin-dependent vector potential acting on a charged particle:

$$\mathbf{A} = \frac{\hbar}{a}\Big[k_x x + k_y y\Big]\hat{\sigma}_z. \tag{4.2}$$

This vector potential is identical, up to a gauge transformation, to the spin-dependent vector potential derived above for an electron in a radially-strained crystal or in a uniformly charged cylinder. This model is known to exhibit a spin Hall effect with finite spin current but vanishing mass currents [80, 14].

In an ultracold atomic realization of this form of spin-orbit coupling, the total magnetization is fixed and no spin-changing collisions occur so the spin index $\sigma_z$ is conserved. In this context, we can intuitively think of this form of spin-orbit coupling as a simultaneous realization of two oppositely oriented quantum Hall systems. As a result, we can gain intuition for the origins of the finite spin current with vanishing mass current by looking at the boundary between the topologically-nontrivial system with a spin-dependent magnetic field and a topologically trivial state. At the interface there exist edge-modes associated with the closing of the topological gap. These modes are chiral with the spin state locked to the direction of propagation. This spin-momentum locking in a single spin component has been directly observed in later experiments with uniform fluxes in a synthetic dimension consisting of a manifold of internal hyperfine states [27, 148, 113] and orbital degrees of freedom in atomic clocks [156, 87], in addition to real-space ladder systems [7, 149]. Our proposal, summarized in figure 4-1, with two spin states realizing a spin-dependent synthetic magnetic field also leads to such chiral edge states as mentioned above which appear simultaneously in each spin component. This scheme implements spin-orbit coupling both in two and three dimensions and with bosons and fermions. For fermions in two dimensions, it realizes the quantized spin Hall effect consisting of two opposite quantum Hall phases. It is protected by a $\mathbb{Z}$ topological index due to the fact that $\sigma_z$ is conserved [81, 80].

We can understand this intuitively by considering that since the magnetic field is oppositely oriented for each spin the edge states associated with each propagate in reverse directions. As a result, we see that the vanishing mass current is associated with the mutual cancellation of both left- and right-moving chiral currents associated with each spin and the resulting spin current is the constructive sum of the two independent chiral currents. Because this spin-orbit coupling does not mix spins like Rashba and Dresselhaus coupling do, spin remains a good quantum number and the total spin current is then the sum of the left- and right-movers. This underlies the statement that the resulting physics consists of two opposite quantum Hall phases which do not mix at the single particle level.

Experimentally, realizing this form of spin-orbit coupling has several advantages. First of all, the tools we used to implement these strong, uniform fluxes are spin-independent, far-detuned lattices and magnetic field gradients so heating due to spontaneous emission of near-resonant lasers is eliminated. Secondly, low entropy states of bosons have been demonstrated in the single-component version of such an experiment, see [82] in the appendix and above in the previous chapter. So a reasonable extension of this work to probe a spinful system might be to implement this experimental setup with a degenerate Fermi gas filling the lowest band as in [79] or via local probing of the edge structure with bosons as done in [7, 148, 113, 149]. And lastly, verification of the opposite fluxes has been established via cyclotron motion of wave packets in isolated plaquettes [2].

At the single-particle level, an intriguing possibility is to couple the two states. This coupling introduces a $\sigma_x$ or $\sigma_y$ term which introduces mixing between the spin states. If this coupling is not done in a time-reversal invariant way Kramers degeneracy is lifted and the spin-polarized edge states are not protected against backscattering. However, if this coupling preserves time-reversal symmetry and, since $\sigma_z$ is no longer conserved, the Fermi energy lies in the bulk band gap, the system should become a topological insulator with the $\mathbb{Z}_2$ classification [69, 81]. This provides a path towards studying topological insulators with cold atoms in both the interacting and non-interacting limits.

## 4.2 Imbalanced Fluxes and Superfluid Shielding

As we have seen from the previous section, this dual quantum Hall system of spins in a spin-dependent synthetic magnetic field is an attractive starting point for breaking different symmetries and adding interactions. One example of this which particularly highlights the power of ultracold atomic systems is the configuration where one spin state feels no synthetic magnetic field when the other feels a strong synthetic magnetic field. This is easily accomplished by using one spin state which experiences zero tilt and thus no synthetic magnetic field while the second spin state is strongly tilted and is thus resonant with a Raman drive.

If the synthetic magnetic field strength is chosen such that the ground state of the second spin component is a vortex lattice, for example $\alpha = 1/4$, an interesting question arises: how does the spin component which does not experience a synthetic magnetic field interact with this density modulation? If we add weak repulsive interactions interactions to the system, mean-field interactions favor a uniform total density ground state so one might expect different phases based on the hierarchy of different spin-spin interactions. Similar to a two-component BEC, the system should exhibit a miscible – immisible transition, and on the miscible side the density of the untilted component should "fill in" the density depletions of the vortex lattice in the component that experiences the synthetic magnetic field. This additional density modulation of the untilted component due to the presence of a vortex lattice in a second component should be observable in a time-of-flight measurement as an additional translation symmetry – that of the vortex lattice – spontaneously appearing in the untilted component.

A similar system – without the second spin component experiencing a synthetic magnetic field – was implemented experimentally in our lab [24], see appendix. In this experiment, one component is a superfluid BEC in a normal three-dimensional lattice. The second component is strongly accelerated by a magnetic field gradient, but no synthetic magnetic field is imprinted in the sample. In this interacting, two-component system we observe coherence lifetimes of Bloch oscillations of the tilted

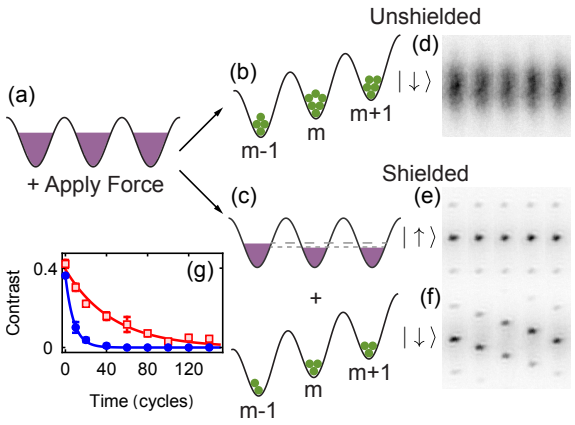


Figure 4-2: Enhancement of the Bloch oscillation lifetime in a two-component BEC in an optical lattice. Before applying a tilt, the atoms are in a superfluid, which is approximately described by a coherent state on each site. The chemical potential is constant across the cloud. (b) In the limit of a strong tilt ($\Delta \gg 4t$), the wavefunction at each lattice site is projected onto the number basis, leading to fluctuations in the number of atoms and chemical potential from site to site. (c) If the gas has two components, one which is localized by the tilt, and one which remains superfluid, the itinerant component can compensate for fluctuations in the localized component. (d-f) Momentum distribution over the course of a single Bloch oscillation after ten cycles. (d) Without superfluid shielding, the diffuse cloud indicates decoherence of the condensate. (e) The itinerant component feels no force and does not Bloch oscillate. (f) For the shielded component, the Bloch oscillation contrast is high. (g) Exponential decay of the Bloch oscillation contrast for a one-component (blue dots) and two component (red squares) gas, for a transverse lattice depth of 11 $E_r$ and $\sim 8 \times 10^3$ atoms.

component longer than the shot-noise limit given by projection noise of the superfluid BEC onto the localized basis of states that form the Wannier-Stark ladder. A schematic representation of the effect along with data showing the visible increase in the Bloch oscillation lifetime of the two-component system is shown in figure 4-2. Briefly, the physical mechanism behind this effect we call "superfluid shielding" is that an excess of density of one component – here the tilted component – on one site of the lattice is correlated with a lower density of the second component on that lattice site due to inter-spin repulsive interactions. In essence, the system tries to minimize density fluctuations of the total particle number density, which produces the correlation between density maxima of one component with the density minima of a second component [24].

This result highlights the microscopic mechanism through which inter-spin interactions can cause the vortex cores of the vortex lattice of one spin to attract the density of a second spin which does not feel a synthetic magnetic field. An analogous effect exists for unpaired electrons in vortex cores and topological defects in superconductors where unpaired states can "fill in" the core of the vortex where the superfluid density necessarily drops to zero. These states are known as Andreev bound states [26], and have been observed in many vortex lattices [70]. Pulling from the intuition derived from both the physics of Andreev bound states as well as the initial results on interacting two-component mixtures in a tilted lattice [24] where the repulsive inter-spin interaction energy causes the density of one spin component to fill in the density depletions of a second spin component, we predict that adding a vortex lattice to the tilted component in figure 4-2 will induce a density-modulation in the untilted component which does not experience a synthetic magnetic field.

## 4.3 A Bosonic Quantum Hall Effect

In the previous section we discussed a spin-dependent flux configuration unique to an ultracold atomic system. Here we discuss another unique feature the ability to realize these states with not just fermionic particles but also bosonic particles. Motivated

by the proposal of ref. [141], we consider a two-component bosonic system with a spin-*independent* synthetic magnetic field. If the two systems do not interact, we can understand them as independent quantum Hall systems which independently have chiral edge states which propagate in the same directions. However, an interesting situation arises when we add inter-spin interactions to the system. If each component individually realizes a $\nu = 1$ filling fraction – defined by an average density of one particle per state in the lowest band – then when we add some short-ranged, repulsive interactions which maintain miscibility the resulting system is a promising candidate for realizing a *bosonic* integer quantum Hall effect. Although [141] does not provide a specific hierarchy of interaction energy scales between intra-spin interactions, $U_{i,i}$, and inter-spin interactions, $U_{i,j}$ (for spin components labeled by the index $i \in \{1, 2\}$) necessary for realization of these phases, the hierarchy of interactions in the hyperfine ground states of $^{87}$Rb, $U_{1,1} \approx U_{2,2} \leq U_{1,2}$, are of the right hierarchy, range, and magnitude for consideration of such a ground state in the two-component system with each realizing $\nu = 1$ phases. A specific implementation might utilize the $|F, m_F\rangle = |1, -1\rangle$ and $|2, -2\rangle$ hyperfine states in a spin independent tilt generated by AC Stark shift. To realize a $\nu = 1$ phase, one might choose a flux of $\alpha = 1/3$ and load an average density of $1/3$ atom per site, per spin state, into the lowest band of the resulting Hofstadter spectrum.

In contrast to the fermionic case, understood via its connection to Landau levels which are understood in the non-interacting limit, the resulting interacting bosonic system is a realization of a symmetry-protected topological (SPT) phase – a generalization of topological insulators to interacting systems that do not necessarily have a non-interacting fermion counterpart. In the condensed ground state, the system exhibits a Hall conductance of the mass of $+2$ and a spin Hall conductance of $-2$ [141], which distinguishes this insulting state from a topologically trivial Mott insulating phase.

An interesting problem arises when we try to construct a wavefunction for this integer quantum Hall state of bosons: creating a properly symmetric state akin to a Laughlin wavefunction is nontrivial, and we must either take absolute values or

squares of the Jastrow factors which encode the relative wavefunction of any two-particles in the system in order to satisfy particle exchange symmetry. Physically, we can examine the states offered in [141] as competing ground state wavefunctions by the effective energy function given by the analogy to a two-dimensional plasma first discussed in chapter 2, equation 1.49. This analogy offers a few simple interpretations of what this state physically looks like. For example, one trial wavefunction takes the form:

$$\Psi = P_{LLL} \prod_{i<j} (z_{i,1} - z_{j,1})^2 \prod_{i<j} (z_{i,2} - z_{j,2})^2 \prod_{i,j} (z_{i,1} - z_{j,2})\, e^{-\sum_{i,\sigma} |z_{i,\sigma}|^2/2}, \tag{4.3}$$

where $z_{i,\sigma}$ are the dimensionless complex coordinates of the $i$-th particle of the spin-component, $\sigma$. By inspection of the wavefunction and by constructing an analogy with a classical, two-dimensional electron gas via the plasma energy: $|\Psi|^2 = e^{-\beta\Phi} = e^{-\frac{2}{m}\Phi}$ (where $m$ is the "charge" of the vortex), we see that this wavefunction corresponds to a system where the individual components pair into doubly-charged composite particles and the relative motion of the two components corresponds to the pairing of a singly-charged vortex of one component with a particle of the second, and vice-versa. This is one of several possible ground states for this system of two spins which experience the same synthetic magnetic field [141], illustrating the richness of the physics which results when we extend the current state-of-the-art realization of the Harper-Hofstadter model to include interacting spins.

To summarize, we have discussed how a simple extension of the experimental setup realized in [118] and first implemented in [2] yields a rich variety of new physics to be observed with ultracold atoms. By choosing the synthetic magnetic field to change direction with the spin state, this system provides an exact realization of a paradigmatic model of spin-orbit coupling arising from radial strain in a two-dimensional electron gas. This system is time-reversal symmetric and therefore exhibits a quantum spin Hall effect consisting of dual quantum Hall phases. Time-reversal invariant coupling of these spins yields a straightforward realization of an ultracold atom topological insulator for fermionic atomic species. We have also discussed additional ways

in which different choices of spins in $^{87}$Rb can realize mixtures where one component feels no synthetic magnetic field and may act similarly to Andeev states in superconduting vortex cores, or choosing two spins to have the same synthetic magnetic field may produce a simple realization of a bosonic quantum Hall effect and a symmetry protected topological state.

## 4.4 The Weyl Hamiltonian

So far, the topological physics we have discussed has been heavily influenced by the paradigmatic system of two-dimensional electronic systems in a magnetic field. However, in reality, the world has more spatial dimensions and we can realize the Harper-Hofstadter Hamiltonian in both two- and three-dimensional lattices. It is worthwhile to ask then, what kind of topological states can exist in three-dimensions? One example comes to us from high energy physics where, in relativistic quantum field theory, there are three types of fermions: Dirac, Majorana, and Weyl fermions [164]. Theoretically, Weyl fermions constitute "half" a Dirac fermion in the sense that two Weyl fermions coupled by a mass term constitute the Dirac spinor. As a result, Weyl fermions are massless particles in three-dimensional space, which, until recently, had not been observed. It was conjectured that neutrinos could be Weyl fermions before the discovery of neutrino oscillations, and corresponding non-vanishing neutrino mass, ruled out such a possibility.

Recently, the possibility of realizing Weyl fermions as collective excitations in condensed matter systems [157, 23] or as engineered dispersions in photonic systems [107] has received much attention. These systems realize analog Weyl fermions as band-touching points in three-dimensional space with linear dispersion such that the effective low-energy Hamiltonian can be expressed in the form: $H = \hbar \mathbf{v} \cdot \mathbf{k}$. Such a system acts like a magnetic monopole in momentum space where a sphere enclosing the band touching point counts the effective magnetic charge of the magnetic monopole. Recently there has been much activity towards realizing Weyl semimetals – gapless topological states of matter with bulk low-energy electrons behaving as

Weyl fermions, with Fermi arc topological surface states [157, 153, 80] – culminating with the recent observation of both in TaAs and NiAs [170, 169, 171, 111, 110] and in three-dimensional photonic crystals [108].

In the work we describe in this chapter, we propose a novel realization of Weyl points in a three-dimensional optical lattice with ultracold atoms. Importantly, this proposal builds on the success of the previous chapter in realizing the ground state of the two-dimensional $\alpha = 1/2$ Harper-Hofstadter Hamiltonian in both two- and three-dimensional optical lattice. It uses the same tools of far-detuned lattices, magnetic field gradients, and far-detuned Raman drive, so in principle, it is a useful scheme for realizing strongly interacting, many-body states in the topological state defined by the single particle spectrum.

We begin by understanding how such a state can emerge from the previous results on the Harper-Hofstadter Hamiltonian in three-dimensions by considering the energy spectrum of the 1/2-flux model in a three-dimensional lattice composed of a tunnel-coupled array of two-dimensional Harper-Hofstadter systems. The Hamiltonian and resulting energy spectrum are given by:

$$H_{3D} = H_{\mathrm{HH}} - t_z \sum_i (\hat{a}_{i+1}^\dagger \hat{a}_i + \hat{a}_i^\dagger \hat{a}_{i+1}) \tag{4.4}$$

$$E_{3D} = \pm 2\sqrt{K^2 \sin^2(k_x a) + t^2 \cos^2(k_y a)} - 2\cos(k_z a), \tag{4.5}$$

where the subscript $H_{HH}$ is the two-dimensional Harper-Hofstadter Hamiltonian with tunneling strengths in $x$- and $y$-directions, $K$ and $t$, respectively, and $t_z$ is the tunneling strength in the $z$-direction. When plotted, the energy spectrum of this model consists of nodal lines along the axes given by coordinates: $\mathbf{k} = (k_x, k_y, k_z) = (0, \pm\frac{\pi}{2}, k_z)$. Despite the fact that the model describes an electron in a strong magnetic field (which normally breaks time-reversal symmetry), the 1/2-flux model is, in fact, protected by time-reversal symmetry due to the equivalence of the tunneling phase imprinted by a $\pi$-flux and a $-\pi$-flux both realizing a staggered, real tunneling phase of $(-1)^i K$. In addition, the system is also inversion symmetric about the center of the bond in the $x$-direction. As a result of these two symmetries, the nodal line in the spectrum

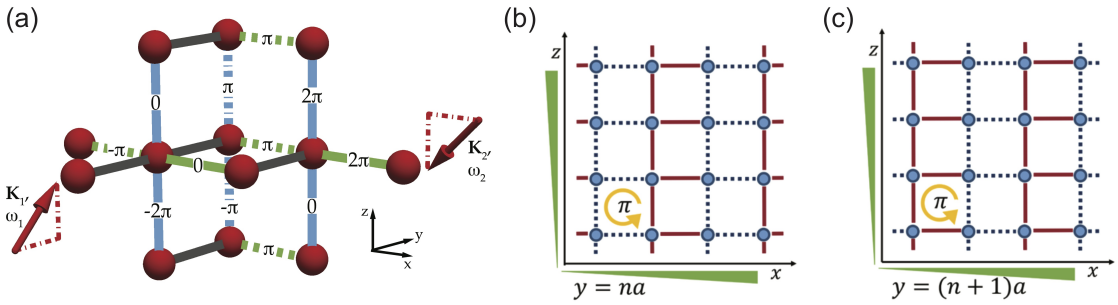


Figure 4-3: Configuration of tunneling phases for realization of Weyl points. (a) Breaking inversion symmetry is accomplished by stacking layers of 1/2-flux models with tunneling phases on the $z$-bonds which alternate sign with the same symmetry as the tunneling phases in the $x-y$ plane. To accomplish this task, an gradient is applied to the $x$- and $z$-directions of the lattice which produces an equal energy offset per site in both directions. The Raman drive is introduced at angles shown by the large, red arrows and imparts a momentum transfer of $\delta\mathbf{k} = \pi(1,1,2)$ driving laser-assisted tunneling processes. We can understand inversion symmetry breaking in an alternative picture looking at the stacking in the $x-z$ plane (b),(c) and noticing the alternatively shifted patterns connected by normal tunneling phases along the $y$-direction.

in equation 4.5 is protected by symmetry. In order to break this degeneracy and establish a topological state with Weyl points, we must either break time-reversal symmetry or break inversion symmetry.

This proposal relies on breaking inversion symmetry of the tunneling in the $z$-direction by driving a laser-assisted tunneling process on these bonds using the same Raman drive field used to drive the laser-assisted tunneling transitions in the $x-y$ plane. To accomplish this, a gradient is now applied to the $\hat{e}_x + \hat{e}_z$ direction, producing an uniform energy offset between adjacent sites along both the $x$- and $z$-directions, assuming equal lattice constants in these two lattice axes for simplicity. Next, resonant tunneling is re-established along these directions with a Raman drive which produces a momentum transfer in all three directions according to: $\delta\mathbf{k} = \pi(1,1,2)$. Figure 4-3 shows the angle of the Raman drive which produces laser-assisted tunneling simultaneously on both $x$- and $z$-bonds. Assuming that the underlying static lattice has the same lattice constant in all three directions, the corresponding tunneling phases induced by the light field are indicated on each bond. An alternate way to view this breaking of inversion symmetry can be seen in figure 4-3(b), (c)

looking at alternating planes in the $x-z$ plane. Comparing 4-3(b) to 4-3(c), we see that both layers have the same pattern of tunneling links but shifted by one lattice constant, $a$, in the $x$-direction. Each plane is connected in the $y$-direction with normal tunneling which is both time-reversal and inversion symmetric.

More formally, the tilt and laser configuration in figure 4-3 produce the following Hamiltonian:

$$\begin{aligned} H_{\text{Weyl}} &= \sum_{m,n,l} \Big( K_x e^{-i\theta_{m,n,l}} \hat{a}^\dagger_{m+1,n,l} \hat{a}_{m,n,l} + t\, \hat{a}^\dagger_{m,n+1,l} \hat{a}_{m,n,l} \dots \\ &\quad \dots + K_z e^{-i\theta_{m,n,l}} \hat{a}^\dagger_{m,n,l+1} \hat{a}_{m,n,l} + \text{H.c.} \Big), \end{aligned} \tag{4.6}$$

with momentum transfer, $\phi_{m,n,l} = \pi(m+n+2l)$. Examining the translation symmetry dictated by this choice of gauge, we see that the unit cell has two atoms per site and has translation symmetry vectors of $\mathbf{R} = \{a\hat{e}_x + a\hat{e}_y, a\hat{e}_x - a\hat{e}_y, a\hat{e}_z\}$. We can therefore diagonalize the Hamiltonian in momentum space and find the following dispersion relation:

$$E_\pm = \pm\sqrt{K_x^2 \sin^2(k_x a) + t^2 \cos^2(k_y a) + K_z^2 \cos^2(k_z a)} \tag{4.7}$$

Taking a cut through the spectrum along the $k_x = 0$ plane, we see the dispersion shown in figure 4-4(b) with four locations in which the upper and lower bands touch with a linear dispersion at $(k_x, k_y, k_z) = (0, \pm\frac{\pi}{2}, \pm\frac{\pi}{2})$. Plotting similar cuts through the first magnetic Brillouin zone for other values of $k_x$, one finds that away from the $k_x = 0$ plane the bands are isolated and do not touch at any other locations within the first magnetic Brillouin zone. Expanding the dispersion in equation 4.7 around the four locations the upper and lower band touch, $(0, \pm\frac{\pi}{2}, \pm\frac{\pi}{2})$, we see the dispersion is linear at zero energy in all three directions with a slope set by the tunneling strengths. If we expand the dispersion to first order in the deviation of the momentum from the Weyl point momentum, $\mathbf{q} = \mathbf{k} = \mathbf{k}_W$, we can define an effective Hamiltonian:

$$H = \sum_{i,j=1}^{3} \hbar k_i v_{ij} \sigma_j \tag{4.8}$$

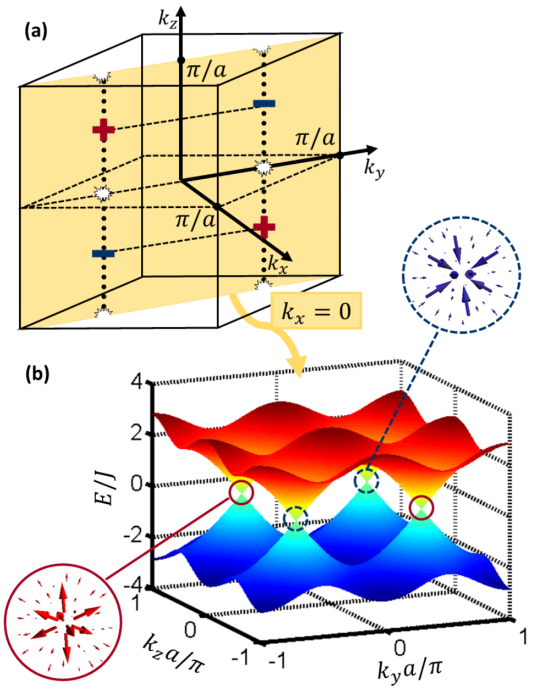


Figure 4-4: Energy spectrum of the Weyl Hamiltonian, shown for a cut through the three-dimensional Brillouin zone on the $k_x = 0$ plane (a,b). Note the four band-touching points with linear dispersion between the upper and lower bands and the synthetic magnetic flux associated with each shown in the circled insets (a). The topological charge of each Weyl point is indicated by a plus of minus in (a). The addition of a $\sigma_z$ symmetry-breaking term moves the Weyl points along the dashed lines, without opening a gap, until Weyl points of opposite chirality annihilate.

with the velocities, $v_{12} = -2K_x a$, $v_{21} = -2ta$, $v_{33} = -2K_z a$, and zero otherwise. This Hamiltonian is linear in all three dimensions and as such, for a Fermi energy at $E = 0$, is exactly analogous to a massless Weyl fermion in three-dimensional space.

One hallmark of the Weyl point is that these points carry topological charge and only appear in oppositely charged pairs – if we sum all the topological charges in the Brillouin zone the result should add up to zero. We can calculate the topological charge for each point by calculating the Berry connection at each point in the Brillouin zone, $\mathbf{A}(\mathbf{k}) = i\langle u(\mathbf{k})|\nabla_{\mathbf{k}}|u(\mathbf{k})\rangle$, and then the Berry curvature, $\mathbf{B} = \nabla_{\mathbf{k}} \times \mathbf{A}(\mathbf{k})$. The Berry curvature for a positive and negative charge within the first Brillouin zone is shown in figure 4-4(a), confirming that these linear band-touching points do, in fact, carry topological charge. We also see from figure 4-4(a) that these four points arise from two pairs, each of which carry opposite topological charges.

One qualitatively different feature of Weyl points compared to Dirac points in a two-dimensional system – or Dirac points in a three-dimensional system composed of two Weyl points which overlap – is their robustness to external perturbations. Any small perturbation of the form $\epsilon\sigma_i$, where $i$ runs over all three dimensions and $\epsilon$ is some arbitrarily small parameter, will not destroy the Weyl point by opening a gap in the spectrum, but instead only cause a small deviation in the location of the Weyl point in momentum space. Weyl points can only be destroyed – therefore opening a gap and destroying the topological charges associated with each Weyl point – when two oppositely charged points are brought together and annihilated. To demonstrate this principle, we add an $A - B$ sublattice offset, resulting in a $\sigma_z$ perturbation with amplitude given by the offset energy, $\epsilon$. Experimentally, this can be implemented by adding a two-dimensional superlattice to the uniform lattice. Increasing the amplitude of the superlattice increases the symmetry breaking term, $\epsilon$, and subsequently moves the weyl points along the dotted line in the $z$-direction shown in figure 4-4(a), confirming the robustness of the spectrum to perturbative symmetry breaking terms.

As the amplitude of the symmetry breaking term is increased, and the Weyl points are moved through the first Brillouin zone, at some critical value of the site-offset,

$\epsilon$, Weyl points of opposite chirality meet and annihilate. At this point the spectrum becomes gapped and Weyl points disappear. In the case of the $A - B$ sublattice offset, this happens at a critical value of $\epsilon = \pm 2K_z$. In figure 4-4(a), this critical value happens at the locations indicated by white stars. Above this critical value, the system makes a transition to a topologically trivial band.

Additional checks can be performed on this system to probe the topology of the Weyl points, such as verify the presence of Fermi arcs on the surface of a slab as seen in [43]. In total, the presence of linear band-crossing points in three-dimensional space, the existence of topological charge associated with each such that they act as magnetic monopoles in momentum space, their robustness to perturbation, and finally the presence of Fermi arcs on the surface presents a compelling case for the existence of Weyl points in this system created with laser-assisted tunneling in an optical lattice. Given that this experimental setup is based on, and represents a simple extension of, the techniques used to implement the Harper-Hofstadter Hamiltonian with far-detuned lattices and magnetic field gradients, its experimental implementation is technically within reach and represents an exciting direction for ultracold atom research. It is worthwhile to highlight that, without phase engineered hopping methods, the creation of Weyl points is more demanding, and its creation is possible only for a reduced number of space groups and points of symmetry in the Brillouin zone [114]. However, with the ability to phase-engineer the tunneling links, its realization is possible in a simple cubic lattice.

### 4.4.1 The Chiral Anomaly

As an outlook, we point out that this system is an ideal platform for realizing the Adler-Bell-Jackiw chiral anomaly in a cold atom system [122, 134]. In short, in the condensed matter context we have seen that Weyl points show up only in pairs, with a positively charged Weyl point is always accompanying a negatively charged one. The chiral anomaly refers to the apparent non-conservation of the number of chiral charges in the system, i.e. the number of fermions associated with a Weyl point that has either a positive or negative topological charge is not conserved. Ref. [134] aptly

makes the analogy between the chiral charge in a Weyl semimetal and the valley degree of freedom in graphene. The non-conservation of chiral charge is seen clearly under simultaneous, parallel application of electric and magnetic fields which results in a pumping of charge from one Weyl node to another and generates a change in the chiral charge [122]:

$$\dot{Q}_5 = \frac{e^2}{h^2}\mathbf{E}\cdot\mathbf{B}. \tag{4.9}$$

We can develop an intuitive understanding of the chiral anomaly by contrasting the material with Weyl points to a topologically trivial three-dimensional semimetal. In a trivial semimetal, when we apply a magnetic field the system forms a series of Landau levels in the directions transverse to the field direction and remains free in the direction parallel to the field. If we then also apply an electric field, current flows normally in this direction. In a Weyl semimetal when we apply a magnetic field, the system again forms the Landau level structure of a relativistic particle in the transverse directions to the applied field direction. However, when we apply an electric field in the longitudinal direction, current now flows away from one Weyl point, down into the bulk of the band either above or below the Fermi surface. Because the band is continuously connected to both Weyl points at high energy, these charges can continue to flow directly to the oppositely handed Weyl point where they annihilate, thus breaking the conservation law for chiral charges. This process is depicted very clearly in figure six of ref. [122]. In a longitudinal transport measurement, the current is flowing between Weyl nodes is flowing opposite to the direction of the applied field, so this appears in a experiment as a negative magnetoresistance observed in recent experiments [74, 168].

This effect is particularly straightforward to implement in the proposed lattice setup with ultracold atoms and laser-assisted tunneling. In this system, an effective magnetic field oriented in the $z$-direction is introduced by tuning the flux enclosed in the $x-y$ plane away from $\alpha = 1/2$ as discussed in the context of the two-dimensional Harper-Hofstadter system and pictured in figure 3-3 of chapter 3. Adding an additional acceleration, analogous to an electric field, can be achieved along any direction

by rotating the direction of the applied magnetic field gradient, effectively tuning the electric field direction relative to the magnetic field axis by changing the detuning from Raman resonance. Recent work has highlighted that this longitudinal current should also exhibit a fractal, Hofstadter-like spectrum [134], and the ability to imprint arbitrarily large tunneling phases in the system highlights the power of cold atomic systems to achieve such strong-field regimes. In conclusion, exploring transport dynamics in the effective Weyl Hamiltonian created with laser-assisted tunneling is an exact realization of the chiral anomaly in an ultracold atom system and represents an exciting direction for future experiments with Weyl semimetals in optical lattices.

# Chapter 5

# The Spin-1 Heisenberg Hamiltonian

If we take a two-component BEC in an optical lattice and drive the phase transition to the Mott insulating phase, what is the configuration of spins in the ground state? This is an important question in many different contexts from electrons in condensed matter physics, atoms and molecules in atomic physics, and ions and other spin-qubit systems in quantum information science platforms. This important question is approached in this chapter in the context of $^{87}$Rb atoms in optical lattices.

We first approached this question in the introduction where the exponential scaling of the basis size with particle number was highlighted with a particular emphasis on the intractability of the general problem on a classical computer. However, as we will find, mean field theory provides a good qualitative, if not quantitative, understanding of the quantum system from which to start. In this chapter we provide a precise mapping of the dynamics of different spin configurations to an effective spin model, and show how this spin model is implemented with ultracold atoms in optical lattices. Here we show how a gapped ground state of such a spin model can be robustly prepared and used to create, detect, and characterize an extremely low entropy state. This highly gapped, low entropy spin state thus represents an excellent starting point for adiabatic ramping to a magnetic state of matter across a quantum phase transition and for potential realization of a long-range ordered spin system at picokelvin temperature scales.

## 5.1 A Mott Insulator with Spin

In chapter 2.3.1 we discussed the nature of the superfluid to Mott insulating transition for a single spin component in an optical lattice. In principle, we can add more spin components to the system such that the the single-band Hamiltonian gains a spin index:

$$H = -\sum_{ij,\sigma} \left( t_\sigma a^\dagger_{i,\sigma} a_{j,\sigma} \; + \; \text{H.c.} \right) + \frac{1}{2} \sum_{i,\sigma,\sigma'} U_{ij,\sigma} a^\dagger_{i,\sigma} a^\dagger_{j,\sigma'} a_{j,\sigma'} a_{i,\sigma}. \tag{5.1}$$

Examining the Bose-Hubbard Hamiltonian with the spin degree of freedom, we see that the inclusion of a new index creates new energy scales associated with spin-dependent tunneling: $t_\uparrow$ and $t_\downarrow$, and spin-dependent interaction energies: $U_{\uparrow\uparrow}$, $U_{\uparrow\downarrow}$, and $U_{\downarrow\downarrow}$. With these new energy scales it is not immediately obvious that the transition to the Mott state for both spin components is preserved; however, in a far detuned lattice the tunneling is spin-independent and in $^{87}$Rb the interaction energy scales are all similar such that both components enter the Mott phase. The interesting question is then: what is the ground state arrangement of spins in the Mott insulating state?

The exact solution to the general problem is intractable due to the exponential complexity of the quantum system; however, in three-dimensions and in certain regimes of lower-dimensional systems we can write down nice mean-field solutions in the limit where either the kinetic energy dominates over the interaction energy, $t \gg U$, or in what we will call the the atomic limit, where the interaction energy dominates over the kinetic energy, $t \ll U$. Since we wish to analyze the configuration of spins in the Mott insulating state, we begin by examining the action of the spin degree of freedom in the atomic limit. This limit is visualized schematically in figure 5-1(a) as different manifolds of local site occupation numbers with a ground state that is uniformly occupied and gapped by some large energy scale to manifolds of excited states that contain one excitation, two excitations, and so on and so forth. Restricting ourselves the the inter-spin interaction hierarchy that exists in $^{87}$Rb, there is only a small difference between the three different interaction energy scales in a

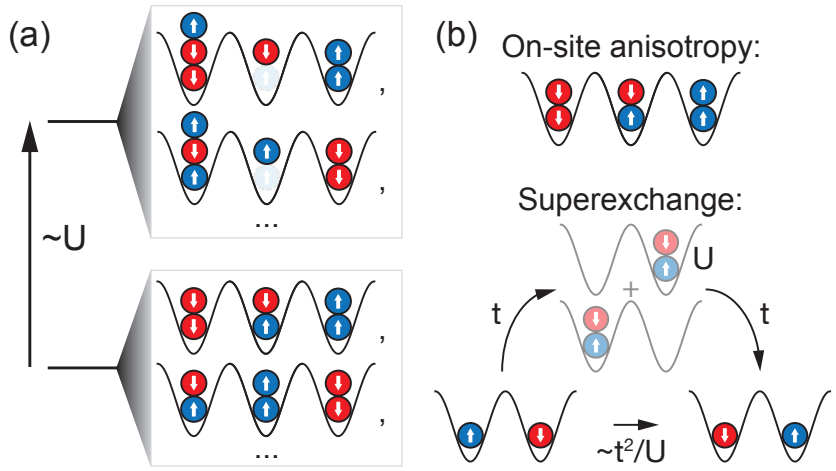


Figure 5-1: Nearly degenerate spin configurations within the Mott insulating state. (a) Manifolds of different occupation number states of both $|\uparrow\rangle$ and $|\downarrow\rangle$ in the Mott insulating phase are gapped by some large energy scale, $U$. Within each manifold, the energy of each different spin configuration is nearly degenerate. (b) Leading order terms which are responsible from breaking the macroscopic spin degeneracy of the ground state manifold. The energy of multiple particles on a lattice site can differ because the scattering lengths, $a_{\downarrow\downarrow}$, $a_{\uparrow\downarrow}$, and $a_{\uparrow\uparrow}$ are not necessarily equivalent. This effect also leads to superexchange terms which depend on the initial and final spin configurations.

spin-independent trapping potential since,

$$U_{\sigma,\sigma'} = \frac{4\pi\hbar^2 a_{\sigma,\sigma'}}{m} \int_{-\infty}^{\infty} d\mathbf{x} |\psi_\sigma(\mathbf{x})|^2 |\psi_{\sigma'}(\mathbf{x})|^2, \tag{5.2}$$

and $a_{\uparrow\uparrow} \approx a_{\downarrow\downarrow} \approx a_{\uparrow\downarrow}$. As a result, within the ground state manifold of $N$ sites occupied two-component bosons of density $n$ – such that there are $nN$ particles in the system – there is a combinatorically large near-degeneracy of different spin configurations. Figure 5-1(a) emphasizes this point by depicting different configurations of doubly-occupied sites which, in the atomic limit with all three scattering lengths equal, are all degenerate.

Beyond this zeroth order treatment in the atomic limit, there are two qualitatively different ways that we will discuss in which the system will break this large degeneracy. Shown in figure 5-1(b), for states with occupation numbers $n > 1$ there is a local, on-site symmetry breaking term which arises due to the deviations of the intra-spin and

inter-spin scattering lengths from degeneracy. Second, virtual tunneling of a particle from one site to an adjacent one enables particles of different spin to swap sites in the lattice in a way which depends on the spin-composition in the adjacent site. In a formal derivation, we find that this corresponds to both a spin-exchange term and an Ising-like spin-spin interaction.

Previous work has also realized spin-dependent tunneling, and as a result, a spin-dependent transition to the Mott state [51, 116]. However, in this thesis we will stay within the regime where the tunneling is spin-independent: $t_\uparrow = t_\downarrow = t$, and therefore both spins enter the Mott phase at similar lattice depths given that both $U_{\uparrow\uparrow} \approx U_{\downarrow\downarrow}$ to the percent level.

## 5.2 Spins and Effective Spins in the Mott Insulator

Building on the intuition of the previous section, we develop an effective low energy theory within the lowest manifold of states which can account for the symmetry-breaking terms introduced in the previous section and shown in figure 5-1(b), which become responsible for lifting the degeneracy of spin configurations and determining a unique ground state. We will show in the following subsections how to represent the symmetry breaking terms between different "real" spin configurations in terms of effective spins which formally map onto a Heisenberg model which describes the action of these effective spins. To develop a complete picture of the mapping from a two-component Bose-Hubbard model with real spins to a Heisenberg model with effective spins, we examine two distinct cases: one for mapping the $n = 1$ Mott state to a spin-1/2 Heisenberg model and a second mapping the $n = 2$ Mott state to a spin-1 Heisenberg model. Examining their qualitative similarities and differences, we'll aim to develop an intuitive understanding of how the distinct ways the symmetry of the atomic limit is broken can help us more effectively prepare the ground state of this effective spin Hamiltonian.

### 5.2.1 The $n = 1$ Mott State

We begin with the simplest case, a two-component Mott insulator consisting on one particle per site, in order to develop some intuition for the formal mathematics of our spin-mapping. In the Mott state with a single atom per site, the local state of a particle on a site is described by an effective spin-1/2 state, shown in figure 5-2(a), where we associate the $m_s = +1/2$ state with an atom in one hyperfine state ("up") occupying a site or the $m_s = -1/2$ state with an atom in another hyperfine state ("down") occupying the site. Since there is only one atom per site, there is no on-site interaction energy to break the symmetry locally as shown in figure 5-1(b). As a result the primary mechanism for lifting the ground state degeneracy in the $n = 1$ Mott state is the movement of spins via the superexchange interaction.

We can understand the superexchange interaction in second-order perturbation theory as the effect of finite tunneling strength virtually admixing states of higher occupation number, which are gapped from the ground state manifold by a large energy scale, $U$, into the ground state wavefunction. This process is depicted schematically as well in figure 5-1(b). The different interaction energies of two particles on one site are thus responsible for lifting the degeneracy of the various ground state spin configurations. More formally, perturbing the uniformly occupied ground state with the tunneling part of the Hamiltonian couples the local state with $n$ particles per site to one with $n \pm 1$ particles per site:

$$-t \, \langle n_i', n_{i+1}' | \hat{a}_i^\dagger \hat{a}_{i+1} | n_i, n_{i+1} \rangle = -t \, \delta_{n_{i+1}-1, n_{i+1}'} \delta_{n_i+1, n_i'} \tag{5.3}$$

at an energy cost of $U$. Since $t \ll U$ in the Mott regime, this process is energetically forbidden to first order. Because tunneling is short ranged, we hope to capture the essential physics by looking at a two-site model perturbed by some finite tunneling amplitude. The singly occupied basis states that describe the ground state on the $i^{\text{th}}$ link of the lattice by $|n_{i,\uparrow}, n_{i,\downarrow}, n_{i+1,\uparrow}, n_{i+1,\downarrow}\rangle = \{|1,0,1,0\rangle, |1,0,0,1\rangle, |0,1,1,0\rangle, |0,1,0,1\rangle\}$ are degenerate, so we move forward by constructing a matrix to perform degenerate perturbation theory. To second order, each ground state couples first to a doubly

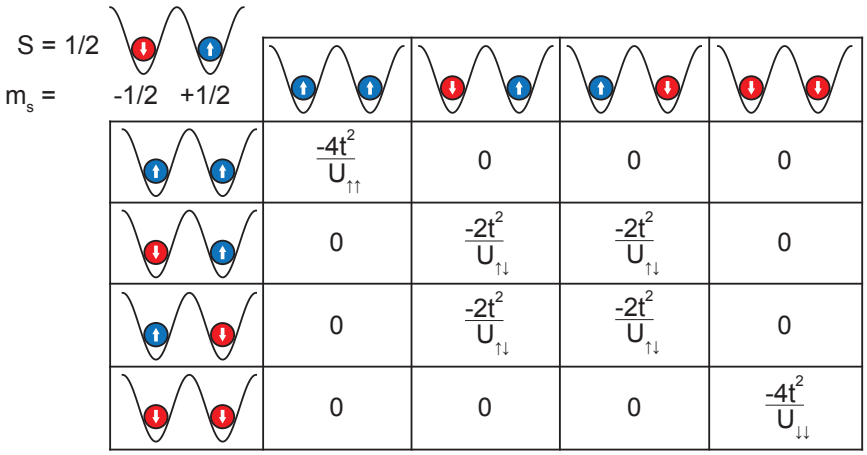


Figure 5-2: Mapping from a two-component, $n = 1$ Mott insulator to an effective spin-1/2. Elements of the sum over all configurations performed to second-order in the tunneling perturbation of the Mott state.

occupied excited state – for example starting from $|1, 0, 0, 1\rangle$ we can couple to both $|1, 1, 0, 0\rangle$ or $|0, 0, 1, 1\rangle$ state – and then either back to the original spin configuration (the diagonal terms), or to another spin configuration (the off-diagonal elements). For each term, a factor of two arises due to the two possible pathways for each process: first tunneling right and then left or first tunneling left and then right. An additional factor of two appears for the spin polarized terms due to bosonic statistics.

Figure 5-2 shows a table of all the possible initial spin configurations and all the resulting terms in the sum over final states to second order in the tunneling. Note that the small parameter used to truncate this series at second order is the ratio $\frac{t}{U} \ll 1$. We now attempt to establish a correspondence between this perturbation series and the anisotropic spin-1/2 Heisenberg model:

$$H_{\text{Spin}} = \sum_{\langle ij \rangle} \left( \frac{J_\perp}{2} \hat{S}_i^+ \hat{S}_j^- + J_z \hat{S}_i^z \hat{S}_j^z + \text{H.c.} \right) + h_z \sum_i \hat{S}_i^z, \tag{5.4}$$

where we define the exchange operators $\hat{S}_i^\pm = \frac{1}{2} \hat{a}^\dagger_{i,\uparrow(\downarrow)} \hat{a}_{i,\downarrow(\uparrow)}$ and the usual $\hat{S}^z$ operator: $\hat{S}_i^z = \frac{1}{2} \hat{a}^\dagger_{i,\uparrow(\downarrow)} \hat{a}_{i,\uparrow(\downarrow)}$. Formally, we take matrix elements of 5.4 with the states listed in the table of figure 5-2 and establish a system of equations whose solution yields the Heisenberg parameters, $J_\perp$, $J_z$, and $h$. For the case of spin-1/2 this is particularly

simple, yielding the system of equations:

$$\frac{1}{2}J_\perp = -\frac{2t^2}{U_{\uparrow\downarrow}} \tag{5.5}$$

$$c - \frac{1}{4}J_z + h_z = -\frac{4t^2}{U_{\uparrow\uparrow}} \tag{5.6}$$

$$c - \frac{1}{4}J_z - h_z = -\frac{4t^2}{U_{\downarrow\downarrow}} \tag{5.7}$$

$$c + \frac{1}{4}J_z + 0 \cdot h_z = -\frac{2t^2}{U_{\uparrow\downarrow}}. \tag{5.8}$$

The constant $c$ here is a spin-independent potential which also ensures self-consistency of the equations. Solving this system yields the parameters of the effective Heisenberg model in terms of the microscopic parameters of the Bose-Hubbard model:

$$J_\perp = -\frac{4t^2}{U_{\uparrow\downarrow}} \tag{5.9}$$

$$J_z = \frac{4t^2}{U_{\uparrow\downarrow}} - \frac{4t^2}{U_{\uparrow\uparrow}} - \frac{4t^2}{U_{\downarrow\downarrow}} \tag{5.10}$$

$$h_z = \frac{2t^2}{U_{\downarrow\downarrow}} - \frac{2t^2}{U_{\uparrow\uparrow}} + h_{\text{ext}}. \tag{5.11}$$

If we include the chemical potentials of up and down spins in the Hamiltonian, the imbalance between up and down potentials acts as an external magnetic field applied to the system, $h_{\text{ext}} = \mu_\uparrow - \mu_\downarrow$, and appears in addition to the effective field arising from the mapping. As a result, we have derived exactly how the parameters of the Heisenberg Hamiltonian scale with respect to the Bose-Hubbard energy scales which we have direct control over in an ultracold atom experiment.

From this we can tell several things about the ordering of spins in the ground state of the two-component Mott state. First, we see that, assuming positive interaction energies (and therefore a condensate stable to collapse), the model describes a ferromagnetic ground state since both exchange and Ising energies are negative, favoring alignment of adjacent spins. In the regime described by the interaction energy hierarchy of $^{87}$Rb, $U_{\uparrow\uparrow} \approx U_{\downarrow\downarrow} \approx U_{\uparrow\downarrow}$, the exchange and Ising terms are nearly the

same:

$$\frac{J_z}{J_\perp} = \frac{U_{\uparrow\downarrow}}{U_{\uparrow\uparrow}} + \frac{U_{\uparrow\downarrow}}{U_{\downarrow\downarrow}} - 1. \tag{5.12}$$

For miscible spins, $U_{\uparrow\downarrow}^2 < U_{\uparrow\uparrow}U_{\downarrow\downarrow}$, the $J_\perp$ term dominates and the ground state should be an easy-plane ferromagnet – also known as a $xy$-ferromagnet [92]. For immiscible spins, the system makes a transition to an easy-axis ferromagnet – commonly known as a $z$-ferromagnet. At exactly the point where $U_{\uparrow\uparrow} = U_{\downarrow\downarrow} = U_{\uparrow\downarrow}$, the system realizes the isotropic Heisenberg model.

In addition to the exchange terms, examining the effective applied magnetic field we see that if the interaction energies $U_{\uparrow\uparrow}$ and $U_{\downarrow\downarrow}$ are different the resulting difference in the self-energy terms of the second-order perturbation expansion act like an effective magnetic field. For $^{87}$Rb, these interaction energies are identical to the percent level, so the effective magnetic field which acts on the system is largely controlled by the chemical potential imbalance, $\mu_\uparrow - \mu_\downarrow$. In our cold atom system, we normally operate with balanced, or nearly balanced mixtures, so the external field is close to zero. However, we do note that the application of an external magnetic field favors a spin orientation in the $z$-axis, so we expect that the chemical potential imbalance can drive a transition to a phase where all spins are polarized along the field direction [42].

So far, we have qualitatively discussed the different phases we expect to be present in the phase diagram at zero temperature. However, one issue for experimental realizations of this system with ultracold atoms has been that the temperatures realized in the lattice are still too high to access these low temperature phases. In $^{87}$Rb, we will assume symmetric intra-spin interactions, $W = U_{\uparrow\downarrow} = U_{\downarrow\downarrow}$, such that the relevant energy scale to compare the temperature to is the exchange energy scale at lattice depths which correspond to Mott insulating states in a 532 nm lattice constant:

$$\frac{4t^2}{U_{\uparrow\downarrow}} \approx \frac{4t^2}{W} \sim 1 \text{ - } 10 \text{ Hz} = 50 \text{ - } 500 \text{ pK}. \tag{5.13}$$

In order to realize long range ordered states where the correlation length, $\xi \propto f(J_\perp/k_BT)$, exceeds the system size, $L$, we need to prepare atoms in the lattice at temperatures lower than those determined by this exchange energy scale – a challeng-

ing task given the state-of-the-art temperatures in optical lattices. Some progress has been made in shaping the local chemical potential in order to realize lower temperature [117], however long range magnetic ordering in the bosonic Heisenberg mapping remains elusive. Next, we will look at the $n = 2$ Mott insulator and see that the mapping to the spin-1 Heisenberg model provides a promising alternative route towards low temperatures in this lattice system.

### 5.2.2 The $n = 2$ Mott State

The mapping from a Mott insulator with two particles per site to a Heisenberg model proceeds in a manner which is similar to that of the $n = 1$ case, however, due to the presence of different intra-spin and inter-spin interaction energies we must account for these additional on-site degeneracy-lifting terms. Shown in figure 5-3(a), the state of two particles – also called a "doublon" – composed of two possible hyperfine pseudo-spin states occupying the lowest band on a lattice site is described by a spin triplet. The three possible projections of this effective spin-1 consist of $m_s = \pm 1$ states which are pseudo-spin polarized and an $m_s = 0$ state which is a symmetric superposition of a hyperfine spin up and a hyperfine spin down particle, $|0\rangle = \frac{1}{\sqrt{2}}(|\uparrow,\downarrow\rangle + |\downarrow,\uparrow\rangle)$, which we will refer to as a "spin-paired doublon". Due to the symmetry requirement of bosonic particles, only the triplet state is populated in the lowest band of the lattice, whereas the antisymmetric singlet state necessarily involves population in a higher band and, as such, is suppressed at low temperature.

As shown in figure 5-1, now that the effective spin-1 particles consist of multiply occupied sites, an additional symmetry-breaking mechanism – in addition to superexchange – can lift the degeneracy of spin configurations in the ground state manifold of the Mott state. These on-site interaction energy differences between each spin projections are parameterized by the scattering lengths and corresponding interaction parameters: $U_{\uparrow\uparrow}$, $U_{\downarrow\downarrow}$, and $U_{\uparrow\downarrow}$. To simplify the mathematics and notation of the derivation presented here, and to mirror the hierarchy of scattering lengths in $^{87}$Rb, we set the intra-spin interactions to be equal, $W = U_{\uparrow\uparrow} = U_{\downarrow\downarrow}$, and parameterized by $W$.

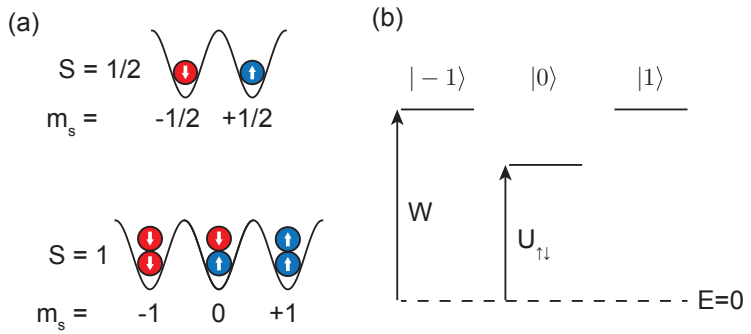


Figure 5-3: Mapping from a two-component, $n = 2$ Mott insulator to an effective spin-1. (a) Comparing the spin-1/2 mapping to the spin-1 mapping, the on-site energy of the spin-1 state directly breaks the symmetry of the local states. (b) The on-site energies of the three projections of the spin-1 state for $^{87}$Rb in a spin-dependent optical lattice. Repulsive interactions raise the energy of all sites relative to singly occupied sites, but, for $U_{\uparrow\downarrow} < W$, the $|0\rangle$ state is less repulsive than either $|\pm\rangle$ states.

Shown in figure 5-3(b), the different interactions of the spin polarized doublons, $|\pm 1\rangle$, and the spin-paired doublons, $|0\rangle$, cause a shifting of the on-site energy that acts like a $(\hat{S}_i^z)^2$ term, plus a constant energy offset, $U_{\uparrow\downarrow}$, in a Heisenberg Hamiltonian. This term is qualitatively new to the higher-spin Heisenberg model composed of multiply-occupied lattice sites, and will be responsible for a qualitatively different phase diagram moving forward. In the big picture, these on-site terms mean that we are no longer performing strictly degenerate perturbation theory to construct an effective low-energy theory of spin ordering, and instead have some diagonal entries we must include to capture the low-energy theory. In the regime where $W \approx U_{\uparrow\downarrow}$, the on-site interaction energies will be nearly spin-independent, so we expect in this regime the spin-ordering to be largely driven by second-order processes similar to those derived for the spin-1/2 Heisenberg mapping. To include these terms in our low energy effective theory, we write out a table of all the terms in the second-order perturbation series for each possible spin configuration on one link of the lattice. The resulting terms are shown in figure 5-4.

To find the parameters of our effective Hamiltonian, we compare the terms of this perturbation series and the on-site interaction energies to the matrix elements of the

| $\lvert m_{s_i}, m_{s_j}\rangle$ | $\lvert -1\,,-1\rangle$ | $\lvert -1\,,0\rangle$ | $\lvert -1\,,1\rangle$ | $\lvert 0\,,-1\rangle$ | $\lvert 0\,,0\rangle$ | $\lvert 0\,,1\rangle$ | $\lvert 1\,,-1\rangle$ | $\lvert 1\,,0\rangle$ | $\lvert 1\,,1\rangle$ |
|---|---|---|---|---|---|---|---|---|---|
| $\lvert -1\,,-1\rangle$ | $-\frac{12t^2}{W}$ | 0 | 0 | 0 | 0 | 0 | 0 | 0 | 0 |
| $\lvert -1\,,0\rangle$ | 0 | $-\frac{5t^2}{U_{\uparrow\downarrow}} - \frac{3t^2}{2W-U_{\uparrow\downarrow}}$ | 0 | $-\frac{4t^2}{U_{\uparrow\downarrow}}$ | 0 | 0 | 0 | 0 | 0 |
| $\lvert -1\,,1\rangle$ | 0 | 0 | $\frac{-4t^2}{2U_{\uparrow\downarrow}-W}$ | 0 | $-\frac{4t^2}{U_{\uparrow\downarrow}}$ | 0 | 0 | 0 | 0 |
| $\lvert 0\,,-1\rangle$ | 0 | $-\frac{4t^2}{U_{\uparrow\downarrow}}$ | 0 | $-\frac{5t^2}{U_{\uparrow\downarrow}} - \frac{3t^2}{2W-U_{\uparrow\downarrow}}$ | 0 | 0 | 0 | 0 | 0 |
| $\lvert 0\,,0\rangle$ | 0 | 0 | $-\frac{4t^2}{U_{\uparrow\downarrow}}$ | 0 | $-\frac{8t^2}{W}$ | 0 | $-\frac{4t^2}{U_{\uparrow\downarrow}}$ | 0 | 0 |
| $\lvert 0\,,1\rangle$ | 0 | 0 | 0 | 0 | 0 | $-\frac{5t^2}{U_{\uparrow\downarrow}} - \frac{3t^2}{2W-U_{\uparrow\downarrow}}$ | 0 | $-\frac{4t^2}{U_{\uparrow\downarrow}}$ | 0 |
| $\lvert 1\,,-1\rangle$ | 0 | 0 | 0 | 0 | $-\frac{4t^2}{U_{\uparrow\downarrow}}$ | 0 | $\frac{-4t^2}{2U_{\uparrow\downarrow}-W}$ | 0 | 0 |
| $\lvert 1\,,0\rangle$ | 0 | 0 | 0 | 0 | 0 | $-\frac{4t^2}{U_{\uparrow\downarrow}}$ | 0 | $-\frac{5t^2}{U_{\uparrow\downarrow}} - \frac{3t^2}{2W-U_{\uparrow\downarrow}}$ | 0 |
| $\lvert 1\,,1\rangle$ | 0 | 0 | 0 | 0 | 0 | 0 | 0 | 0 | $-\frac{12t^2}{W}$ |

Figure 5-4: Matrix elements for the mapping from a two-component, $n = 2$ Mott insulator to an effective spin-1. Elements of the sum over all configurations performed to second-order in the tunneling perturbation of the Mott state. For simplicity, we have set $U_{\uparrow\uparrow} = U_{\downarrow\downarrow} = W$.

spin-1 Heisenberg model:

$$H = \sum_{\langle ij \rangle} \Big( \frac{J_\perp}{2} \hat{S}_i^+ \hat{S}_j^- + J_z \hat{S}_i^z \hat{S}_j^z + \text{H.c.} \Big) + u \sum_i (\hat{S}_i^z)^2 + h_z \sum_i \hat{S}_i^z. \tag{5.14}$$

In order to properly constrain the problem and reach a closed-form solution, we must add a higher-order term to the Hamiltonian of the form, $\gamma \sum_i (\hat{S}_i^z)^2 (\hat{S}_{i+1}^z)^2$, which accounts for a higher-order Ising interaction generated by the energetic difference between states with both combinations of $|\pm 1\rangle$ states on a link compared to ones with $|0\rangle$ states on a link. To simplify the resulting math, we initially restrict ourselves to a spin-balanced cloud with $\mu_\uparrow = \mu_\downarrow$ such that $h_z = 0$. This will not affect the spin mapping since we have set $U_{\uparrow\uparrow} = U_{\downarrow\downarrow} = W$ and thus the underlying Hamiltonian is symmetric between exchange of up- and down-spins.

As a result of adding the higher-order Ising term while sending $h_z$ to zero, the Heisenberg Hamiltonian we use to compare to degenerate perturbation theory of the $n = 2$ Mott state becomes:

$$H_{h_z=0} = \sum_{\langle ij \rangle} \Big( \frac{J_\perp}{2} \hat{S}_i^+ \hat{S}_j^- + J_z \hat{S}_i^z \hat{S}_j^z + \text{H.c.} \Big) + u \sum_i (\hat{S}_i^z)^2 + \gamma \sum_i (\hat{S}_i^z)^2 (\hat{S}_{i+1}^z)^2. \tag{5.15}$$

Equating matrix elements of this Hamiltonian to the matrix elements in figure 5-4 we can write a system of equations to determine the Heisenberg parameters:

$$\begin{aligned}
J_\perp &= -\frac{4t^2}{U_{\uparrow\downarrow}} && (5.16)\\
c + J_z + 2u + \gamma &= -\frac{12t^2}{W} + 2W && (5.17)\\
c + u &= -\frac{5t^2}{U_{\uparrow\downarrow}} - \frac{3t^2}{2W - U_{\uparrow\downarrow}} + W + U_{\uparrow\downarrow} && (5.18)\\
c - J_z + 2u + \gamma &= -\frac{4t^2}{2U_{\uparrow\downarrow} - W} + 2W && (5.19)\\
c &= -\frac{8t^2}{W} + 2U_{\uparrow\downarrow}. && (5.20)
\end{aligned}$$

Solving this system of equations we get the Heisenberg parameters for the effective

spin-1 model:

$$J_\perp = -\frac{4t^2}{U_{\uparrow\downarrow}} \tag{5.21}$$

$$J_z = -\frac{6t^2}{W} + \frac{2t^2}{2U_{\uparrow\downarrow} - W} \tag{5.22}$$

$$u = (W - U_{\uparrow\downarrow}) + \frac{8t^2}{W} - \frac{5t^2}{U_{\uparrow\downarrow}} - \frac{3t^2}{2W - U_{\uparrow\downarrow}} \tag{5.23}$$

$$\gamma = -\frac{14t^2}{W} + \frac{10t^2}{U_{\uparrow\downarrow}} + \frac{6t^2}{2W - U_{\uparrow\downarrow}} - \frac{2t^2}{2U_{\uparrow\downarrow} - W}. \tag{5.24}$$

So far this result is exact assuming equal intra-spin interactions. To reach an simple, intuitive result we can make an additional approximation that $U_{\uparrow\downarrow} \approx W$ – the regime of interest for understanding the $xy$-ferromagnet. Intuitively, this limit is reasonable because in the perturbation of the Mott phase we are ignoring terms which are gapped from the ground state by an energy $\sim W$. Therefore, if $U_{\uparrow\downarrow}$ gets too small and approaches zero, these states are now gapped from the rest of the Mott states by an energy $\sim W$, and the underlying assumptions of the spin-mapping break down.

Working in the limit where $\frac{W-U_{\uparrow\downarrow}}{W} \ll 1$, the denominator for terms in the spin-mapping can be approximated by expanding the fractions, $\frac{1}{(2W-U_{\uparrow\downarrow})} \approx \frac{1}{W}(1 - \frac{W-U_{\uparrow\downarrow}}{W} + \ldots)$, and $\frac{1}{(2U_{\uparrow\downarrow}-W)} \approx \frac{1}{W}(1 + \frac{2(W-U_{\uparrow\downarrow})}{W} + \ldots)$ and dropping terms of order $\frac{W-U_{\uparrow\downarrow}}{W}$ and higher. As a useful check, if we make the additional assumption that $U_{\uparrow\downarrow} = W$, then the parameters of the spin-1 Heisenberg mapping become particularly simple expressions for the isotropic Heisenberg point.

$$J_\perp = -\frac{4t^2}{U_{\uparrow\downarrow}} \tag{5.25}$$

$$J_z \approx -\frac{4t^2}{W} \tag{5.26}$$

$$u \approx (W - U_{\uparrow\downarrow}) \tag{5.27}$$

$$\gamma \approx \frac{10t^2}{U_{\uparrow\downarrow}}\left(\frac{W - U_{\uparrow\downarrow}}{W}\right) \approx 0. \tag{5.28}$$

We can also re-introduce an effective magnetic field $h_z$ by introducing a chemical potential imbalance which in turn defines the field: $h_z = \mu_\uparrow - \mu_\downarrow$. Also note that

the first non-vanishing term in the higher-order Ising parameter is first order in the expansion parameter, $\frac{W-U_{\uparrow\downarrow}}{W}$, and is therefore small compared to all other parameters in the Hamiltonian, and can be effectively ignored moving forward.

We see that the resulting effective spin-1 mapping is similar to that of the effective spin-1/2 model, with a few key differences. Most prominently, we note the presence of an additional term in the Hamiltonian, the $u(\hat{S}_i^z)^2$ term, that is diagonal in our spin occupation number basis. As a result, we anticipate a qualitative difference in the ground state phase diagram with the appearance of states for which this term dominates the other terms in the Hamiltonian. As the interaction energy difference between spin projections becomes small, the system becomes qualitatively more similar to the spin-1/2 model with the repulsively interacting insulator displaying both an easy-axis ferromagnetic ground state controlled by the Ising term or an easy-plane ferromagnetic ground state controlled by the exchange term.

Much work has been done numerically examining this spin-1 Hamiltonian [5, 90] and its generalizations in one-dimension [133, 39]. From such systems we see the existence of a $z$-ferromagnetic and $xy$-ferromagnetic ground state in addition to a ground state determined by the large $u$ term in the $J < 0$ regime. In the $J > 0$ regime, a $z$- and $xy$-antiferromagnetic state appear. For our system of $^{87}$Rb where all the scattering lengths are nearly equal, the system is near-isotropic and, depending on the choice of hyperfine spin state, should either be weakly $xy$-ferromagnetic if we use the $|F, m_f\rangle = |1, -1\rangle + |2, -2\rangle$ mixture [71], or weakly $z$-ferromagnetic if we use the $|1, -1\rangle + |1, 1\rangle$ mixture [28].

### 5.2.3 The Case of a "Real" Spin-1

An alternative realization of a spin-1 Heisenberg model which has been featured in some proposals [133, 39] is realized with three-component bosons in an $n = 1$ Mott insulator. In this case, the three spin projections of the effective spin-1 model is composed of one particle per site with one of the three hyperfine pseudo-spins, more similar to the spin-1/2 mapping of the two-component $n = 1$ mapping. If we now follow the procedure for generating matrix elements and creating a correspondence with

an effective Heisenberg spin model, the resulting spin-1 Hamiltonian – alternatively known as the bilinear-biquadratic Heisenberg model – is written as:

$$H = \sum_{\langle ij \rangle} J_1 \hat{\mathbf{S}}_i \cdot \hat{\mathbf{S}}_j + \sum_{\langle ij \rangle} J_2 (\hat{\mathbf{S}}_i \cdot \hat{\mathbf{S}}_j)^2 + h_z \sum_i \hat{S}_i^z. \tag{5.29}$$

For simplicity, we have assumed isotropic tunneling and interactions. Most importantly, we see that the effective spin-1 Heisenberg Hamiltonian for a two-component gas in an $n = 2$ Mott state is qualitatively different than the effective spin-1 Heisenberg mapping for three-component bosons in an $n = 1$ Mott state. First, the local symmetry-breaking given by the different inter-spin interactions in the $n = 2$ case provides access to a novel spin-insulating phase in the ground state that does not appear in the $n = 1$ case. In addition, the $n = 1$ case contains both a bilinear and biquadratic term which allows spin fluctuations of both $\pm 1$ as well as $\pm 2$. Intuitively, this enables matrix elements between different states on a link the look like $\{1, 0\} \rightarrow \{0, 1\}$ as well as $\{1, -1\} \rightarrow \{-1, 1\}$, the latter of which is zero in the $n = 2$ mapping. This additional term for spin hopping, which changes the spin index by $\pm 2$ for each hopping event, contributes to the appearance of a dimer phase in the $n = 1$ spin-1 chain that does not exist for the $n = 2$ spin-1 chain [39].

Both realizations of the spin-1 chain contain a Haldane phase on the antiferromagnetic side of the phase diagram. The Haldane phase is a paradigmatic example of a short-range entangled state which hosts topologically protected states at the ends of the chain. These effective spin-1/2 states which terminate the chain are of interest for use as qubits for topologically protected quantum information processing. Therefore, the realization of a Haldane phase in an ultracold atomic setting is an attractive direction for experimental realizations of this spin-1 mapping.

### 5.2.4 Why Spin-1?

As mentioned previously, one of the most important outstanding challenges in the field of ultracold atoms is to prepare even colder samples in an optical lattice such as to realize ultralow entropy magnetic ground states in the Mott insulator. As the two-

component superfluid is driven across the superfluid-Mott insulator quantum phase transition, the system is simultaneously forming a Mott state as well as magnetic order. One question is how these two states form and how $xy$-order evolves across the quantum phase transition. One challenge faced in $^{87}$Rb is that since the native scattering lengths are nearly degenerate the Heisenberg model realized is nearly isotropic. At the isotropic Heisenberg point, the linear dispersion of spin waves disappears and the spin-superfluid Landau critical velocity goes to zero. Therefore, any perturbation of the system such as magnetic field gradients can produce spin excitation.

The greatest advantage of realizing the spin-1 model – in addition to the presence of interesting phases not present in the spin-1/2 model – is the presence of the "large u" state, a state we will call the *spin Mott*, which allows the ground state of the Heisenberg model to be prepared in the Mott insulator with high fidelity. The reason for this is that the spin Mott state, dominated by the $u(\hat{S}_i^z)^2$ term in the Hamiltonian, is a gapped state which does not break any symmetries and as a result does not have a low-energy Goldstone mode at the exchange energy scale, $J_\perp$ or $J_z$. In the spin Mott, the excitation gap in the system is controlled by the splitting between the on-site energies of the respective spins, $u = W - U_{\uparrow\downarrow}$, and can easily be controlled by varying the inter-spin scattering length.

The spin Mott is a local state, without long-range ordering, in contrast to both ferromagnetic and anti-ferromagnetic states which break rotational symmetry on the system. As a result, the spin Mott state lacks a low-energy Goldstone mode and remains fully gapped and rotationally invariant. Practically speaking, the spin Mott should thus be an easy to prepare, robust state in the ground state phase diagram of the Heisenberg model and is directly connected to both the $xy$- and $z$-ferromagnetic states as well as the Haldane and Neél states of the phase diagram of the spin-1 chain by variation of easily controlled experimental parameters.

With this picture, we come to the main message of this chapter laid out in the introduction: creating a low entropy state in the spin-1 Heisenberg model by preparing the spin Mott phase represents an excellent starting point for adiabatic ramping to a magnetic state of matter across a quantum phase transition and for potential

realization of a long-range ordered spin system at picokelvin temperature scales.

Now that we have covered the basics of the Heisenberg spin-1 mapping and its predicted ground state phases in addition to the qualitative advantages of the spin Mott state, the rest of this chapter will cover the experimental aspects of the realization of the spin Mott and $xy$-ferromagnetic phase transition in an optical lattice.

## 5.3 The Spin-Dependent Lattice

In order to realize and control the transition between the spin Mott and the $xy$-ferromagnet in $^{87}$Rb, we need to control the inter-spin interactions, $U_{\uparrow\downarrow}$, relative to the intra-spin interactions, $W$. Normally, this is trivial in an ultracold atoms experiment because the interactions are proportional to the $s$-wave scattering length which can be directly controlled by use of a Feshbach resonance:

$$U_{\sigma\sigma'} = \frac{4\pi\hbar^2 a_{\sigma\sigma'}}{m} \int_{-\infty}^{\infty} d\mathbf{x}\, |w_\sigma(\mathbf{x} - \mathbf{x}_{0\sigma})|^2 |w_\sigma(\mathbf{x} - \mathbf{x}_{0\sigma'})|^2. \tag{5.30}$$

Unfortunately, in $^{87}$Rb, the series of low-field ($< 1000$ Gauss) Feshbach resonances between the $|F, m_F\rangle = |1, 1\rangle$ state and the $F = 2$ manifold of states are accompanied by strong spin-relaxation losses especially detrimental in the doubly-occupied sites of an $n = 2$ Mott insulator. Therefore, for realizing ultralow entropy states of matter, tuning the inter-spin scattering length by ramping close to a Feshbach resonance is not favorable.

If we examine equation 5.30 more closely, another option becomes immediately obvious – the interactions can also be tuned by manipulating the overlap integral between the density of the two species! If we change the locations of the Wannier functions, $\mathbf{x}_{0\sigma}$, by moving the center of the trapping potential, the value of the integral can be reduced from its maximal value where the two wavefunctions experience a spin-independent trapping potential to almost zero. To accomplish this displacement of the relative centers of the two lattice potentials, we will need to apply a spin-dependent force to the atoms. This can be accomplished by using spin states with different

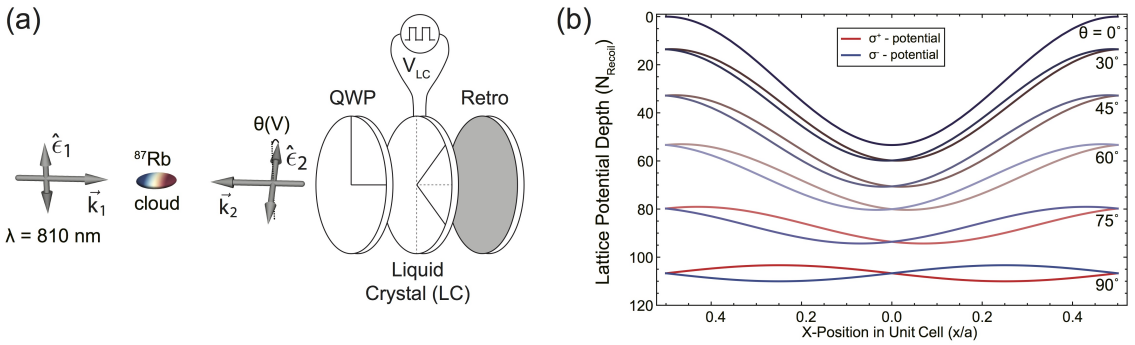


Figure 5-5: Optical setup for generation of a dynamically-tunable spin-dependent lattice. (a) A laser beam is incident upon the atomic cloud with a linear polarization aligned to the optical axis of a quarter-waveplate (QWP) which is in turn aligned at 45° to the axes of a liquid crystal retarder. Upon retroreflection, the beam passing back through the liquid crystal and QWP is transformed into a linear polarization oriented at a voltage tunable angle, $\theta$, with respect to the input polarization. The angle is tuned by changing the amplitude of a 2 kHz square wave driving the liquid crystal retarder. (b) The resulting spin-dependent potential for the $|1, \pm 1\rangle$ hyperfine states at a wavelength of 810 nm.

magnetic moments and either applying a magnetic field gradient or a polarization gradient of an optical field, thus utilizing the vector Stark shift as discussed in section 2.2. For the work described here we will use the vector stark shift of an optical lattice to accomplish this task.

We can create a spatially-distinct optical potential for different spin states in an optical lattice where $\sigma^+$ and $\sigma^-$ polarizations see different interference patterns. One classic implementation of such a configuration is used in optical molasses cooling where two laser beams counter-propagate with polarizations aligned perpendicular to each other – an optical setup that we will refer to as a lin$\perp$lin configuration. Figure 5-5 depicts an optical setup which realizes an optical lattice with a tunable polarization between the extreme limits of a fully-spin-dependent lattice composed solely of vector stark shifts in lin$\perp$lin configuration to a spin-independent lattice where all spin states occupy the same spatial mode in lin$\parallel$lin configuration. Polarization rotation of the retroreflected beam is achieved using the setup outlined in figure 5-5. The input beam is linearly polarized and aligned to an optical axis of the quarter waveplate. The optical axes of the liquid crystal are then aligned at a 45° angle with respect

to the optical axes of the quarter waveplate. The lattice beam is then retroreflected and, after a second pass through the liquid crystal where the optical axes pick up an additional retardance, the beam is elliptically polarized. The final pass through the quarter waveplate converts this elliptical polarization back into a linear polarization rotated away from the input axis by an angle equal to twice the retardance of the liquid crystal. It is important to note here an important difference between a liquid crystal polarization rotator and a liquid crystal optical retarder. The liquid crystal polarization rotator has an integrated waveplate such that the output wavelength is always linearly polarized whereas a liquid crystal variable retarder produces elliptical polarization and must be paired with an appropriate quarter waveplate in order to produce a linear polarization. The liquid crystal device we utilize in the lab is an LCR-1-NIR half-wave polarization retarder from Thorlabs, which produces a continuously variable polarization retardance of the slow optical axis compared to the fast axis by varying the amplitude of a 2 kHz square wave drive, depicted in figure 5-5. Importantly, this optical retardance device is a zero-order device – that is the phase delay of the fast and slow axes are varied from some integer number of wavelengths $m\lambda$, at zero phase delay to exactly $m\lambda + \lambda/4$ at maximal phase delay. In the catalog of optical components, "zero-order" typically means that $m$ is non-zero, whereas "true-zero-order" typically means that $m = 0$. This is important because changing the index of refraction changes the optical path length between the retroreflection mirror and the atoms resulting in a translation of the lattice sites with respect to the external trapping potential. In addition, this liquid crystal device produces no detectable beam deflection and has a flatness better than $\lambda/4$ such that the beam quality is preserved, in contrast to some cheaper EOM options.

Several practical concerns often associated with using a liquid crystal for polarization rotation include the noise imprinted on the intensity and polarization by the AC drive voltage, as well as the slow switching times from one retardance to another. Figure 5-6 shows two tests of the liquid crystal performance. First, the polarization and intensity noise imprinted on a laser beam passing through the liquid crystal device and subsequently a polarizer is seen in figure 5-6(a). Following the calculation

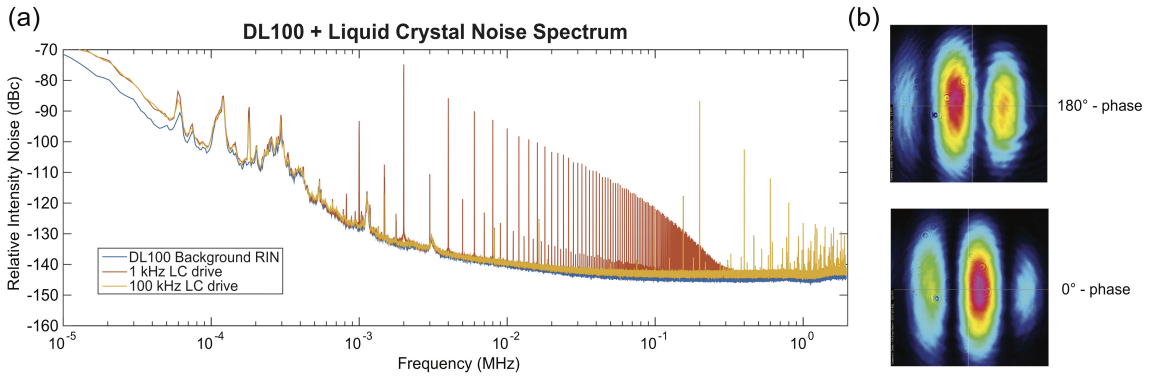


Figure 5-6: Characterization of the liquid crystal retarder. (a) The intensity noise spectrum of the liquid crystal device driven with both a 2 kHz square wave, as recommended by the manufacturer, and a 100 kHz square wave, which moves the noise peaks above the trap frequencies of the harmonic oscillator. (b) Interference fringe in the output port of a Michelson interferometer shows minimal wavefront distortion as well as zero-order retardation important for optical lattice applications.

of intensity noise scattering rate from chapter 2, this residual noise at typical trap frequencies is approximately equal to the native noise in the servo loop, corresponding to excitation rates of $10^{-2}$ to $10^{-4}$ $s^{-1}$ (depending on the trap frequency), negligible compared to expected light scattering rates of $\sim$1 $s^{-1}$. Next, figure, 5-6(b) shows the interference of two beams in the exit port of a Michelson interferometer with one arm of the interferometer passing through the liquid crystal device. The two beams are aligned at a slight angle to produce a fringe and check that the optical device is indeed a zero-order device – changing the optical path length by only a fraction of one wavelength and not many wavelengths – as well as to verify the uniformity of phase retardance. Finally, it was verified in figure 5-6 that if the intensity and polarization noise of the liquid crystal is detrimental to the lattice lifetime, the device can also be driven at higher frequencies, here shown to be a 100 kHz square wave, and still perform similarly, albeit with reduced dynamic range and switching time.

### 5.3.1 Which Wavelength is the Best?

In section 2.2 we discussed the implications of using the vector stark shift on inelastic light scattering: the ratio of the vector Stark shift to the scattering rate scales does

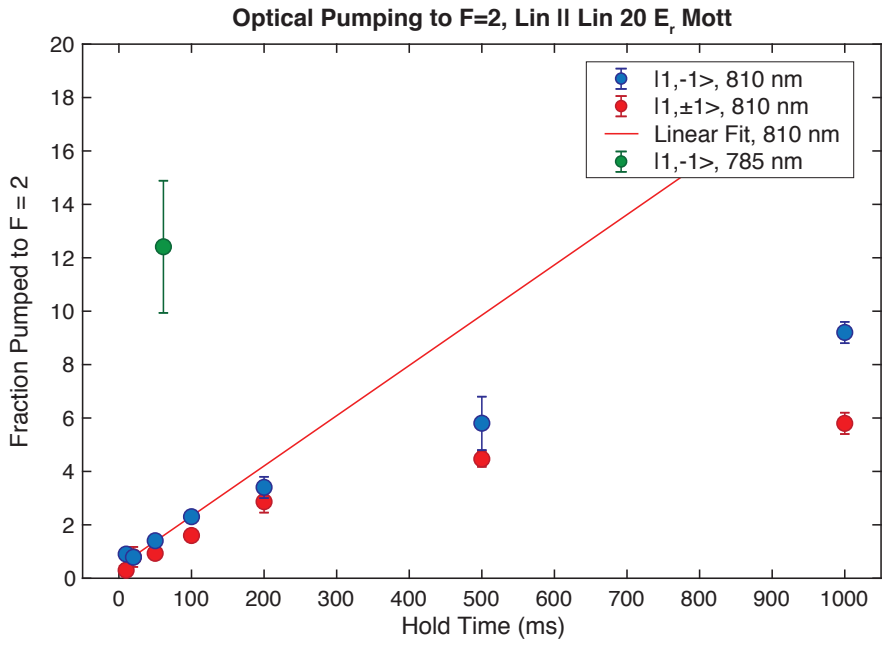


Figure 5-7: Comparison of optical pumping rates in a $\lambda = 810$ nm versus a 785 nm lattice. Number of atoms appearing in the $F = 2$ manifold of states starting from atoms in either the $|1, -1\rangle$ state (blue) or a $|1, \pm 1\rangle$ mixture (red) as a function of hold time in a $20E_r$, $n = 2$, Mott insulator in the lin$\|$lin configuration. A linear fit to early times, $t \leq 200$ ms, is shown for the 810 nm lattice. For comparison, the fraction of atoms optically pumped in 66 ms hold in a 785 nm lattice is shown (green).

not improve with far-detuning but instead is fixed by the ratio of the fine-structure splitting to the linewidth of the excited state. In theory, this means that using a near-detuned lattice will produce just as much heating via light scattering as a far-detuned lattice producing the same total vector stark shift. Practically, there are several key differences between the two limiting cases which indicate that the optimal detuning is an intermediate detuning between the limiting cases.

To begin, if we choose a near-detuning for the spin-dependent lattice there are two main drawbacks to consider: optical pumping to other hyperfine states and resonant photons from amplified spontaneous emission. At first glance, working near the tune-out potential for the scalar stark shift seems like a good choice. For example, working with the $|1, \pm 1\rangle$ hyperfine mixture in a spin-dependent lattice at 785 nm gives roughly equal scalar and vector contributions to the potential such that one can easily tune in between the two configurations. However, a strong lattice with such close-detuning

from both excited states produces an appreciable population in the excited state and as such can optically pump atoms from the states we define to be within our state space to other hyperfine states in an uncontrolled manner. For example, in a $|1, \pm 1\rangle$ mixture in a spin-dependent lattice the circularly polarized light can excite atoms to the $m_F = 0$ states in either of the excited state manifolds which can then decay either back into the original state or into the $|1, 0\rangle$ state or into the $F = 2$ manifold. For detunings between the D1 and D2 lines, the scattering rates interfere destructively whereas the population in the excited state does not interfere. As a result, the relative importance of optical pumping of atoms out of the target states can be tuned by detuning away from between the two excited state lines. This effect is demonstrated in figure 5-7 which shows a comparison of the number of atoms optically pumped into the F=2 hyperfine states as a function of hold time in two different lattices wavelengths: one at 785 nm compared to a second at 810 nm. In an incoherent light scattering model, the optical pumping rate should be constant and would fit a straight line; however, from figure 5-7, it is clear that the rate at short times when the cloud is colder is higher than that at later times when the cloud is more thermal and therefore more dilute. This interesting behavior seems to indicate that there is some multi-particle or collective nature to the optical pumping rate which is not captured in the single-particle light scattering model.

An additional negative impact of a close-detuned lattice is the impact of resonant photons on the spontaneous scattering lifetime. In the first experimental attempts, an external-cavity diode laser with nominal center wavelength of 782 nm was operated at 785 nm to provide power for the optical lattice laser. In this case, the wavelength tunability offered by a diode laser and its broad gain profile is detrimental to the atomic lifetime due to the presence of near resonant photons generated by the high gain of the diode laser and amplified spontaneous emission (ASE). Figure 5-8, shows an optical spectrum analysis of the diode laser used to generate a near-resonant lattice at 785 nm wavelength. Clearly visible is the line of the laser (off-scale) and at lower power a $> 5$ nm wide spectral pedestal of light generated by amplified spontaneous emission. Consequent filtering of the lattice light with narrowband interference filters

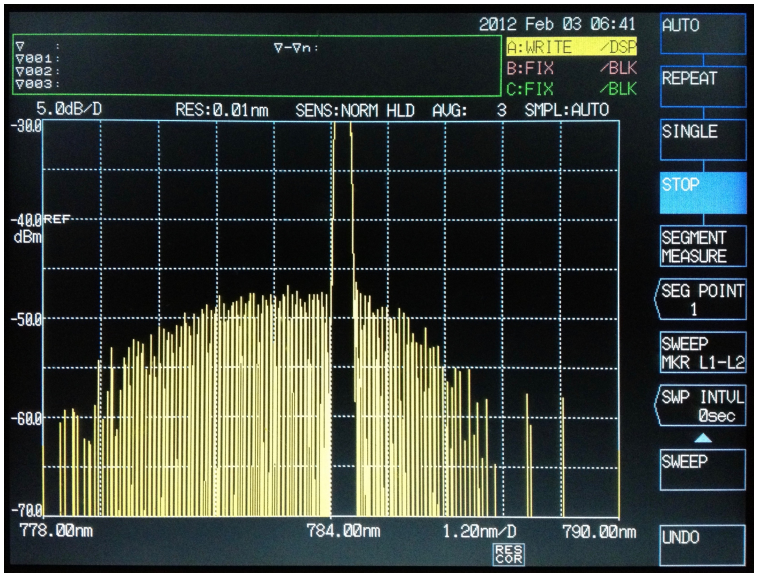


Figure 5-8: Broadband amplified spontaneous emission from a diode laser. Resonant photons emitted spontaneously, and subsequently amplified, by the high gain of the diode laser are a strong source of heating when used as the laser source for an optical lattice experiment.

and by passing through a heated Rb vapor cell led to a marked increase in the atomic population lifetime in the lin⊥lin lattice up to the 100 ms scale. This result highlights another complication of working with a close-detuning to the excited atomic states, the generation of resonant photons either by the laser source itself, or by nonlinear processes such as Stokes scattering of high intensity light propagating through an optical fiber. One final concern is the effects of re-scattering of near-detuned photons since the high optical density of the condensate, OD $\gg 1$. To avoid all the above issues, we examine the opposite limit for a spin-dependent lattice, the far-detuned limit.

In contrast to the close-detuned case, we see that an additional set of constraints arise in the limit of far-detuning due to the finite available power and the confinement coming from the finite size of the lattice laser beam. Spin-dependent potentials can be created at the 1064.2 nm wavelength which composes our normal lattice setup. However, one limitation of using such a far-detuned lattice is that the power needed becomes large, on the order of 10 W in a several hundred $\mu$m $1/e^2$diameter beam in order to reach up to 20 Er of vector Stark shift. In principle, this power is avail-

able in the lab; however, due to the power requirements of the other lattices and dipole traps for which the 1064 nm light is also used, designating this power to a lattice is impractical. Regardless, there are more fundamental limitations to using a far-detuned wavelength as a spin-dependent lattice. One is the sensitivity of the spin-dependent potential to polarization impurity. The liquid crystal device used to dynamically rotate the polarization has a polarization purity of ∼150:1. If we consider that a small misalignment of the incoming and retroreflected polarization vectors from the ideal lin⊥lin configuration results in a small scalar shift, then there is a maximum amount of polarization impurity we can tolerate before the scalar shift arising from impurity polarizations dominates over the weak residual vector Stark potential. Practically, this means that the separation of the potentials for up and down spins as a function of polarization angle is mostly flat as a function of angle before dropping sharply around 90°. In addition, if we wish to maintain a constant lattice depth as a function of polarization angle, then the power used in the lin⊥lin versus lin∥lin configurations will be drastically different. Therefore, we will need to ramp the optical power over a few orders of magnitude to maintain constant lattice depth. If the beam is large, then the confining potential will be determined solely by the dipole traps. However, since we are already marginal on power for the lin⊥lin configuration at such a large detuning, we need a smaller lattice beam to create deep enough vector Stark potentials. Unfortunately, this means that the high power used will also create a strong transverse confining potential which compresses the Mott insulator at its deepest lattice depths. Taking the ratio of the scalar lattice potential to the vector lattice potential, at 1064 nm we expect a factor of ∼90, meaning the confining potential will be ∼9.5 times greater in the lin⊥lin configuration than the lin∥lin configuration, an undesirable result for maintaining low temperatures in the Mott state.

As a result, we see that the optimal detuning for our spin-dependent lattice is at an intermediate detuning. An improved realization of the experiment utilizes an M Squared SolsTiS laser to generate the lattice potential that can be detuned below both D1 and D2 transitions. In this way the optical pumping rate is reduced relative

to the close-detuning and resonant light generated by ASE is eliminated, at the same time that we gain a greater degree of tunability over the lattice wavelength and the lattice phase noise is reduced by use of a narrower optical linewidth laser source. At a wavelength of 810 nm the ratio of the scalar lattice potential to the vector lattice potential is ∼8, so the difference in trapping potential added by the optical lattice will be a factor of $\sqrt{8} \approx 2.8$ between lin⊥lin and lin∥lin configurations, meaning as long as the potential is largely dominated by the dipole trapping lasers, the changing external confinement of the optical lattice beam plays a diminished role. Finally, at this 15 nm detuning from the D1 line, the power requirements are modest, simply requiring $\sim 100$ mW, a power easily deliverable with a Ti:sapphire laser.

As we will see in the next section, for detecting spin correlations in our Heisenberg mapping we will make use of the lin∥lin configuration, so in our experiment it is advantageous to go to larger detunings for longer lifetimes in the detection sequence. Practically, 810 nm is the farthest we can detune before becoming power limited in the lin⊥lin configuration, but in principle with more power one might continue to increase the detuning to increase the lifetime in the lin∥lin configuration until the compression of the cloud due to the finite size of the beam becomes the dominant heating mechanism.

With the lattice wavelength chosen, we can calculate the resulting spin-dependent potentials and the corresponding inter-spin interaction integral from equation 5.30. The resulting interaction energy as a function of the angle of the retroreflected lattice polarization relative to the input lattice polarization is shown in figure 5-9. From this curve we see that separating the spin-up and spin-down wavefunctions spatially has a profound effect on the inter-spin interactions, and can tune the effective interaction from nearly non-interacting over more than 5 orders of magnitude to as strongly interacting as a spin-independent lattice. In many ways this has the same effect as a Feshbach resonance tuning the inter-spin scattering length, $a_{\uparrow\downarrow}$, with the limitation of not being able to increase the scattering length above its value in the lin∥lin lattice. Nevertheless, the spin-dependent lattice gives us precisely the control necessary in the correct parameter regime to prepare the spin Mott ground state and drive the

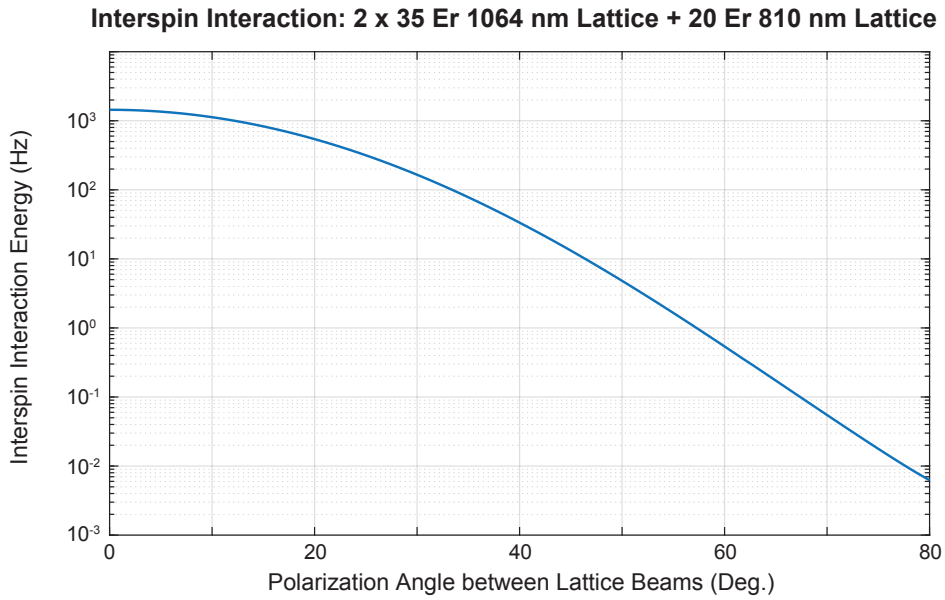


Figure 5-9: The inter-spin interaction as a function of polarization angle. Calculation of the inter-spin interaction in the lowest band of the optical lattice with two, 1064 nm lattices of 35 $E_r$ depth, in the $y$- and $z$-directions in addition to a spin-dependent, 20 $E_r$, 810 nm lattice in the $x$-direction.

quantum phase transition to a magnetic state of matter.

One final piece of intuition we can gather from the curve in figure 5-9 is that the lattice does not necessarily need to be in full lin⊥lin polarization in order to suppress the inter-spin interactions sufficiently to prepare the spin Mott state. For polarization angles $> 45°$, $U_{\uparrow\downarrow}$ is the smallest energy scale in the problem, even smaller than tunneling, $t$, and as such we can think of the system as two independent Mott insulators spaced one-half a lattice constant away from each other. This has the additional advantage that away from full lin⊥lin the amount of laser power needed to produce a deep lattice is reduced, so the amount of spontaneous scattering can be reduced as well. For polarization angles $\sim 45°$, $U_{\uparrow\downarrow}$ becomes comparable to $t$ and the system becomes qualitatively less like two independent, interlaced Mott insulators and more similar to the spin-1 Heisenberg mapping described previously. These two different regimes will become important in understanding several non-idealities of the system that will be discussed in section 5.6.3.

Now that we have developed an understanding of the spin-dependent lattice, un-

derstood the relevant physics for tuning the interaction energy, $U_{\uparrow\downarrow}$, and understood how to achieve long lattice lifetime, we wish to demonstrate the ability to load, with high fidelity, the charge and spin ground states of the spin Mott, detect spin correlations, and drive the transition to a magnetic ground state.

## 5.4 The Spin-Mott Insulator

With $^{87}$Rb in a spin-dependent optical lattice there are three parts of the spin-1 Heisenberg phase diagram that we can access: the spin Mott, the $xy$-ferromagnet, and the near-isotropic $z$-ferromagnet. We begin by discussing the spin Mott state with the goal of understanding the Heisenberg model in this limit and subsequently demonstrating and characterizing this ground state in our spin-dependent optical lattice.

As a reminder, the form of the spin-1 Heisenberg we realize is:

$$H = \sum_{\langle ij \rangle} \left( \frac{J_\perp}{2} \hat{S}_i^+ \hat{S}_j^- + J_z \hat{S}_i^z \hat{S}_j^z + \text{H.c.} \right) + u \sum_i (\hat{S}_i^z)^2 + h \sum_i \hat{S}_i^z, \tag{5.31}$$

assuming that, as is the case with $^{87}$Rb, the intra-spin interactions are nearly equal, $W = U_{\uparrow\uparrow} = U_{\downarrow\downarrow}$, and that the deviations from isotropic are not large, $\frac{W - U_{\uparrow\downarrow}}{W} \ll 1$, such that the parameters of the effective Hamiltonian are:

$$J_\perp = -\frac{4t^2}{U_{\uparrow\downarrow}} \tag{5.32}$$

$$J_z \approx -\frac{14t^2}{W} + \frac{10t^2}{U_{\uparrow\downarrow}} \tag{5.33}$$

$$u \approx (W - U_{\uparrow\downarrow}) - \frac{5t^2}{W} + \frac{5t^2}{U_{\uparrow\downarrow}} \tag{5.34}$$

$$h_z \approx -\frac{10t^2}{W} + \frac{10t^2}{U_{\uparrow\downarrow}} + h_{\text{ext}} \tag{5.35}$$

For the remainder of this chapter, we will work solely in the regime of a balanced Bose gas, such that $\mu_\uparrow = \mu_\downarrow$ and therefore $h_z = 0$.

In the limit that $u$ is large compared to all other energy scales in the system,

corresponding to $U_{\uparrow\downarrow} < W$, the Hamiltonian is dominated by the $u(\hat{S}_i^z)^2$ term. Analogous to a Mott insulating state of a single spin component, we can write down a wavefunction which corresponds to a product state of all particles in the lowest energy state of this term:

$$|\Psi\rangle_{\mathrm{SM}} = \prod_i^N |m_s = 0\rangle_i \tag{5.36}$$

where $N$ is the number of spins in the system or half of the total number of particles in the $n = 2$ Mott state. Intuitively, we can understand this state as a purely local state of exactly one spin up and one spin down per state. The spin Mott has no long range order and does not break any symmetries of the Hamiltonian.

Experimentally, we implement this system with the $|\uparrow\rangle = |1, -1\rangle$ and $|\downarrow\rangle = |1, 1\rangle$ mixture of $^{87}$Rb hyperfine ground states. To make this mixture, we begin with $\sim 10^3$ atoms in the $|1, -1\rangle$ state whose atom number is easily adjusted by varying the evaporation knife in a tightly confining dimple potential with a horizontally applied gradient. In a series of two fast RF frequency sweeps we quickly make a 50:50 mixture of the $|1, -1\rangle$ and $|2, 0\rangle$ states and then quickly transfer the $|2, 0\rangle$ atoms to the $|1, 1\rangle$ state. At the end of this sequence we produce a two-component BEC with no visible thermal fraction and no detectable residual $|2, 0\rangle$ atoms. We work at a finite bias field of $\sim$9.09 G, so this spin mixture is stable to spin-changing collisions due to the quadratic Zeeman shift of the $|1, 0\rangle$ state, and is stable to spin-relaxation due to the use of the lowest hyperfine manifold. The mixture can decay via dipolar relaxation, but this process is slower than the background gas collisions. The $|\uparrow\rangle = |1, -1\rangle$ and $|\downarrow\rangle = |1, 1\rangle$ mixture is weakly immiscible, so we turn on a weak $\sim$1 $E_r$ spin-dependent lattice to maintain miscibility. After a short hold to reset the integrator of the lattice intensity servo, the atoms are loaded into a three dimensional optical lattice where two directions of the lattice have a wavelength of 1064 nm and one direction is a spin-dependent lattice operating at a wavelength of 810 nm with a liquid crystal variable retarder controlling the polarization rotation of the retroreflected beam.

To begin, we probe the separation between spin-up and spin-down wavefunctions to demonstrate the power of the spin-dependent lattice to tune the inter-spin inter-

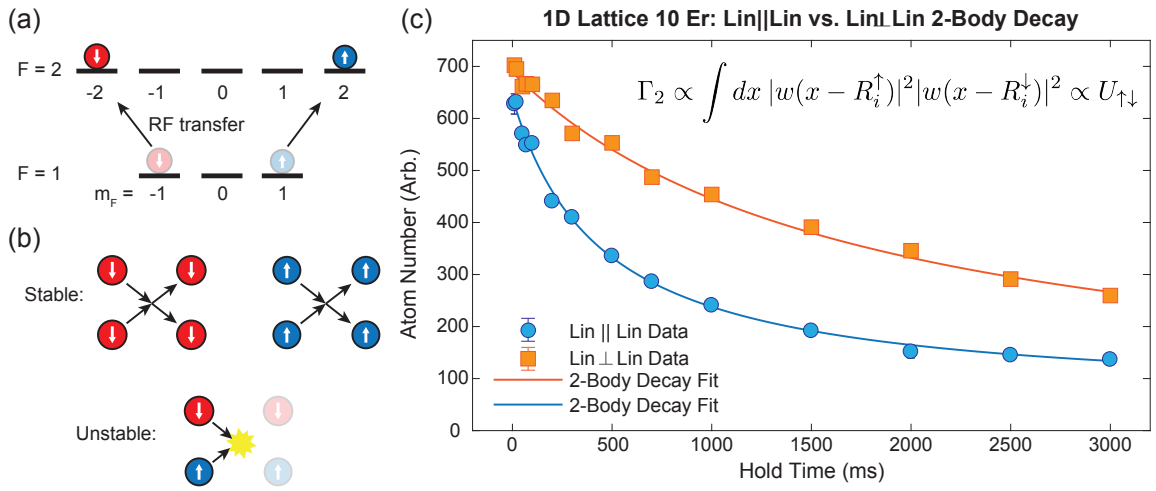


Figure 5-10: Using two-body loss to detect the wavefunction overlap between different spins. (a) Starting in the $|1,\pm1\rangle$ states, atoms are transferred to the $|2,\pm2\rangle$ mixture. (b) Collisions between $|2,2\rangle$ atoms and $|2,-2\rangle$ atoms are stable whereas collisions between $|2,2\rangle$ and $|2,-2\rangle$ atoms are unstable to spin relaxation. (c) The suppression of two-body decay by rotating the lattice polarization from lin||lin to lin⊥lin indicates the suppression of the density overlap integral which appears in both the loss rate as well as the inter-spin interaction parameter.

action energy via the wavefunction overlap integral. To measure this, we work in a one-dimensional lattice where the two 1064 nm lattices are turned to zero intensity and the 810 nm spin-dependent lattice is tuned to 10 $E_r$. To measure the overlap, we will induce two-body loss in a spin-selective way such that the loss rate is proportional to the same matrix element as the inter-spin interactions. Practically, this is accomplished by transferring both spin states $|1,\pm1\rangle$ to the $|2,\pm2\rangle$ states with a fast RF frequency sweep as depicted in 5-10(a). In this mixture, intra-spin collisions are stable because the collision partners are of maximal angular momentum projection whereas inter-spin collisions can lead to decay by spin relaxation as depicted in 5-10(b). As a result, the corresponding two-body loss rate, shown in 5-10(c) is proportional to the density overlap of inter-spin wavefunction, the same as that which appears in the inter-spin interaction energy. The resulting two-body loss curve for the total atom number is shown in figure 5-10(c) and clearly shows that the spin-dependent lattice suppresses the overlap of the up- and down-spin wavefunctions. The residual decay of the atom number in the lin⊥lin polarization configuration is likely due to the light

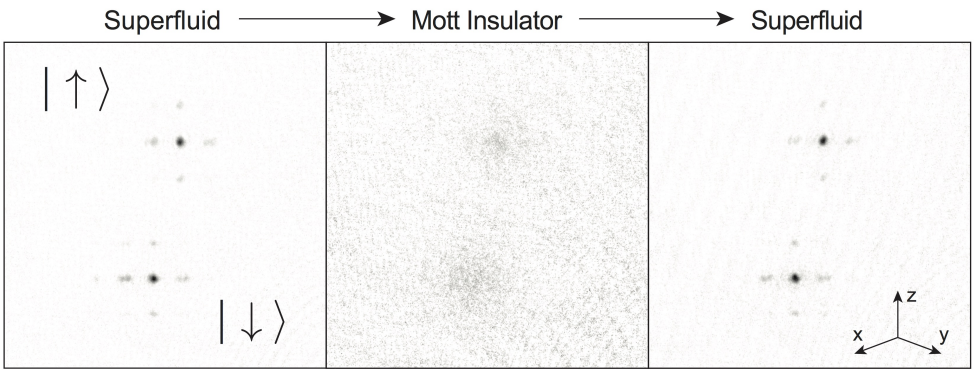


Figure 5-11: Reversible loading of the two-component superfluid into a Mott insulating state. The first two panels show the initial two-component superfluid – separated by a Stern-Gerlach pulse in time-of-flight – entering the Mott transition as the lattice is ramped from $10E_r$ to $20E_r$. The last panel shows the reversibility of the Mott state upon ramping back to $10E_r$, indirectly showing the preparation of the Mott state of the two-component system.

scattering lifetime of atoms in the lattice.

With the ability to tune the spin-dependent interactions now demonstrated, the spin Mott insulating state can now be prepared in the lattice by increasing the lattice depths in all three dimensions to 20 $E_r$. With the waveplate in lin$\perp$lin configuration, we can tune the inter-spin interactions to be less than the intra-spin interactions, $U_{\uparrow\downarrow} \ll W$, and realize the spin Mott insulating groundstate of the spin-1 Heisenberg model. To prove this, we will demonstrate five different aspects of this spin Mott state. To begin, we demonstrate that this loading of the condensate into the Mott state happens in a reversible manner and does not add excessive entropy. Qualitatively, this is demonstrated in the images shown in figure 5-11. All three images are taken in 15 ms time-of-flight where a large magnetic field gradient is applied for the first 3 ms of the free evolution to spatially separate spin components. Arranged from left to right, the images in figure 5-11 are taken before the two-component superfluid enters the Mott insulating regime, in the Mott regime, and upon adiabatically reversing the Mott state back to the superfluid. Note that these images are taken with the camera oriented along an axis which is at 45° to the $x$- and $y$-axis of the lattice, so the diffraction orders of the 810 nm lattice in the $x$-direction and the 1064 nm lattice in the $y$-direction do not overlap when viewed from the $x + y$ direction, hence the

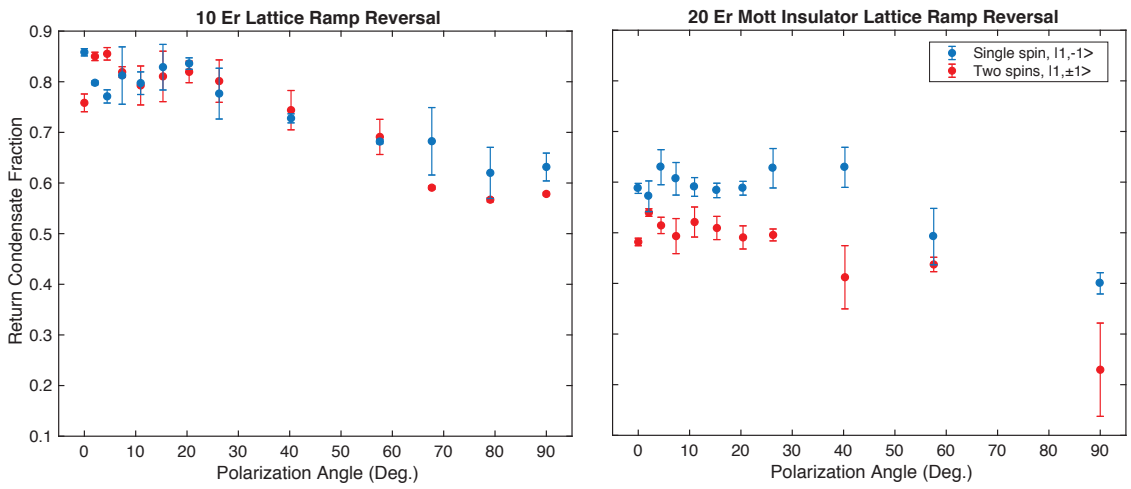


Figure 5-12: Measurement of the BEC condensate fraction after reversible loading of the spin Mott. (Left) After ramping all three lattice directions to 10 $E_r$ depth, the condensate fraction retrieved upon return to the BEC state is plotted as a function of polarization angle. (Right) The same sequence as the left panel, but ramping to a higher lattice depths of $20E_r$. After crossing the Mott transition, the BEC retrieved from the spin mixture has a lower condensate fraction than that where only a single component, at the same total density, is subjected to the same ramp reversal.

doubling of the diffraction orders in the horizontal direction in the first and third panels as well as the different apparent length scales for the vertical and horizontal diffraction orders.

The ability to adiabatically retrieve a superfluid diffraction pattern from the featureless time-of-flight image of the Mott state is indirect evidence for the preparation of the Mott insulating ground state in the second panel. If, instead of taking a superfluid diffraction image, we ramp back to BEC, we can measure the condensate fraction more reliably and infer some bounds on the entropy of the state in the Mott regime. This method only allows us to set a bound on the entropy, since as we dynamically ramp across the quantum phase transition the system does not generally follow adiabatically, but instead sees some domain formation from crossing the transition at a finite rate. Regardless, the result of changing the waveplate angle, and adjusting the intensity to compensate for the different potential depth at each waveplate angle, and ramping into and out of the spin Mott state is shown in figure 5-12. For lattice ramps not limited by light scattering, we expect the fidelity of the ramp to the Mott state

and back to be independent of polarization angle. For small deviations this is true, but for polarization angles approaching lin$\perp$lin the condensate fraction gets worse, approaching a minimum at fully lin$\perp$lin of 25%. Using a model of entropy creation in the lattice ramp which is symmetric for the ramp in and the ramp out of the superfluid, we can calculate the entropy of the BEC and determine the trap-averaged entropy of the cloud in the Mott state. Next, using the model of frozen particle-hole excitations in the Mott state that we developed in chapter 2, we can estimate the number of thermally-driven particle and hole excitations in the Mott state. For condensate fractions of $\sim 70\%$ after ramping back to the two-component BEC, we can infer that the hole population is about 10% and the same for the particle fraction. As a result, we expect that in a typical chain of 10 $n = 2$ sites in the Mott state, we should have approximately one particle and hole excitation if we can achieve a $\sim 70\%$ round-trip condensate fraction. Realization of the Heisenberg mapping requires us to ramp beyond the one-dimensional Mott transition, so a typical experimental cycle requires us to ramp the lattice depth of the spin-dependent lattice anywhere from 10 to 20 $E_r$, two limits shown in figure 5-12, while the two transverse lattices are at a high depth of 20 $E_r$. The difference between the condensate fraction of a single spin component and two spin components in the deepest lattice depths at 20 $E_r$ is not currently understood experimentally.

Particle and hole excitations lie outside of the Hilbert space of the mapping to the spin-1 Heisenberg model we developed earlier, but we can understand how they can create spin excitations by considering that they move dominantly via direct, spin-independent tunneling in the lattice – the Mott state can be considered a particle or a hole vacuum such that these excitations move freely to first approximation – and as such can destroy an $xy$- or anti-ferromagnetically ordered state. Similar phenomenology is seen by doping the fermionic Mott insulator which quickly destroys antiferromagnetic order. In such systems, doping on the order of 10% typically destroys magnetic order, highlighting the need for high fidelity preparation of cold Mott insulators.

Given the ability to adiabatically prepare the spin Mott groundstate in a spin-

dependent lattice and estimate the charge entropy, we next aim to demonstrate a long coherence lifetime of this state such that we can begin to manipulate the spins in this lattice in order to directly detect microscopic spin correlations as well as to drive the phase transition between the spin Mott and the $xy$-ferromagnet. In order to measure the lifetime of the Mott state we either measure the visibility of the matter wave diffraction pattern from the lattice in time-of-flight or we measure the condensate fraction after ramping the Mott state back to a bulk condensate. In the lin$\perp$lin configuration we have between 100 and 200 ms lifetime and the lifetime increases up to 1.5 seconds in the lin$\parallel$lin configuration. No appreciable particle loss is detected on these timescales. These lifetimes are the $1/e$ times for an exponential fit, so in a hand-waving sense we can say that we maintain high fidelity for some 10% of this total time. The complex interplay of light scattering effects and adiabatic ramps from the spin Mott have been studied in [137], indicating that 100 ms is sufficiently long to see algebraically decaying correlations over a finite spin-1 chain. Most of the ramp time in this picture is spent close to the lin$\parallel$lin configuration so over the 100 ms timescale we should maintain appreciable state fidelity. These lattice lifetimes are shorter than the theoretically predicted light scattering lifetimes; however, as discussed in chapter 2, the heating and thermalization mechanisms in the lattice are complex and nevertheless are within an order of magnitude of what is predicted by a single particle calculation. In addition, during the hold, the number of atoms optically pumped to other spins states remain at maximum 1% of the total atom number.

## 5.5 Detecting Local Spin Correlations

Although the reversibility of the spin Mott state to a two-component superfluid suggests the successful loading of the ground state of the spin Hamiltonian, it does not constitute proof of preparing this state. Spin excitations may be long-lived and might relax without creating much excitation energy in the final state so that the measurement of condensate fraction is not sensitive to spin excitations. As a result, we develop a detection technique in order to directly probe the local composition of the spins and

show the existence of the spin Mott.

The spin Mott is a special state in the ground state of the Heisenberg phase diagram because it does not break any symmetries and thus features a large gap. In the limit of large $u = W - U_{\uparrow\downarrow}$, the wavefunction can be written as a product state of pairs of up- and down-spin atoms localized on each site – a perfect array of exactly two particles, one up- and one down-spin, on each site. A clear prediction emerging from this picture is that the on-site correlation function between spin-up and spin-down atoms should feature a 100% probability of finding this pair of spins localized on a site. Taking a lesson from the success of using two-body spin relaxation losses as a measure of the overlap between up- and down-spins, we have developed a detection method to detect spin correlations within the $n = 2$ subspace of the two-component Mott insulator in order to probe the local spin correlations in the Mott insulator.

A schematic of the technique we developed to measure local spin correlations is shown in figure 5-13. The measurement involves taking the starting state of interest and merging sites within the unit cell to create a spin-independent potential at the same time that the lattice depth is ramped into a deep, 35 $E_r$ lattice in order to freeze all tunneling dynamics on the ∼200 ms timescale. The detection sequence is then composed of three independent measurements: counting the total atom number, $N_{\mathrm{all}}$, the atom number remaining after removing all doublons (doubly occupied sites), $N_{\mathrm{dbl}}$, and finally the atom number remaining after removing all spin-paired doublons composed of one spin-up and one spin-down atom localized on a site, $N_{\mathrm{pair}}$. From these three measurements we can construct the fraction of doublons in the sample which occupy the $|m_s = 0\rangle$ state:

$$f = \frac{\text{Number of spin-pairs}}{\text{Total doublon number}} = \frac{N_{\mathrm{all}} - N_{\mathrm{pair}}}{N_{\mathrm{all}} - N_{\mathrm{dbl}}}. \tag{5.37}$$

Due to the presence of the harmonic trap, in the lin‖lin configuration only up to approximately half of the atoms in the sample exist in the $n = 2$ Mott insulating shell. As a result, we need a method to normalize the signal in the spin-dependent channel by a measure of the total number of doublons in the sample. Starting with the

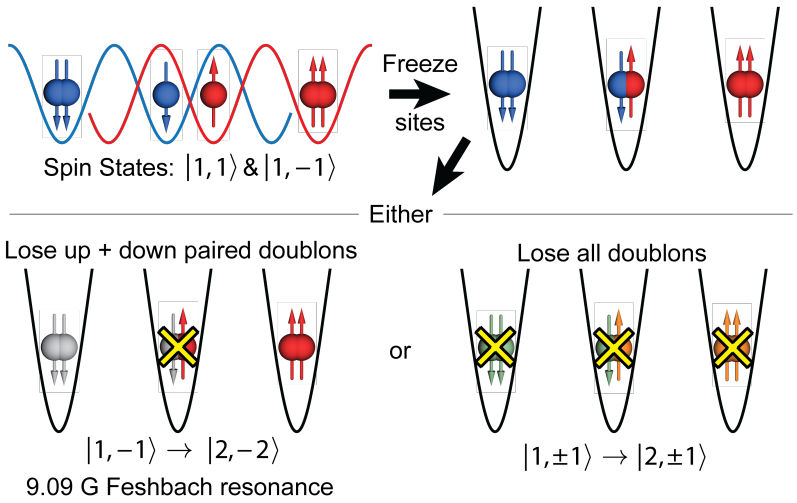


Figure 5-13: Detection scheme utilizing spin-dependent losses as a probe of local spin-spin correlations. Starting from an arbitrary state of interest, the local spin state is frozen in by quickly ramping the lattice to 35 $E_r$ in all three directions at the same time the spins are merged by ramping to the lin||lin configuration. Losses are induced by RF transfer to the unstable states indicated in which either all doublons are lost or only spin-up and spin-down pairs are lost due to the presence of a lossy low-field Feshbach resonance.

$|1, \pm 1\rangle$ mixture, we can accomplish this normalization by transferring both spin states to the collisionally unstable states $|2, \pm 1\rangle$. After transfer, lattice sites which contain a single particle have no collision partner and thus remain trapped in the sample. However, lattice sites which contain two particles can collide with each other and are subsequently lost – independent of the on-site spin composition of the doublon – from the lattice due to spin relaxation collisions after a 200 ms hold in the lattice. The difference between counting the total atom number and the atom number remaining after removing all doublons in a spin-independent way yields the total atom number within the $n = 2$ subspace.

Next, we determine the spin composition of the doublons by transferring only the $|1, -1\rangle$ spins to the $|2, -2\rangle$ state with a fast RF frequency sweep. In this configuration collisions between spin-polarized doublons, $|m_s = \pm 1\rangle$ – corresponding to collisions between two $|1, 1\rangle$ atoms or two $|2, -2\rangle$ atoms – are stable. However, rapid loss in the inter-spin collision channel can be induced by ramping the magnetic field to the $\sim$9.095 gauss a Feshbach resonance between $|1, 1\rangle$ and $|2, -2\rangle$ atoms. Measuring the number of atoms remaining after a 200 ms hold on the Feshbach resonance and subtracting this result from the total atom number reveals the total number of spin-paired doublons in the sample. Unfortunately, the $|2, \pm 2\rangle$ mixture used to detect microscopic separation between the spin states in the previous section proved unsuitable for this detection channel since spin relaxation happened too slowly compared to the total lattice lifetime.

With a measure of the total number of spin-paired doublons normalized by a measurement of the total number of $n = 2$ atoms, we can finally construct the quantity we call the spin-paired doublon fraction, $f$. Figure 5-14(a) shows the result of these three different measurements as a function of the polarization angle of the spin-dependent lattice during the ramp to the Mott insulating state. The corresponding spin-paired doublon fraction, $f$, is shown in figure 5-14(b). There are three different regions to note within figure 5-14. Most importantly, at large polarization angle, $> 45°$, the majority of spins are in the paired $|0\rangle$ state with the maximum occurring at exactly 90° polarization angle with more than 95% of spins in the paired channel. This

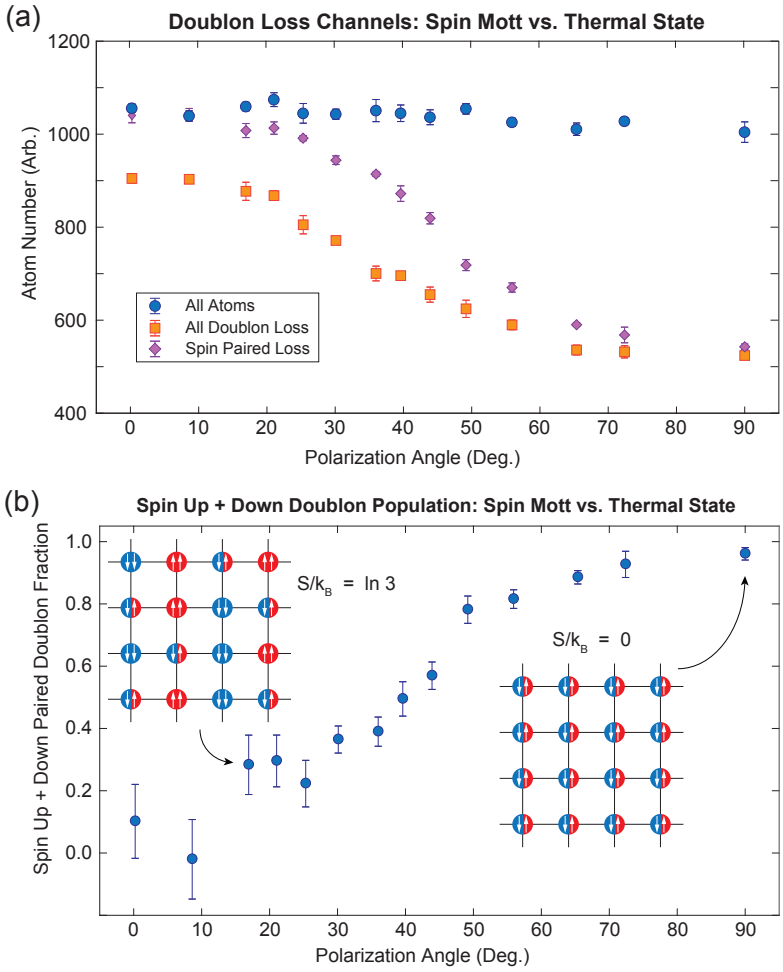


Figure 5-14: Spin correlations in the two-component Mott as a function of the retroreflected polarization angle. Loading a balanced spin mixture into a $20E_r$ deep lattice with varying retroflection polarization angle and measuring the projection of the local spin onto the spin-paired $|0\rangle$ state of doublons. (Top) the final signal is composed of three independent measurements at each polarization angle of the total atom number, the atom number remaining after removing all doublons, and the atom number remaining after removing all spin-paired doublons. (Bottom) The resulting fraction of doublons in the $|0\rangle$ state, showing the high fidelity preparation of the spin Mott in the lin$\perp$lin configuration.

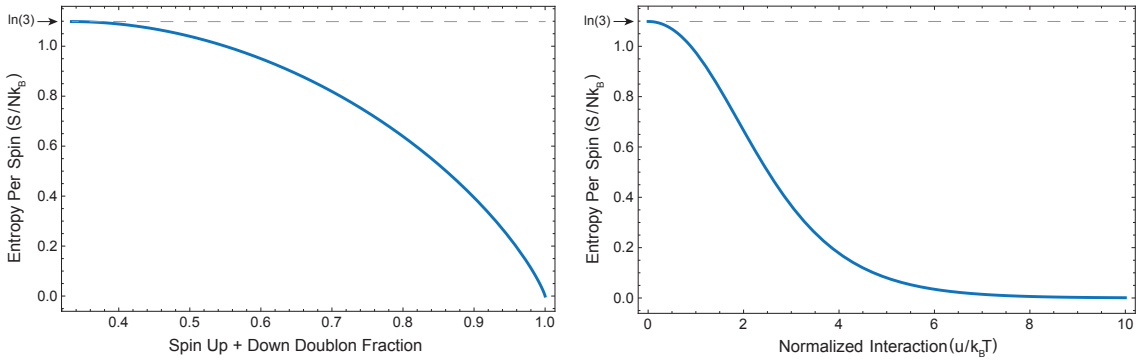


Figure 5-15: Temperature and entropy in the spin Mott as a function of the spin-paired doublon fraction. (Left) Assuming a balanced mixture, the spin entropy can be determined from the spin-paired doublon fraction in the limit of vanishing exchange, $J_\perp = J_z = 0$. (Right) From the entropy the dimensionless spin temperature, $u/k_BT$ can be determined.

decreases slowly but remains high as the polarization crosses 45° before the population enters a second regime where it slowly decreases – consistent with a decreasing spin gap – down to the third regime where the spin-paired doublon fraction reaches its thermal value of 1/3, which corresponds to an incoherent mixture of all three spin states within the lowest band of the optical lattice.

From the values of the spin-paired doublon fraction in the first region we conclude that, by tuning the spin-dependent interaction energy, we have successfully loaded the spin Mott insulating ground state of the spin-1 Heisenberg model. To develop a sense of the residual spin entropy in the spin Mott, we can use the local triplet basis of states to construct an estimate of the spin entropy via Boltzmann's formula, $S/k_B = \sum_i p_i \ln p_i$. The resulting entropy as a function of the spin-paired doublon fraction is shown in figure 5-15. In addition, using this local basis of states, and assuming spin excitations remain localized and are not itinerant, we can make an estimate of the partition function of our effective spin Hamiltonian to be, $Z = (1 + 2e^{-\beta u})^N$, which comes simply from the $(\hat{S}_i^z)^2$ term of the Hamiltonian, where $u$ is the spin interaction, $\beta$ is the inverse spin temperature in the $n = 2$ Hilbert space, and $N$ is the number of spins in the sample. Using this information we can derive an estimate of the relation between the entropy and the normalized temperature/interaction energy, $\beta u = u/k_BT$, seen plotted on the right side of figure 5-15. From these plots, we

can estimate that at a 95% spin-paired doublon fraction that the corresponding spin entropy is $\sim 0.2\ k_B$ per spin. At a maximum interaction energy of $\sim$1 kHz, this then corresponds to a temperature of $\sim$10 nK. This highlights the power of the spin Mott to allow us to prepare a Heisenberg ground state at higher initial temperatures than that set by the $\sim$10 pK superexchange energy scale. The power of the spin Mott is that this highly gapped state is adiabatically connected to the magnetic ground states with a gap, set by the frequency of the lowest spin wave in the system which is $\sim$1000 times lower energy. As a result, a ramp at constant entropy can produce a temperature which is $\sim$1000 times lower, providing direct access to the temperature scales needed to observe long-range magnetic ordering in the system.

One caveat to note here, which will become important in the next section, is that our detection channel can only observe spins that are within the $n = 2$ Hilbert space. As a result, hole excitations only appear as a reduction in the total contrast of the total number of doublons relative to the total number of atoms, but do not impact the difference between the total number of doublons and the number of spin-paired doublons, and therefore do not impact the spin-paired doublon fraction. Our earlier estimate of the entropy in this sector found that on average we have one particle and hole excitation in a chain of ten sites.

In contrast to region close to the lin$\perp$lin polarization configuration shown in figure 5-14, when the lattice is raised in the region close to the lin$\parallel$lin configuration, the system is ramped into a state with either a low spin gap, or across the quantum phase transition directly into the magnetic part of the phase diagram. For understanding this state, it is useful to consider the limiting cases of thermal spins and a perfectly ordered $xy$-ferromagnet. In the limit of infinite spin temperature, the spin occupation in any site is random, as depicted in the upper left inset in figure 5-14(b), and the population in the $|m = 0\rangle$ state is $1/3$. As we will see in the next section, in a perfectly ordered $xy$-ferromagnet, the spin state can be thought of as an equal superposition of up and down spins, so the spin-paired doublon fraction would go to $1/2$ in this limit. Therefore, for polarizations close to lin$\parallel$lin, the spin-paired doublon fraction of $\sim 1/3$ indicates the thermal nature of the resulting spin state produced by a typical ramp

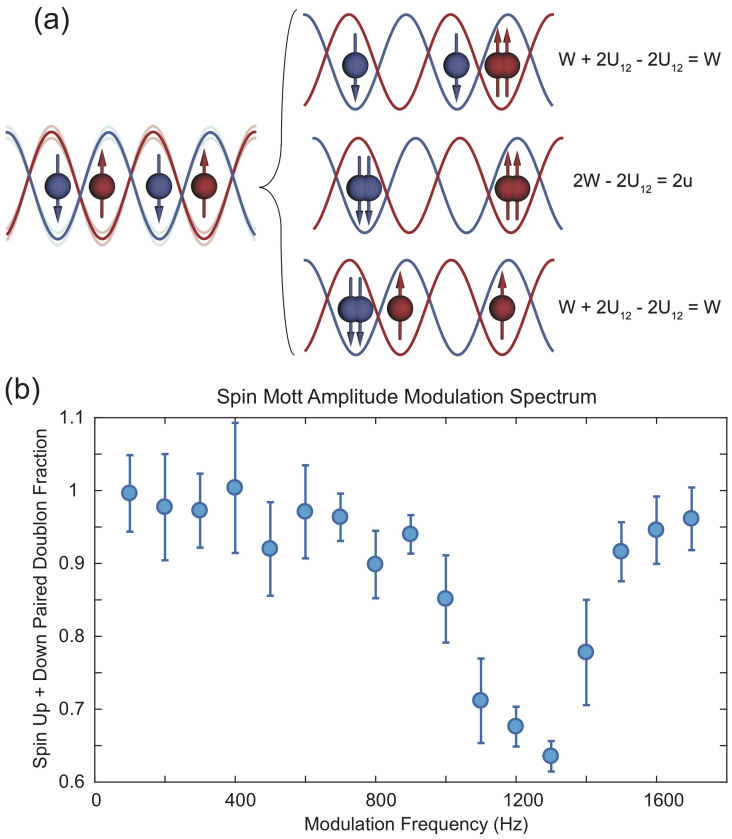


Figure 5-16: Amplitude modulation spectroscopy of the spin Mott. (Top) In the lin⊥lin configuration, modulation of the amplitude can couple to the three final states with the lowest lying excitation being a charged excitation to a particle-hole excitation in either the $|\uparrow\rangle$ or the $|\downarrow\rangle$ Mott component. (Bottom) Response of the spin-paired doublon fraction in the spin Mott to a 12% amplitude modulation of the lattice depth for 30 ms. Consistent with the picture of a gapped state, the system exhibits no response at low frequencies.

into the two-component Mott insulator, and highlights the difficulty in observing spin correlations to date in spin-independent lattices with a system close to the isotropic point of the Heisenberg model.

One important feature of the spin Mott is the existence of a finite excitation gap in both the spin and charge degrees of freedom. The gapped nature of the ground state is what enables the high fidelity preparation of the spin ground state of the effective Heisenberg model. Two different types of excitations which compose the first excited states are shown in figure 5-16(a). One reflects an excitation in the charge sector of the Mott state, depicted schematically in the top and bottom final

states on the righthand side of 5-16(a). The second reflects an excitation in the spin sector but not the charge sector, depicted in the central frame of 5-16(a). In the limit of $U_{\uparrow\downarrow} \to 0$, the charge gap is the lowest lying mode, and in the limit of finite $U_{\uparrow\downarrow} > W/2$, the spin gap becomes the lowest lying mode. The existence of this finite excitation gap in the spin Mott state is probed in the lin⊥lin configuration by amplitude-modulation spectroscopy. Experimentally, after loading the spin-Mott state into a three dimensional optical lattice of depth 20 $E_r$ in the spin-independent directions and 12 $E_r$ in the spin-dependent direction, the amplitude of the lattice laser intensity is modulated by ∼10% for 20 ms, after which the modulation is stopped and the lattice depth is increased to enter the doublon detection sequence. The resulting spectrum of the spin-paired doublon fraction is shown in figure 5-16(b). Examining the spectrum we see a clear resonance at a frequency corresponding to $W$ in the system. More importantly, below this frequency the system does not respond to the modulation, consistent with the presence of a gap in the ground state.

So far, we have discussed the nature of the spin Mott insulating state in the spin-1 Heisenberg mapping, its realization with two-component bosons in an optical lattice, and how to detect and characterize this state. Most importantly, we have highlighted how this state enables the preparation of a low spin-entropy state in the Mott insulator. This state, which is perfectly ordered in both the charge and spin degrees of freedom, now is perfectly situated to perform an adiabatic ramp to a magnetic phase of matter where the low spin and charge entropies should allow preparation of a long-range ordered state.

## 5.6 The $xy$-Ferromagnet

The power of the low spin entropy of the spin Mott state comes from the ability to controllably ramp from this highly gapped state to a magnetic state with a small gap. Given the initial spin entropy of 0.2 $k_B$ per spin, such an adiabatic ramp would give access to physics in the regime of temperatures as low as ∼10 pK where long-range spin-ordering should occur. In this chapter we present some initial attempts at such

an adiabatic ramp and describe challenges for the experiment moving forward.

### 5.6.1 The Groundstate Phase Diagram

The ability use the low entropy of the spin Mott in order to adiabatically connect to the $xy$-ferromagnetic state was first highlighted in the context of two-component bosons in an $n = 2$ state in the proposal and numerical work of ref [137]. Experiments exploring this transition will be described in the following subsection, but for context and interpretation we first present a theoretical framework in which we want to understand the resulting state. Following the arguments of ref. [5], the ground state wavefunction of the spin-1 chain can be approximated by the following ansatz wavefunction for variational calculations:

$$|\Psi\rangle_{S=1} = \prod_{i=1}^{N} \left( \cos\frac{\theta}{2}|0\rangle_i + e^{i\eta}\sin\frac{\theta}{2}\left(e^{i\phi}\cos\frac{\chi}{2}|1\rangle_i + e^{-i\phi}\sin\frac{\chi}{2}|-1\rangle_i\right)\right). \tag{5.38}$$

The transition from the spin Mott to a magnetic state is controlled by the parameter, $\theta$, which accounts for the amplitude of the wavefunction in the $|\pm 1\rangle$ states, and has phase of the superposition, $\phi$. Using the intuition of a coherent state of bosons to formulate an order parameter, the average value of the spin annihilation operator is used to formulate the spin-order parameter, $\psi$:

$$\langle \hat{S}_i^- \rangle = \frac{1}{\sqrt{2}} e^{i\eta}\sin\theta\left(e^{-i\phi}\sin\frac{\chi}{2} + e^{i\phi}\cos\frac{\chi}{2}\right) \propto \sin\theta \equiv \psi. \tag{5.39}$$

The spin-order parameter, $\psi$ is a real number and is multiplied by a phase which encodes the phase of the superposition state, $\phi$ at each point in space.

Using the general ansatz wavefunction in equation 5.38, we can gain intuition for the ground state and phase diagram by calculating a variational energy function for the spin-1 Heisenberg Hamiltonian seen in equation 5.31. Assuming that the amplitude order parameter, $\psi$ is small near the phase boundary we can expand to

second order near the transition point:

$$\begin{aligned} E &= -\frac{J_\perp}{2}\sin^2\theta\big(1+\sin\chi\cos 2\eta\big) - J_z\sin^4\frac{\theta}{2}\cos^2\chi + u\sin^2\frac{\theta}{2} - h\sin^2\frac{\theta}{2}\cos\chi \\ &= -\frac{J_\perp}{2}\psi^2\big(1+\sin\chi\cos 2\eta\big) - J_z(1-\sqrt{1-\psi^2})^2\cos^2\chi + \dots \\ &\quad \dots(u - h\cos\chi)(1-\sqrt{1-\psi^2}) \qquad (5.40) \\ &\approx \left[-\frac{J_\perp}{2}\big(1+\sin\chi\cos 2\eta\big) + \frac{u}{4} - \frac{h}{4}\cos\chi\right]\psi^2. \qquad (5.41) \end{aligned}$$

Note that the Ising term, proportional to $J_z$, appears first in the second term, at the order of $\psi^4$, in the expansion of the energy functional. Assuming that the spins are miscible and $J_z < J_\perp$, the fourth order term is always positive and the system makes the transition to the $xy$-ferromagnetic phase. Past the isotropic point where $J_z \geq J_\perp$, this assumption breaks down and the system makes a transition to a $z$-ferromagnetic phase. Here, we restrict the treatment to the $xy$-regime.

We can now extract variational solutions for the spin-1 $xy$-ferromagnet by minimizing the energy functional. We see by inspection that this will happen for $\eta = 0, \pi$, which then allows us to extract the critical point for the spin Mott to $xy$ transition by looking at the point where the $xy$ order parameter picks up a finite value. This point occurs when the coefficient of the quadratic term in $\psi^2$ in equation 5.41 switches from positive to negative, so the transition point happens when this prefactor is zero. From equation 5.41 we can also see that the phase transition point depends on the variational parameter $\chi$ as well. If we also minimize the energy functional with respect to $\chi$, we get a minimization relation for $\chi$:

$$\begin{aligned} \frac{\partial E}{\partial \chi} &= \left[-\frac{J_\perp}{2}\cos\chi + \frac{h}{4}\sin\chi\right]\psi^2 = 0 \\ \sin\chi &= \frac{2J_\perp}{h}\cos\chi, \text{ or: } \quad \tan\chi = \frac{2J_\perp}{h}. \qquad (5.42) \end{aligned}$$

Looking back at the expression for the phase transition point, we can use the information from the minimization procedure with respect to $\chi$ to simplify the expression

for the phase boundary:

$$\frac{2J_\perp}{h}\big(1+\sin\chi\big)-\frac{u}{h}+\cos\chi=0 \tag{5.43}$$

$$\Big(\tan\chi+\tan\chi\sin\chi+\cos\chi=\frac{u}{h}\Big)\times\cos\chi \tag{5.44}$$

$$\sin\chi+1=\frac{u}{h}\cos\chi. \tag{5.45}$$

Together with equation 5.42, this expression can be used to solve for the angles $\sin\chi=\frac{2J_\perp}{u-2J_\perp}$ and $\cos\chi=\frac{h}{u-2J_\perp}$. Plugging this back into the phase boundary expression, we get a critical value for the mean field phase transition point given by:

$$\left.\frac{J_\perp}{u}\right|_c=\frac{1}{4}\left(1-\left(\frac{h}{u}\right)^2\right). \tag{5.46}$$

In the absence of an externally applied magnetic field ($\mu_\uparrow=\mu_\downarrow$ and $U_{\uparrow\downarrow}\approx W$) the external magnetic field, $h_z$, goes to zero and we find that this mean-field variational treatment predicts a phase boundary of $\left.\frac{J_\perp}{u}\right|_c=\frac{1}{4}$. This prediction for the phase boundary is shown in figure 5-17(a) as a black curve overlayed on a numerically calculated phase diagram. Because this is a one-dimensional system, we can expect quantum fluctuations to strongly modify the physics from the mean-field predictions and this can be seen in the deviation of the shape of the numerically calculated gap shown in figure 5-17 from the mean-field boundary.

Nevertheless, the mean-field wavefunction is useful for gaining intuition about the $xy$ phase and the relations between the variational parameters and Heisenberg model parameters can be used to calculate other quantities, such as the wavefunction or the expectation value of any operator. For example, the wavefunction has a particularly simple form in the limit of no effective magnetic field, $h=0$. In this limit $\tan\chi\to\infty$ such that $\chi\to\frac{\pi}{2}$ the wavefunction takes a particularly simple form:

$$|\Psi\rangle\overset{h\to0}{=}\prod_i^N\left(\cos\frac{\theta}{2}|0\rangle_i+\sin\frac{\theta}{2}\left(\frac{e^{i\phi}}{\sqrt{2}}|1\rangle_i+\frac{e^{-i\phi}}{\sqrt{2}}|-1\rangle_i\right)\right). \tag{5.47}$$

This limit makes intuitive sense when we look at the angle of the magnetization

vector and see that it is not canted out of the $xy$ plane; the wavefunction instead contains equal $|1\rangle$ and $|-1\rangle$ amplitudes. As a result, we understand that the action of a small magnetic field due to mismatch between $W$ and $U_{\uparrow\downarrow}$ does not destroy magnetic ordering, but instead suppresses the transition point quadratically in the parameter $1-\left(\frac{h}{u}\right)^2$. Examining the wavefunction for small $h$ or equivalently $\chi < \frac{\pi}{2}$, this corresponds to a tipping of the magnetization vector out of plane – a canted $xy$-ferromagnet.

Finally, looking at the amplitude of the different spin components in the $xy$ wavefunction in 5.47 we see that the parameter, $\theta$ encodes the order parameter density, $\psi$ – which we will call the spin superfluid order parameter – and controls the amount the $|\pm 1\rangle$ states are admixed into the $|0\rangle$ state as we ramp from the spin Mott to the $xy$ ferromagnet. Rewriting the phase terms as functions of the spin superfluid order parameter:

$$\cos\frac{\theta}{2} = \sqrt{\frac{1}{2}(1+\cos\theta)} = \sqrt{\frac{1}{2}(1+\sqrt{1-\psi^2})} \tag{5.48}$$

$$\sin\frac{\theta}{2} = \sqrt{\frac{1}{2}(1-\cos\theta)} = \sqrt{\frac{1}{2}(1-\sqrt{1-\psi^2})}, \tag{5.49}$$

we see that the population in the $|0\rangle$ state decreases quadratically as the state enters the $xy$ phase: $f = |\langle 0|\Psi\rangle|^2 \approx 1-\frac{1}{4}\psi^2$. Furthermore, as the system goes deep into the $xy$ phase the wavefunction corresponding to the $xy$-ferromagnet simplifies considerably to:

$$|\Psi\rangle_{xy} = \prod_{i=1}^{N}\left(\frac{1}{\sqrt{2}}|0\rangle_i + \frac{1}{\sqrt{2}}\left(\frac{e^{i\phi}}{\sqrt{2}}|1\rangle_i + \frac{e^{-i\phi}}{\sqrt{2}}|-1\rangle_i\right)\right). \tag{5.50}$$

The $xy$ state in this extreme limit has an intuitive interpretation in terms of the constituent two-component bosons: it is composed of the product of two symmetric superpositions of up and down spins on a site:

$$\left(e^{i\phi/2}|\uparrow_1\rangle + e^{-i\phi/2}|\downarrow_1\rangle\right)\otimes\left(e^{i\phi/2}|\uparrow_2\rangle + e^{-i\phi/2}|\downarrow_2\rangle\right)/2, \tag{5.51}$$

with a phase which indicates the orientation of the magnetization in-plane. This is in stark contrast to the $z$-ferromagnet which consists of up- and down-spins which phase separate into polarized domains.

From this mean field treatment, we can see that one signature of the $xy$ phase immediately becomes visible in the local spin correlation channel used to detect the spin-paired doublons in the spin Mott. Deep in the $xy$ phase the fraction of spin-paired doublons goes to $f = |\langle 0|\Psi_{xy}\rangle|^2 = 1/2$ compared to $f = 1$ for the spin Mott and $f = 1/3$ for a thermal gas. In addition, this treatment shows how the Goldstone mode shows up in the wavefunction: given a phase $\phi$ for the magnetization vector, any uniform rotation of this phase changes the state without changing the energy. In fact, $\phi$ does not show up at all in the energy functional. The lowest contribution of the magnetization phase to the energy comes from spatial deformations of the phase, $\phi(x)$, which in turn become the lowest lying excitations of the ferromagnet, the spin waves of the $xy$ state. In a more realistic treatment of the $xy$ state in one dimension, a situation in which mean field theory is known to be quantitatively incorrect, these spin waves are admixed into the ground state wavefunction by quantum fluctuations, and at finite temperature, by thermal excitations.

Such fluctuations can be described by the spin-spin correlation function:

$$\langle \hat{S}_i^+ \hat{S}_{j\neq i}^- \rangle = f\left(\frac{|x_i - x_j|}{\xi}\right) \tag{5.52}$$

which, in one dimension, is some exponentially decaying function above a critical temperature or a polynomially decaying function below a critical temperature with characteristic length scale set by the correlation length $\xi$, which is a function of the Hamiltonian parameters [137]. Ref. [137] shows a calculation of this phase ordering taking into account quantum and thermal fluctuations. In such a calculation, and in a realistic experiment, the spatial order of the phase is accounted for by the spin-spin correlation function discussed earlier in equation 5.52. The mean-field $xy$ wavefunc-

tion deep in the $xy$-phase, seen in equation 5.50, predicts a correlation function:

$$\langle \Psi_{xy} | \hat{S}_i^+ \hat{S}_{j\neq i}^- | \Psi_{xy} \rangle = 1 \tag{5.53}$$

compared to 0 in the spin Mott. In [137], this correlation is shown to decay exponentially above the transition point and algebraically below the transition point. Fortunately, at short length scales compared to the correlation length, the system appears to follow closely the mean field prediction and the system appears to have long-range order. In our cold atom system, the maximum chain length is $\sim$10 sites, so these calculations show that, at reasonable entropies, $xy$ ordering over the sample size is within reasonable reach.

### 5.6.2 Ramping from Spin Mott to the $xy$ Regime

All the experiments in this section begin with the sample in the spin Mott insulating state of the spin-1 Heisenberg Hamiltonian. At this point, the lattice consists of two 1064 nm beams in the $y$- and $z$-directions at 20 $E_r$ depth and one 810 nm beam in the $x$-direction at a variable lattice depth of 10 to 15 $E_r$ and in the lin$\perp$lin polarization configuration. To begin, we ramp the system into the $xy$ regime of the phase diagram along an "adiabatic" path given by the ramp trajectory shown by an orange arrow in figure 5-17(a). The first, and simplest, ramp shape implemented experimentally was a linear ramp of the liquid crystal voltage from the spin Mott regime to the $xy$ regime of the phase diagram in a variable amount of time. Due to the nonlinear relationship between the liquid crystal voltage and retardance, in addition to the nonlinear relationship between the polarization angle and $U_{\uparrow\downarrow}$, this linear ramp of voltage is not an optimal ramp which is fast in regions of higher gap and slower in regions of smaller gaps. Nevertheless, this is a good starting place for optimizing the system parameters and detection schemes which can be used to characterize and optimize more complex ramp shapes.

To detect the appearance of an $xy$ phase, we begin by measuring the local, on-site correlations between up- and down-spins by looking at the $|0\rangle$ detection channel used

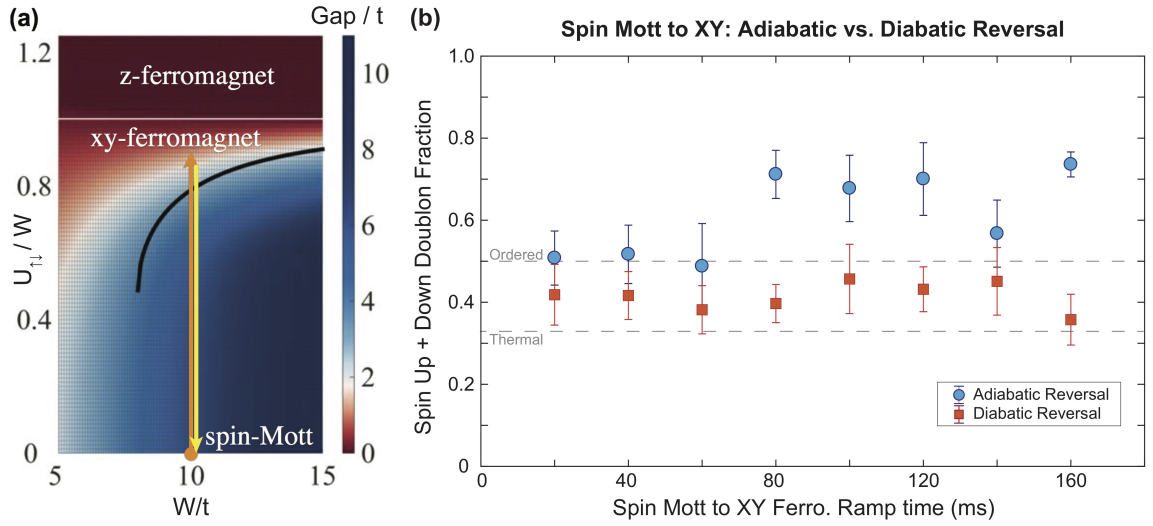


Figure 5-17: Probing the reversibility of an Adiabatic ramp to the $xy$ regime. (a) Phase diagram calculated in ref. [137] showing the crossover from the spin Mott to the $xy$-ferromagnet and an idealized ramp trajectory given by the orange and yellow arrows. (b) Comparison of the state in the $xy$-regime projected onto the $|0\rangle$ state (red squares) versus the state which is adiabatically ramped back to the spin Mott (blue circles). Dotted lines show the limiting cases of a thermal sample at 1/3 and, for the diabatic reversal, a long-range ordered $xy$ state at 1/2.

to detect the spin Mott insulator. Although seeing a spin-paired doublon fraction of 1/2 in this signal is suggestive of $xy$ order it does not constitute a conclusive detection of this order. In short, this is because this measurement is probing the overlap of the wavefunction with the $|0\rangle$ state at zero range, whereas the $xy$ phase is characterized by a spatial ordering of the superposition phase $\phi(x)$. An alternate, although indirect method, to check for the preparation of the $xy$ ferromagnetic ground state is to test the reversibility of the ramp from the spin Mott. If the ramp does not create any excitations and the system remains in a pure state, then the magnetically ordered state we ramp into should be fully reversible such that returning to the spin Mott – where we can quantitatively measure the entropy and temperature – can be achieved with high fidelity. These two methods form the backbone of the initial set of experiments towards ramping from the spin Mott to the $xy$ ferromagnet.

Practically, these two measurements are accomplished by comparing the results of two different return ramps. First, after entering the $xy$ phase we analyze the spin-paired doublon fraction of the resulting state by rapidly jumping back to the spin

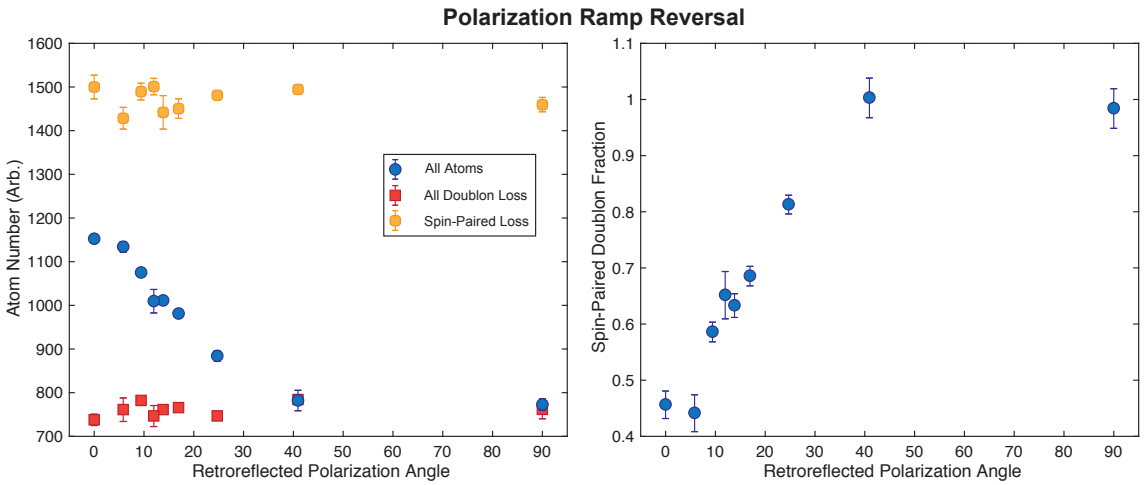


Figure 5-18: Adiabatic ramp reversal for different turn-around polarization angles. (Left) Raw data and (right) spin-paired doublon fraction as a function of different turn-around polarization angles. The total number of doublons (left, red squares subtracted from yellow dots) does not change during the ramp, indicating no pair-breaking is occurring. (Right) Consistent with the gapped spin Mott, the spin-paired fraction is robust to small rotations of the polarization, but begins to show strong heating below 30°, before the expected transition to the $xy$-phase. Closer to the $xy$-transition around $\sim 10°$ the system shows a sharp drop in the spin-paired doublon fraction.

Mott in order to project the local doublon spin composition onto the basis of states of the spin Mott. The resulting spin-paired doublon fraction is shown by the red squares in figure 5-17(b). A perfectly ordered $xy$ ferromagnet would have a local fraction of $f = 1/2$ denoted by the upper dotted line in 5-17(b), compared to a thermal state for which $f = 1/3$ shown by the lower dotted line. Encouragingly, we observe a spin polarization between these two limits, suggesting the presence of some correlation in the system. Whether this arises due to a mixed state or a pure state is probed in by a second adiabatic ramp back to the spin Mott along the entrance path. The resulting spin polarization recovered with this ramp is shown by the blue dots in figure 5-17(b). The reduction of the polarization from 100% to 70% indicates a ramp which produces a nearly four-fold increase in the spin entropy from 0.2 $k_B$ to 0.8 $k_B$ by examining figure 5-15. Nevertheless, figure 5-17(b) possibly indicates that some part of the state is retrievable upon a ramp reversal.

An interesting question to ask with this setup is where along the adiabatic pathway

the ramp stops becoming adiabatic and this significant heating shows up? To answer this question, we use the adiabatic ramp reversal from above, but instead of going all the way to the $xy$ regime of the phase diagram, we stop the ramp at different polarization angles and reverse back to the spin Mott. The result of these adiabatic ramp reversals is shown in figure 5-18. From the data we can clearly see that for small rotations of the retroreflected polarization the spin Mott is robust and maintains near perfect spin polarization, consistent with the picture of the spin Mott as a highly gapped state robust to small perturbations. However, in the regime of polarization angles below 45° the spin-paired doublon fraction starts to reduce, dropping to <70% by the time the polarization gets to ∼20°. For the calculated exchange rates at 11 $E_r$, the spin Mott to $xy$ ferromagnet transition should happen below 10°, so in the regime of larger polarization angles we are still in the spin Mott phase, despite the fact that we see the spin-paired doublon fraction begin to reduce. Finally, as the polarization ramp goes fully to lin‖lin the spin-paired doublon population drops even farther to below 50% consistent with the shorter ramp times seen in figure 5-17(b).

Figure 5-18 clearly shows that we are observing behavior not consistent with entropy creation at the crossover to the $xy$-ferromagnet, but instead happening much earlier in the ramp of $U_{\uparrow\downarrow}$. In the remainder of this chapter, we discuss several possible mechanisms by which the spin-paired fraction can decay outside of those contained within the $n = 2$ Hilbert space and the spin-1 mapping.

### 5.6.3 Particle and Hole Motion in the Mott State

One possible mechanism behind the anomalous decay of the spin-paired doublon fraction comes from the direct tunneling of particles and/or holes in the Mott state. Whether these excitations are present in the initial state due to the finite temperature of the sample or they are dynamically produced by some intrinsic heating mechanism, in essence they can cause the spin-paired doublon fraction to decay because direct tunneling, $t$, in the spin chain is a large energy scale compared to $J_\perp = \frac{4t^2}{U_{\uparrow\downarrow}}$ and $u = (W - U_{\uparrow\downarrow})$ in the regime close to the $xy$ transition. To illustrate this, consider a chain of atoms in the $|0\rangle$ state of the spin Mott with one spin-down hole present

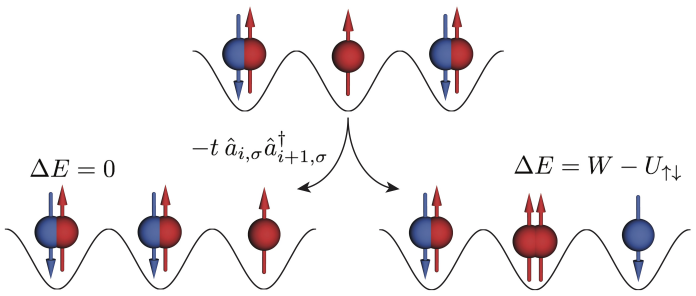


the hole can thermalize and transfer its kinetic energy t into spin excitations ---- but only until its energy is used up

Figure 5-19: Spin flips induced by direct tunneling of holes in the Mott state. Starting from a spin Mott state with one hole, the hole is able to propagate through the spin chain with a rate set by the tunneling energy scale, $t$. In the regime where the hole tunneling bandwidth is greater than the energy splitting between spin states, $u = W - U_{\uparrow\downarrow}$, hole propagation can induce spin flips.

shown in figure 5-19. The hole can tunnel through the spin chain at a rate $t$ because its motion is not blocked by the interaction with another hole on adjacent sites. In this sense, the Mott insulating state can be seen as a hole vacuum – the ground state of a Mott insulator with one hole is the hole delocalized over the whole sample, practically destroying the Mott state due to the addition of low-lying excitations of the hole wavefunction. From the initial state of figure 5-19, direct tunneling of the hole can couple the system to two possible types of final states: one where the hole does not produce a spin excitation, and another where the hole flips the local spin state from a $|0\rangle$ spin to a $|1\rangle$ spin. In the $xy$ regime where $U_{\uparrow\downarrow} \approx W$ the energetic difference between these two final states is small compared to the tunneling energy scale.

For example, at 10 $E_r$ the bandwidth is $4 \times 67 = 268$ Hz in the $\lambda = 810$ nm lattice. Compared to the interaction energy, $u$ – which changes from 860 Hz at a polarization angle of 70° to 860 - 730 = 130 Hz at a polarization angle of 20° – the bandwidth for single particle tunneling becomes dominant around a polarization angle of 30°, consistent with the polarization angles at which the spin-paired doublon fraction begins decaying in figure 5-18. At the same lattice depth and 30° polarization angle, the exchange term, $J_\perp$ is 22 Hz so the critical parameter $\frac{J_\perp}{u} \approx \frac{1}{12}$ indicates that the system should still be well within the spin Mott phase.

While the argument above is formulated for a hole excitation of the spin chain,

the same argument can be applied to an excess particle excitation of the spin chain with the addition of an extra bosonic enhancement of the tunneling bandwidth. The situation becomes more complicated when we consider that in order to destroy all ordering in the spin chain, particle and hole excitations must travel across the whole spin chain but in a harmonic trap are largely localized to the edges of the spin chain close to the superfluid phase that exists on the outside of the Mott state. This highlights the important role that understanding the harmonic confinement of the cloud has in understanding heating due to particle and hole excitations.

### 5.6.4 Effects of the Harmonic Trap

Looking back at figure 5-14(a), note that the total number of doublons in the sample is decreasing as the polarization is changed from the lin$\perp$lin polarization to the lin$\parallel$lin polarization. This reflects the fact that in the harmonic trap changing $U_{\uparrow\downarrow}$ changes the equilibrium Thomas-Fermi profile for the two-component BEC, and therefore at fixed mean atom number the number of doublons in the Mott state changes as well. When the system is initialized in the spin Mott with lin$\perp$lin polarization configuration, we can picture the state as two $n = 1$ Mott states for each spin which are interlaced between each other and as such do not interact. In this regime, the majority of the cloud is in an $n = 2$ state because the pairing energy of two spins is very high, set by the intra-spin interaction $W$. However, as we ramp towards the lin$\parallel$lin polarization configuration, the emergence of the inter-spin interaction energy scale, $U_{\uparrow\downarrow}$, means that the ground state intrap density distribution has significant $n = 1$ component. This highlights an issue the harmonically trapped system exhibits when $U_{\uparrow\downarrow}$ is ramped in order to move through the magnetic phase diagram, dynamically ramping the polarization of the spin-dependent lattice creates a non-equilibrium density distribution.

This non-equilibirum density distribution creates several effects which we will need to take into account in a harmonic trap. One is that the system, in order to relax to the ground state distribution, wants to break doublons on the edges of the cloud into singly occupied sites because the repulsive energy of a doublon is greater than

the potential energy added by placing a single particle farther out in the harmonic trapping potential. The process of breaking a doublon is suppressed in the strongly interacting regime to first order by energy conservation; the energy of a $|0\rangle$ doublon is $U_{\uparrow\downarrow}$, which, compared to the energy of the two single atom states after breaking the pair $(V_{\text{trap}}(x_f) - V_{\text{trap}}(x_i)) + 2\langle E_{\text{bandwidth}}\rangle$, can suppress the breaking of a pair [165]. However, in the regime of polarization angles where $U_{\uparrow\downarrow} \sim t$, the pairs in the $|0\rangle$ state are not protected by repulsive energy and can resonantly tunnel and relax into an $n = 1$ state. When $U_{\uparrow\downarrow}$ gets large, the relaxation of doublons to a state of two singly occupied sites happens at second order on a time scale set by the amplitude $t^2/U_{\uparrow\downarrow}$. As a result, this decay mechanism is assumed to be slow [165] and only effects a few doublons on the edge of the $n = 2$ state.

should be energetically forbidden

Therefore, with this mechanism of pair breaking in mind, we have two options for avoiding the regime where $U_{\uparrow\downarrow} \sim t$, we can either ramp up into the spin Mott in a regime where $t < U_{\uparrow\downarrow} < W$, or we can ramp into the spin Mott where $U_{\uparrow\downarrow} \approx 0$, and quickly jump into the regime where $t < U_{\uparrow\downarrow} < W$, in order to protect those pairs on the edge of the could from decaying. Experimentally, we have implemented both and choose to work with the former configuration purely for technical reasons: the rotation rate of the liquid crystal device is rather slow compared to tunneling rates. Unfortunately, initializing the spin Mott in a polarization configurations away from lin$\perp$lin does not significantly change the results of figures 5-17 and 5-18.

both can decay, since the band has a WIDTH of t.

Another effect which arises due to the harmonic trap is the equilibration of spin temperatures in the $n = 1$ shell with the temperatures in the $n = 2$ shell. The $n = 1$ state does not have a spin Mott ground state, so the spins here remain unordered, and the spin entropy and temperature correspondingly high, as a function of $U_{\uparrow\downarrow}$. As the spin Mott is ramped into the $xy$ state particles from the $n = 1$ shell can either tunnel into the core of the Mott state via the distillation of holes [167], or high temperature spins can enter from the boundary of the $n = 1$ and $n = 2$ states by spin exchange, $J_\perp$. These two processes will cause the spin temperature in the core of the Mott state to equilibrate, after sufficient hold times, with the charge degree of freedom. The regime necessary for the observation for $xy$ ordering is that the equilibration

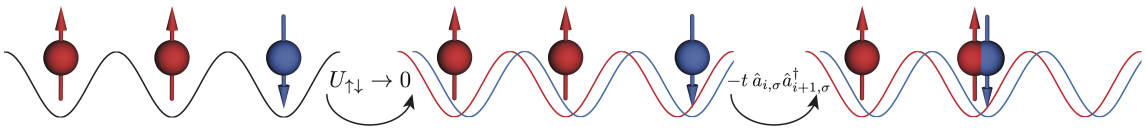


Figure 5-20: False doublon signal arising from the $n = 1$ Mott. In the $n = 1$ regions outside of the central core of $n = 2$ states, a spin-paired doublon signal can arise in the polarization ramp from the $xy$-regime to the spin Mott regime when ramping $U_{\uparrow\downarrow}$ to zero removes the interaction blockade for a $|\downarrow\rangle$ atom to tunnel onto a site with an $|\uparrow\rangle$ atoms.

time happens primarily with the exchange time times the size of the spin chain, $\tau_{\text{exch.}} \sim 2\pi N/J_{\perp} \sim 100$ ms for a 10-site chain, instead of driven by direct tunneling of holes happening on timescales, $\tau_{\text{tun.}} \sim 2\pi N/t \sim 10$ ms. In the experiment, this means that the entropy per particle we observe after a ramp into the Mott state and then reversing back to BEC should be sufficiently low such that we expect less than one hole per one-dimensional chain in the core of the Mott plateau.

Not sure: for 50 % holes, the current would be t. But for one hole per chain, the current should be t/N, and the relaxatio time N^2/t.

One final effect of the presence of a harmonic trap that can effect our measurements in the doublon channel is a false spin-correlation signal that can arise from the $n = 1$ plateau. Beginning with an infinite spin temperature $n = 1$ Mott insulator in a spin independent lattice – the regime the $n = 1$ shell around the $n = 2$ atoms should be in with the lin$\|$lin polarization corresponding to the $xy$ regime – if we then adiabatically ramp the lattice polarization to lin$\perp$lin and then freeze the atoms in place in order to enter the detection sequence as shown in figure 5-13 we can end up with a fake doublon signal. This false signal arises due to tunneling events occurring in the regime where $U_{\uparrow\downarrow} \approx 0$ as depicted in figure 5-20. If the initial state contains an up atom in a site adjacent to a down atom and the up or down atom tunnels to the adjacent site as $U_{\uparrow\downarrow} \to 0$, then in the doublon detection sequence, when these sites are merged the two atoms will be lost, mimicking a doublon signal that did not exist in the initial state. As a result, one interpretation of the spin revival seen in figure 5-17 is that the experiment does not discriminate which part of the cloud the revival signal arose from and as a result we cannot tell whether it comes from the cold inner part of the cloud or is a fake signal from the $n = 1$ wings of the cloud.

This effect can be eliminated if the atoms occupy a uniform box potential instead

of a harmonic trap. Recent progress in this direction raises the possibility of such a solution [52, 120, 34, 115], and will be discussed in more detail in the next chapter.

In summary, looking back at figure 5-18, we hypothesize that this finite hole occupation probability is one major contributing factor to the reduction of the spin-paired doublon fraction in the spin Mott phase of the adiabatic ramp reversal. The combination of all the factors discussed above suggests the following comprehensive picture: a finite hole occupation probability per spin chain, combined with the non-equilibrium density profile created by tuning $U_{\uparrow\downarrow}$ and the natural equilibration of the spin temperatures of the $n = 1$ and $n = 2$ Mott shells, provides a mechanism shown in figure 5-19 by which a hole propagating through the spin chain can flip the doublon spin state, driving the low temperature $xy$ state towards higher temperatures and correspondingly lower spin-paired doublon fraction.

### 5.6.5 Effects of Magnetic Field Gradients

A final complication that we need to account for arises from the effect of a magnetic field gradient on the phase of the $xy$-state. A magnetic field gradient causes the spin precession frequency on each site of the lattice to be different, causing dephasing of the spin-up and spin-down superposition phase across the spin chain, effectively imprinting an unwanted spatially-varying phase $\phi(x)$. In the limit of a large field gradient per lattice site, $\delta h_z$, the spin state is localized by the addition of a large term: $\delta h_z \sum_i i\hat{S}_i^z$ to the Hamiltonian. As such, we wish to eliminate any such terms competing with the spin-exchange process.

Such magnetic field gradients can be detected by looking at the intrap density distribution of a two-component BEC, without applying a lattice, and varying a gradient compensation field [161]. Such a measurement of the magnetic field gradient is shown in figure 5-21. The current in the compensation coil which produces a reversal of the relative positions of the different atomic spins signals the compensation current for which the gradient is zeroed. This procedure is repeated to compensate for magnetic field gradients along the ∼9 G bias field direction as well as to compensate for field curvature in the other, transverse, directions. We can then evaluate the success

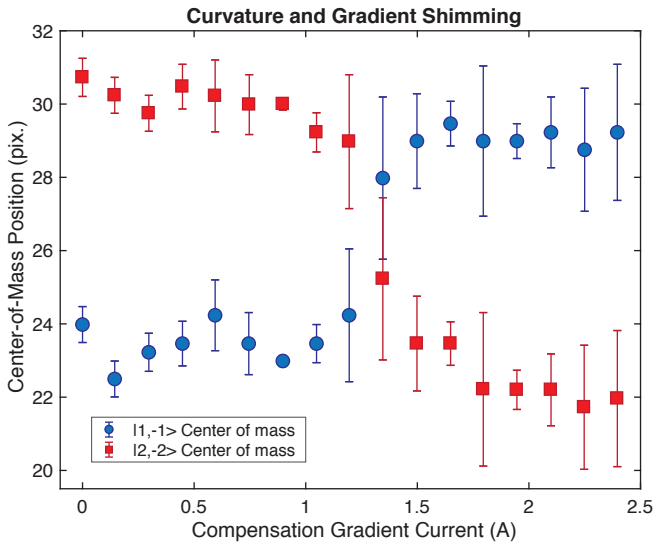


Figure 5-21: Minimizing residual magnetic field gradients. Magnetic field gradients along the bias direction and magnetic field curvature in the transverse directions is measured and compensated for by active cancellation. The effect of residual gradients and curvature is measured by finding the cross-over point where the two spins in a two-component BEC change position in the harmonic trap in response to an externally applied field.

of such a scheme in extending the coherence time of a superposition of spin states by performing Ramsey spectroscopy on the cloud. Figure 5-22 shows the evolution of the contrast of Ramsey fringes before (a) and after (b) the compensation of the gradient and curvature fields in the system. Without compensation, the coherence time of a spin superposition is short, $\sim$5 ms, comparable to the fastest exchange rate in a one-dimensional chain. This is alleviated by three dimensional compensation of the gradient and curvature, resulting in a spin coherence time exceeding 60 ms, much slower than the exchange rate in our system. As a result, the coherence length of the $xy$ state should not be limited by the residual magnetic fields. Note that in figure 5-22 after a short time the Ramsey fringes are not reproducible but fluctuate from shot-to-shot due to a fluctuating background field of a few mG. For the $xy$-state, a uniform, fluctuating background field does not couple to excitation terms in the spin Hamiltonian.

After addressing the issues with the harmonic trapping potential and eternal magnetic field gradients discussed above, the current state-of-the-art for the experiment is

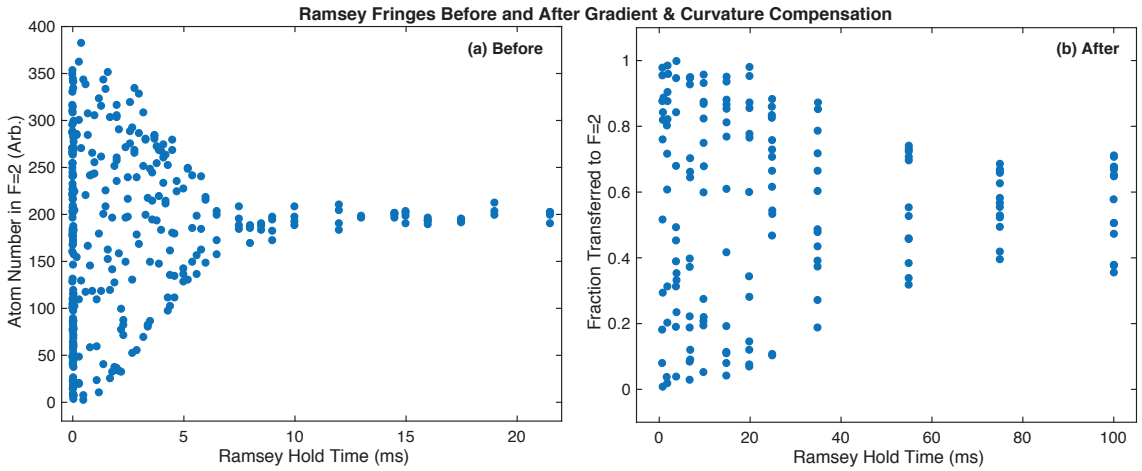


Figure 5-22: Increased Ramsey coherence time from gradient compensation. (a) Field gradients cause Ramsey dephasing times of ∼5 ms, which may be faster than the superexchange time, leading to a localization of the spin wavefunction in the $xy$-phase. (b) Compensation of inhomogeneous fields leads to a greatly increased Ramsey coherence time exceeding 60 ms.

to make progress on preparing colder samples with fewer holes in each chain in addition to optimizing the shape of the ramp from the spin Mott to the $xy$ ferromagnetic state such as to make the coldest final state in a finite time ramp. Progress along both fronts are ongoing in the lab. A final direction is in developing better probes of long-range ordering such as to better characterize any magnetic correlations that appear in the $xy$-regime. A promising development in this direction is the construction of a quantum gas microscope with single-site resolution.

# Chapter 6

# Conclusions and Outlook

The work detailed in this thesis is based on the central themes of artificial magnetism and artificial magnetic fields. Progress in both of these areas is largely enabled by the clean and controllable potentials created in ultracold atom systems as well as the isolated nature of the samples from external reservoirs. Two examples of new opportunities this level of isolation and control affords us include the ability to shape the single-particle spectrum using Floquet engineering as well as the ability to independently control the potentials of different spin states to exert control over parameters of the many-body Hamiltonian.

In chapter 3, we developed and demonstrated one particularly powerful technique for creating synthetic magnetic states and topological states of matter using magnetic field gradients and far-detuned lasers. Most importantly, we have shown how to shake a many-body system to order to generate arbitrarily strong, uniform synthetic gauge potentials while simultaneously maintaining a low entropy state. The excellent signal-to-noise of measurements in atomic systems, especially with Bose-Einstein condensates, highlights the power of this platform no only to realize phases of matter not accessible to condensed matter systems but also to provide simple, intuitive systems to teach new physics. A prime example is how the superfluid diffraction pattern in time-of-flight images reveal the gauge-dependent momenta of the wavefunction. In addition, the ability to prepare a low entropy state in a three-dimensional lattice highlights the power of these systems to tune the interactions from a non-interacting

system to a strongly interacting system in a precisely controllable manner. An additional power of this system is discussed next in chapter 4, where we show how this work highlights the power of laser-assisted tunneling as a tool to realize other paradigmatic effects of condensed matter physics, such as the quantum spin Hall effect and the Weyl Hamiltonian, or to even engineer flux configurations which are not realizable in condensed matter contexts.

In chapter 5, we discussed the realization of the spin-1 Heisenberg chain in a two-component, $n = 2$ state. The unique properties of the $n = 2$ state with an on-site symmetry breaking term is used in conjunction with a spin-dependent lattice to prepare the spin Mott insulating ground state of the Heisenberg model with a spin entropy below 0.2 $k_B$ per spin. The cooling power of the spin Mott state is highlighted where adiabatically lowering the many-body gap gives access to temperature scales on the order of 10 pK. Initial experiments exploring the adiabatic preparation of an $xy$-ferromagnetic state from the spin Mott are described, and preliminary results highlight the various challenges faced in realizing such an adiabatic cooling technique. Moving forward, we look to exert even higher levels of control over these systems to move to even lower temperatures and to probe correlations at the single particle level.

## 6.1 A New Quantum Gas Microscope

The development of the quantum gas microscope for imaging single atoms [9, 143, 127, 32, 124, 66, 44] has led to a revolution in the measurement and control capabilities of ultracold atom systems. This technology enables direct *in situ* imaging of the superfluid to Mott insulating phase transition in bosons [10, 143] as well as the band insulating to Mott insulating crossover in fermions [60, 31]. This detection capability has enabled experimental achievements such as simulation of an Ising magnet [145], detection of many-body localization [140], detection of antiferromagnetic correlations – seen first in bulk measurements [61, 68] but later directly imaged with high resolution [18, 30, 41] – and antiferromagnetic ordering [115, 22], among many other results.

One powerful aspect of the quantum gas microscope for the purpose of achieving lower temperatures is the ability to measure temperatures *in situ* enabling, for example, the detection of the superfluid amplitude mode excitation by thermometry in a deep lattice [46]. This local detection ability can in turn be leveraged to create the ability to locally control the many-body state by shaping the external potential on the single-site scale in order to create well-defined potentials important for long-range interacting systems [138], for performing interferometric operations on a many-particle state in order to measure quantities such as entanglement entropy [75], or for creating flat bottomed potentials for entropy redistribution schemes [115].

For the new quantum states described in this thesis, the ability to project and shape the external confining potential in such a way as to realize a uniform box potential in the lattice is an exciting prospect that gives the experiments several key advantages. First of all, as mentioned in chapter 5, as the inter-spin interaction is changed – in order to tune the system through the phase diagram – in a harmonic trap the equilibrium density profile is changes due to the changing repulsive energy of the system. This creates several unwanted effects such as pair-breaking on the edges of the sample and inhomogeneous spin temperatures between $n = 1$ and $n = 2$ portions of the trap. Although these two effects are specific to the Mott insulating phase, generically, any experiment in an inhomogeneously trapped system that calls for dynamically tuning a large energy scale, such as the inter-spin interaction, faces a similar challenge since all broken symmetry phases have low-lying excitations (Goldstone modes) of the order parameter. Second, the projection capability allows the realization of effectively lower temperatures since the regions of high entropy outside of a Mott plateau can be cut away and removed from the sample. In the spin Mott, cutting out the $n = 1$ shell and the superfluid region between the $n = 1$ and $n = 2$ plateaus means that the remaining array is perfectly ordered in both the spin and density degrees of freedom effectively removing all entropy from the resulting state and creating the ideal starting point for ramping to a magnetically ordered state of matter. Finally, the local detection capabilities enabled by a quantum gas microscope allow the realization of effectively lower entropies by post-selection techniques select-

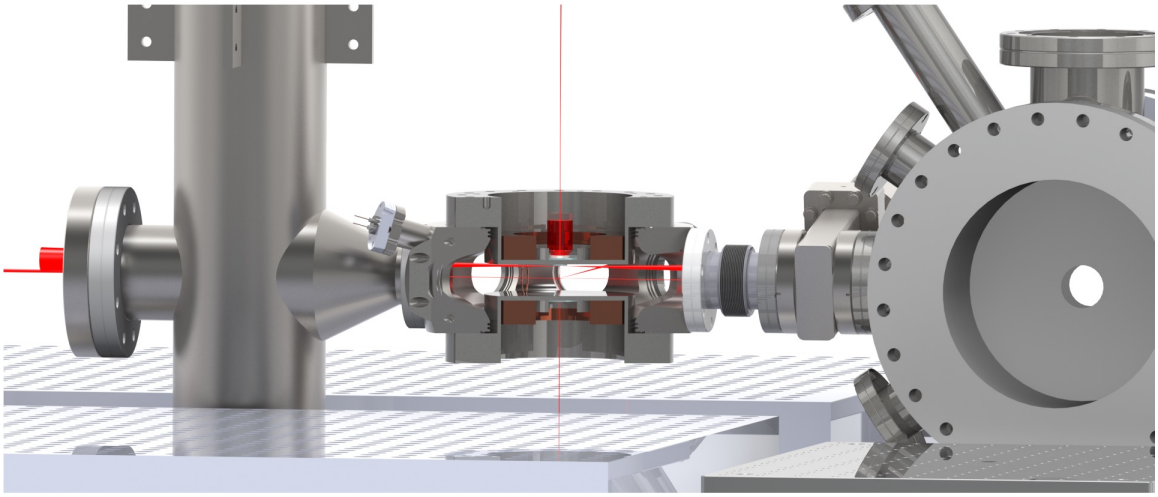

Figure 6-1: A design rendering of the new science chamber.

ing for samples which are free of thermal particle or hole excitations. As a result of these advantages, we have begun the process of upgrading the science chamber of our experiment to a new, improved vacuum chamber capable of housing a quantum gas microscope.

The design of our quantum gas microscope is based around using a long working distance objective in order to work ∼5 mm away from any window or super-polished substrate surface. The objective, designed and manufactured by Special Optics, features a high numerical aperture (NA= 0.80) at a window thickness of 6 mm and a vacuum working distance of 5 mm. The vacuum chamber, shown with a cutout through the chamber in figure 6-1, is designed around this custom objective is meant to solve a myriad of issues which exist with the current vacuum chamber and optical setup and should enable the stability and optical access necessary for single-atom imaging.

First, the design will feature a lower background vacuum pressure by increased conductance to the ion pump and titanium sublimation pump in order to increase the background gas collision lifetime of the atoms in the lattice and allow high fidelity imaging. Next, the side and bottom vacuum windows will be broadband antireflection coated for all the laser wavelengths we might want to use between 532 and 1596 nm, and the top window will be highly transmissive for highly angled rays at 780 nm in

addition to highly reflective at 1064 nm. Seen in figure 6-1, the new chamber features re-entrant bucket windows on the top and bottom to allow for the insertion of the microscope objective and magnetic field coils. The field coils will be wound such as to produce uniform bias and gradient fields in the axis of the microscope in addition to the two lattice axes as well. Each coil will be securely mounted to prevent movement during operation. Between the science chamber and the main chamber, the bellows will be expanded from a 1.33" flange to a 2.75" flange to allow for higher transport efficiency by reducing beam clipping on the inner bore of the Conflat nipple at the same time the total transport distance is reduced. This design also allows vertical transport of the beam from the centerline of the chamber to below the microscope objective, controlled either by an acousto-optic deflector or a galvo mirror and an f-theta lens, for vertical transport and transfer to an accordion lattice trap. The new science chamber design is accompanied by a unibody breadboard design in the horizontal plane which greatly reduces both thermally driven relative drift as well as acoustic and seismic position noise of non-unibody designs. Finally, covering the new setup in an enclosure which blocks ambient air currents and can be temperature controlled below the $<1^{\circ}$C level eliminates residual thermal drift of the optical setup. The exact implementation of these design criteria is beyond the scope of this thesis, and will be addressed in forthcoming theses from the BEC4 lab.

In the big picture, by upgrading our science chamber to a quantum gas microscope, we aim to bring the expertise gained in realizing the Harper-Hofstadter model and the spin-1 Heisenberg chain to the improved detection and control capabilities of the microscope. Among the many future directions for the lab, some exciting possibilities include looking for composite bosons and fermions at low particle densities due to flux-pinning in the interacting Harper-Hofstadter model. Recent numerical results for interacting lattice systems [53] indicate the presence of a $\nu = 1/2$ fractional quantum Hall effect in precisely such a system. In addition to the single-component gas, in two-component gases this flux-pinning mechanism underlies proposals for observing such states as a bosonic integer quantum Hall state [141]. Additionally, by integrating the spin-dependent lattice with the microscope, local detection and pro-

jection capabilities allow the creation of ultra-low entropy samples and enable further studies of magnetic ordering in the spin-1 chain. An interesting merger of off-resonant modulation techniques with a spin-dependent lattice might realize antiferromagnetic exchange couplings and enable a realization of the Haldane phase which exhibits protected edge modes due to the short-range entangled nature of the bulk states.

## 6.2 Outlook

From the broader viewpoint of the field of ultracold atoms, one of the most exciting directions in the field is to create systems with gauge structure that does not, or can not, exist in traditional condensed matter or high energy contexts. While the work described here succeeded in creating a static synthetic gauge field – akin to applying a large magnetic field with a large current in the lab – one interesting prospect is to create *dynamic* synthetic gauge fields where the field configuration and the particle configuration are dynamically coupled to each other via an optical cavity [12, 174, 11]. Such a dynamical coupling has the ability to generate qualitatively new phases of matter based on the principle of cavity-mediated self-organization – where the intracavity field is generated dynamically by the emission of photons from a transverse pumping field which in turn exert forces on the atoms via the atomic recoil and AC Stark shifts – and represents a promising avenue for exploration of new quantum phases [98, 97]. If a dynamically generated cavity field is used to induce a synthetic gauge potential, the power of the ultracold atomic platform is then the ability to tune the coupling of the gauge field to matter, akin to tuning the fine structure constant, $\alpha$, freely. In addition, the gauges that are implemented in cold gases are not limited to Abelian fields, so another exciting direction is to generate non-Abelian gauge fields and even dynamic, non-Abelian fields.

One last direction that emerges from this work is the possibility to create interacting topological states of matter. To date, theory predicts that there are many interacting topological states of matter which do not necessarily have an analogue to non-interacting electrons [109, 29, 158, 159]. Especially for bosonic systems, many

of these states of matter do not have any physical realizations or understanding of the microscopic Hamiltonians from which these states of matter emerge. Given the success of realizing states of matter which are typically inaccessible to condensed matter systems in cold atom systems, hopes of realizing strongly interacting topological states of matter such as a bosonic quantum Hall states lie partly in the flexible platforms of cold atomic and molecular gases.

Many fundamental questions remain and many challenges stand in the way to achieving such goals. For example, it remains an open question how to achieve temperatures into the picokelvin regime in optical lattices or Floquet engineered optical lattices. Also for many dynamic, non-Abelian gauge fields, it remains an open question how to physically generate the new types of interactions necessary for realizing such models [12]. Regardless, cold atoms remains an exciting frontier for such physics and represents a dynamic test-bed where cutting-edge technology and cutting-edge physics collide.

# Bibliography


[1] JR Abo-Shaeer, C Raman, JM Vogels, and Wolfgang Ketterle. Observation of vortex lattices in bose-einstein condensates. *Science*, 292(5516):476–479, 2001.

[2] Monika Aidelsburger, Marcos Atala, Michael Lohse, Julio T Barreiro, B Paredes, and Immanuel Bloch. Realization of the hofstadter hamiltonian with ultracold atoms in optical lattices. *Physical review letters*, 111(18):185301, 2013.

[3] Monika Aidelsburger, Marcos Atala, Sylvain Nascimbène, Stefan Trotzky, Y-A Chen, and Immanuel Bloch. Experimental realization of strong effective magnetic fields in an optical lattice. *Physical review letters*, 107(25):255301, 2011.

[4] Monika Aidelsburger, Michael Lohse, C Schweizer, Marcos Atala, Julio T Barreiro, S Nascimbene, NR Cooper, Immanuel Bloch, and N Goldman. Measuring the chern number of hofstadter bands with ultracold bosonic atoms. *Nature Physics*, 11(2):162–166, 2015.

[5] Ehud Altman, Walter Hofstetter, Eugene Demler, and Mikhail D Lukin. Phase diagram of two-component bosons on an optical lattice. *New Journal of Physics*, 5(1):113, 2003.

[6] Mike H Anderson, Jason R Ensher, Michael R Matthews, Carl E Wieman, and Eric A Cornell. Observation of bose-einstein condensation in a dilute atomic vapor. *science*, 269(5221):198, 1995.

[7] Marcos Atala, Monika Aidelsburger, Michael Lohse, Julio T Barreiro, Belén Paredes, and Immanuel Bloch. Observation of chiral currents with ultracold atoms in bosonic ladders. *Nature Physics*, 10(8):588–593, 2014.

[8] M Ya Azbel. Energy spectrum of a conduction electron in a magnetic field. *Sov. Phys. JETP*, 19(3):634–645, 1964.

[9] Waseem S Bakr, Jonathon I Gillen, Amy Peng, Simon Fölling, and Markus Greiner. A quantum gas microscope for detecting single atoms in a hubbard-regime optical lattice. *Nature*, 462(7269):74–77, 2009.

[10] Waseem S Bakr, Amy Peng, M Eric Tai, Ruichao Ma, Jonathan Simon, Jonathon I Gillen, Simon Foelling, Lode Pollet, and Markus Greiner. Probing

the superfluid–to–mott insulator transition at the single-atom level. *Science*, 329(5991):547–550, 2010.

[11] Kyle E. Ballantine, Benjamin L. Lev, and Jonathan Keeling. Meissner-like effect for a synthetic gauge field in multimode cavity qed. *Phys. Rev. Lett.*, 118:045302, Jan 2017.

[12] Debasish Banerjee, Michael Bögli, M Dalmonte, E Rico, Pascal Stebler, U-J Wiese, and P Zoller. Atomic quantum simulation of u (n) and su (n) non-abelian lattice gauge theories. *Physical review letters*, 110(12):125303, 2013.

[13] Gordon Baym and Christopher Pethick. *Landau Fermi-liquid theory: concepts and applications*. John Wiley & Sons, 2008.

[14] B Andrei Bernevig and Shou-Cheng Zhang. Quantum spin hall effect. *Physical Review Letters*, 96(10):106802, 2006.

[15] Felix Bloch. Über die quantenmechanik der elektronen in kristallgittern. *Zeitschrift für Physik A Hadrons and Nuclei*, 52(7):555–600, 1929.

[16] Immanuel Bloch, Jean Dalibard, and Wilhelm Zwerger. Many-body physics with ultracold gases. *Reviews of modern physics*, 80(3):885, 2008.

[17] Niels Bohr and Léon Rosenfeld. *Collected Works: Vol. 1*. North-Holland Publishing Company, 1972.

[18] Martin Boll, Timon A Hilker, Guillaume Salomon, Ahmed Omran, Jacopo Nespolo, Lode Pollet, Immanuel Bloch, and Christian Gross. Spin-and density-resolved microscopy of antiferromagnetic correlations in fermi-hubbard chains. *Science*, 353(6305):1257–1260, 2016.

[19] Parsa Bonderson, Alexei Kitaev, and Kirill Shtengel. Detecting non-abelian statistics in the $\nu = 5/2$ fractional quantum hall state. *Physical review letters*, 96(1):016803, 2006.

[20] Cl C Bradley, CA Sackett, JJ Tollett, and Randall G Hulet. Evidence of bose-einstein condensation in an atomic gas with attractive interactions. *Physical Review Letters*, 75(9):1687, 1995.

[21] Simon Braun, Jens Philipp Ronzheimer, Michael Schreiber, Sean S Hodgman, Tim Rom, Immanuel Bloch, and Ulrich Schneider. Negative absolute temperature for motional degrees of freedom. *Science*, 339(6115):52–55, 2013.

[22] Peter T Brown, Debayan Mitra, Elmer Guardado-Sanchez, Peter Schauß, Stanimir S Kondov, Ehsan Khatami, Thereza Paiva, Nandini Trivedi, David A Huse, and Waseem S Bakr. Observation of canted antiferromagnetism with ultracold fermions in an optical lattice. *arXiv preprint arXiv:1612.07746*, 2016.

[23] AA Burkov and Leon Balents. Weyl semimetal in a topological insulator multilayer. *Physical review letters*, 107(12):127205, 2011.

[24] William Cody Burton, Colin J Kennedy, Woo Chang Chung, Samarth Vadia, Wenlan Chen, and Wolfgang Ketterle. Coherence times of bose-einstein condensates beyond the shot-noise limit via superfluid shielding. *Physical Review Letters*, 117(27):275301, 2016.

[25] Daniel L Campbell and Ian B Spielman. Rashba realization: Raman with rf. *New journal of physics*, 18(3):033035, 2016.

[26] C Caroli, P Gr De Gennes, and J Matricon. Bound fermion states on a vortex line in a type ii superconductor. *Physics Letters*, 9(4):307–309, 1964.

[27] Alessio Celi, Pietro Massignan, Julius Ruseckas, Nathan Goldman, Ian B Spielman, G Juzeliūnas, and M Lewenstein. Synthetic gauge fields in synthetic dimensions. *Physical review letters*, 112(4):043001, 2014.

[28] Ming-Shien Chang, Qishu Qin, Wenxian Zhang, Li You, and Michael S Chapman. Coherent spinor dynamics in a spin-1 bose condensate. *Nature physics*, 1(2):111–116, 2005.

[29] Xie Chen, Zheng-Cheng Gu, Zheng-Xin Liu, and Xiao-Gang Wen. Symmetry protected topological orders and the group cohomology of their symmetry group. *Physical Review B*, 87(15):155114, 2013.

[30] Lawrence W Cheuk, Matthew A Nichols, Katherine R Lawrence, Melih Okan, Hao Zhang, Ehsan Khatami, Nandini Trivedi, Thereza Paiva, Marcos Rigol, and Martin W Zwierlein. Observation of spatial charge and spin correlations in the 2d fermi-hubbard model. *Science*, 353(6305):1260–1264, 2016.

[31] Lawrence W Cheuk, Matthew A Nichols, Katherine R Lawrence, Melih Okan, Hao Zhang, and Martin W Zwierlein. Observation of 2d fermionic mott insulators of k 40 with single-site resolution. *Physical Review Letters*, 116(23):235301, 2016.

[32] Lawrence W Cheuk, Matthew A Nichols, Melih Okan, Thomas Gersdorf, Vinay V Ramasesh, Waseem S Bakr, Thomas Lompe, and Martin W Zwierlein. Quantum-gas microscope for fermionic atoms. *Physical review letters*, 114(19):193001, 2015.

[33] Lawrence W Cheuk, Ariel T Sommer, Zoran Hadzibabic, Tarik Yefsah, Waseem S Bakr, and Martin W Zwierlein. Spin-injection spectroscopy of a spin-orbit coupled fermi gas. *Physical Review Letters*, 109(9):095302, 2012.

[34] Lauriane Chomaz, Laura Corman, Tom Bienaimé, Rémi Desbuquois, Christof Weitenberg, Sylvain Nascimbène, Jérôme Beugnon, and Jean Dalibard. Emergence of coherence via transverse condensation in a uniform quasi-two-dimensional bose gas. *Nature Communications*, 6, 2015.

[35] Sayan Choudhury and Erich J Mueller. Transverse collisional instabilities of a bose-einstein condensate in a driven one-dimensional lattice. *Physical Review A*, 91(2):023624, 2015.

[36] Eugene D Commins and Philip H Bucksbaum. *Weak interactions of leptons and quarks*. cambridge university press, 1983.

[37] Nigel R Cooper and Jean Dalibard. Reaching fractional quantum hall states with optical flux lattices. *Physical review letters*, 110(18):185301, 2013.

[38] Kendall B Davis, M-O Mewes, Michael R Andrews, NJ Van Druten, DS Durfee, DM Kurn, and Wolfgang Ketterle. Bose-einstein condensation in a gas of sodium atoms. *Physical review letters*, 75(22):3969, 1995.

[39] Gabriele De Chiara, M Lewenstein, and A Sanpera. Bilinear-biquadratic spin-1 chain undergoing quadratic zeeman effect. *Physical Review B*, 84(5):054451, 2011.

[40] Arya Dhar, Maheswar Maji, Tapan Mishra, RV Pai, Subroto Mukerjee, and Arun Paramekanti. Bose-hubbard model in a strong effective magnetic field: Emergence of a chiral mott insulator ground state. *Physical Review A*, 85(4):041602, 2012.

[41] JH Drewes, LA Miller, E Cocchi, CF Chan, N Wurz, M Gall, D Pertot, F Brennecke, and M Köhl. Antiferromagnetic correlations in two-dimensional fermionic mott-insulating and metallic phases. *Physical Review Letters*, 118(17):170401, 2017.

[42] L-M Duan, E Demler, and Mikhail D Lukin. Controlling spin exchange interactions of ultracold atoms in optical lattices. *Physical review letters*, 91(9):090402, 2003.

[43] Tena Dubček, Colin J Kennedy, Ling Lu, Wolfgang Ketterle, Marin Soljačić, and Hrvoje Buljan. Weyl points in three-dimensional optical lattices: synthetic magnetic monopoles in momentum space. *Physical review letters*, 114(22):225301, 2015.

[44] GJA Edge, R Anderson, D Jervis, DC McKay, R Day, S Trotzky, and JH Thywissen. Imaging and addressing of individual fermionic atoms in an optical lattice. *Physical Review A*, 92(6):063406, 2015.

[45] Manuel Endres, Marc Cheneau, Takeshi Fukuhara, Christof Weitenberg, Peter Schauß, Christian Gross, Leonardo Mazza, Mari Carmen Bañuls, L Pollet, Immanuel Bloch, et al. Observation of correlated particle-hole pairs and string order in low-dimensional mott insulators. *Science*, 334(6053):200–203, 2011.

[46] Manuel Endres, Takeshi Fukuhara, David Pekker, Marc Cheneau, Peter Schau$\beta$, Christian Gross, Eugene Demler, Stefan Kuhr, and Immanuel Bloch.

The/higgs/'amplitude mode at the two-dimensional superfluid/mott insulator transition. *Nature*, 487(7408):454–458, 2012.

[47] Patrick Fazekas. *Lecture notes on electron correlation and magnetism*, volume 5. World scientific, 1999.

[48] Gaston Floquet. Sur les équations différentielles linéaires à coefficients périodiques. In *Annales scientifiques de l'École normale supérieure*, volume 12, pages 47–88, 1883.

[49] Takeshi Fukuhara, Sebastian Hild, Johannes Zeiher, Peter Schauß, Immanuel Bloch, Manuel Endres, and Christian Gross. Spatially resolved detection of a spin-entanglement wave in a bose-hubbard chain. *Physical review letters*, 115(3):035302, 2015.

[50] Takeshi Fukuhara, Peter Schauß, Manuel Endres, Sebastian Hild, Marc Cheneau, Immanuel Bloch, and Christian Gross. Microscopic observation of magnon bound states and their dynamics. *Nature*, 502(7469):76–79, 2013.

[51] Bryce Gadway, Daniel Pertot, René Reimann, and Dominik Schneble. Superfluidity of interacting bosonic mixtures in optical lattices. *Physical review letters*, 105(4):045303, 2010.

[52] Alexander L. Gaunt, Tobias F. Schmidutz, Igor Gotlibovych, Robert P. Smith, and Zoran Hadzibabic. Bose-einstein condensation of atoms in a uniform potential. *Phys. Rev. Lett.*, 110:200406, May 2013.

[53] M. Gerster, M. Rizzi, P. Silvi, M. Dalmonte, and S. Montangero. Fractional quantum Hall effect in the interacting Hofstadter model via tensor networks. *ArXiv e-prints*, May 2017.

[54] SM Girvin and AH MacDonald. Off-diagonal long-range order, oblique confinement, and the fractional quantum hall effect. *Physical review letters*, 58(12):1252, 1987.

[55] Steven M Girvin. Introduction to the fractional quantum hall effect. In *The Quantum Hall Effect*, pages 133–162. Springer, 2005.

[56] N Goldman and J Dalibard. Periodically driven quantum systems: effective hamiltonians and engineered gauge fields. *Physical Review X*, 4(3):031027, 2014.

[57] N Goldman, J Dalibard, Monika Aidelsburger, and NR Cooper. Periodically driven quantum matter: The case of resonant modulations. *Physical Review A*, 91(3):033632, 2015.

[58] Nathan Goldman. Characterizing the hofstadter butterfly's outline with chern numbers. *Journal of Physics B: Atomic, Molecular and Optical Physics*, 42(5):055302, 2009.

[59] Nathan Goldman, G Juzeliūnas, P Öhberg, and Ian B Spielman. Light-induced gauge fields for ultracold atoms. *Reports on Progress in Physics*, 77(12):126401, 2014.

[60] Daniel Greif, Maxwell F Parsons, Anton Mazurenko, Christie S Chiu, Sebastian Blatt, Florian Huber, Geoffrey Ji, and Markus Greiner. Site-resolved imaging of a fermionic mott insulator. *Science*, 351(6276):953–957, 2016.

[61] Daniel Greif, Thomas Uehlinger, Gregor Jotzu, Leticia Tarruell, and Tilman Esslinger. Short-range quantum magnetism of ultracold fermions in an optical lattice. *Science*, 340(6138):1307–1310, 2013.

[62] Markus Greiner, Olaf Mandel, Tilman Esslinger, Theodor W Hänsch, and Immanuel Bloch. Quantum phase transition from a superfluid to a mott insulator in a gas of ultracold atoms. *nature*, 415(6867):39–44, 2002.

[63] Markus Greiner, Cindy A Regal, and Deborah S Jin. Emergence of a molecular bose–einstein condensate from a fermi gas. *Nature*, 426(6966):537–540, 2003.

[64] Rudolf Grimm, Matthias Weidemüller, and Yurii B Ovchinnikov. Optical dipole traps for neutral atoms. *Advances in atomic, molecular, and optical physics*, 42:95–170, 2000.

[65] Elmar Haller, Russell Hart, Manfred J Mark, Johann G Danzl, Lukas Reichsöllner, and Hanns-Christoph Nägerl. Inducing transport in a dissipation-free lattice with super bloch oscillations. *Physical review letters*, 104(20):200403, 2010.

[66] Elmar Haller, James Hudson, Andrew Kelly, Dylan A Cotta, Bruno Peaudecerf, Graham D Bruce, and Stefan Kuhr. Single-atom imaging of fermions in a quantum-gas microscope. *Nature Physics*, 11(9):738–742, 2015.

[67] Philip George Harper. Single band motion of conduction electrons in a uniform magnetic field. *Proceedings of the Physical Society. Section A*, 68(10):874, 1955.

[68] Russell A Hart, Pedro M Duarte, Tsung-Lin Yang, Xinxing Liu, Thereza Paiva, Ehsan Khatami, Richard T Scalettar, Nandini Trivedi, David A Huse, and Randall G Hulet. Observation of antiferromagnetic correlations in the hubbard model with ultracold atoms. *Nature*, 519(7542):211–214, 2015.

[69] M. Z. Hasan and C. L. Kane. Colloquium: Topological insulators. *Rev. Mod. Phys.*, 82:3045–3067, Nov 2010.

[70] HF Hess, RB Robinson, RC Dynes, JM Valles Jr, and JV Waszczak. Scanning-tunneling-microscope observation of the abrikosov flux lattice and the density of states near and inside a fluxoid. *Physical review letters*, 62(2):214, 1989.

[71] Sebastian Hild, Takeshi Fukuhara, Peter Schauß, Johannes Zeiher, Michael Knap, Eugene Demler, Immanuel Bloch, and Christian Gross. Far-from-equilibrium spin transport in heisenberg quantum magnets. *Physical review letters*, 113(14):147205, 2014.

[72] Douglas R Hofstadter. Energy levels and wave functions of bloch electrons in rational and irrational magnetic fields. *Physical review B*, 14(6):2239, 1976.

[73] Lianghui Huang, Zengming Meng, Pengjun Wang, Peng Peng, Shao-Liang Zhang, Liangchao Chen, Donghao Li, Qi Zhou, and Jing Zhang. Experimental realization of two-dimensional synthetic spin-orbit coupling in ultracold fermi gases. *Nature Physics*, 12(6):540–544, 2016.

[74] Xiaochun Huang, Lingxiao Zhao, Yujia Long, Peipei Wang, Dong Chen, Zhanhai Yang, Hui Liang, Mianqi Xue, Hongming Weng, Zhong Fang, et al. Observation of the chiral-anomaly-induced negative magnetoresistance in 3d weyl semimetal taas. *Physical Review X*, 5(3):031023, 2015.

[75] Rajibul Islam, Ruichao Ma, Philipp M Preiss, M Eric Tai, Alexander Lukin, Matthew Rispoli, and Markus Greiner. Measuring entanglement entropy in a quantum many-body system. *Nature*, 528(7580):77–83, 2015.

[76] Dieter Jaksch and Peter Zoller. Creation of effective magnetic fields in optical lattices: the hofstadter butterfly for cold neutral atoms. *New Journal of Physics*, 5(1):56, 2003.

[77] Gyu-Boong Jo, Jennie Guzman, Claire K Thomas, Pavan Hosur, Ashvin Vishwanath, and Dan M Stamper-Kurn. Ultracold atoms in a tunable optical kagome lattice. *Physical review letters*, 108(4):045305, 2012.

[78] Robert Jördens, Niels Strohmaier, Kenneth Günter, Henning Moritz, and Tilman Esslinger. A mott insulator of fermionic atoms in an optical lattice. *Nature*, 455(7210):204–207, 2008.

[79] Gregor Jotzu, Michael Messer, Rémi Desbuquois, Martin Lebrat, Thomas Uehlinger, Daniel Greif, and Tilman Esslinger. Experimental realization of the topological haldane model with ultracold fermions. *Nature*, 515(7526):237–240, 2014.

[80] Charles L Kane and Eugene J Mele. Quantum spin hall effect in graphene. *Physical review letters*, 95(22):226801, 2005.

[81] Charles L Kane and Eugene J Mele. Z 2 topological order and the quantum spin hall effect. *Physical review letters*, 95(14):146802, 2005.

[82] Colin J Kennedy, William Cody Burton, Woo Chang Chung, and Wolfgang Ketterle. Observation of bose-einstein condensation in a strong synthetic magnetic field. *Nature Physics*, 11(10):859–864, 2015.

[83] Colin J Kennedy, Georgios A Siviloglou, Hirokazu Miyake, William Cody Burton, and Wolfgang Ketterle. Spin-orbit coupling and quantum spin hall effect for neutral atoms without spin flips. *Physical review letters*, 111(22):225301, 2013.

[84] W Ketterle, DS Durfee, DM Stamper-Kurn, et al. Making, probing and understanding bose-einstein condensates. *arXiv preprint cond-mat/9904034*, 5, 1999.

[85] Wolfgang Ketterle and Martin W Zwierlein. Making, probing and understanding ultracold fermi gases. *arXiv preprint arXiv:0801.2500*, 2008.

[86] Michael Knap, Adrian Kantian, Thierry Giamarchi, Immanuel Bloch, Mikhail D Lukin, and Eugene Demler. Probing real-space and time-resolved correlation functions with many-body ramsey interferometry. *Physical review letters*, 111(14):147205, 2013.

[87] S Kolkowitz, SL Bromley, T Bothwell, ML Wall, GE Marti, AP Koller, X Zhang, AM Rey, and J Ye. Spin–orbit-coupled fermions in an optical lattice clock. *Nature*, 542(7639):66–70, 2017.

[88] Andrey R Kolovsky. Creating artificial magnetic fields for cold atoms by photon-assisted tunneling. *EPL (Europhysics Letters)*, 93(2):20003, 2011.

[89] Mark JH Ku, Ariel T Sommer, Lawrence W Cheuk, and Martin W Zwierlein. Revealing the superfluid lambda transition in the universal thermodynamics of a unitary fermi gas. *Science*, 335(6068):563–567, 2012.

[90] AB Kuklov and BV Svistunov. Counterflow superfluidity of two-species ultracold atoms in a commensurate optical lattice. *Physical review letters*, 90(10):100401, 2003.

[91] Dong Lai, Edwin E Salpeter, and Stuart L Shapiro. Hydrogen molecules and chains in a superstrong magnetic field. *Physical Review A*, 45(7):4832, 1992.

[92] Lev Davidovich Landau, Evgenii Mikhailovich Lifshitz, John Bradbury Sykes, John Stewart Bell, and EH Dill. Electrodynamics of continuous media, 1961.

[93] Robert B Laughlin. Anomalous quantum hall effect: an incompressible quantum fluid with fractionally charged excitations. *Physical Review Letters*, 50(18):1395, 1983.

[94] Robert B Laughlin. Nobel lecture: fractional quantization. *Reviews of Modern Physics*, 71(4):863, 1999.

[95] LJ LeBlanc, K Jiménez-García, RA Williams, MC Beeler, WD Phillips, and IB Spielman. Gauge matters: observing the vortex-nucleation transition in a bose condensate. *New Journal of Physics*, 17(6):065016, 2015.

[96] Yuri Lensky and Colin Kennedy. Scheme for generalized maximally localized wannier functions in one dimension. *arXiv preprint arXiv:1412.3734*, 2014.

[97] Julian Léonard, Andrea Morales, Philip Zupancic, Tobias Donner, and Tilman Esslinger. Monitoring and manipulating higgs and goldstone modes in a supersolid quantum gas. *arXiv preprint arXiv:1704.05803*, 2017.

[98] Julian Léonard, Andrea Morales, Philip Zupancic, Tilman Esslinger, and Tobias Donner. Supersolid formation in a quantum gas breaking a continuous translational symmetry. *Nature*, 543(7643):87–90, 2017.

[99] Guohong Li, Adina Luican-Mayer, Dmitry Abanin, Leonid Levitov, and Eva Y Andrei. Evolution of landau levels into edge states in graphene. *Nature communications*, 4:1744, 2013.

[100] Jun-Ru Li, Jeongwon Lee, Wujie Huang, Sean Burchesky, Boris Shteynas, Furkan Çağrı Top, Alan O Jamison, and Wolfgang Ketterle. A stripe phase with supersolid properties in spin–orbit-coupled bose–einstein condensates. *Nature*, 543(7643):91–94, 2017.

[101] Junru Li, Wujie Huang, Boris Shteynas, Sean Burchesky, Furkan Çağrı Top, Edward Su, Jeongwon Lee, Alan O Jamison, and Wolfgang Ketterle. Spin-orbit coupling and spin textures in optical superlattices. *Physical review letters*, 117(18):185301, 2016.

[102] Lih-King Lim, Andreas Hemmerich, and C Morais Smith. Artificial staggered magnetic field for ultracold atoms in optical lattices. *Physical Review A*, 81(2):023404, 2010.

[103] Y-J Lin, Rob L Compton, K Jimenez-Garcia, James V Porto, and Ian B Spielman. Synthetic magnetic fields for ultracold neutral atoms. *Nature*, 462(7273):628–632, 2009.

[104] Y-J Lin, K Jiménez-García, and IB Spielman. Spin-orbit-coupled bose-einstein condensates. *Nature*, 471(7336):83–86, 2011.

[105] Netanel H Lindner, Gil Refael, and Victor Galitski. Floquet topological insulator in semiconductor quantum wells. *Nature Physics*, 7(6):490–495, 2011.

[106] Ana Lopez and Eduardo Fradkin. Fractional quantum hall effect and chern-simons gauge theories. *Physical Review B*, 44(10):5246, 1991.

[107] Ling Lu, Liang Fu, John D Joannopoulos, and Marin Soljačić. Weyl points and line nodes in gyroid photonic crystals. *Nature photonics*, 7(4):294–299, 2013.

[108] Ling Lu, Zhiyu Wang, Dexin Ye, Lixin Ran, Liang Fu, John D Joannopoulos, and Marin Soljačić. Experimental observation of weyl points. *Science*, 349(6248):622–624, 2015.

[109] Yuan-Ming Lu and Ashvin Vishwanath. Theory and classification of interacting integer topological phases in two dimensions: A chern-simons approach. *Physical Review B*, 86(12):125119, 2012.

[110] BQ Lv, HM Weng, BB Fu, XP Wang, H Miao, J Ma, P Richard, XC Huang, LX Zhao, GF Chen, et al. Experimental discovery of weyl semimetal taas. *Physical Review X*, 5(3):031013, 2015.

[111] BQ Lv, N Xu, HM Weng, JZ Ma, P Richard, XC Huang, LX Zhao, GF Chen, CE Matt, F Bisti, et al. Observation of weyl nodes in taas. *Nature Physics*, 2015.

[112] KW Madison, F Chevy, W Wohlleben, and Jl Dalibard. Vortex formation in a stirred bose-einstein condensate. *Physical Review Letters*, 84(5):806, 2000.

[113] M Mancini, G Pagano, G Cappellini, L Livi, M Rider, J Catani, C Sias, P Zoller, M Inguscio, M Dalmonte, et al. Observation of chiral edge states with neutral fermions in synthetic hall ribbons. *Science*, 349(6255):1510–1513, 2015.

[114] Juan L Manes. Existence of bulk chiral fermions and crystal symmetry. *Physical Review B*, 85(15):155118, 2012.

[115] Anton Mazurenko, Christie S Chiu, Geoffrey Ji, Maxwell F Parsons, Márton Kanász-Nagy, Richard Schmidt, Fabian Grusdt, Eugene Demler, Daniel Greif, and Markus Greiner. Experimental realization of a long-range antiferromagnet in the hubbard model with ultracold atoms. *arXiv preprint arXiv:1612.08436*, 2016.

[116] D McKay and B DeMarco. Thermometry with spin-dependent lattices. *New Journal of Physics*, 12(5):055013, 2010.

[117] Patrick Medley, David M Weld, Hirokazu Miyake, David E Pritchard, and Wolfgang Ketterle. Spin gradient demagnetization cooling of ultracold atoms. *Physical review letters*, 106(19):195301, 2011.

[118] Hirokazu Miyake, Georgios A Siviloglou, Colin J Kennedy, William Cody Burton, and Wolfgang Ketterle. Realizing the harper hamiltonian with laser-assisted tunneling in optical lattices. *Physical review letters*, 111(18):185302, 2013.

[119] Gunnar Möller and Nigel R Cooper. Condensed ground states of frustrated bose-hubbard models. *Physical Review A*, 82(6):063625, 2010.

[120] Biswaroop Mukherjee, Zhenjie Yan, Parth B. Patel, Zoran Hadzibabic, Tarik Yefsah, Julian Struck, and Martin W. Zwierlein. Homogeneous atomic fermi gases. *Phys. Rev. Lett.*, 118:123401, Mar 2017.

[121] Chetan Nayak, Steven H Simon, Ady Stern, Michael Freedman, and Sankar Das Sarma. Non-abelian anyons and topological quantum computation. *Reviews of Modern Physics*, 80(3):1083, 2008.

[122] Holger Bech Nielsen and Masao Ninomiya. The adler-bell-jackiw anomaly and weyl fermions in a crystal. *Physics Letters B*, 130(6):389–396, 1983.

[123] Kostya S Novoselov, Andre K Geim, SVb Morozov, Da Jiang, MIc Katsnelson, IVa Grigorieva, SVb Dubonos, and AAb Firsov. Two-dimensional gas of massless dirac fermions in graphene. *Nature*, 438(7065):197–200, 2005.

[124] Ahmed Omran, Martin Boll, Timon A Hilker, Katharina Kleinlein, Guillaume Salomon, Immanuel Bloch, and Christian Gross. Microscopic observation of pauli blocking in degenerate fermionic lattice gases. *Physical review letters*, 115(26):263001, 2015.

[125] K Osterloh, M Baig, L Santos, P Zoller, and M Lewenstein. Cold atoms in non-abelian gauge potentials: from the hofstadter" moth" to lattice gauge theory. *Physical review letters*, 95(1):010403, 2005.

[126] Belén Paredes, Artur Widera, Valentin Murg, Olaf Mandel, Simon Fölling, Ignacio Cirac, Gora V Shlyapnikov, Theodor W Hänsch, and Immanuel Bloch. Tonks–girardeau gas of ultracold atoms in an optical lattice. *Nature*, 429(6989):277–281, 2004.

[127] Maxwell F Parsons, Florian Huber, Anton Mazurenko, Christie S Chiu, Widagdo Setiawan, Katherine Wooley-Brown, Sebastian Blatt, and Markus Greiner. Site-resolved imaging of fermionic li 6 in an optical lattice. *Physical review letters*, 114(21):213002, 2015.

[128] Michael E Peskin, Daniel V Schroeder, and Emil Martinec. An introduction to quantum field theory, 1996.

[129] Marco Polini, Rosario Fazio, AH MacDonald, and MP Tosi. Realization of fully frustrated josephson-junction arrays with cold atoms. *Physical review letters*, 95(1):010401, 2005.

[130] Stephen Powell, Ryan Barnett, Rajdeep Sensarma, and Sankar Das Sarma. Bogoliubov theory of interacting bosons on a lattice in a synthetic magnetic field. *Physical Review A*, 83(1):013612, 2011.

[131] Mikael C Rechtsman, Julia M Zeuner, Yonatan Plotnik, Yaakov Lumer, Daniel Podolsky, Felix Dreisow, Stefan Nolte, Mordechai Segev, and Alexander Szameit. Photonic floquet topological insulators. *Nature*, 496(7444):196–200, 2013.

[132] CA Regal, Markus Greiner, and Deborah S Jin. Observation of resonance condensation of fermionic atom pairs. *Physical review letters*, 92(4):040403, 2004.

[133] K Rodriguez, A Argüelles, AK Kolezhuk, L Santos, and T Vekua. Field-induced phase transitions of repulsive spin-1 bosons in optical lattices. *Physical review letters*, 106(10):105302, 2011.

[134] Sthitadhi Roy, Michael Kolodrubetz, Joel E Moore, and Adolfo G Grushin. Chern numbers and chiral anomalies in weyl butterflies. *Physical Review B*, 94(16):161107, 2016.

[135] VMH Ruutu, VB Eltsov, AJ Gill, TWB Kibble, et al. Vortex formation in neutron-irradiated superfluid 3he as an analogue of cosmological defect formation. *Nature*, 382(6589):334, 1996.

[136] Indubala I Satija. Hidden quasicrystal in hofstadter butterfly. *arXiv preprint arXiv:1405.0263*, 2014.

[137] Johannes Schachenmayer, David M Weld, Hirokazu Miyake, Georgios A Siviloglou, Wolfgang Ketterle, and Andrew J Daley. Adiabatic cooling of bosons in lattices to magnetically ordered quantum states. *Physical Review A*, 92(4):041602, 2015.

[138] Peter Schauss, Marc Cheneau, Manuel Endres, Takeshi Fukuhara, Sebastian Hild, Ahmed Omran, Thomas Pohl, Christian Gross, Stefan Kuhr, and Immanuel Bloch. Observation of spatially ordered structures in a two-dimensional rydberg gas. *Nature*, 491(7422):87–91, 2012.

[139] U Schneider, L Hackermüller, S Will, Th Best, Immanuel Bloch, TA Costi, RW Helmes, D Rasch, and A Rosch. Metallic and insulating phases of repulsively interacting fermions in a 3d optical lattice. *Science*, 322(5907):1520–1525, 2008.

[140] Michael Schreiber, Sean S Hodgman, Pranjal Bordia, Henrik P Lüschen, Mark H Fischer, Ronen Vosk, Ehud Altman, Ulrich Schneider, and Immanuel Bloch. Observation of many-body localization of interacting fermions in a quasirandom optical lattice. *Science*, 349(6250):842–845, 2015.

[141] T Senthil and Michael Levin. Integer quantum hall effect for bosons. *Physical review letters*, 110(4):046801, 2013.

[142] T Senthil, Ashvin Vishwanath, Leon Balents, Subir Sachdev, and Matthew PA Fisher. Deconfined quantum critical points. *Science*, 303(5663):1490–1494, 2004.

[143] Jacob F Sherson, Christof Weitenberg, Manuel Endres, Marc Cheneau, Immanuel Bloch, and Stefan Kuhr. Single-atom-resolved fluorescence imaging of an atomic mott insulator. *Nature*, 467(7311):68–72, 2010.

[144] C Sias, H Lignier, YP Singh, A Zenesini, D Ciampini, O Morsch, and E Arimondo. Observation of photon-assisted tunneling in optical lattices. *Physical review letters*, 100(4):040404, 2008.

[145] Jonathan Simon, Waseem S Bakr, Ruichao Ma, M Eric Tai, Philipp M Preiss, and Markus Greiner. Quantum simulation of antiferromagnetic spin chains in an optical lattice. *Nature*, 472(7343):307–312, 2011.

[146] Horst L Stormer. Nobel lecture: the fractional quantum hall effect. *Reviews of Modern Physics*, 71(4):875, 1999.

[147] Julian Struck, Malte Weinberg, Christoph Ölschläger, Patrick Windpassinger, Juliette Simonet, Klaus Sengstock, Robert Höppner, Philipp Hauke, André Eckardt, Maciej Lewenstein, et al. Engineering ising-xy spin-models in a triangular lattice using tunable artificial gauge fields. *Nature Physics*, 9(11):738–743, 2013.

[148] BK Stuhl, H-I Lu, LM Aycock, D Genkina, and IB Spielman. Visualizing edge states with an atomic bose gas in the quantum hall regime. *Science*, 349(6255):1514–1518, 2015.

[149] M Eric Tai, Alexander Lukin, Matthew Rispoli, Robert Schittko, Tim Menke, Dan Borgnia, Philipp M Preiss, Fabian Grusdt, Adam M Kaufman, and Markus Greiner. Microscopy of the interacting harper-hofstadter model in the few-body limit. *arXiv preprint arXiv:1612.05631*, 2016.

[150] Shintaro Taie, Hideki Ozawa, Tomohiro Ichinose, Takuei Nishio, Shuta Nakajima, and Yoshiro Takahashi. Coherent driving and freezing of bosonic matter wave in an optical lieb lattice. *Science advances*, 1(10):e1500854, 2015.

[151] Leticia Tarruell, Daniel Greif, Thomas Uehlinger, Gregor Jotzu, and Tilman Esslinger. Creating, moving and merging dirac points with a fermi gas in a tunable honeycomb lattice. *Nature*, 483(7389):302–305, 2012.

[152] Daniel C Tsui. Nobel lecture: Interplay of disorder and interaction in two-dimensional electron gas in intense magnetic fields. *Reviews of Modern Physics*, 71(4):891, 1999.

[153] Ari M Turner, Ashvin Vishwanath, and Chapter Outline Head. Beyond band insulators: topology of semimetals and interacting phases. *Topological Insulators*, 6:293–324, 2013.

[154] R Onur Umucalılar and M Özgür Oktel. Phase boundary of the boson mott insulator in a rotating optical lattice. *Physical Review A*, 76(5):055601, 2007.

[155] D Van Oosten, Peter van der Straten, and HTC Stoof. Quantum phases in an optical lattice. *Physical Review A*, 63(5):053601, 2001.

[156] Michael L Wall, Andrew P Koller, Shuming Li, Xibo Zhang, Nigel R Cooper, Jun Ye, and Ana Maria Rey. Synthetic spin-orbit coupling in an optical lattice clock. *Physical review letters*, 116(3):035301, 2016.

[157] Xiangang Wan, Ari M Turner, Ashvin Vishwanath, and Sergey Y Savrasov. Topological semimetal and fermi-arc surface states in the electronic structure of pyrochlore iridates. *Physical Review B*, 83(20):205101, 2011.

[158] Chong Wang, Andrew C Potter, and T Senthil. Classification of interacting electronic topological insulators in three dimensions. *Science*, 343(6171):629–631, 2014.

[159] Chong Wang and T Senthil. Interacting fermionic topological insulators/superconductors in three dimensions. *Physical Review B*, 89(19):195124, 2014.

[160] Pengjun Wang, Zeng-Qiang Yu, Zhengkun Fu, Jiao Miao, Lianghui Huang, Shijie Chai, Hui Zhai, and Jing Zhang. Spin-orbit coupled degenerate fermi gases. *Physical review letters*, 109(9):095301, 2012.

[161] David M Weld, Patrick Medley, Hirokazu Miyake, David Hucul, David E Pritchard, and Wolfgang Ketterle. Spin gradient thermometry for ultracold atoms in optical lattices. *Physical review letters*, 103(24):245301, 2009.

[162] Xiao-Gang Wen. Topological order: From long-range entangled quantum matter to a unified origin of light and electrons. *ISRN Condensed Matter Physics*, 2013, 2013.

[163] Xiao-Gang Wen and Qian Niu. Ground-state degeneracy of the fractional quantum hall states in the presence of a random potential and on high-genus riemann surfaces. *Physical Review B*, 41(13):9377, 1990.

[164] Hermann Weyl. Elektron und gravitation. i. *Zeitschrift für Physik A Hadrons and Nuclei*, 56(5):330–352, 1929.

[165] K Winkler, G Thalhammer, F Lang, R Grimm, J Hecker Denschlag, AJ Daley, A Kantian, HP Büchler, and P Zoller. Repulsively bound atom pairs in an optical lattice. *Nature*, 441(7095):853–856, 2006.

[166] Zhan Wu, Long Zhang, Wei Sun, Xiao-Tian Xu, Bao-Zong Wang, Si-Cong Ji, Youjin Deng, Shuai Chen, Xiong-Jun Liu, and Jian-Wei Pan. Realization of two-dimensional spin-orbit coupling for bose-einstein condensates. *Science*, 354(6308):83–88, 2016.

[167] Lin Xia, Laura A Zundel, Juan Carrasquilla, Aaron Reinhard, Joshua M Wilson, Marcos Rigol, and David S Weiss. Quantum distillation and confinement of vacancies in a doublon sea. *Nature Physics*, 11(4):316–320, 2015.

[168] Jun Xiong, Satya K Kushwaha, Tian Liang, Jason W Krizan, Max Hirschberger, Wudi Wang, RJ Cava, and NP Ong. Evidence for the chiral anomaly in the dirac semimetal na3bi. *Science*, 350(6259):413–416, 2015.

[169] Su-Yang Xu, Nasser Alidoust, Ilya Belopolski, Zhujun Yuan, Guang Bian, Tay-Rong Chang, Hao Zheng, Vladimir N Strocov, Daniel S Sanchez, Guoqing Chang, et al. Discovery of a weyl fermion state with fermi arcs in niobium arsenide. *Nature Physics*, 2015.

[170] Su-Yang Xu, Ilya Belopolski, Nasser Alidoust, Madhab Neupane, Guang Bian, Chenglong Zhang, Raman Sankar, Guoqing Chang, Zhujun Yuan, Chi-Cheng Lee, et al. Discovery of a weyl fermion semimetal and topological fermi arcs. *Science*, 349(6248):613–617, 2015.

[171] LX Yang, ZK Liu, Yan Sun, Han Peng, HF Yang, Teng Zhang, Bo Zhou, Yi Zhang, YF Guo, Marein Rahn, et al. Weyl semimetal phase in the non-centrosymmetric compound taas. *Nature physics*, 11(9):728–732, 2015.

[172] J Zak. Magnetic translation group. *Physical Review*, 134(6A):A1602, 1964.

[173] Yuanbo Zhang, Yan-Wen Tan, Horst L Stormer, and Philip Kim. Experimental observation of the quantum hall effect and berry's phase in graphene. *Nature*, 438(7065):201–204, 2005.

[174] Wei Zheng and Nigel R Cooper. Superradiance induced particle flow via dynamical gauge coupling. *Physical review letters*, 117(17):175302, 2016.

[175] Wojciech H Zurek, Uwe Dorner, and Peter Zoller. Dynamics of a quantum phase transition. *Physical review letters*, 95(10):105701, 2005.

[176] Martin W Zwierlein, Jamil R Abo-Shaeer, Andre Schirotzek, Christian H Schunck, and Wolfgang Ketterle. Vortices and superfluidity in a strongly interacting fermi gas. *Nature*, 435(7045):1047–1051, 2005.

[177] MW Zwierlein, CA Stan, CH Schunck, SMF Raupach, AJ Kerman, and W Ketterle. Condensation of pairs of fermionic atoms near a feshbach resonance. *Physical Review Letters*, 92(12):120403, 2004.

# Appendix A

# Technical Notes

The BEC4 experiment was originally built in the early 2000's as a general purpose ultracold atoms machine that produced large atom number Rb BECs. As a result, the implementation of the optical lattice was a retrofit to the existing machine. Unfortunately, this means that certain aspects of the machine are not optimal for lattice physics and debugging the setup to reach cold temperatures in the lattice has been a long-running project in the lab. In this appendix, I share with the reader some helpful technical notes for designing an optical lattice of your own.

Beginning with basic infrastructure, the first important step is to actively climate control the lab space. Considering that a typical optical lattice setup has two dipole traps, six lattice beams, and possibly two different imaging beams means that for the experiment to run at its most basic level all ten laser beams must stay aligned and well-calibrated. Typically, the state-of-the-art experiment will also need other novel optical elements, for example a magnetic field gradient and two additional Raman lasers which also must stay well-aligned and calibrated, thereby adding additional levels of complexity to the experiment. For me, the sign of a healthy lattice experiment is the ability to get a cold BEC in the first shot of the day and a cold, $n = 1$ Mott insulator in the second shot of the day. This level of experimental stability frees up the students' time and energy so that they can explore the physics of interest rather than spending a significant fraction of the time in each day re-aligning and re-calibrating lasers.

One crucial aspect for achieving this goal is to control thermal drifts of the beam pointing by stabilizing the temperature to a constant value. The easiest way to achieve this level of thermal control is to work with a small, enclosed area with minimal heat load. As a result, if we were to rebuild BEC4, a crucial element of the redesign would be to add an enclosure to avoid dust and air currents, and to install a laminar flow AC to stabilize the temperature.

A second aspect of a redesigned experimental setup would be the inclusion of a thick, unibody optical breadboard design. One of the largest contributors to the phase noise of the Raman drive comes from the relative motion of two different optical breadboards which hold the retroreflection mirrors for two different lattice directions. As shown in chapter 2, mounting two mirrors on the same optical breadboard greatly reduces the relative position noise of the two surfaces when compared to mounting two mirrors on different breadboards. It is helpful to think of the optical table as the mechanical "ground plane" setting the absolute spatial position of the lattice – analogous to an electrical ground plane on a circuit board which determines the reference voltage for an electrical signal. Just like the quietest analog electrical signals are derived from a system with only one electrical grounding point, the quietest mechanical positions are similarly derived from a system with only one breadboard setting the spatial reference frame for the optical system.

The next time- and frustration-saving aspect of a good lattice experiment is to properly wind magnetic field coils such that the application of a bias field does not introduce gradients and the application of the gradient does not introduce field curvature. An easily-avoidable headache, which plagues many of our experiments, is the fact that the magnetic field coils are wound in such a way that changing the bias field also changes the gradients and curvatures of the field. Ideally, the coils which produce the fields for an experiment should, at the very least, have point-symmetry about the position of the atoms. This ensures that each current element, $d\mathbf{j}$, in Biot-Savart's law which produces a certain field at the position of the atoms, $d\mathbf{B} \propto d\mathbf{j} \times \mathbf{r}$, has an identical current element located exactly at, $-\mathbf{r}$, by which the transverse components of the bias cancel. With a properly wound magnetic field coil, it is then important

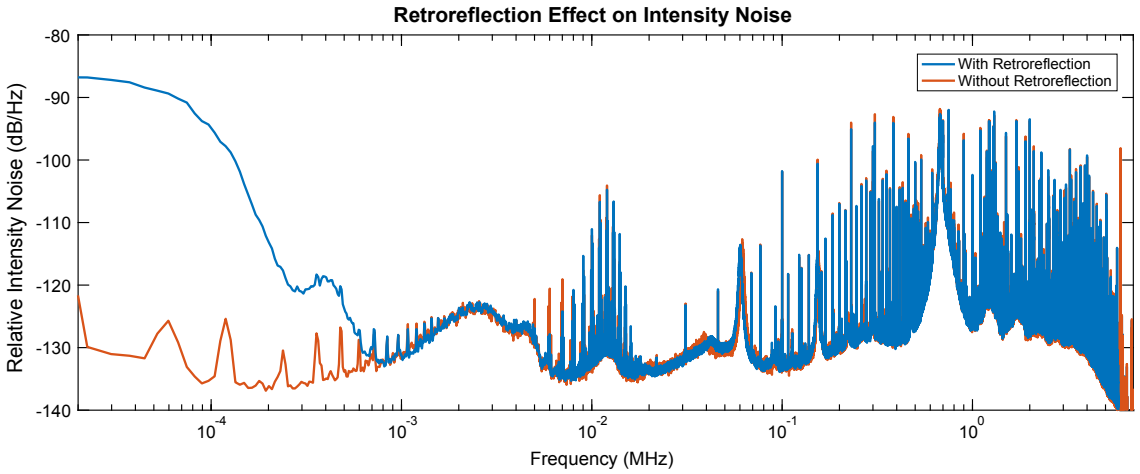


Figure A-1: Intensity noise generated by the retroreflected lattice beam. Comparison of the lattice intensity noise spectrum without any lattice retroreflection (orange) versus the intensity noise spectrum with the lattice retroreflection properly aligned to the atoms (blue). The low frequency noise is a result of the reflection of the retroreflected bean off the fiber tip and interfering with the forward propagating beam.

to align the coils to be oriented coaxial with each other and then rigidly mounted so that they don't move during operation. Note that much of this care can be undone by the ferromagnetism of the steel typically used for the chamber. Especially if the chamber design utilizes welded components, these ferromagnetic components can cause substantial hysteresis and inhomogeneity in the field at the position of the atoms.

Moving from the mechanical to the optical setup, it is very useful to sample the lattice intensity with two independent photodiodes. One photodiode can be used to generate an error signal and used to provide feedback to the AOM RF power, and the other photodiode serves as a truly independent measurement of the residual noise in the transmitted beam. It is good engineering practice to use shot noise limited, transimpedance amplified photodiodes for this application. The main advantage is that the amplification of the photocurrent allows the output of high, $\sim$1 mA, currents with simultaneously high bandwidth. This dual photodiode setup will then allow one to successfully debug issues with the feedback highlighted by the next important step: use an optical isolator to block the retroreflected lattice beam from shining back onto

the optical fiber tip.

Figure A-1 shows the intensity noise spectrum of a lattice laser beam with and without the lattice retroreflection. The appearance of excess noise at low frequencies arises due to the retroreflected beam hitting the fiber tip and the reflection from the surface of the fiber tip once again propagates in the forward direction. In this case the fiber tip is angle-cleaved, so there is a small angle between the beam coming out of the fiber and the one reflected from the surface. However, the angle is small enough, and the beam is large enough that these two beams overlap after the collimator and subsequently interfere with each other. Due to the mounting of the retroreflection mirror on a different optical breadboard from the fiber launch, there is substantial motion between the two surfaces, the spectrum of which is seem as the excess noise in figure A-1. To eliminate this low frequency noise, an optical isolator is used to block the retroreflected lattice beam before it has the chance to enter the intensity stabilization feedback photodiode. For optical surfaces after the isolator, every optical back reflection should be intentionally misaligned from the atoms.

Examining the intensity noise spectrum in figure A-1, we see a dense spectrum of relatively strong noise peaks at high frequencies. Normally, this noise is not a limiting issue because atoms primarily absorb energy at the low-energy scales of the lattice band energies. An important exception to this argument arises when we have multiple lasers beams confining the atoms. Figure A-2 illustrates this effect. In this experiment, a BEC is confined in a crossed dipole trap and is subsequently loaded into the Mott insulating phase at a lattice depth of 20 $E_r$. After a 1 second hold, the lattices are ramped back to the superfluid side of the Mott insulating transition and the momentum distribution is measured in a time-of-flight image.

All the laser beams used for trapping the atoms are derived from the same laser source and their frequencies are deliberately offset in order to avoid unwanted interferences between different directions of the lattice or dipole trapping lasers. One beam that forms part of the dipole trapping potential is offset in frequency from the main laser source by -30 MHz using an AOM. The offset frequency of another beam which forms one direction of a three dimensional lattice is then deliberately set to

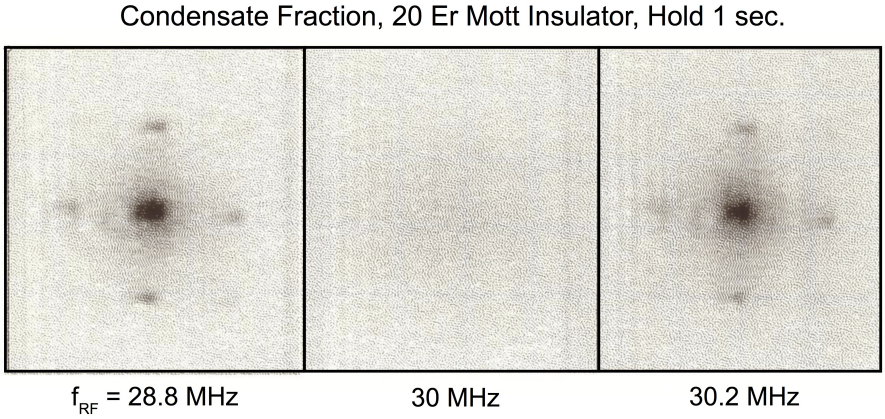


Figure A-2: Effect of opposite AOM frequencies. Two beams derived from the same laser source are passed through two different AOMs. One beam that forms the dipole trapping potential is offset in frequency by -30 MHz. The frequency of another beam which forms one direction of a three dimensional lattice is offset in frequency and changed from +28.8 MHz to +30.2 MHz going from left to right as indicated by the labels. As a test of the heating rate, the atoms are held in a 20 $E_r$ deep Mott insulating state for 1 second, before the state is ramped back across the phase transition to the superfluid state.

be nearly opposite the frequency of the dipole trapping beam and varied from +28.8 MHz to +30.2 MHz. The resulting effect on the recovered condensate fraction is clearly visible in figure A-2 indicating some heating in the lattice due to interference between the two beams when they are offset at exactly opposite frequencies.

To understand this result, we note that any modulation of the carrier at 60 MHz generates frequency sidebands that cannot couple into the optical fiber which carries the light from one part of the experiment to another part of the experiment. However, the same acoustic wave that is applied to the AOM crystal in order to generate the frequency-shifted diffraction orders may reflect from the end of the crystal and propagate in the opposite direction of the applied wave. This backward propagating wave can in turn couple light at a frequency of -30 MHz into the mode which ends up coupled into the fiber. With this picture in mind, we can understand the heating we see in figure A-2 as the interference of this unwanted frequency sideband with the carrier of another laser beam offset by an exactly opposite frequency. Therefore, it is good practice to set the RF frequency driving each AOM to non-opposite values if

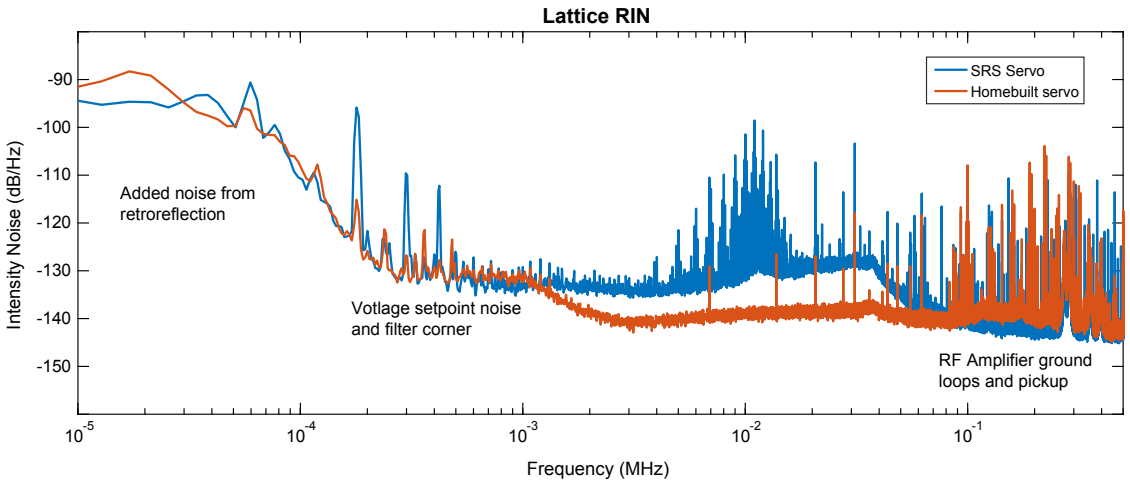


Figure A-3: Improved noise spectrum from a homebuilt servo controller. Comparison of a commercial servo controller to a homebuilt servo controller. In the frequency regime of interest for lattice bandgaps (1-100 kHz), the homebuilt servo easily beats the commercial servo. At higher frequencies the noise arises from ground loops associated with the high power RF amplifier. Known sources of noise are also indicated with text.

the laser light is derived from a common source.

With this understanding in hand, we look back once again at the intensity noise spectrum in figure A-1 and consider the dense spectrum of high frequency peaks. In the simplest three-dimensional lattice setup the presence of five different frequency components each with a similarly noisy high frequency spectrum how can we guarantee that none of these frequency components can interfere and cause heating processes as seen in figure A-2?

The noise spectrum can easily be improved by building custom feedback electronics for the noise-critical parts of the experiment. Figure A-3 shows a comparison of a commercial servo controller compared to a homebuilt servo controller. Noise floors well below those of the commercial servo controller are shown for the frequency regimes of interest for direct excitation of the lattice band gap. Another distinct advantage of the homebuilt servo controller is that the board ground can be easily floated and referenced to the ground defined by the RF amplifier, which in turn can be referenced to the ground of the optical table, such that all ground loops in in the feedback and control network are removed. Removal of all ground loops results in

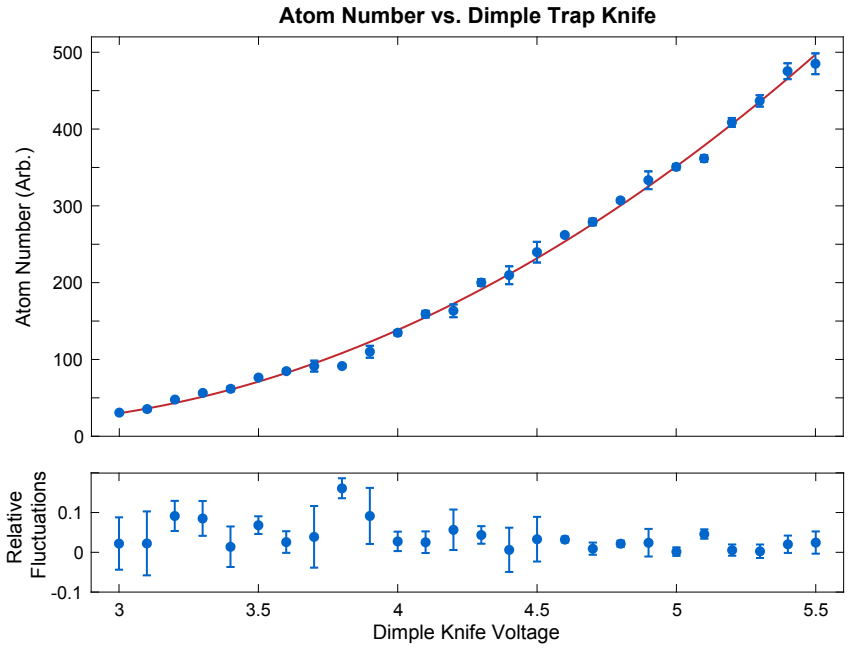


Figure A-4: Precise atom number control using a tightly confining dimple trap. At the highest atom numbers of ∼10000 the relative atom number fluctuations are at the few percent level, limited by detection noise and close to the atomic shot noise limit.

a significant reduction in the number of high frequency peaks visible in the intensity noise spectrum. In addition to lowering the overall intensity noise, the homebuilt servo electronics have the added benefit of reducing the probability of unwanted interferences between different lattice and dipole trapping beams on during an experiment.

Now that we have covered the mechanical, optical, and electronic aspects of a great optical lattice. We turn to the best ways to exert control over the atoms we want to load into our lattice. As we have explored in this thesis, the density of atoms in the lattice is a very important parameter which can qualitatively change the physics of the Mott insulator. Therefore, in order to precisely control the density and thus the location in the superfluid-to Mott insulating phase diagram, we use a tightly confining dimple trap in conjunction with a strong gradient to vary the atom number in our BEC as shown in figure A-4.

Practically, we begin by preparing a large-atom number ($\sim 10^5$) BEC in the $|1, -1\rangle$ hyperfine state in a loosely-confining crossed dipole trap. A tightly confining beam of

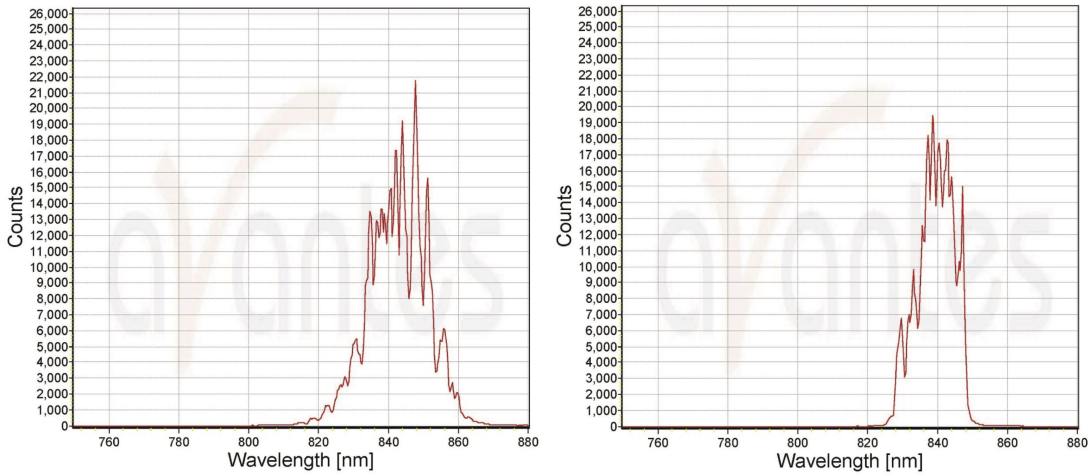


Figure A-5: Spectrum of the superluminescent diode used for the dimple trap. (Left) Superluminescent diode spectrum without any filtering. (Right) Superluminescent diode spectrum with band pass filtering to remove near-resonant photons at 780 nm and 795 nm.

temporally-incoherent light propagating along the vertical direction is then focused with a $\sim$5 $\mu$m spot size onto the center of the condensate and the intensity is ramped to some variable value. A large magnetic field gradient is ramped on in the horizontal direction, removing all residual thermal atoms from the trap. Finally, the magnetic field gradient is ramped off and the tightly confining dimple trap is ramped down to transfer the condensate, with a precisely controllable atom number and no visible thermal fraction, back into the loosely confining crossed dipole trap. The resulting atom number control and stability is shown in figure A-4.

The light source used for the dimple trap is a high-power superluminescent diode with a 50 nm spectrum centered at a wavelength of 840 nm (Superlum SLD-37-HP). The spectrum is filtered to remove all resonant light as shown in figure A-5.